

AN ABSTRACT OF THE DISSERTATION OF

Mark Christopher Surette for the degree of Doctor of Philosophy in Environmental Engineering presented on May 30, 2019.

Title: The Influence of Engineered Surface Coatings on Nanoparticle Aggregation and Corona Formation: Examinations in Simulated and Real Aquatic Media

Abstract approved: _____
Jeffrey A. Nason

Engineered nanomaterials (ENMs) are small anthropogenic colloids with at least one length dimension <100 nanometers. Due to the nature of their use, ENMs are being increasingly released to the environment. Yet the environmental risks posed by ENMs are unknown due to a variety of challenges, including limitations with detecting and quantifying ENMs in environmental systems. To support ENM risk assessments, environmental fate models have been developed to estimate predicted environmental concentrations (PECs). The objective of this research was to (1) aid the refinement of these models by investigating certain processes that have been shown to influence ENM environmental fate and (2) identifying the dominant factors affecting those processes under highly realistic environmental conditions. In particular, this research explores the aggregation behavior of ENMs in freshwater systems and how surface coatings applied to ENMs during their manufacture and the transformation of ENMs during their life-cycle may alter this behavior.

To accomplish this, the aggregation of a suite of model ENMs was first investigated in simulated freshwater media under varying but well-controlled aquatic chemistry. This allowed mechanistic insights into how variations in the physiochemical properties of the surface coatings alter ENM aggregation. This was followed by examining the aggregation of the model ENMs under more realistic conditions using an actual freshwater media. Then, to better understand the form of ENMs being released to the environment, the transformations of the ENMs during conventional wastewater treatment processes was

investigated. The impact of these transformations on the aggregation behavior of the ‘aged’ ENMs was then evaluated and compared against the behavior of their ‘pristine’ analogs in an actual freshwater media.

From this body of work, it was found that variations in the surface coating physiochemical properties can alter the aggregation behavior of ENMs in both simulated and actual freshwater media. Of particular importance was the role of surface coatings in mediating the adsorption of natural organic macromolecules that are ubiquitous in the environment. Likewise, we find that the transformations occurring to the ENMs during conventional wastewater treatment processes were influenced by the initial properties of the surface coatings. More importantly, however, was that the ‘aged’ ENMs no longer resembled their ‘pristine’ analogs, likely due to the formation of a corona layer comprised of organic macromolecules from the wastewater media. In an actual freshwater media, the aggregation behavior of the ‘aged’ ENMs was found to differ from that of the ‘pristine’ ENMs.

These findings have significant implications when trying to understand the processes and factors influencing the environmental fate of ENMs. First, surface coatings influence ENM aggregation behavior in complex aquatic media, which can be explained by studying their behavior in simulated media. However, under highly realistic conditions mimicking the nature of ENMs being released to the environment (i.e., ‘aged’ ENMs to actual freshwater environments), the environmental fate of ENMs is best explored using ‘aged’ ENMs. It is recommended that future studies examining the processes and factors impacting ENM environmental fate consider the life-cycle of ENMs in order to reflect the nature of ENMs released to the environment.

©Copyright by Mark Christopher Surette

May 30, 2019

All Rights Reserved

The Influence of Engineered Surface Coatings on Nanoparticle Aggregation and Corona
Formation: Examinations in Simulated and Real Aquatic Media

by
Mark Christopher Surette

A DISSERTATION

submitted to

Oregon State University

in partial fulfillment of
the requirements for the
degree of

Doctor of Philosophy

Presented May 30, 2019
Commencement June 2019

Doctor of Philosophy dissertation of Mark Christopher Surette presented on May 30, 2019.

APPROVED:

Major Professor, representing Environmental Engineering

Head of the School of Chemical, Biological, and Environmental Engineering

Dean of the Graduate School

I understand that my dissertation will become part of the permanent collection of Oregon State University libraries. My signature below authorizes release of my dissertation to any reader upon request.

Mark Christopher Surette, Author

ACKNOWLEDGEMENTS

First and foremost, I would like to express my sincere gratitude to my doctoral advisor, Dr. Jeffrey A. Nason. Your guidance was instrumental in shaping my education and research. More importantly, your constant support enabled so many wonderful opportunities that I never envisioned undertaking when I first arrived at Oregon State University. Whenever I felt lost or discouraged, a short visit to your office quickly removed any doubts I had. I am forever indebted to you for helping shape my future in such a profound way and look forward to continuing our friendship.

I would also like to express my appreciation to Dr. Ralf Kägi for the opportunity to join your research group. My time at Eawag impacted my research in countless ways, while my time in Switzerland provided fond memories that I will look back on for many years to come. There were many colleagues and friends that made my time at Eawag such an impactful experience but I would particularly like to thank Dr. Denise Mitrano and Brian Sinnet for making my stay so enjoyable.

To the members of my graduate committee, Drs. Field, Harper, Radniecki, and Semprini, thank you for your helpful insights and instructional guidance. During intense research, it is easy to become too narrowly-focused. I always left our meetings with a better sense of perspective and motivation.

To the members of the Nason Research Group, both past and present, thank you for making the day-to-day life of graduate school such a joy. My time at Oregon State resulted in so many amazing friendships. Thank you to all of those in the department who impacted my life in so many positive ways.

None of the experiences I have had over the past few years would have occurred if it were not for the support of my family. To Mark and Julie Spitzer, thank you for letting me move your daughter across the country and around the world in pursuit of my ambitions. I know

how difficult it was for both of you (and the extended family) to say goodbye. To my parents, Robert and Elizabeth Surette, words cannot adequately express my appreciation for all that you have done. You have always supported my dreams, even when those dreams moved me far away. Thank you for the opportunities that you continually make possible.

Lastly, the path I took to complete my doctoral degree is not something I did alone. To my best friend, adventure partner, and wife, Kristen, thank you for your unwavering support as I pursued my goals. If it were not for the love and continual support I received from you, I do not think I would have succeeded. As this chapter in our life together comes to an end, I look forward to the opportunities that our time in Oregon will make possible.

CONTRIBUTION OF AUTHORS

Dr. Ralf Kägi from the Swiss Federal Institute of Aquatic Science and Technology (Eawag) assisted with the experimental design, interpretation of the data, and writing of Chapter 4.

TABLE OF CONTENTS

	<u>Page</u>
1. GENERAL INTRODUCTION	1
1.1 Background	1
1.2 Problem Statement	2
1.3 Objectives	3
1.4 Approach	4
1.5 Significance	6
1.6 Organization	7
2. EFFECTS OF SURFACE COATING CHARACTER AND INTERACTIONS WITH NATURAL ORGANIC MATTER ON THE COLLOIDAL STABILITY OF GOLD NANOPARTICLES	9
2.1 Abstract	9
2.2 Introduction	10
2.3 Experimental	13
2.3.1 Materials	13
2.3.2 Methods	14
2.4 Results and Discussion	17
2.4.1 Influence of PEG Coating Molecular Weight	17
2.4.2 Influence of pH	18
2.4.3 AuNP Stability Mechanisms	19
2.4.4 Influence of Natural Organic Matter	20
2.5 Conclusions	26
2.6 Acknowledgements	28
2.7 Supplementary Information	28
3. NANOPARTICLE AGGREGATION IN A FRESHWATER RIVER: THE ROLE OF ENGINEERED SURFACE COATINGS	30
3.1 Abstract	30
3.2 Introduction	31
3.3 Materials and Methods	33

TABLE OF CONTENTS (Continued)

	<u>Page</u>
3.3.1 Engineered Nanoparticles	33
3.3.2 Complex Aquatic Medium	34
3.3.3 Batch Experiments	35
3.3.4 Time-Resolved Dynamic Light Scattering	36
3.3.5 Electrophoretic Mobility	37
3.4 Results and Discussion	37
3.4.1 Filtered River Water	37
3.4.2 Raw River Water	43
3.4.3 Surface Affinity Functional Assay	52
3.5 Implications on ENP Environmental Fate	55
3.6 Conclusions	56
3.7 Acknowledgements	57
3.8 Supplementary Information	58
4. THE INFLUENCE OF SURFACE COATING FUNCTIONALITY ON THE AGING OF NANOPARTICLES IN WASTEWATER	60
4.1 Abstract	60
4.2 Introduction	61
4.3 Materials and Methods	63
4.3.1 Engineered Nanomaterials	63
4.3.2 Preparation of Wastewater Matrices	64
4.3.3 Batch Experiments (Single Wastewater Matrix)	64
4.3.4 TFF Experiments (Changing Wastewater Matrices)	66
4.4 Results and Discussion	68
4.4.1 Transformations in Single Wastewater Matrices	68
4.4.2 Transformations during Changing Wastewater Matrices	80
4.5 Implications for Modelling ENM Environmental Fate	84

TABLE OF CONTENTS (Continued)

	<u>Page</u>
4.6 Acknowledgements	85
4.7 Supplementary Information	86
5. THE INFLUENCE OF SURFACE COATING FUNCTIONALITY ON THE FATE OF PRISTINE AND WASTEWATER-AGED GOLD NANOPARTICLES IN FRESHWATER	88
5.1 Abstract	88
5.2 Introduction	89
5.3 Materials and Methods	91
5.3.1 Engineered Nanomaterials	91
5.3.2 River Water	92
5.3.3 Engineered Nanomaterial Aging	93
5.3.4 Batch Experiments	94
5.3.5 Supporting Analytics	96
5.4 Results and Discussion	96
5.4.1 Pristine AuNPs in Filtered River Water	97
5.4.2 Pristine AuNPs in Raw River Water	102
5.4.3 Aged AuNPs in Filtered River Water	103
5.4.4 Aged AuNPs in Raw River Water	107
5.5 Implications for ENM Environmental Fate	108
5.6 Acknowledgements	109
5.7 Supplementary Information	109
6. CONCLUSIONS	110
6.1 Summary	110
6.2 Conclusions	112
6.3 Significance	114
6.4 Recommendations for Future Work	114
7. REFERENCES	117

TABLE OF CONTENTS (Continued)

	<u>Page</u>
APPENDICES	129
A. SUPPLEMENTARY INFORMATION – FIRST MANUSCRIPT.....	130
B. SUPPLEMENTARY INFORMATION – SECOND MANUSCRIPT.....	149
C. SUPPLEMENTARY INFORMATION – THIRD MANUSCRIPT.....	172
D. SUPPLEMENTARY INFORMATION – FOURTH MANUSCRIPT.....	206

LIST OF FIGURES

<u>Figure</u>	<u>Page</u>
2.1	Electrophoretic mobility (EPM) for each AuNP type as a function of pH in the presence of 1 mM KCl.....19
2.2	Extent of aggregation ($D_{h,30} / D_{h,0}$) for each AuNP type in the presence of 1 mM KCl and varying ratios of [SRNOM]:[AuNPs].....21
2.3	Electrophoretic mobility of bPEI-AuNPs in the presence of 1 mM KCl as a function of varying ratios of [SRNOM]:[AuNPs] and pH.....23
2.4	Extent of aggregation ($D_{h,30} / D_{h,0}$) for bPEI-AuNPs in the presence of 1 mM KCl as a function of both pH and the ratio of [SRNOM]:[AuNPs].....24
3.1	Average percent removal (η) for each model ENP after 480 minutes and average extent of aggregation ($D_{h,final} / D_{h,initial}$) after 30 minutes and initial aggregation rate ($dD_h/dt _{t \rightarrow 0}$) for each model ENP in filtered WRW..... 38
3.2	Electrophoretic mobility (EPM) of each model ENP in filtered WRW at pH 7.6 ± 0.04 and synthetic WRW at pH 7.0 ± 0.140
3.3	Ratio of initial aggregation rate ($dN_{NP}/dt _{t \rightarrow 0}$) due to homoaggregation alone to the rate due to the combination of homo- and heteroaggregation as a function of d_{NC}47
3.4	Conceptual reactions taking place upon addition of an ENP to an aquatic system containing NOM and NCs.....50
3.5	Conceptual variation of α_{homo} and α_{hetero} for a positively-charged ENP as a function of [NOM] at fixed N_{NP} and N_{NC}51
4.1	Extent of aggregation ($D_{h,final} / D_{h,initial}$) of each AuNP type in each matrix after ≈ 45 minutes.....69
4.2	TEM-HAADF micrographs of PEG-AuNPs, COOH-AuNPs, and bPEI-AuNPs in influent, denitrification and nitrification wastewater matrices after incubating for ≈ 120 minutes.....70

LIST OF FIGURES (Continued)

<u>Figure</u>	<u>Page</u>
4.3	Background-corrected and normalized (A/A_{max}) UV-Vis spectra for PEG-AuNPs, COOH-AuNPs, and bPEI-AuNPs in influent, denitrification and nitrification wastewater matrices.....71
4.4	Electrophoretic mobility (EPM) of each AuNP type in each wastewater matrix at pH 8.0 ± 0.04 and in 1 mM NaCl.....74
4.5	Extent of aggregation ($D_{h,final}/D_{h,initial}$) of each AuNP type during batch experiments and the wastewater matrix exchange procedure with only the influent wastewater matrix after ≈ 45 minutes.....80
4.6	Background-corrected and normalized (A/A_{max}) UV-Vis spectra for PEG-AuNPs, COOH-AuNPs, and bPEI-AuNPs during wastewater matrix exchange testing.....81
4.7	Extent of aggregation ($D_{h,final}/D_{h,initial}$) of each AuNP type during the wastewater matrix exchange procedure after ≈ 120 minutes.....83
5.1	Illustrative example of experimental approach.....95
5.2	$C_{NP,initial}$ and $C_{NP,final}$ for each AuNP type/form in raw and filtered river water98
5.3	Extent of aggregation ($D_{h,final}/D_{h,initial}$) of pristine AuNPs in filtered river water99
5.4	Electrophoretic mobility (μ_E) of each pristine AuNP type in pH-adjusted 1 mM KCl (pH ≈ 7.4) and filtered river water (pH 7.2 – 7.4).....99
5.5	Average background-corrected and normalized (A/A_{max}) UV-Vis spectra of PEG-AuNPs, COOH-AuNPs, and bPEI-AuNPs in various media.....100
5.6	Increase in D_h of aged AuNPs relative to D_h of pristine AuNPs ($D_{h,aged}/D_{h,pristine}$) measured in DDI.....104
5.7	Electrophoretic mobility (μ_E) of each aged AuNP type in wastewater permeate (pH 6.9 – 7.6) and filtered river water (pH 7.2 – 7.4).....104

LIST OF FIGURES (Continued)

<u>Figure</u>		<u>Page</u>
6.1	Illustrative example comparing advantages and disadvantages of working in model and actual environmental systems	112

LIST OF TABLES

<u>Table</u>		<u>Page</u>
2.1	Summary of manufacturer reported specifications for each AuNP type and properties of each surface coating.....	14
3.1	Manufacturer reported specifications and measured characteristics of model ENPs.....	34
3.2	Water quality characteristics of the Willamette River water sampled on June 30, 2017.....	35
4.1	Measured and manufacturer reported properties of pristine AuNPs.....	64
4.2	Average center-to-center separation distance (d_s) and its ratio to nanoparticle diameter ($d_s/2r_c$) calculated for each AuNP type in each wastewater matrix.....	72
5.1	Measured and manufacturer reported properties of pristine AuNPs.....	91
5.2	Water quality characteristics of Willamette River water used in batch tests.....	92
5.3	Water quality characteristics of primary clarifier effluent used in batch tests.....	94

LIST OF APPENDIX FIGURES

<u>Figure</u>	<u>Page</u>
A1. Intensity-weighted hydrodynamic diameter (D_h) as a function of time for 1 mg/L bPEI-AuNPs in the presence of 1 mM KCl and 1.0 mg C/L. SRNOM.....	131
A2. Hydrodynamic diameter (D_h) as a function of PEG surface coating molecular weight (kDa) for the PEG-AuNPs at pH 5.9 ± 0.1	132
A3. Hydrodynamic diameter (D_h) as a function of time for PEG-AuNPs with different molecular weight coatings in the presence of 1 M KCl at pH 5.6 ± 0.1 and 1 M CaCl_2 at pH 7.8 ± 0.1 at various molecular weight.....	133
A4. Hydrodynamic diameter (D_h) as a function of time for the 30 kDa PEG-AuNPs in the presence of 1 mM KCl and at varying mass concentration ratios of [SRNOM]:[AuNPs].....	134
A5. Intensity-weighted hydrodynamic diameter (D_h) of 3 kDa PEG-Amine-AuNP as a function of time in the presence of KCl and CaCl_2 at 40 mM; 120 mM; and 500 mM and pH 5.9 ± 0.9	135
A6. Intensity-weighted hydrodynamic diameter (D_h) of 3 kDa PEG-COOH-AuNP as a function of time in the presence of KCl and CaCl_2 at 40 mM; 120 mM; and 500 mM and pH 6.6 ± 1.2	136
A7. Intensity-weighted hydrodynamic diameter (D_h) of 2 kDa PEG-AuNPs as a function of time in the presence of KCl and CaCl_2 at 40 mM; 120 mM; and 500 mM and pH 5.9 ± 1.0	137
A8. Intensity-weighted hydrodynamic diameter (D_h) of bPEI-AuNPs as a function of time in the presence of KCl and CaCl_2 at 40 mM; 120 mM; and 500 mM and pH 6.0 ± 1.1	138
A9. Intensity-weighted hydrodynamic diameter (D_h) as a function of time for the 3 kDa PEG-Amine-AuNPs at pH 10.0 and bPEI-AuNPs at pH 10.5 in the presence of 500 mM KCl.....	139
A10. Intensity-weighted hydrodynamic diameter (D_h) as a function of pH for the bPEI-AuNPs in the presence of 1 mM KCl.....	140

LIST OF APPENDIX FIGURES (Continued)

<u>Figure</u>	<u>Page</u>
A11a. Intensity-weighted hydrodynamic diameter (D_h) as a function of time for bPEI-AuNPs at varying pH and [SRNOM]:[AuNPs] = 0.007 mg C / mg AuNPs. $I = 1$ mM KCl.....	141
A11b. Intensity-weighted hydrodynamic diameter (D_h) as a function of time for bPEI-AuNPs at varying pH and [SRNOM]:[AuNPs] = 0.07 mg C / mg AuNPs. $I = 1$ mM KCl.	141
A11c. Intensity-weighted hydrodynamic diameter (D_h) as a function of time for bPEI-AuNPs at varying pH and [SRNOM]:[AuNPs] = 0.2 mg C / mg AuNPs. $I = 1$ mM KCl.	142
A11d. Intensity-weighted hydrodynamic diameter (D_h) as a function of time for bPEI-AuNPs at varying pH and [SRNOM]:[AuNPs] = 0.4mg C / mg AuNPs. $I = 1$ mM KCl.	142
A11e. Intensity-weighted hydrodynamic diameter (D_h) as a function of time for bPEI-AuNPs at varying pH and [SRNOM]:[AuNPs] = 0.66 mg C / mg AuNPs. $I = 1$ mM KCl.	143
A11f. Intensity-weighted hydrodynamic diameter (D_h) as a function of time for bPEI-AuNPs at varying pH and [SRNOM]:[AuNPs] = 1.0 mg C / mg AuNPs. $I = 1$ mM KCl.	143
A11g. Intensity-weighted hydrodynamic diameter (D_h) as a function of time for bPEI-AuNPs at varying pH and [SRNOM]:[AuNPs] = 1.3 mg C / mg AuNPs. $I = 1$ mM KCl.	144
A11h. Intensity-weighted hydrodynamic diameter (D_h) as a function of time for bPEI-AuNPs at varying pH and [SRNOM]:[AuNPs] = 1.7 mg C / mg AuNPs. $I = 1$ mM KCl.	144
A12. Extent of aggregation ($D_{h,30} / D_{h,0}$) for the bPEI-AuNPs as a function of pH and [SRNOM]:[AuNPs] in the presence of 1 mM KCl.....	145
A13. Initial aggregation rate (dD_h/dt) and extent of aggregation ($D_{h,30} / D_{h,0}$) for bPEI-AuNPs in the presence of 1 mM KCl as a function of both pH and the ratio of [SRNOM]:[AuNPs].....	147

LIST OF APPENDIX FIGURES (Continued)

<u>Figure</u>	<u>Page</u>
A14. Intensity-weighted hydrodynamic diameter (D_h) as a function of time for 0.66 mg C/L SRNOM in standard synthetic hard freshwater ($I \approx 0.02M$) at pH 8.0 and pH 8.4.....	148
B1. Particle size distribution of natural colloids in raw WRW measured via Coulter Counter.....	152
B2. Normalized absorbance (A/A_0) over time for PEG-COOH- and PEG-AuNPs	160
B3. Standard curve generated during spike/recovery testing.	162
B4. Z-average hydrodynamic diameter (D_h) as a function of time for PEG; PEG-COOH; PEG-Amine; bPEI; and Cit-AuNPs dispersed in filtered WRW.	165
B5. Collision frequency function for each transport mechanism during heteroaggregation (β_{NP-NC}) and the total collision frequency function during heteroaggregation ($^{TOT}\beta_{NP-NC}$) and homoaggregation ($^{TOT}\beta_{NP-NP}$).	168
B6. Characteristic time (τ) for (dashed) homoaggregation and (solid) heteroaggregation as a function of d_{NC} , with α_{homo} and α_{hetero} varying between [$10^{-4} - 10^0$].	170
C1. Concentration of each AuNP remaining in suspension in unaltered wastewater matrices after ≈ 45 minutes	174
C2. Illustrative example of UV-Vis data treatment steps, shown for PEG-AuNPs in influent wastewater matrix.	176
C3. Process flow diagram for TFF system coupled with in-line DLS and UV-Vis detectors.	178
C4. Estimated volume fraction of each wastewater matrix in the TFF system during the double matrix exchange.	179
C5. Illustrative example of UV-Vis data treatment steps during matrix exchange procedure, shown for bPEI-AuNPs in influent wastewater matrix (baseline).	182

LIST OF APPENDIX FIGURES (Continued)

<u>Figure</u>	<u>Page</u>
C6. Intensity-weighted hydrodynamic diameter (D_h) over time for PEG-AuNPs in influent, denitrification, and nitrification wastewater matrices.....	184
C7. Intensity-weighted hydrodynamic diameter (D_h) over time for COOH-AuNPs in influent, denitrification, and nitrification wastewater matrices.....	185
C8. Intensity-weighted hydrodynamic diameter (D_h) over time for bPEI-AuNPs in influent, denitrification, and nitrification wastewater matrices.....	186
C9. Intensity-weighted hydrodynamic diameter (D_h) over time for PEG-AuNPs, COOH-AuNPs, and bPEI-AuNPs in influent wastewater matrix	187
C10. Average red-shift of the primary peak (λ_{max}) in relation to λ_{SPR} for each AuNP type after incubating for 120 minutes in each wastewater matrix	188
C11. Background-corrected and background-corrected and normalized (A/A_{max}) UV-Vis spectra for PEG-AuNPs in influent wastewater matrix	189
C12. Background-corrected and background-corrected and normalized (A/A_{max}) UV-Vis spectra for PEG-AuNPs in denitrification wastewater matrix	190
C13. Background-corrected and background-corrected and normalized (A/A_{max}) UV-Vis spectra for PEG-AuNPs in nitrification wastewater matrix	191
C14. Background-corrected and background-corrected and normalized (A/A_{max}) UV-Vis spectra for COOH-AuNPs in influent wastewater matrix	192
C15. Background-corrected and background-corrected and normalized (A/A_{max}) UV-Vis spectra for COOH-AuNPs in denitrification wastewater matrix	193

LIST OF APPENDIX FIGURES (Continued)

<u>Figure</u>	<u>Page</u>
C16. Background-corrected and background-corrected and normalized (A/A_{max}) UV-Vis spectra for COOH-AuNPs in nitrification wastewater matrix	194
C17. Background-corrected and background-corrected and normalized (A/A_{max}) UV-Vis spectra for bPEI-AuNPs in influent wastewater matrix	195
C18. Background-corrected and background-corrected and normalized (A/A_{max}) UV-Vis spectra for bPEI-AuNPs in denitrification wastewater matrix	196
C19. Background-corrected and background-corrected and normalized (A/A_{max}) UV-Vis spectra for bPEI-AuNPs in nitrification wastewater matrix	197
C20. Illustrative example of center-to-center separation distances (d_s) calculated for PEG-AuNPs incubated in influent wastewater matrix.....	200
C21. Distribution of center-to-center separation distances (d_s) calculated for PEG-AuNPs incubated in influent, denitrification, and nitrification wastewater matrices after $t = 120$ minutes.....	201
C22. Distribution of center-to-center separation distances (d_s) calculated for COOH-AuNPs incubated in influent, denitrification, and nitrification wastewater matrices after $t = 120$ minutes.....	202
C23. Distribution of center-to-center separation distances (d_s) calculated for bPEI-AuNPs incubated in influent, denitrification, and nitrification wastewater matrices after $t = 120$ minutes.....	203
C24. TEM-HAADF micrograph of PEG-, COOH-, and bPEI-AuNPs after incubating for ≈ 240 minutes during the double matrix exchange procedure.....	204
D1. Intensity-weighted hydrodynamic diameter (D_h) as a function of time for pristine PEG-AuNPs, COOH-AuNPs, and bPEI-AuNPs in filtered river water.....	217
D2. $C_{NP,initial}$ and $C_{NP,final}$ for each AuNP type/form in centrifuged river water and DDI.....	218

LIST OF APPENDIX FIGURES (Continued)

<u>Figure</u>	<u>Page</u>
D3. Intensity-weighted hydrodynamic diameter of each aged AuNP type ($D_{h,aged}$) in DDI, TFF permeate, and filtered river water	220

LIST OF APPENDIX TABLES

<u>Table</u>	<u>Page</u>
B1. Manufacturer reported intensity-weighted D_h and ‘as-received’ intensity- and number-weighted D_h of model ENPs.....	149
B2. Electrophoretic mobility (EPM) of model ENPs.....	150
B3. Inputs used to calculate ζ from μ_E	151
B4. Summary of Willamette River water quality parameters/characteristics.....	153
B5. Measured organic carbon concentration following each filtration step.....	154
B6. Inputs used to calculate the average shear rate (G).	155
B7. Measurement of D_h of the background natural colloids following centrifugation	156
B8. Pre- and post-centrifugation turbidity of unaltered WRW.....	156
B9. Measurement of AuNP concentration before and after centrifugation (5-minute duration).....	158
B10. Measurement of AuNP concentration before and after centrifugation (2-minute duration).	159
B11. Measured AuNP concentration and percent recovery.....	163
B12. Composition of synthetic Willamette River water.....	163
B13. Initial aggregation rates ($dD_h/dt _{t \rightarrow 0}$) of model ENPs in filtered WRW.....	165
B14. Inputs used to calculate β for each transport mechanism.....	167
C1. Inputs used to calculate ζ from μ_E	173
C2. Characteristics of 0.45 μm -filtered wastewater matrices.....	175
C3. Concentration of bPEI-AuNPs in TFF permeate.....	180
C4. Lower- and upper-bounds applied to each AuNP type during TEM analysis.....	199

LIST OF APPENDIX TABLES (Continued)

<u>Table</u>		<u>Page</u>
D1.	Inputs used to calculate ζ from μ_E	207
D2.	Summary of Willamette River water quality parameters/characteristics.....	208
D3.	Summary of primary clarifier effluent water quality parameters/characteristics.....	209
D4.	Concentration of COOH-AuNPs in TFF permeate.....	211
D5.	Intensity-weighted hydrodynamic diameter (D_h) of aged AuNPs measured before and after overnight storage.....	212
D6.	Measured AuNP concentration and percent recovery of pristine and aged COOH-AuNPs in centrifuged river water.....	214
D7.	Surface plasmon resonance (λ_{SPR}) of pristine and aged AuNPs in various media.....	219
D8.	Full-width at half max (FWHM) of pristine and aged AuNPs in various media.....	220

DEDICATION

To Kristen, for her constant encouragement and patience.

1. GENERAL INTRODUCTION

1.1 Background

Engineered nanomaterials (ENMs) are small anthropogenic colloids with at least one length dimension <100 nanometers (nm). They are found in a variety of consumer goods, such as paints, plastics, and cosmetics, as well as a growing number of industrial items.^{1,2} Consequently, ENMs are being increasingly released to the natural environment through the manufacture, use, and disposal of these products.³ Pathways for release include point sources, such as effluent from wastewater treatment systems, and non-point sources, such as soils amended with ENM-containing biosolids.^{1,4-6}

While toxicological effects have been demonstrated for some ENMs, the environmental risks they pose are still unknown.^{7,8} One challenge hindering ENM risk assessments is a lack of data regarding their abundance in the environment. This is due, in part, to analytical limitations related to detecting and quantifying ENMs in environmental systems with naturally-occurring colloids (NCs) of similar composition.⁹ For this reason, ENM risk assessments are reliant on environmental fate models to estimate exposure concentrations.¹⁰⁻¹² To improve the accuracy of predicted environmental concentrations (PECs) generated by these models, extensive research has been conducted into the processes influencing the environmental fate of ENMs.¹³ These include physical processes, such as aggregation¹⁴⁻¹⁶, and chemical processes, such as oxidation-reduction processes and dissolution.¹⁷⁻¹⁹ In addition, the adsorption of various organic macromolecules to the surface of ENMs has been investigated.²⁰⁻²²

Focusing on surface water environments, aggregation has been identified as an important process influencing ENM environmental fate.²³ During aggregation there are two types of particle interactions to consider—those between similar particle types, termed homoaggregation, and those between dissimilar particle types, termed heteroaggregation. It is often assumed ENMs will predominately heteroaggregate in natural aquatic environments since the number concentration of NCs is expected to be several orders of magnitude greater than that of ENMs.^{23,24} If ENMs undergo homo- or heteroaggregation

and form large colloidal assemblages, then these ENM-containing aggregates will settle out of suspension and eventually accumulate in riverbeds where their environmental fate will be dictated by sediment transport processes.^{25,26}

In modelling particle aggregation, the attachment efficiency factor (α) is used to indicate the likelihood of two colliding particles attaching and forming a larger particle aggregate.^{27,28} In the context of understanding ENM environmental fate, values of $\alpha < 1.0$ indicate that the ENMs are less likely to aggregate and will remain relatively mobile in the environment, whereas $\alpha = 1.0$ indicates that aggregation is favorable and each particle-particle interaction will result in attachment. Simulated aquatic media with simplified and well-defined properties are often used when studying this phenomena.^{29,30} This enables systematic investigations of individual factors influencing ENM aggregation and the quantification of that effect via established methods for estimating α .^{14,31,32}

Aside from their anthropogenic origin, ENMs differ from NCs due to the variety of unique surface coatings applied to ENMs during their manufacture. These surface coatings, herein referred to as “engineered surface coatings”, are designed to promote specific interactions, such as the targeted delivery of nano-medicines,^{33,34} or to enhance certain nano-specific features.^{35,36} These surface coatings can also enhance ENM colloidal stability by affecting particle-particle interactions (and thus α) by imparting certain physiochemical properties to the ENMs.^{20,37,38} These properties are not static, but change in response to the aquatic chemistry of their environment and various physical, chemical, and biological processes.^{39–42} These processes complicate the prediction of ENM environmental fate, as those predictions are often made on the basis of the ENM’s initial physiochemical properties.

1.2 Problem Statement

Using simulated aquatic media, the physiochemical properties of engineered surface coatings have been shown to impact ENM aggregation behavior through a number of mechanisms.^{23,43} While this approach has yielded important mechanistic insights, it lacks the complexity of actual aquatic media where numerous, interrelated processes occur

simultaneously.³⁸ Furthermore, these investigations are typically performed using ‘pristine’ ENMs. In reality, ENMs will undergo various transformation processes throughout their life-cycle that alter their physiochemical properties.^{42,43} One example of where these transformations can occur is during wastewater treatment.⁴⁴⁻⁴⁶ These engineered systems also represent one pathway through which ENMs are released to the environment.⁴⁷⁻⁵⁰

In light of these considerations, examining the aggregation behavior of pristine ENMs in simulated aquatic media may provide an incomplete assessment of the factors influencing ENM environmental fate. From the perspective of ENM environmental fate modelling, the α values derived using pristine ENMs in simulated aquatic media may not accurately reflect ENM behavior in the environment. Instead, the environmental fate of ENMs will depend on the properties of the ‘aged’ ENMs and their interactions with other constituents in complex aquatic media. It is therefore critical that a more holistic approach be used to identify the relevant factors that dictate the environmental fate of ENMs. In particular, it is unknown whether engineered surface coatings remain an important factor influencing ENM aggregation behavior in actual aquatic media following their transformation during wastewater treatment.

1.3 Objectives

The overall aim of this research was to determine whether engineered surface coatings are an important factor affecting the fate of ENMs in surface water environments. Unfortunately, it is not possible to directly examine, from a mechanistic standpoint, how a given engineered surface coating alters the aggregation behavior of ENMs in actual aquatic media. Complicating matters is the myriad combinations of engineered surface coatings and aquatic chemistry that would need to be evaluated. Instead, the relative influence of engineered surface coatings on ENM aggregation behavior in actual aquatic environments can be determined by investigating the issue from complementary perspectives employing experimental systems with varying degrees of complexity.

Towards that end, four objectives were established:

- 1) Identify the mechanisms through which engineered surface coatings with various physiochemical properties alter the aggregation behavior of ENMs dispersed in simulated aquatic media;
- 2) Determine whether engineered surface coatings with various physiochemical properties alter the aggregation behavior of ENMs dispersed in actual aquatic media;
- 3) Determine if engineered surface coatings with various physiochemical properties influence ENM transformations ('aging') during conventional wastewater treatment processes; and
- 4) Compare the aggregation behavior of 'pristine' and 'aged' ENMs dispersed in actual aquatic media.

1.4 Approach

To meet these objectives, a series of experimental phases were designed utilizing gold nanoparticles (AuNPs) with different engineered surface coatings as model ENMs. For several reasons, AuNPs serve as an ideal platform to probe the effect of engineered surface coating functionality on ENM aggregation behavior:

- 1) Ambient concentrations of gold (Au) are relatively low in the natural and engineered systems of interest, thus aiding their detection;
- 2) Gold is relatively inert compared to other ENM types (e.g., silver, zinc, etc.) where competing physiochemical processes, such as dissolution or sulfidation, would confound our analysis;
- 3) AuNPs possess certain features, such as surface plasmon resonance and high X-ray scattering cross-sections, that enable a suite of complementary and corroborative analytical techniques for characterization and detection; and
- 4) AuNPs are readily available with well-characterized shapes, sizes, and surface functionalities.

During the first experimental phase, dynamic light scattering (DLS) and phase analysis light scattering (PALS) were used to examine the homoaggregation behavior of the AuNPs in simulated aquatic media with different aquatic chemistry. A range of conditions were explored, including variations in pH, ionic strength, electrolyte valance, and the concentration of natural organic matter (NOM). The results were used to identify the mechanisms affecting the colloidal stability of each AuNP type.

In the second experimental phase, samples from the Willamette River were collected and used to examine the aggregation behavior of the AuNPs in actual aquatic media. Batch experiments were performed using a recently developed functional assay. Filtered and raw river water were used to provide an assessment of homoaggregation alone (filtered) and the combined effect of homo- and heteroaggregation (raw). After dosing and a period of continuous mixing, aliquots were collected from each batch, centrifuged and the concentration of AuNPs remaining in suspension was measured using inductively-coupled plasma optical emission spectroscopy (ICP-OES). The analytical techniques employed during the first experimental phase were used to further explore the homoaggregation behavior of the AuNPs in the filtered river water. The results were compared to the previous experimental phase to see if the mechanisms affecting the colloidal stability of the AuNPs identified using simulated aquatic media described the behavior of the AuNPs in actual aquatic media.

During the third experimental phase, samples from the primary clarifier and activated sludge treatment stage of a pilot wastewater treatment plant (WWTP) were used to explore ENM transformations during wastewater treatment. Transformations of the AuNPs were first examined in samples collected from individual treatment stages using a suite of complementary techniques, including DLS, PALS, time-resolved UV-Vis spectroscopy, and scanning transmission electron microscopy (STEM). The results from these experiments provided the foundation to examine the transformations that occur to ENMs during sequential wastewater treatment stages, mimicking the changing aquatic chemistry that ENMs would experience during transport in a WWTP. In addition to exploring ENM

transformations during wastewater treatment, this experimental phase produced a novel method for simulating ENM transformations during wastewater treatment.

To complete the final experimental phase, the previous experimental techniques were combined to compare the aggregation behavior of pristine and aged AuNPs in actual aquatic media. Batch experiments using filtered and raw river water samples from the Willamette River were performed, using the pristine form of each AuNP type to confirm the previous findings and provide a foundation for evaluating the aggregation behavior of the corresponding aged form. This final phase, informed by the previous research phases, was intended to examine a more environmentally-relevant form of ENMs released to the environment and establish the importance of engineered surface coatings on ENM environmental fate.

1.5 Significance

Given that aggregation plays an important role in altering the environmental fate of ENMs, it is imperative that environmental fate models accurately depict this process and the factors that influence it. Otherwise, ENM risk assessments based on the PECs generated by these models could significantly over- or underestimate the ‘true’ exposure concentration. The overarching goal of this research was to address current knowledge gaps by examining ENM aggregation behavior under highly-realistic conditions.

From this work, the need to include engineered surface coatings as a factor in future experimental designs can be known. This can help reduce the complexity of future studies by focusing their experimental design on the factors and processes that have been shown to alter ENM environmental fate under environmentally-relevant conditions that account for an ENM’s life-cycle. Furthermore, the necessity of parameterizing the effect of engineered surface coatings within ENM environmental fate models can be established. This has the potential to reduce the overall experimental space defined in ENM environmental fate models and accelerate their refinement. Finally, to meet the objectives of this research, a novel approach was developed to simulate ENM transformations during

wastewater treatment. This method can serve as the foundation for future experiments that aim to elucidate the fate of more realistic forms of ENMs in the environment.

1.6 Organization

The remainder of this dissertation is organized as follows:

- Chapter 2 presents a published, peer-reviewed manuscript detailing the aggregation behavior of the model ENMs in simulated aquatic media;
- Chapter 3 presents a published, peer-reviewed manuscript detailing the aggregation behavior of the model ENMs in actual aquatic media;
- Chapter 4 presents a draft manuscript, currently in-review, detailing the transformations of the model ENMs during conventional wastewater treatment processes;
- Chapter 5 presents a draft manuscript, currently in preparation, that compares the aggregation behavior of aged ENMs to their pristine analogs in actual aquatic media; and
- Chapter 6 discusses the overall conclusions from this body of work and provides recommendations for future studies.

EFFECTS OF SURFACE COATING CHARACTER AND INTERACTIONS WITH
NATURAL ORGANIC MATTER ON THE COLLOIDAL STABILITY OF GOLD
NANOPARTICLES

Mark C. Surette and Jeffrey A. Nason

Environmental Science: Nano

Royal Society of Chemistry
1050 Connecticut Ave NW
Suite 500
Washington, D.C. 20036

2016 Volume 3, Issue 5, Pages 1144-1152

2. EFFECTS OF SURFACE COATING CHARACTER AND INTERACTIONS WITH NATURAL ORGANIC MATTER ON THE COLLOIDAL STABILITY OF GOLD NANOPARTICLES

2.1 Abstract

Aggregation is one of the dominant processes controlling the environmental fate of engineered nanomaterials (ENMs) in aquatic systems. Engineered coatings and coronas obtained through interactions with natural organic matter (NOM) and other macromolecules are known to play a significant role in controlling these processes. However, our ability to predict environmental fate on the basis of nanoparticle properties and the properties of the surrounding medium is still developing. To better understand the interplay between ENM surface coatings and their interaction with NOM, the aggregation of gold nanoparticles (AuNPs) with four different surface coatings—polyethylene glycol of varying molecular weight (PEG-AuNPs), carboxylated PEG-AuNPs (PEG-COOH-AuNPs), aminated PEG-AuNPs (PEG-Amine-AuNPs), and branched polyethylenimine (bPEI-AuNPs)—was investigated as a function of pH, ionic strength and the presence of a model organic matter (Suwannee River NOM, SRNOM). Time-resolved dynamic light scattering and electrophoretic mobility titrations were used to investigate how changes in the solution chemistry affect the ability of the different AuNPs to resist aggregation. Under the conditions investigated, the PEG-AuNPs and PEG-COOH-AuNPs remained stable across a range of conditions and in the presence of SRNOM due to steric and/or electrosteric stabilization. In contrast, the PEG-Amine-AuNPs and bPEI-AuNPs were destabilized in the presence of SRNOM at circumneutral pH. It is hypothesized that aggregation of these AuNP types occurs via adsorption and interparticle bridging that is strongly dependent on pH and the concentration of SRNOM. At mass ratios of NOM to ENMs expected in natural systems, all the AuNP types investigated here are expected to be stable with respect to homoaggregation in the presence of SRNOM. These findings provide a foundation to investigate more complex systems where competing interactions between NOM, ENMs and natural colloids are expected to control ENM environmental fate.

2.2 Introduction

Worldwide, engineered nanomaterials (ENMs) are being increasingly used in a variety of industrial applications and consumer goods, such as paints, plastics, and cosmetics.¹ Due to the nature of their use, ENMs can enter natural surface water environments from point sources (e.g., effluent from wastewater treatment systems) or from non-point sources (e.g., soils amended with ENM-containing biosolids).^{1,4-6,10} During their transport through engineered systems and upon their release to natural systems, ENMs are modified by biological, physical, and chemical transformations, as well as interactions with macromolecules (e.g., natural organic matter [NOM], humic substances, proteins, etc.) and natural colloids (NCs).^{42,51} These processes, both individually and in combination, have the potential to influence particle-particle interactions and thus the extent to which ENMs aggregate in these environments.

Previous research in colloidal science has shown that the aggregation of natural colloids can generally be explained according to Derjaguin-Landau-Verwey-Overbeek (DLVO) theory.^{41,52,53} More recently, DLVO theory has been applied to describe the aggregation of ENMs in aquatic systems.^{37,54} A number of studies have shown that the aggregation of ENMs can strongly influence both their environmental fate^{4-6,10,13,26,27,43,51,55,56} and toxicological effects.⁵⁷⁻⁵⁹ Focusing on the environmental fate of ENMs, aggregates containing ENMs can settle from the water column and accumulate within lake and river sediments, where their environmental fate is hypothesized to be closely linked to sediment transport processes.^{26,55} However, if ENMs remain unaggregated they are likely to be more mobile and transport through freshwater systems and ultimately migrate towards marine environments.^{13,27,56} In general, particle aggregates form via two processes—homoaggregation (aggregation of similar particles) or heteroaggregation (aggregation of dissimilar particles). Recent research has indicated that the potential for ENMs to aggregate depends on both the characteristics of the aquatic system, including the type and concentration of natural macromolecules and NCs present, as well as the properties of the ENMs.^{32,54,60-66}

While the study of ENM aggregation is greatly informed by decades of colloidal science research, there are a number of challenges associated with understanding nanoparticle-nanoparticle interactions using DLVO theory alone.⁴³ One of those challenges is to explain the role that natural and engineered surface coatings play in ENM aggregation processes. For a detailed treatment of this subject, the reader is directed to the recent review by Louie et al.²⁰ Typically, engineered surface coatings are applied to ENMs to minimize ENM aggregation in dispersions or to impart specific functionality to promote or enhance a desired outcome.^{33–36,43}

Depending upon the properties and structure of the surface coating, ENMs can be stabilized via an electrostatic mechanism or more robust steric or electrosteric mechanisms that are beyond the scope of classic DLVO theory.⁴³ Furthermore, the likelihood of “pristine” ENMs absent an engineered surface coating or an adsorbed layer of natural macromolecules existing in the environment is expected to be minimal.⁴ Thus, investigating the interactions between ENMs with engineered surface coatings and natural macromolecules is crucial to further our understanding of the role these interactions have upon the environmental fate of ENMs.

Previously, our group has utilized gold nanoparticles (AuNPs) with various engineered surface coatings as a model system for investigating ENM colloidal stability (i.e., the ability for ENMs to resist aggregation). It was demonstrated that Suwannee River Humic Acid (SRHA) interacted nearly universally with the AuNPs, regardless of the initial surface coating. SRHA stabilized AuNPs in the presence of monovalent electrolyte solutions (KCl); however, in the presence of high concentration divalent electrolytes ($I \geq 50$ mM MgCl₂/CaCl₂), SRHA aided in AuNP aggregation, likely through divalent cation bridging (DCB).⁶⁰ In related work focused on citrate-stabilized AuNPs (Cit-AuNPs), it was found that the ability of NOM to stabilize AuNPs was dependent on both the NOM type and concentration.³²

Building upon this foundation, the aim of the current work is to investigate the mechanisms by which engineered surface coatings of varying character respond to changes in the suspending medium and what effects those interactions have on ENM stability. The stability of AuNPs with four different common surface coatings of varying character—polyethylene glycol (PEG-AuNPs) of varying molecular weight, carboxylated PEG (PEG-COOH-AuNPs), aminated PEG (PEG-Amine-AuNPs), and branched polyethylenimine (bPEI-AuNPs)—are reported. Complementary techniques are used to assess how the properties of the surface coatings respond to changes in aquatic chemistry and the presence of Suwannee River NOM (SRNOM). Ultimately, the resultant properties shaped by these interactions will influence particle-particle interactions and thus ENM aggregation and environmental fate.

Since the number concentration of NCs is typically much greater than the expected number concentration of ENMs, it is assumed that heteroaggregation, as opposed to homoaggregation, is the dominant mode of aggregation affecting ENMs in typical freshwater aquatic conditions. These conditions include moderate ionic strength (including a mixture of mono-, di- and trivalent ions),⁶⁷ circumneutral pH,⁶⁷ and a high mass concentration ratio of NOM ($\approx 0.1 - 10$ mg C/L)⁶⁸ to ENMs (\approx ng – μ g/L)^{1,5,56} (i.e., $[\text{NOM}]:[\text{AuNPs}] \approx 10^3 - 10^6$). Recognizing this, the extent of the current work is to assess ENM homoaggregation under simplified conditions (e.g., lower ionic strength and NOM concentrations). These conditions were chosen to enable a mechanistic investigation of how ENM surface coatings interact with NOM macromolecules while minimizing the potential for other processes to occur that may complicate this understanding (e.g., heteroaggregation, NOM-NOM adsorption and bridging in the presence of di- and trivalent cations, etc.). While the results presented here are bounded to a subset of expected freshwater aquatic conditions in the environment, they nonetheless provide insights into the complex interplay that the aquatic medium, the ENM surface coating, and the presence of NOM macromolecules have upon the stability of ENMs and represent an important step towards examining more complex systems where the abovementioned processes are also operational.

2.3 Experimental

2.3.1 Materials

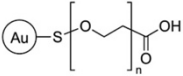
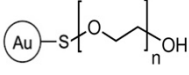
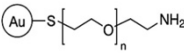
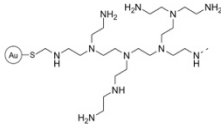
2.3.1.1 Nanoparticles

bPEI-AuNPs and PEG-AuNPs were purchased from nanoComposix, Inc. (San Diego, CA). bPEI-AuNPs were from available stock supplies (12 nm bPEI NanoXact™ Gold) but the PEG-AuNPs were custom synthesized to provide a range of PEG-chain molecular weights, ranging from 2 – 30 kDa. The PEG-COOH-AuNPs and PEG-Amine-AuNPs were purchased from Cytodiagnosics (Burlington, Ontario, CA). Manufacturer reported specifications and measured parameters for each AuNP type are summarized in Table 2.1. The surface coatings selected in this research were chosen to represent a range in molecular weight and surface charge in addition to investigating the influence of functional groups sharing a common polymer base chain.

2.3.1.2 Natural Organic Matter

Suwannee River Natural Organic Matter (SRNOM; Cat. No. 1R101N) was purchased from the International Humic Substances Society (IHSS) and was chosen to represent a “whole” water NOM isolate. Lyophilized SRNOM was dissolved in 18 M Ω -cm distilled, deionized (DDI) water (EGLA Purelab) to a concentration of approximately 45 mg of total organic carbon per liter (mg C/L) at pH 4 to mimic the conditions under which the NOM was isolated.⁶⁹ The solution was allowed to stir for 24-hours in the dark and then sequentially filtered using a 0.22 μ m PVDF membrane filter (Millipore Durapore) and 0.02 μ m alumina-based membrane syringe filter (Whatman Anotop). Following preparation, the total organic carbon (TOC) of the SRNOM solution was measured via Hach® TOC Method 10173 Direct (Mid-Range TOC 15 – 150 mg C/L).

Table 2.1. Summary of manufacturer reported specifications for each AuNP type and properties of each surface coating.

Parameter	PEG-COOH-AuNPs	PEG-AuNPs ^a	PEG-Amine-AuNPs	bPEI-AuNPs
Chemical Structure				
Approximate Functional Group pK _a	< 5 ⁷⁰	16 ⁷¹	9 – 11 ⁷²	4.5, 6.7, 11.6 ⁷³
Molecular Weight (kDa)	3	2 – 30	3	25
Core Diameter (nm)	15 ± 2	10.5 ± 0.9	15 ± 2	12.1 ± 0.8
Hydrodynamic Diameter ^b (nm)	49.7 ± 23.8	28.6 ± 8.3 – 68.7 ± 8.2	82.2 ± 15.6	46.9 ± 9.1
Zeta Potential (mV) ^{c,d}	-20.4 (pH 7.1)	-20.1 – -13.8 (pH 6.0 – 6.5)	+7.2 (pH 7.0)	+46.3 (pH 7.7)

Error bars indicate ± 1 SD.

^a Where applicable, the range of values correlates to the range in PEG-chain molecular weights that were tested (2 kDa to 30 kDa).

^b Hydrodynamic diameters were measured during procedures outlined in main text; $n = 16$ for 2 kDa PEG, $n = 11$ for 30 kDa PEG, $n = 9$ for 3 kDa PEG-Amine, $n = 6$ for 3 kDa PEG-COOH, and $n = 20$ for bPEI.

^c Zeta potential was calculated using the Hückel model and relevant to the pH listed in parentheses.

^d Values for PEG-Amine-AuNPs and PEG-COOH-AuNPs were measured using procedure outlined in main text, other values are as reported by the manufacturer.

2.3.1.3 Chemical Reagents

All solutions were made using ACS reagent-grade chemicals, prepared in DDI water, and were sequentially filtered using a 0.22 μm PVDF membrane filter (Millipore Durapore) and 0.02 μm alumina based membrane syringe filter (Whatman Anotop).

2.3.2 Methods

To investigate the importance of solution chemistry and surface coating on ENM aggregation behavior, complementary techniques including time-resolved dynamic light

scattering (TR-DLS) and electrophoretic mobility (EPM) titrations were used. TR-DLS was chosen to provide experimental data on the extent and rate of ENM aggregation, whereas EPM titrations reveal changes in the ENM surface charge. By comparing systematic experiments assessing the effect of solution chemistry and the concentration of SRNOM on the stability of the four AuNP types, insights are gained into the parameters controlling ENM aggregation behavior.

2.3.2.1 Experimental Conditions

All experiments were performed in aquatic media designed to mimic well-controlled and simplified freshwater conditions and were performed at approximately 22 – 25 °C. Ionic strength was varied between 1 mM and 1.5 M and pH was varied from approximately pH 5 – 11.

For the TR-DLS experiments, a constant AuNP concentration of 1 mg/L (as Au) was maintained, whereas during the EPM titrations the AuNP concentration was held at 10 mg/L (as Au). The higher AuNP concentration during the EPM titrations was needed to achieve stable and repeatable measurements. While the concentrations of ENMs used in the present research are much higher than expected in the environment (e.g., ng/L - µg/L),^{1,5,56} they are necessitated by the experimental methods utilized in this study. The concentration of SRNOM was varied between 0.007 – 1.7 mg C/L for the TR-DLS experiments and between 0.07 – 17 mg C/L during the EPM experiments. These ranges were chosen to maintain the same mass concentration ratio of SRNOM to AuNPs ([SRNOM]:[AuNPs] = 0.007 – 1.7 mg C/mg AuNPs) and allowed comparison of the results generated from the two analytical methods.

3.3.2.2 Time-Resolved Dynamic Light Scattering

The aggregation of each AuNP type was studied as a function of electrolyte concentration (40 – 500 mM), electrolyte valence (1:1 KCl and 2:1 CaCl₂), pH, and the concentration of SRNOM using TR-DLS (Brookhaven 90 Plus, Holtsville, NY). For experiments not involving the addition of SRNOM, samples were prepared in disposable 4.0 mL cuvettes

in the following sequence: (1) preparation of a 3.5 mL DDI particle-free blank; (2) removal of DDI for the required volume of AuNPs, electrolyte and KOH (for pH adjustment, if applicable); (3) addition of the AuNPs and KOH (if applicable); (4) initial size verification via DLS (3 DLS measurements, each 3 minutes long); (5) addition of electrolyte; and (6) the cuvette was inverted and immediately analyzed via TR-DLS (120 DLS measurements, each 15 seconds long). For experiments assessing the influence of SRNOM, a similar procedure was followed, except the electrolyte was added in Step 3 (prior to the addition of the AuNPs) and the SRNOM was added after the initial size verification (Step 4). As is detailed in Appendix A, it was found that for the experiments involving the addition of SRNOM, the order of addition (i.e., AuNPs then SRNOM vs. SRNOM then AuNPs) had no effect on the outcome of the experiments.

The aggregation of the AuNP suspensions was quantified from TR-DLS measurements using procedures detailed previously.^{60,74,75} Briefly, the extent of aggregation was calculated by averaging the final five measurements of the intensity-weighted hydrodynamic diameter ($D_{h,30}$) recorded during the TR-DLS measurement sequence and normalizing that value by the initial intensity-weighted hydrodynamic diameter ($D_{h,0}$).⁷⁴ The initial rate of aggregation was determined from the slope (dD_h/dt) of a linear regression of the TR-DLS data between the initial intensity-weighted hydrodynamic diameter ($D_{h,0}$) up to when $D_h = 1.3(D_{h,0})$.^{60,75}

Because aggregation rates are second order with respect to particle concentration, the rates of aggregation measured in these experiments are certain to be significantly greater than those expected in the environment. However, it is not the absolute value of the rate or extent of aggregation that is the focus of this work, but the trends in behavior with respect to changing aquatic chemistry. The same mechanistic behavior is expected at much lower AuNP concentrations, just at significantly reduced rates. The AuNP concentrations used in this work facilitates the use of the chosen analytical methods but also enables the observation of AuNP behavior on a reasonable timescale.

3.3.2.3 Electrophoretic Mobility Titrations

To understand the influence of solution properties and SRNOM on AuNP surface charge, two different sets of EPM titrations were performed. To test the influence of pH, AuNP suspensions (10 mg/L) were held at an approximately fixed ionic strength (1 mM KCl) while the pH was varied. Samples were prepared in 100 mL disposable cups by combining 15.8 mL of DDI, 200 μ L of 100 mM KCl and adding 4 mL of the stock AuNP suspension (stock suspension [AuNPs] = 50 mg/L). Samples were then loaded to a Brookhaven BI-ZTU autotitrator unit and EPM was analyzed via a Brookhaven ZetaPALS (Holtzville, NY). EPM measurements were obtained at roughly 0.5 – 1 pH unit increments as the pH was increased from approximately pH 5 – 11. At each pH, 5 EPM measurements of 30 cycles each were collected.

To test the influence of SRNOM on AuNP surface charge, AuNP suspensions (10 mg/L) were held at a fixed pH and ionic strength (1 mM KCl) while the concentration of SRNOM was varied between 0.07 – 17 mg C/L. Samples were prepared in disposable 4.0 mL cuvettes in the following sequence: (1) preparation of a 3.5 mL DDI particle-free blank; (2) removal of DDI for the required volume of AuNPs, electrolyte, SRNOM and KOH (for pH adjustment, if applicable); (3) addition of the AuNPs and KOH (if applicable); (4) addition of electrolyte; (5) addition of SRNOM; (6) samples were inverted and allowed to rest for approximately 10 minutes; and (7) samples were then immediately analyzed via 5 EPM measurements of 30 cycles each.

2.4 Results and Discussion

2.4.1 Influence of PEG Coating Molecular Weight

As expected, the hydrodynamic diameter (D_h) of the PEG-AuNPs was found to increase with increasing molecular weight of the PEG surface coating (Table 2.1; Appendix A Figure A2). These findings indicate that thicker polymer layers surround the AuNPs as the PEG molecular weight increases. Despite this fact, there was no apparent difference in the stability of the various PEG-AuNPs in response to increasing concentrations of 1:1 (KCl) and 2:1 (CaCl₂) electrolytes up to 1 M (Appendix A Figure A3). The resistance of the PEG-

AuNPs to aggregation upon compression of the double layer is evidence that the particles are stabilized by the steric forces that arise between polymer layers on adjacent particles. Furthermore, these forces do not appear to diminish as the molecular weight of the PEG coating decreases from 30 kDa to 2 kDa. PEG molecular weight also did not influence aggregation in the presence of SRNOM (Appendix A Figure A4). On the basis of these results, it was concluded that the molecular weight of the PEG surface coating in the range of 2-30 kDa had little effect on the stability of the PEG-AuNPs under the conditions being investigated. Stated another way, PEG surface coatings with molecular weights greater than 2 kDa are sufficient to stabilize AuNPs in the presence of high ionic strength. The remaining testing focused on the 2 kDa PEG-AuNPs due to the similarity in molecular weight to the other PEG-based surface coatings under investigation.

2.4.2 Influence of pH

EPM titrations of the four AuNP types are shown in Figure 2.1. These trends are expected based on the functionality of these surface coatings (see Table 2.1 for pK_a values). The PEG-AuNPs are near neutral for the majority of the pH range, becoming slightly more negative at $pH > 8.5$. It is unclear why the EPM becomes negative at this pH, as PEG is expected to be neutral over the entire pH range. The PEG-COOH is negatively charged over the entire pH range investigated, whereas the PEG-Amine and the bPEI are positively charged at neutral pH and experience charge reversal at approximately pH 9.7 and 10.3, respectively. Over the entire pH range, bPEI-AuNPs exhibit a larger magnitude EPM compared to the PEG-Amine-AuNPs, indicative of the higher charge density on the bPEI-AuNPs (likely attributable to its branched structure).

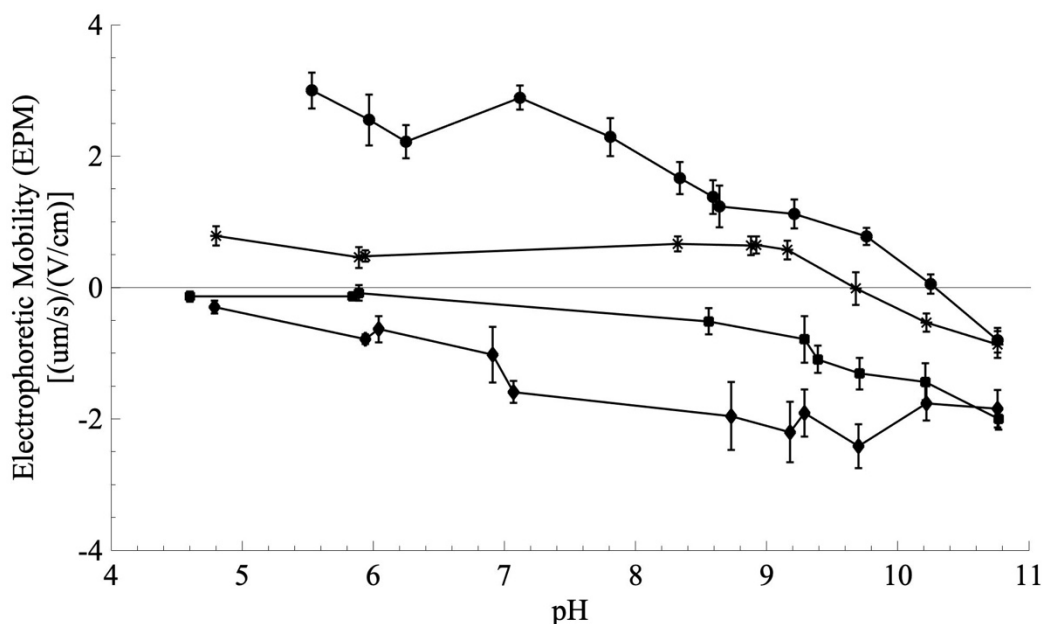


Figure 2.1. Electrophoretic mobility (EPM) for each AuNP type as a function of pH in the presence of 1 mM KCl. (●) bPEI; (*) 3 kDa PEG-Amine; (■) 2 kDa PEG; (◆) 3 kDa PEG-COOH. Error bars indicate ± 1 SD.

2.4.3 AuNP Stability Mechanisms

According to DLVO theory, reduction of repulsive electrostatic forces via electric double-layer (EDL) compression or adsorption of counterions should result in particle destabilization and subsequent aggregation. However, our investigations confirm that each of the AuNP types investigated here are stabilized via mechanisms beyond the scope of classic DLVO theory.^{34,36} For example, all four AuNP types were stable in 1:1 KCl and 2:1 CaCl₂ up to concentrations of 500 mM (Appendix A Figures A5 – A8), indicating that each ENM is highly stable and resistant to aggregation via double-layer compression. Furthermore, all four AuNPs types were stable even at near-zero values of EPM. For example, the PEG-based AuNPs remained stable upon the addition of mono- and divalent electrolytes at circumneutral pH, where the EPM of these three AuNP types is between ± 1 ($\mu\text{m/s})/(\text{V/cm})$ (Figure 2.1, Appendix A Figures A5 – A7 and A9). Likewise, the bPEI-AuNPs were stable across the entire pH range investigated, including at the point of charge reversal and in the presence of 500 mM KCl (Figure 2.1, Appendix A Figures A8 – A10).

In combination, these results confirm that the PEG surface coating sterically-stabilizes the PEG-AuNPs through physical interactions between surface coating molecules on adjacent AuNPs, whereas the bPEI, PEG-COOH, and PEG-Amine surface coatings electrosterically-stabilize the AuNPs through a combination of both electrostatic and physical interactions.

2.4.4 Influence of Natural Organic Matter

Previous research with electrostatically stabilized Cit-AuNPs found that SRNOM stabilized the ENMs in the presence of monovalent electrolytes, increasing the critical coagulation concentration (CCC) from 56 mM to 74 mM KCl.³² However, the four AuNP types investigated here are known to be stabilized via steric and electrosteric mechanisms and are not destabilized via EDL compression. Based on the EPM titrations shown in Figure 2.1, it was hypothesized that the charged functional groups present on the surface coatings of each AuNP type would control particle-particle interactions in the presence of NOM. This expectation is based on the understanding that functional groups on NOM macromolecules generally have a negative charge at the conditions being tested.^{20,53} If the surface coatings are negatively charged, they are likely to repel the NOM macromolecules, while positively charged surface coatings would be expected to attract NOM macromolecules. Unlike an electrostatically bound surface coating like citrate, all of the surface coatings investigated here are covalently bound to the surface of the AuNP core via thiol bonds (Table 2.1) that are notably difficult to remove and thus unlikely to be displaced by NOM.^{76,77} Regardless, the possibility of higher affinity sites on NOM macromolecules displacing the surface coatings via ligand replacement is discussed in the context of the observed mechanisms.

Initial aggregation studies conducted at pH 5.4 – 6.3 and 1 mM KCl indicate that the stability of the different AuNP types is dependent on both the surface coating present and the concentration of SRNOM. As can be seen in Figure 2.2, the addition of SRNOM was found to have no appreciable effect on the stability of the PEG-AuNPs and the PEG-COOH-AuNPs. In contrast, both the bPEI-AuNPs and PEG-Amine-AuNPs were

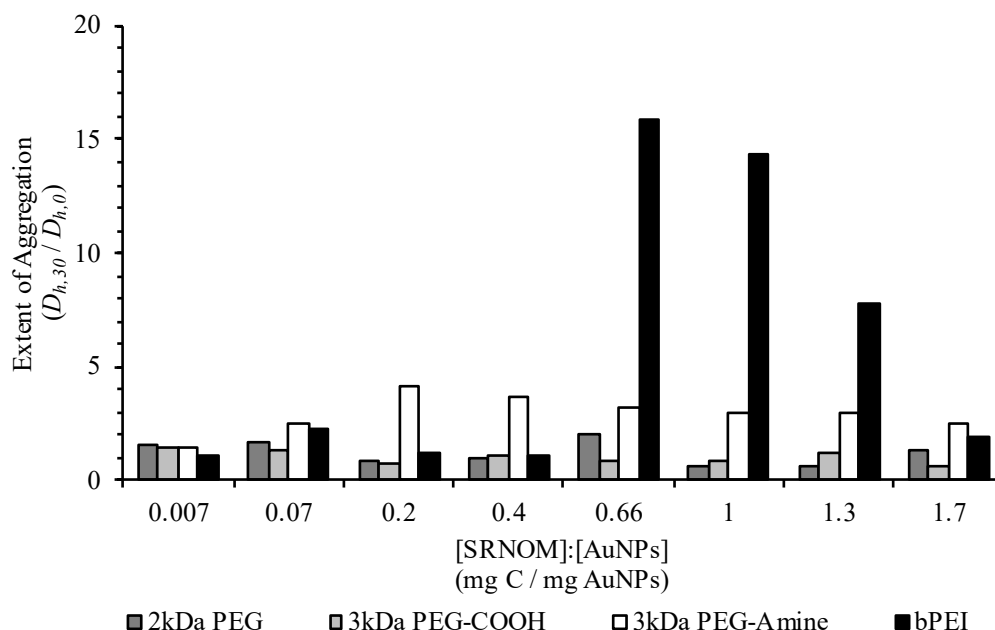


Figure 2.2. Extent of aggregation ($D_{h,30}/D_{h,0}$) for each AuNP type in the presence of 1 mM KCl and varying ratios of [SRNOM]:[AuNPs] at pH 5.4 ± 0.1 (2 kDa PEG); pH 5.5 ± 0.4 (3 kDa PEG-COOH); pH 5.4 ± 0.4 (3 kDa PEG-Amine); and pH 6.3 ± 0.1 (bPEI).

destabilized by the presence of SRNOM, with the bPEI-AuNPs aggregating between $0.4 < [\text{SRNOM}]:[\text{AuNPs}] < 1.7$ and the PEG- Amine-AuNPs aggregating between $0.07 < [\text{SRNOM}]:[\text{AuNPs}] < 1.7$.

Focusing first on the PEG-AuNPs and PEG-COOH-AuNPs, there is likely little affinity between the negatively charged surface coatings on these AuNP types and the negatively charged SRNOM macromolecules. Thus, the steric (PEG-AuNPs) and electrosteric (PEG-COOH-AuNPs) stabilization provided by the surface coating on these AuNP types appear to dominate interactions between adjacent particles, with SRNOM having little effect on those interactions.

In contrast, the addition of SRNOM to the dispersions containing the bPEI-AuNPs and PEG-Amine-AuNPs results in rapid destabilization. As this process continues over time, larger and larger aggregates continue to form (Appendix A Figure A11). However, the extent to which aggregates form varies dramatically between the bPEI-AuNPs and the

PEG-Amine-AuNPs, with the latter limited to $D_{h,30} / D_{h,0} < 4.5$ (Figure 2.2). The disparity in aggregate size is attributed to the differences in surface charge and chemical structure of the bPEI and PEG-Amine surface coatings. The branched polymer structure of the bPEI surface coating (Table 2.1) exhibits a highly positive surface charge at circumneutral pH (EPM ≈ 3 [$\mu\text{m/s}$]/[V/cm]), indicating a large number of positively-charged moieties per bPEI molecule. In the presence of SRNOM, the numerous charged moieties could enable a large number of SRNOM macromolecules to adsorb to the surface coating of the bPEI-AuNPs. In contrast, the linear structure of the PEG-Amine surface coating (Table 2.1) imparts only a slightly positive surface charge (EPM ≈ 1 [$\mu\text{m/s}$]/[V/cm] at pH 7) and contains just a single moiety per molecule. Thus, the nature of this surface coating presumably limits the extent to which SRNOM macromolecules can adsorb to the PEG-Amine-AuNPs.

These favorable interactions were found to be highly pH dependent, in particular for the bPEI-AuNPs which showed a considerable change in surface charge with respect to pH (Figure 2.1). To investigate the mechanisms by which SRNOM destabilizes the bPEI-AuNPs, EPM titrations were performed to investigate the surface charge of the bPEI-AuNPs in response to changes in pH and [SRNOM]:[AuNPs] ratio. The results, shown in Figure 2.3, highlight the interrelated role that these two factors play in controlling the overall surface charge of the bPEI-AuNPs. In general, increasing the ratio of [SRNOM]:[AuNPs] at a given pH results in charge neutralization and subsequent charge reversal.

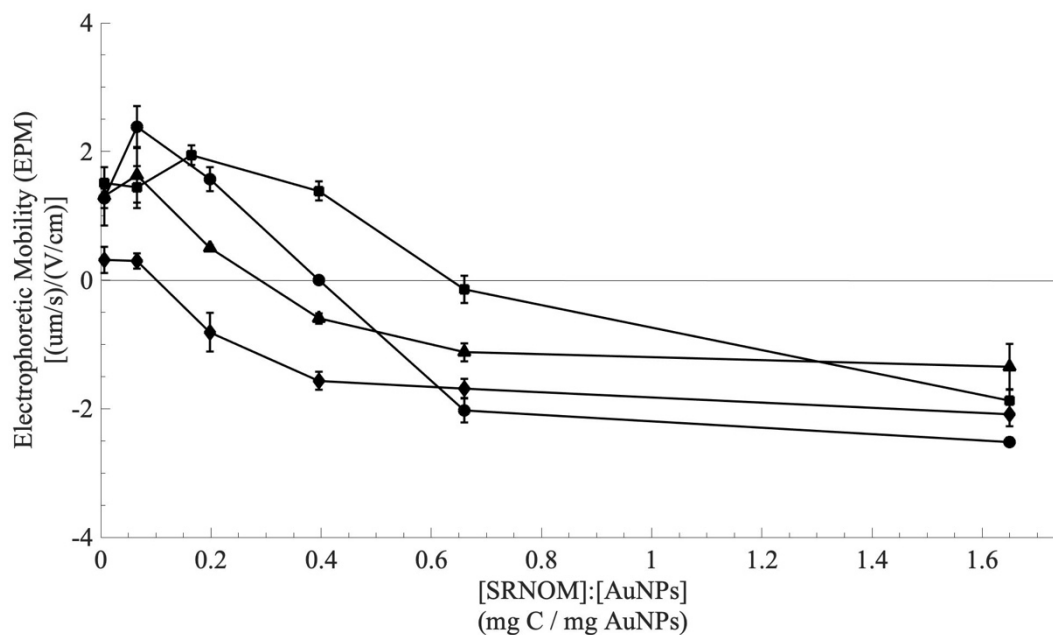


Figure 2.3. Electrophoretic mobility of bPEI-AuNPs in the presence of 1 mM KCl as a function of varying ratios of [SRNOM]:[AuNPs] and pH: (■) pH 6.0 ± 0.1 ; (●) pH 6.7 ± 0.1 ; (▲) pH 8.0 ± 0.1 ; and (◆) pH 9.9 ± 0.1 . Error bars indicate ± 1 SD.

These trends indicate the adsorption of SRNOM macromolecules to the surface of the bPEI-AuNPs (or potentially ligand replacement of the surface coating by SRNOM macromolecules). Furthermore, as the pH of the dispersion increases, charge neutralization via SRNOM adsorption (or ligand replacement) is achieved at lower [SRNOM]:[AuNPs]. This is consistent with the decreasing positive charge density with increasing pH as the amine groups are deprotonated (Figure 2.1). In the absence of SRNOM, there is good agreement between Figure 2.1 and Figure 2.3, indicating that the isoelectric point (IEP) for the bPEI-AuNPs occurs at approximately pH 10.3.

As seen in Figure 2.2, the extent to which the bPEI-AuNPs aggregate varies in response to changes in [SRNOM]:[AuNPs]. This trend is shared by the PEG-Amine-AuNPs, albeit to a lesser degree. Using a series of TR-DLS measurements, it was found that the stability of the bPEI-AuNPs is a function of both the [SRNOM]:[AuNPs] ratio and pH. The results illustrating this dependence, shown in Figure 2.4, were generated by applying a combination of extrapolation and interpolation techniques to the numerous TR-DLS

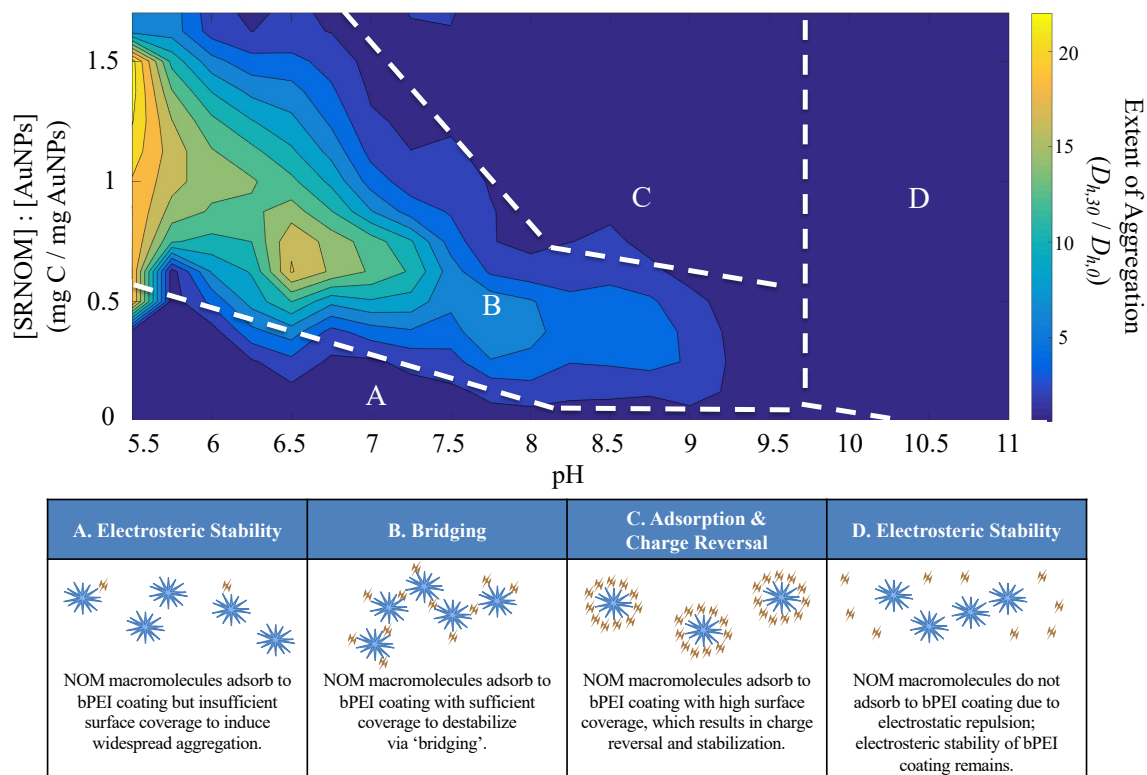


Figure 2.4. Extent of aggregation ($D_{h,30} / D_{h,0}$) for bPEI-AuNPs in the presence of 1 mM KCl as a function of both pH and the ratio of [SRNOM]:[AuNPs] (see Appendix A for details). Based upon the results of this investigation, four main ‘regions’ have been delineated regarding the dominant processes that are hypothesized to be occurring.

datasets that were obtained (see Appendix A for details; Appendix A Figure A12). In general, as pH increases, lower ratios of [SRNOM]:[AuNPs] are needed to destabilize the bPEI-AuNPs until the pH approaches the IEP. At the IEP, the bPEI-AuNPs remain stable across a broad range of [SRNOM]:[AuNPs], likely because there is little affinity between the bPEI surface coating and the SRNOM macromolecules. At relatively low [SRNOM]:[AuNPs], the bPEI-AuNPs remain stable regardless of dispersion pH. As the ratio of [SRNOM]:[AuNPs] increases, the stability and overall extent of aggregation is related to both the dispersion pH and [SRNOM]:[AuNPs]. However, as the ratio of [SRNOM]:[AuNPs] continues to increase, the bPEI-AuNPs are again stable across a range of pH. These trends, summarized in Figure 2.4, highlight the overall function of the electrosteric stabilization mechanism—even in conditions where the surface charge has

been reduced to the IEP (at high pH), the bPEI-AuNPs remain stable. Presumably, the stability of the bPEI-AuNPs at the IEP occurs because the steric stability imparted by the surface coating remains unaffected by changes in solution chemistry (Appendix A Figures A8 – A10). The bPEI-AuNPs are also stable at high [SRNOM]:[AuNPs] ratios. Here, it is hypothesized that rapid adsorption of the SRNOM macromolecules to the bPEI-AuNPs results in charge reversal. At this condition, where the particles are presumably completely coated by SRNOM, the particles are stabilized by electrosteric forces between the negatively-charged SRNOM-coated bPEI-AuNPs.

Based on these results, it is hypothesized that destabilization of the bPEI-AuNPs occurs via adsorption and interparticle bridging that results from favorable interactions between oppositely charged regions on the surface coatings and SRNOM macromolecules. This mechanism is envisioned to occur when a negatively-charged SRNOM macromolecule attaches to positively-charged regions on the coating of two adjacent AuNPs, thus ‘bridging’ between the neighboring AuNPs. It is worth noting that whether NOM adsorption occurs via interactions with the surface coating or displacement, the end result would be distinct regions of positive and negative charge distributed across the ENM surface, facilitating the same type of interactions between adjacent particles.

The following evidence supports the hypothesis that adsorption and interparticle bridging, as opposed to other particle destabilization mechanisms, is the dominant process driving aggregation of bPEI-AuNPs (and presumably the PEG-Amine-AuNPs) in the presence of SRNOM. As was detailed previously, all four of the AuNP types investigated here are stabilized via mechanisms (i.e., steric and electrosteric forces) unaffected by double layer compression and charge neutralization by pH adjustment to the IEP. Furthermore, little-to-no aggregation was observed at the point of charge neutralization by adsorbed SRNOM, suggesting destabilization via this mechanism can also be ruled out. Significant aggregation was observed only after adsorption and charge reversal had occurred, i.e., when the combination of pH and [SRNOM]:[AuNPs] resulted in an overall net negative surface charge (see Appendix A for details; Appendix A Figure A13). It is further

hypothesized that this process is largely governed by the surface coverage of the SRNOM macromolecules on the positively charged bPEI-AuNP surface. As we have demonstrated in previous work, the destabilization of positively charged hematite ($\alpha\text{-Fe}_2\text{O}_3$) colloids by negatively charged Cit-AuNPs was demonstrated to occur via a similar electrostatic patch mechanism that was strongly controlled by surface coverage as opposed to net surface charge of aggregates.⁷⁴

2.5 Conclusions

While this research was focused on a limited range of conditions relevant to (but not necessarily representative of) freshwater aquatic environments, the general findings nonetheless highlight the complex relationship between the ENM surface coating and the environmental medium (i.e., ionic strength, pH, concentration of NOM) by illustrating how these two factors can, in combination, affect the stability of ENMs. As noted previously, the overall environmental fate of ENMs is believed to be closely tied to their colloidal stability. ENMs that remain stable have the potential to remain mobile within an aquatic environment^{13,27,56} whereas ENMs that readily aggregate have an environmental fate that is expected to be more aligned with that of the natural sediments.^{26,55}

In this work it was found that the PEG-AuNPs and PEG-COOH-AuNPs, were stable across a range of ionic strengths (up to 1.5 M), electrolyte valence, and in the presence of SRNOM at relatively high mass ratios of [SRNOM]:[AuNPs]. In contrast, the PEG-Amine-AuNPs and bPEI-AuNPs, while stable in the presence of both mono- and divalent electrolytes at high ionic strengths, were both destabilized in the presence of SRNOM. Furthermore, the stability of the bPEI-AuNPs was linked to both the pH and the ratio of [SRNOM]:[AuNPs] present within the dispersion. It is important to recognize that the overall stability of the AuNP types investigated here were not necessarily dependent upon the stabilization mechanism imparted by the surface coating but how the properties of the surface coating, such as surface charge, can be influenced by the solution chemistry. Overall, the results from the AuNP types investigated here illustrate that charged functional groups provided

by the surface coating played a significant role in influencing interactions between ENMs and SRNOM macromolecules.

While the bPEI-AuNPs and PEG-Amine-AuNPs were found to be destabilized in the presence of SRNOM, their instability only occurred at relatively low mass concentration ratios (i.e., between $0.07 < [\text{SRNOM}]:[\text{AuNPs}] < 1.7$) that are unlikely to occur in most freshwater systems. At mass concentration ratios of SRNOM to ENMs that are more representative of natural systems (i.e., $[\text{SRNOM}]:[\text{AuNPs}] \approx 10^3 - 10^6$), all the AuNP types investigated here are expected to be stable with respect to homoaggregation in the presence of SRNOM. It is hypothesized that rapid adsorption of SRNOM macromolecules to the ENM surface coating followed by charge reversal will likely stabilize these ENMs, although additional work is necessary to verify these trends for other classes of NOM.

In the context of expected conditions in natural systems, the potential remains that these ENMs could associate with larger colloids via heteroaggregation or be destabilized via other mechanisms (e.g., divalent cation bridging between NOM-decorated ENMs). In the context of heteroaggregation, the insights gained from this research remain relevant. It is believed that the kinetics of the NOM adsorption observed during this research (and the stability imparted by this process) compared to the rate of heteroaggregate formation remains an important facet that will control the environmental fate of ENMs. Which of these competing processes dominates will be influenced by a number of factors including the number concentration of ENMs and NCs, the concentration and types of NOM present, the available surface area on the ENMs and NCs for favorable interactions to occur in the presence of NOM, and the effect that the solution chemistry has upon these simultaneous processes. Research is currently underway that transitions to more complex environmental mediums. The work outlined herein will serve as the basis from which we can begin to probe and understand the aggregation of ENMs and natural colloids in complex media and determine the key factors controlling the environmental fate of ENMs.

2.6 Acknowledgements

This research was supported by the National Science Foundation under Grant No. CBET-1067794. We thank J. Werle from nanoComposix, Inc. for synthesizing the PEG-AuNPs with different molecular weights. We also gratefully acknowledge the work of A. Dondick and S. McDowell for their effort collecting the TR-DLS and EPM data and K. Motter at the Institute for Water and Watersheds Collaboratory for her assistance with analyzing the SRNOM isolates.

2.7 Supplementary Information

The Supplementary Information for this manuscript is located in Appendix A.

NANOPARTICLE AGGREGATION IN A FRESHWATER RIVER:
THE ROLE OF ENGINEERED SURFACE COATINGS

Mark C. Surette and Jeffrey A. Nason

Environmental Science: Nano

Royal Society of Chemistry
1050 Connecticut Ave NW
Suite 500
Washington, D.C. 20036

2019 Volume 6, Issue 5, Pages 540-553

3. NANOPARTICLE AGGREGATION IN A FRESHWATER RIVER: THE ROLE OF ENGINEERED SURFACE COATINGS

3.1 Abstract

Within aquatic environments, the aggregation of ENPs has been identified as an important process affecting their environmental fate. Previous research using simple model mediums has demonstrated that engineered surface coatings applied to ENPs can alter their aggregation behavior. However, the relevance and effect of these surface coatings on ENPs dispersed in complex aquatic mediums is largely unknown. The objective of the current work was to explore this topic further using gold nanoparticles (AuNPs) with different engineered surface coatings as model ENPs. AuNPs with neutral or negatively-charged, covalently-bound surface coatings (polyethylene glycol [PEG] or carboxylated PEG, respectively) were found to be stable in both raw and filtered river water, while AuNPs with positively-charged (branched polyethylenimine, aminated PEG) or electrostatically-bound (citrate) surface coatings readily aggregated. For the model ENPs that aggregated, their average percent removal after mixing in the filtered river water was similar to that measured after the same period in raw river water, revealing that homoaggregation was dominant relative to heteroaggregation. To quantify the effect of the surface coatings on the colloidal stability of the model ENPs, we attempted to estimate homo- and heteroaggregation attachment efficiency factors (α_{homo} and α_{hetero} , respectively) using a recently reported functional assay. A number of challenges preventing these direct calculations in this system are discussed. However, from modelling it was inferred that $\alpha_{homo} \geq \alpha_{hetero}$. We find that ENP colloidal stability was related to eco-corona formation (i.e., adsorption of natural organic matter), which was regulated by the properties of the engineered surface coatings. Overall, the results of the batch experiments demonstrate that engineered surface coatings can affect ENP colloidal stability in a complex medium, further highlighting the need to consider this factor when investigating the environmental fate of ENPs.

3.2 Introduction

Currently, there is a lack of data regarding the concentration of engineered nanoparticles (ENPs) in the environment. Researchers and regulators examining the implications of ENPs currently rely on environmental fate and transport models to define environmentally-relevant exposure concentrations. This reliance is partly due to challenges with the detection and analysis of ENPs in the environment.^{7,9} Substantial work has been done to adapt multimedia environmental fate models originally developed for organic chemicals to capture the processes relevant to ENPs.¹⁰⁻¹² Among other insights, these models have shown that within aquatic environments the aggregation of ENPs is an important physical-chemical process affecting their environmental fate. While there remains some debate regarding the appropriate fate descriptors to use when modelling particle aggregation^{28,78,79}, current environmental fate models have adopted the use of particle-based rate constants to describe this process (e.g., $k_{hetero} = \alpha_{hetero} \times k_{coll.}$). To refine their predictive capability, the parameters used in modelling particle aggregation require accurate quantification under environmentally relevant conditions.^{5,13,27,80}

When particles aggregate, there are two types of particle interactions to consider—those between similar particles (homoaggregation) and those between dissimilar particles (heteroaggregation). An important parameter used in modelling either type of particle interaction is the attachment efficiency factor (α_{homo} or α_{hetero} , respectively). These factors account for short-range forces that are not well-defined mechanistically but nonetheless affect the likelihood that particle collisions will result in attachment. When assessing particle aggregation, simplified model aquatic mediums are typically used.^{29,30} This approach enables systematic investigations of individual factors influencing ENP aggregation, such as natural macromolecules (e.g., proteins, humic and fulvic acids, etc.)^{81,82} and the chemistry of the surrounding aquatic medium.^{83,84} It also permits the effect of those factors to be quantified using established methods to estimate α_{homo} and α_{hetero} .^{14,31,32} A limitation of this approach, however, is that it does not capture the inherent complexity of real environmental mediums.³⁸

Previous research using model aquatic mediums has shown that an important factor affecting the colloidal stability of ENPs is their surface coating.²⁰ These surface coatings can be intentionally applied to ENPs during their production (herein termed ‘engineered surface coating’) or acquired via interactions between the ENP and naturally occurring macromolecules (often termed ‘eco-corona’). Regardless of their origin, surface coatings can influence ENP environmental fate. For example, the presence of different engineered surface coatings on gold nanoparticles dispersed in model aquatic mediums have been shown to alter the adsorption of natural macromolecules to ENPs and effect their colloidal stability.^{60,85} From the perspective of modelling ENP aggregation in real environmental systems, however, it is unknown if the results obtained in the model aquatic mediums are still applicable. Thus arises a significant challenge—how best to translate the results of mechanistic investigations into predictions of ENP fate in complex environmental mediums. While engineered surface coatings have been shown to be a relevant factor influencing ENP stability in model aquatic mediums, whether they remain relevant in a real environmental medium has yet to be determined. It is hypothesized that in a real aquatic medium an ENP’s engineered surface coating will influence eco-corona formation and in turn affect the aggregation behavior of the ENPs.

The main objective of this work was to examine whether the aggregation behavior of ENPs dispersed in a real aquatic medium was affected by their engineered surface coating. To accomplish this, the colloidal stability of gold nanoparticles (AuNPs) stabilized with five different engineered surface coatings was assessed in raw and filtered river water using a protocol adapted from Barton et al. (2014)¹⁵. Samples of the river water were spiked to an ENP mass concentration of 500 µg/L, lower than is typically used when investigating particle aggregation.^{14,31,32} The raw river water contained naturally-occurring colloids at their native concentration to accurately represent environmentally relevant conditions. The results were compared with previous research using model aquatic mediums to help bridge the gap between these different approaches and assess whether engineered surface coatings are a relevant factor affecting the aggregation of ENPs in a complex aquatic medium.

In addition to reporting on the effects of engineered surface coatings on ENP aggregation, we attempted to quantify their effect via estimating α_{homo} and α_{hetero} . To accomplish this, the functional assay detailed by Wiesner and colleagues regarding the ‘surface affinity’ parameter was evaluated. This assay has been used to evaluate the heteroaggregation of ENPs in activated sludge, probe the uptake and trophic transfer of model ENPs in a simplified food web, and investigate the attachment of silver nanoparticles with various surface coatings to different model collectors (glass beads and kaolinite).^{15,16,86–88} These studies demonstrate the utility of this assay for comparing the relative aggregation behavior of ENPs in different matrices and correlating that behavior with important environmental outcomes like uptake and transport. For the current work we discuss the challenges and limitations of working in the experimental space required by this functional assay.

3.3 Materials and Methods

3.3.1 Engineered Nanoparticles

Gold nanoparticles (AuNPs) with core diameters of 10.5 – 15 nm were selected as model ENPs. Each AuNP was stabilized by one of five different engineered surface coatings: 2 kiloDalton (kDa) polyethyleneglycol (PEG), 3 kDa carboxyl-functionalized PEG (PEG-COOH), 3 kDa amine-functionalized PEG (PEG-Amine), 25 kDa branched polyethylenimine (bPEI), and citrate (Cit). Manufacturer reported specifications and measured characteristics for the model ENPs are provided in Table 3.1. The PEG-, bPEI-, and Cit-AuNPs were purchased from nanoComposix, Inc. (NanoXact 0.05 mg/mL) while the PEG-COOH- and PEG-Amine-AuNPs were purchased from Cytodiagnosics (carboxyl-PEG3000-SH and amine-PEG3000-SH, respectively). As detailed in Appendix B (Table B1), the difference in the intensity-weighted hydrodynamic diameter (D_h) and core diameter (D_c) reported in Table 3.1 is attributed to the presence of few, small aggregates and/or particle contaminants in the samples during measurement. Per the number-weighted D_h , the majority of the model ENPs had primary particle sizes of ≈ 20 – 30 nm (Table B1), which is within expectations given the engineered surface coatings possessed by the model ENPs.

Table 3.1. Manufacturer reported specifications and measured characteristics of model ENPs.

Surface Coating	Core-Surface Coating Binding Mechanism	Core Diameter (nm) ^a	Z-Average Hydrodynamic Diameter (nm) ^b	Zeta Potential (mV) ^c
2 kDa PEG	Covalent (Thiol)	10.5	34.4 ± 7.4	-25.9 ± 4.2 (pH 6.8 ± 0.03)
3 kDa PEG-COOH	Covalent (Thiol)	15	52.5 ± 12.4	-25.9 ± 4.2 (pH 7.1 ± 0.1)
3 kDa PEG-Amine	Covalent (Thiol)	15	59.0 ± 15.3	-14.9 ± 2.1 (pH 7.0 ± 0.1)
25 kDa bPEI	Covalent (Thiol)	12.1	40.4 ± 8.9	+25.4 ± 2.1 (pH 6.8 ± 0.1)
Citrate	Electrostatic	15	61.7 ± 39.8	-47.5 ± 4.2 (pH 7.4 ± 0.1)

Error bars indicate ± 95% confidence interval.

^a Per manufacturer's specifications, measured via transmission electron microscopy (TEM).

^b Measured via dynamic light scattering (DLS) at 1-10 mg Au/L in 0.02 µm filtered 18.2 MΩ-cm distilled, deionized water (DDI; EGLA Purelab); (PEG) *n* = 4; (PEG-COOH) *n* = 7; (PEG-Amine) *n* = 7; (bPEI) *n* = 2; (Cit) *n* = 4.

^c Measured in pH-adjusted 1 mM KCl at 10 mg Au/L at the pH listed in parentheses; *n* = 15. Calculation of the zeta potential (ζ) from measured electrophoretic mobility (EPM) is detailed in Appendix B.

3.3.2 Complex Aquatic Medium

The Willamette River (Oregon, USA) receives effluent from multiple sources that may release ENPs to the environment (e.g., storm water, agricultural runoff, industrial and municipal wastewater), making it a representative medium to study the environmental fate and transport of ENPs. Samples of Willamette River water (WRW) were collected from the intake line to the City of Corvallis' municipal drinking water treatment facility (H.D. Taylor Water Treatment Plant, Corvallis, OR). In total, approximately 15 L of WRW were collected on June 30, 2017 using acid-washed 1-L high-density polyethylene (HDPE) containers (Nalgene®). Prior to sample collection, the containers were rinsed with river water and then filled to minimize the headspace in the container. Water quality characteristics of the WRW were measured within 21-days of sample collection per method-specific holding times. A portion of WRW was sequentially filtered through 0.45 µm (Supor®, Pall Corporation) and 0.02 µm (Anotop®, Whatman) filters following the procedures outlined by Karanfil et al. (2003)⁸⁹ to limit organics leaching from the filters.

A summary of the measured water quality characteristics is provided in Table 3.2. Additional

Table 3.2. Water quality characteristics of the Willamette River water sampled on June 30, 2017.

Parameter	Value	
Dissolved Organic Carbon (DOC)	0.83 ± 0.1	mg C/L
Ionic Strength	0.68	mM
pH	7.9 ± 0.1	
Total Suspended Solids (TSS)	3.9 ± 0.4	mg/L
Total Alkalinity	25.0	mg/L as CaCO ₃
Total Hardness	18.6	mg/L as CaCO ₃

Error bars indicate \pm one standard deviation of the mean ($n = 3$).

details regarding the preparation and analysis of the WRW are provided in Appendix B (Tables B4 and B5).

3.3.3 Batch Experiments

Six separate 50-mL batches were prepared for each AuNP type: three containing 0.02 μm filtered WRW to examine the effects of homoaggregation in isolation and three containing raw WRW to examine the combined effects when both homo- and heteroaggregation are possible. All batch experiments were completed within ten days of collecting the WRW. Each batch was continuously-stirred at 400 rpm, corresponding to an average shear rate of 15.6 s^{-1} (Table B6).⁹⁰ Upon mixing, each batch was dosed to an AuNP mass concentration ($C_{NP,0}$) of 500 $\mu\text{g Au/L}$, equivalent to an initial number concentration ($N_{NP,0}$) of $1.5 - 4.3 \times 10^{13}$ particles/L depending on the Au core diameter. This mass concentration, while higher than the expected mass concentration of ENPs in the environment (e.g., ng/L – $\mu\text{g/L}$), was chosen to balance representativeness while minimizing analytical complications that arise at lower concentrations.⁵ Upon dosing, the temperature ($T = 25 \pm 1 \text{ }^\circ\text{C}$) and pH (pH 7.9 ± 0.1) of each batch were recorded.

Each batch was continuously mixed for 480 minutes, with 5-mL aliquots collected from each batch at predetermined time-points. Upon collection, each aliquot was immediately centrifuged at 3,500 rpm ($\approx 2,200g$ RCF) for 2 minutes. This centrifugation speed and duration was found to remove large natural colloids ($d_{NC} \geq \approx 300$ nm) and ENP-containing aggregates while minimizing the removal of unaggregated ENPs (Tables B7 – 10). However, it is possible that very small ENP-containing aggregates may have remained in suspension following the centrifugation step (see Appendix B for details). After centrifugation, the supernatant ($V = 4$ mL) was removed, transferred to a perfluoroalkoxy alkane (PFA) vial, and acid-preserved via the addition of 10 μ L of concentrated (70% w/w), ultra-pure HNO_3 (VWR International). Once all the aliquots were collected, they were acid-digested using freshly prepared *aqua regia* (3:1 ultra-pure $\text{HCl}:\text{HNO}_3$; see Appendix B for details) and then analyzed via inductively-coupled plasma optical emission spectroscopy (ICP-OES; Spectro Analytical Instruments) to quantify the AuNP number concentration in the supernatant ($N_{NP,i}$) at each time-point.

3.3.4 Time-Resolved Dynamic Light Scattering

To substantiate the trends observed in the batch experiments, time-resolved dynamic light scattering (TR-DLS) measurements were performed. Since DLS is not capable of distinguishing between model ENPs and background natural colloids (NCs), the technique was limited to the filtered WRW. Briefly, 3.5 mL samples containing the filtered WRW were dosed with a given model ENP to $C_{NP} = 500$ $\mu\text{g Au/L}$, matching the conditions of the batch experiments. Upon dosing, the intensity-weighted hydrodynamic diameter (D_h) was measured over time (120 measurements, each 15 seconds long) using a Brookhaven 90-Plus particle size analyzer (Brookhaven Instrument Corporation). Using the TR-DLS data, the colloidal stability of the model ENPs was assessed by calculating the extent of aggregation ($D_{h,final}/D_{h,initial}$) and the initial aggregation rates ($dD_h/dt|_{t \rightarrow 0}$) according to the procedures described previously.^{85,91}

3.3.5 Electrophoretic Mobility

Electrophoretic mobility (EPM) measurements were conducted to investigate the surface charge of the model ENPs in WRW. Due to the same limitations as the DLS, the EPM analytical technique was limited to the filtered WRW. To probe the effect of the natural organic matter (NOM) in the WRW on the surface charge of the model ENPs, measurements were also conducted using a synthetic water that mimicked the pH, ionic strength, and the ionic composition of the WRW but did not contain any NOM (Table B12). For each sample, 1.5 mL of the chosen medium was spiked with a given model ENP to $C_{NP} = 500 \mu\text{g Au/L}$, matching the conditions of the batch and TR-DLS experiments. The samples were allowed to incubate for 30 minutes before the EPM of the sample was measured (5 measurements of 30 cycles each) using a Brookhaven ZetaPALS (Brookhaven Instrument Corporation).⁸⁵

3.4 Results and Discussion

3.4.1 Filtered River Water

The loss of ENPs from homoaggregation was assessed by calculating the average percent removal (η) in filtered WRW after 480 minutes (Figure 3.1a). The PEG-AuNPs were highly resistant to aggregation, with negligible removal at the completion of the batch experiment. Likewise, only minimal removal of the PEG-COOH-AuNPs was observed ($\eta = 18 \pm 10\%$; mean \pm 95% confidence interval [$n = 3$]). The remaining three model ENPs were removed to varying degrees: the Cit-AuNPs to a moderate extent ($\eta = 37 \pm 23\%$) and the bPEI- and PEG-Amine-AuNPs more significantly ($\eta = 75 \pm 15\%$ and $78 \pm 5\%$, respectively).

Time-resolved dynamic light scattering (TR-DLS) was used to confirm these trends and calculate the extent of aggregation ($D_{h,final}/D_{h,initial}$) and the initial aggregation rates ($dD_h/dt|_{t \rightarrow 0}$). Values of $D_{h,final}/D_{h,initial} \approx 1$ denote particle stability whereas $D_{h,final}/D_{h,initial} > 1$ indicates that particles are aggregating. The TR-DLS measurements show that the PEG- and PEG-COOH-AuNPs were stable while the PEG-Amine- and bPEI-AuNPs readily homoaggregated (Figure 3.1b). The Cit-AuNPs underwent homoaggregation during the TR-DLS measurement period, however, $D_{h,final}/D_{h,initial}$ was much lower compared to the

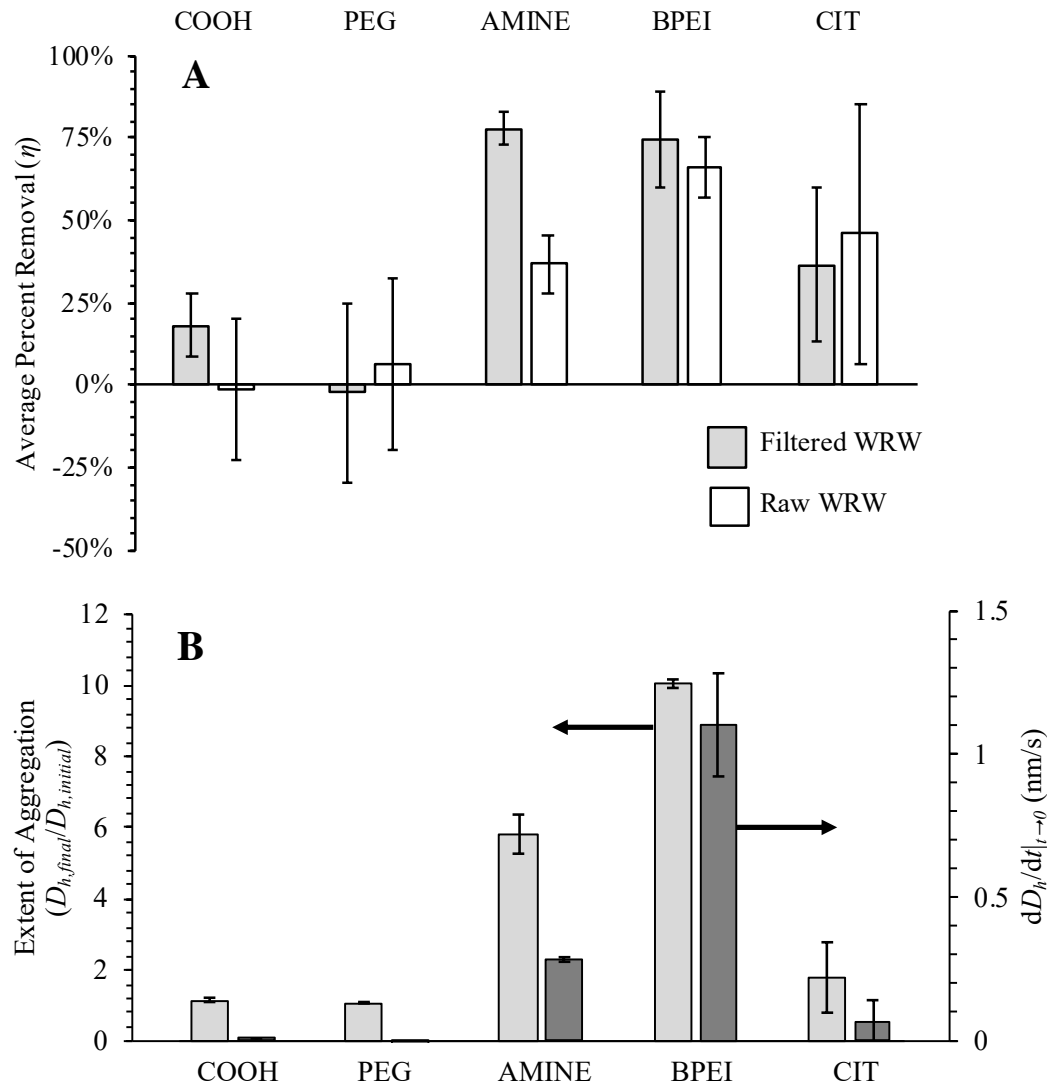


Figure 3.1. (a) Average percent removal (η) for each model ENP after 480 minutes. Error bars indicate $\pm 95\%$ confidence interval ($n = 3$). (b; left) Average extent of aggregation ($D_{h,final}/D_{h,initial}$) after 30 minutes and (b; right) initial aggregation rate ($dD_h/dt|_{t \rightarrow 0}$) for each model ENP in filtered WRW. Error bars indicate \pm one standard deviation ($n = 2 - 3$).

PEG-Amine- and bPEI-AuNPs. This is consistent with the initial aggregation rate, which indicates that the Cit-AuNPs aggregated more slowly compared to the PEG-Amine- and bPEI-AuNPs (Figure 3.1b).

Overall, the results from the TR-DLS measurements match the observations from the batch experiments. In combination they reveal that the Cit-, bPEI-, and PEG-Amine-AuNPs were destabilized in the filtered WRW and underwent homoaggregation. Furthermore, the extent of aggregation measured via TR-DLS tracks the removal measured in the batch experiments. The PEG-Amine- and bPEI-AuNPs, which rapidly homoaggregated, were removed to a greater degree during the batch experiments while the Cit-AuNPs, which homoaggregated more slowly, were removed to a lesser extent. The TR-DLS data for each model ENP is provided in Appendix B (Table B13 and Figure B4).

The EPM measurements for all five model ENPs in synthetic and filtered WRW are shown in Figure 3.2. In both mediums the PEG- and PEG-COOH-AuNPs had slightly negative EPM that did not vary with the suspending medium (PEG: paired t -test(14) = 0.37, p = 0.72; PEG-COOH: paired t -test(14) = 0.35, p = 0.73). In contrast, the EPM of the PEG-Amine-, bPEI-, and Cit-AuNPs did vary when suspended in the two mediums. The PEG-Amine- and bPEI-AuNPs had positive EPM in the synthetic WRW whereas they had negative EPM in the filtered WRW (bPEI: paired t -test(9) = 5.93, p << 0.01; PEG-Amine: paired t -test(14) = 15.62, p << 0.01). The Cit-AuNPs had negative EPM in both the synthetic and filtered WRW; however, their EPM was more negative in the filtered WRW (paired t -test(14) = 2.99, p = 0.01). For all five model ENPs the EPM measured in the synthetic WRW differed from the baseline measurements conducted in pH-adjusted 1 mM KCl (Table 3.1). The cause for this is unclear, as the ionic strength of the synthetic WRW is slightly lower (I = 0.68 mM) than the simple electrolyte medium and the pH is similar. This disparity may be attributable to the presence of polyvalent ions in the synthetic WRW.

Comparing the findings from the current work with previous research using the same ENPs in model aquatic mediums^{31,60,85} is useful to help elucidate the mechanisms affecting their colloidal stability in the filtered WRW. The PEG and PEG-COOH surface coatings were previously shown to stabilize against homoaggregation in both mono- and divalent electrolyte solutions up to I = 1.5 M and across Suwannee River NOM-to-ENP mass concentration ratios ([NOM]:[ENPs]) spanning 0 – 1.7 mg C/mg Au.⁸⁵ Thus, these surface

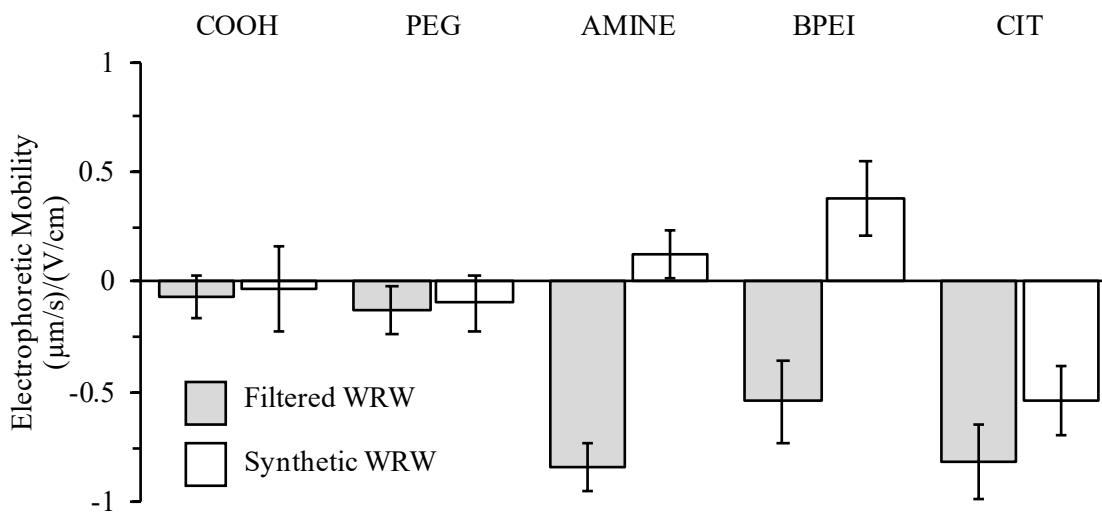


Figure 3.2. Electrophoretic mobility (EPM) of each model ENP in filtered WRW at pH 7.6 ± 0.04 (grey) and synthetic WRW at pH 7.0 ± 0.1 (white). Error bars indicate $\pm 95\%$ confidence interval ($n = 10 - 15$).

coatings have been shown to prevent homoaggregation via electrical double-layer (EDL) compression and were not influenced by the presence of NOM at the conditions tested. The current research was performed at significantly lower ionic strength ($I = 0.68$ mM) that is composed of a mixture of mono- and divalent ions and at $[\text{NOM}]:[\text{ENPs}] = 1.66$ mg C/mg Au (see Appendix B Table B4). The batch experiments and TR-DLS measurements reported here show that the PEG- and PEG-COOH-AuNPs were stable at the conditions present in the filtered WRW. Individually, these model ENPs had comparable EPM in both the synthetic and filtered WRW, suggesting that these surface coatings did not adsorb NOM present in the filtered WRW. The near-neutral EPM of these model ENPs in the filtered WRW (Figure 3.2) suggests that their stability may be primarily attributed to steric interactions. As a whole, the results reported herein match the trends observed using the model aquatic medium.

Like the PEG and PEG-COOH surface coatings, the PEG-Amine and bPEI surface coatings were previously found to stabilize the model ENPs against homoaggregation by EDL compression in both mono- and divalent electrolyte solutions up to $I = 1.5$ M.⁸⁵ However,

at certain [NOM]:[ENPs] these cationic surface coatings were shown to promote homoaggregation by interparticle bridging after NOM adsorbs to the ENP surface. The EPM results in the filtered WRW demonstrate that the PEG-Amine- and bPEI-AuNPs underwent charge reversal, an indication that these surface coatings adsorbed NOM (Figure 3.2). Furthermore, the current work was conducted at [NOM]:[ENPs] = 1.66 mg C/mg Au, which is comparable to previous research conducted at [NOM]:[ENPs] = 1.7 mg C/mg Au.⁸⁵ In both mediums at this [NOM]:[ENPs], the PEG-Amine- and bPEI-AuNPs undergo homoaggregation. In combination, these findings would seem to suggest that NOM-facilitated interparticle bridging destabilizes the PEG-Amine- and bPEI-AuNPs in the filtered WRW. However, $D_{h,final}/D_{h,initial}$ measured in the previous work was much lower compared to that reported here (PEG-Amine: 2.50 vs. 5.82; bPEI: 1.96 vs. 10.05, respectively). This disparity may reflect the presence of polyvalent cations in the filtered WRW, which were absent from the model aquatic mediums (i.e., testing at the various [NOM]:[ENPs] was performed in 1mM KCl). This suggests that following NOM adsorption, divalent cation bridging (DCB) may be occurring in the filtered WRW. The increased $D_{h,final}/D_{h,initial}$ could also be due to variations in the NOM composition in the filtered WRW compared to the model NOM from the Suwannee River (SRNOM), as prior research has demonstrated that differences in NOM composition, in particular the molecular weight distribution, can affect colloidal stability.^{21,82} However, additional testing is warranted to test this hypothesis. Overall, the aggregation behavior of the PEG-Amine- and bPEI-AuNPs is consistent with that observed in the model aquatic mediums, revealing that the mechanisms identified previously are still relevant in the filtered WRW. Namely, these model ENPs were destabilized in the filtered WRW following NOM adsorption, either directly from NOM-facilitated interparticle bridging alone or in combination with DCB.

Finally, the electrostatically-stabilized Cit-AuNPs have been shown to readily homoaggregate following EDL compression and from DCB when in the presence of both divalent cations and NOM.^{31,32,60,92} However, in the current work it is unlikely that the relatively low ionic strength ($I = 0.68$ mM) of the filtered WRW resulted in

homoaggregation via EDL compression. This is based on previous research that found the Cit-AuNPs were resistant to aggregation via EDL compression in mono- and divalent electrolyte solutions at the ionic strength encountered in the current research.³² Instead, their homoaggregation in the filtered WRW is likely due to DCB following NOM adsorption. While the Cit-AuNPs possess a negative surface charge in the filtered WRW (Figure 3.2), the citrate surface coating is weakly-bound to the AuNPs through electrostatic attraction. As such, NOM macromolecules possessing moieties with a stronger binding affinity (e.g., organothiols) could displace it.⁹³ The similarity in the EPM of the Cit-AuNPs in the filtered WRW to the NOM-coated PEG-Amine- and bPEI-AuNPs indicates that the citrate surface coating was likely displaced. This phenomena has also been observed across a wide pH range where the EPM of Cit-AuNPs was consistently lower when Suwannee River Humic Acid (SRHA) was present in the solution.⁶⁰ Following displacement of the citrate surface coating, the NOM macromolecules could then destabilize the Cit-AuNPs through either interparticle bridging alone or in combination with DCB. As with the PEG-Amine- and bPEI-AuNPs, either mechanism could be occurring; however, the results of previous work suggest that DCB may be more relevant for the citrate particles.⁶⁰

The results from the corroborative techniques conducted with the filtered WRW demonstrate that engineered surface coatings play an influential role in determining the aggregation behavior of ENPs in a complex medium. Differences in colloidal stability were related to the way that the engineered surface coatings regulate eco-corona formation (i.e., NOM adsorption). The negatively-charged PEG- and PEG-COOH-AuNPs did not adsorb NOM and were electrosterically stable. In contrast, the positively-charged PEG-Amine- and bPEI-AuNPs readily adsorbed NOM, undergoing charge reversal and subsequently homoaggregating. The Cit-AuNPs, which possess an electrostatically-bound, negatively-charged citrate surface coating, also homoaggregated. While the exact mechanism causing these three model ENPs to homoaggregate is unclear, the results indicate that it occurred following NOM adsorption. As such, their homoaggregation is attributed to either NOM-facilitated interparticle bridging or DCB. In the case of the citrate coating, these

mechanisms likely occurred after the citrate surface coating was displaced by NOM macromolecules possessing a stronger binding affinity for the AuNP core.

3.4.2 Raw River Water

The experiments using the filtered WRW highlight the relevance of the engineered surface coatings in affecting the homoaggregation of the model ENPs. It is also important to assess how they influence ENP colloidal stability when natural colloids are present in the aquatic medium and heteroaggregation is possible. The loss of ENPs by aggregation in the raw WRW, the combined result of homo- and heteroaggregation, was assessed by calculating the average percent removal (η) after 480 minutes. The results, presented in Figure 3.1a, show that the PEG- and PEG-COOH-AuNPs underwent minimal removal ($\eta = -6 \pm 26\%$ and $1 \pm 26\%$, respectively). In contrast, the remaining three model ENPs were removed to varying extents: the PEG-Amine- and Cit-AuNPs to a moderate extent ($\eta = 37 \pm 9\%$ and $46 \pm 40\%$) and the bPEI-AuNPs to a more significant amount ($\eta = 66 \pm 9\%$).

The aggregation behavior of the PEG- and PEG-COOH-AuNPs was similar in the filtered and raw WRW. Thus, the electrosteric stability provided by their surface coatings not only prevents their homoaggregation, as was demonstrated in the filtered WRW, but also their heteroaggregation with the natural colloids in the raw WRW. This is attributed to the moderate molecular weight and neutral- (PEG) or negatively-charged (PEG-COOH) surface coatings repelling the negatively-charged natural colloids (NCs).⁵³ The overall trends observed for the PEG-Amine-, bPEI-, and Cit-AuNPs are similar in the filtered and raw WRW. Individually the bPEI- and Cit-AuNPs were removed to comparable extents in both the filtered and raw WRW while the PEG-Amine-AuNPs were removed to a lesser extent in the raw WRW compared to the filtered WRW (paired t -test(2) = 13.07, $p \ll 0.01$). As the aquatic chemistry of the filtered and raw WRW are the same, it is likely that the mechanisms causing the PEG-Amine-, bPEI-, and Cit-AuNPs to homoaggregate in the filtered WRW are still affecting their colloidal stability in the raw WRW. It is also plausible that these model ENPs heteroaggregated with the NCs present in the raw WRW. As noted previously, it is possible that very small ENP-NC heteroaggregates (if formed) may have

remained in suspension after centrifugation. This may account for the decrease in η for the PEG-Amine-AuNPs in the raw WRW relative to that measured in the filtered WRW. This process is also expected to be relevant for the bPEI- and Cit-AuNPs, although there was no measurable difference in η for these model ENPs between the filtered and raw WRW. Regardless, it is not possible to distinguish between homo- and heteroaggregation with our experimental approach when they are occurring simultaneously. Instead, the results obtained with the raw WRW can be compared to those obtained using the filtered WRW to provide insights into the relative importance of each process.

It was originally anticipated that removal in the raw WRW would be higher than the filtered WRW due to the additional particle-particle interactions occurring between the ENPs and the NCs in the raw WRW. The finding that removal via homoaggregation alone (filtered WRW) was comparable to or higher than the combined effect of homo- and heteroaggregation (raw WRW) conflicts with the expectation that heteroaggregation is the dominant mode of aggregation under environmentally relevant conditions.^{14,23} This expectation is rooted in the assumption that the number concentration of NCs (N_{NC}) is much higher than the number concentration of ENPs (N_{NP}), thus favoring removal via heteroaggregation. To understand why our findings contradict this expectation, it is useful to assess the components driving particle aggregation and thus the removal of the model ENPs. These components include the rate at which particle-particle interactions occur and the likelihood that particle interactions will result in attachment and the formation of particle aggregates.

The overall rate of particle-particle interactions is dependent on two, interrelated factors—the number concentration of particles in the system (i.e., N_{NP} and N_{NC}) and the frequency of particle collisions. While higher than expected in the environment, N_{NP} in the current work ($1.5 - 4.3 \times 10^{13}$ particles/L) was an order of magnitude or more lower than is often used when studying ENP aggregation.^{14,31,32} Due to various challenges associated with detecting and analyzing NCs of varying composition and size, accurate estimates of N_{NC} in the raw WRW are unavailable. Particle size distribution measurements performed via

Coulter Counter (Figure B1) indicate that the median $d_{NC} < 0.746 \mu\text{m}$, the instrument detection limit. This expectation is supported by previous research reporting a large fraction of N_{NC} in the range of $d_{NC} \leq 10^3 \text{ nm}$, with the majority (>90%) smaller than 200 nm.^{24,94,95} As such, values of N_{NC} were instead calculated across the range $d_{NC} = 1 - 10^4 \text{ nm}$ using the measured TSS (Table 3.2) and assuming the particles were spherical, had uniform density equal to 2.65 g/cm^3 , and were represented by a single size-class (i.e., a single value of d_{NC}).

Using the known properties of the model ENPs and assumed properties of the NCs, the frequency of particle collisions was estimated (see Appendix B for details). For collisions involving either two model ENPs or a model ENP with a NC smaller than $5 \mu\text{m}$, Brownian motion ($^{BR}\beta$) was the dominant collision mechanism (Figure B5). This finding was expected due to the small size of the model ENPs.⁹⁶ Up to $d_{NC} \leq 10^3 \text{ nm}$, the collision frequency of two model ENPs via Brownian motion ($^{BR}\beta_{NP-NP}$) was within approximately one order of magnitude of that calculated for the collision of a model ENP and a NC via the same mechanism ($^{BR}\beta_{NP-NC}$), with the values converging as d_{NC} approaches d_{NP} .

Adjusting the estimated values of $^{BR}\beta_{NP-NP}$ and $^{BR}\beta_{NP-NC}$ to account for the short-range forces arising as two particles approach one another (i.e., $^{BR}[\alpha\beta]_{NP-NP}$ and $^{BR}[\alpha\beta]_{NP-NC}$, respectively),⁹⁶ the overall rate of particle-particle interactions via Brownian motion can be determined. In combination with N_{NP} and N_{NC} (with the latter varying with d_{NC}), the initial rate of homo- and heteroaggregation can be estimated according to Equations 1 and 2, respectively.

$$\left(\frac{dN_{NP}}{dt}\bigg|_{t \rightarrow 0}\right)_{homo} = -\alpha_{homo}^{BR}(\alpha\beta)_{NP-NP}N_{NP}^2 \quad (1)$$

$$\left(\frac{dN_{NP}}{dt}\bigg|_{t \rightarrow 0}\right)_{hetero} = -\alpha_{hetero}^{BR}(\alpha\beta)_{NP-NC}N_{NP}N_{NC} \quad (2)$$

These equations describe the initial rate of change in the number concentration of unaggregated ENPs ($dN_{NP}/dt|_{t \rightarrow 0}$) via homo- or heteroaggregation at early times (see

Appendix B for details). In Equations 1 and 2, the terms α_{homo} and α_{hetero} are attachment efficiencies denoting the likelihood that two colliding particles will attach to form a larger aggregate.

The precise value of these parameters is unknown; however, the trends predicted according Equations 1 and 2 can be compared with the experimental results to identify the relative importance of each process (i.e. homo- and heteroaggregation) and provide insights into the relationship between α_{homo} and α_{hetero} . This is accomplished by recognizing that in the filtered WRW, the loss of ENPs via aggregation can be modelled according to Equation 1. Since both homo- and heteroaggregation can occur simultaneously within the raw WRW, the loss of ENPs via aggregation in the raw WRW is more accurately modelled by the total initial aggregation rate (i.e., the summation of Equations 1 and 2). The ratio of the initial aggregation rates within these two experimental systems can then be compared according to Equation 3.

$$\frac{\left(\frac{dN_{NP}}{dt}\right)_{t \rightarrow 0}^{homo}}{\left(\frac{dN_{NP}}{dt}\right)_{t \rightarrow 0}^{homo} + \left(\frac{dN_{NP}}{dt}\right)_{t \rightarrow 0}^{hetero}} = \frac{1}{1 + \chi \left(\frac{BR(\alpha\beta)_{NC-NP} N_{NC}}{BR(\alpha\beta)_{NP-NP} N_{NP}}\right)} \quad (3)$$

with $\chi = \frac{\alpha_{hetero}}{\alpha_{homo}}$, where values of $\chi < 1$ indicate $\alpha_{homo} > \alpha_{hetero}$ whereas $\chi > 1$ indicate $\alpha_{homo} < \alpha_{hetero}$.

Using the inputs discussed previously and the range $\chi = [10^{-3} - 10^3]$, Equation 3 can be plotted as a function of d_{NC} to convey the importance of homoaggregation alone versus the combination of homo- and heteroaggregation. According to Equation 3, the removal of the model ENPs via heteroaggregation becomes increasingly negligible relative to removal via homoaggregation as the ordinate approaches 1. Defining a criterion where the loss of ENPs via heteroaggregation is $\leq 10\%$ of the loss via homoaggregation, it is possible to delineate relevant combinations of χ and d_{NC} that meet this criterion.

As shown in Figure 3.3, there are two overall conditions that satisfy this criterion: (1) either $\chi \leq 1$ must be true (regardless of d_{NC}) or (2) if $\chi > 1$, then d_{NC} must be increasingly larger

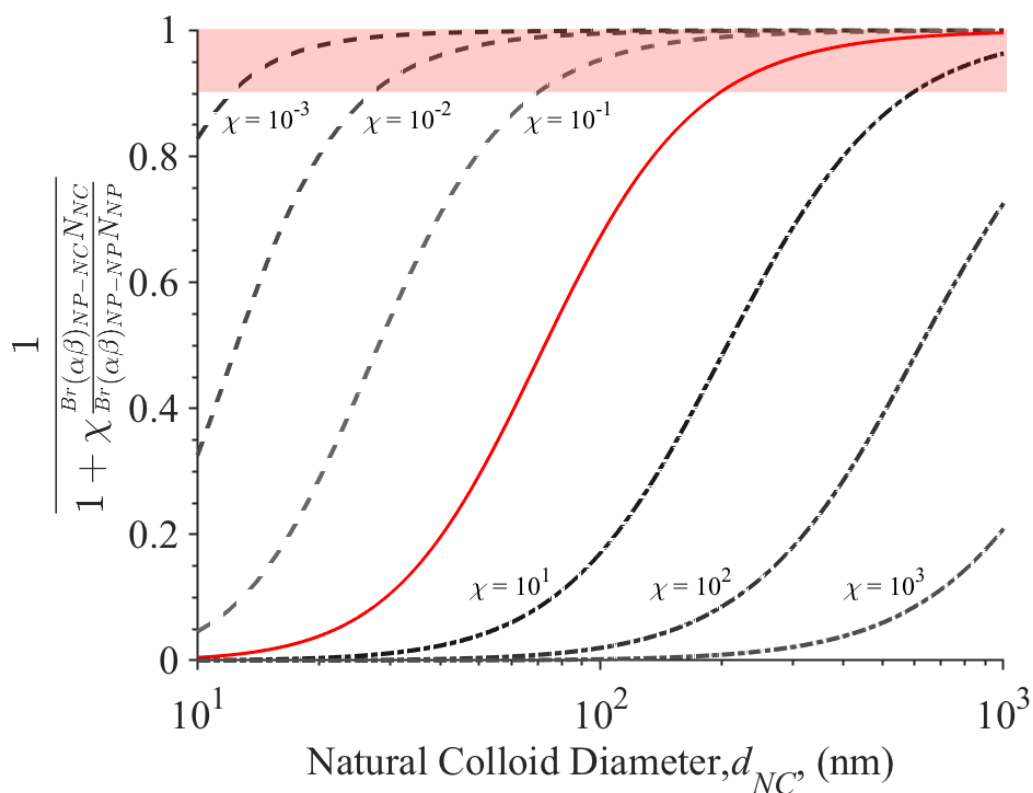


Figure 3.3. Ratio of initial aggregation rate ($dN_{NP}/dt|_{t \rightarrow 0}$) due to homoaggregation alone to the rate due to the combination of homo- and heteroaggregation as a function of d_{NC} , with $\chi = [10^{-3} - 10^3]$ where (dashed) $\chi < 1$, (red) $\chi = 1$, and (dash-dot) $\chi > 1$. Red box denotes region where $dN_{NP}/dt|_{t \rightarrow 0}$ from heteroaggregation is $\leq 10\%$ of $dN_{NP}/dt|_{t \rightarrow 0}$ from homoaggregation.

the greater χ becomes. For example, at $\chi = 10$ (i.e., $\alpha_{hetero} = 10x \alpha_{homo}$), for the loss of the model ENPs via heteroaggregation to be less than 10% of the loss via homoaggregation, $d_{NC} \geq 590$ nm. As noted previously, the similarity in η measured in the filtered and raw WRW reveals that in our experimental system heteroaggregation was negligible relative to homoaggregation. As the majority of the NCs are expected to have $d_{NC} \ll 1 \mu\text{m}$, the second condition is unlikely to have been attained in our experimental system and therefore suggests that $\chi \leq 1$ was likely valid (i.e., $\alpha_{homo} \geq \alpha_{hetero}$).

Why homoaggregation was more favorable than heteroaggregation is unclear; however, this finding illustrates the importance of the processes accounted for by α that are currently

not understood but nonetheless influence the outcome of particle-particle interactions. One of these processes is eco-corona formation via NOM adsorption. For cationic surface coatings, such as the PEG-Amine and bPEI, the initial positive charge provided by the engineered surface coatings should promote heteroaggregation with the negatively-charged NCs as well as the adsorption of NOM.

The finding that heteroaggregation was negligible suggests that eco-corona formation occurred faster than heteroaggregation. It has been previously shown that the negative surface charge and steric interactions provided by adsorbed NOM can hinder heteroaggregation.^{20,31,97} This phenomena could explain the results of the current work. For this to occur, the characteristic timescale for eco-corona formation must be less than that for heteroaggregation. Nason et al. (2012)³² reported that the adsorption of various model NOMs to the surface of Cit-AuNPs occurred relatively fast and was complete after only a few minutes. Using $dN_{NP}/dt|_{t \rightarrow 0}$ for heteroaggregation, the characteristic time for heteroaggregation ($t_{char,hetero}$) was calculated (see Appendix B for details). At $d_{NC} = 500$ nm (the mid-point of $d_{NC} = 10^2 - 10^3$ nm), $t_{char,hetero}$ was estimated between approximately $400 - 4.3 \times 10^6$ s across the range of $10^0 > \alpha_{hetero} > 10^{-4}$ (Figure B6). While dependent on both the assumed value of d_{NC} and α_{hetero} , the estimates reveal that $t_{char,hetero}$ was on the order of 10^2 s or higher and, therefore, likely greater than the characteristic time for eco-corona formation reported by Nason et al. (2012)³².

In the current work, if the eco-corona formation outpaced ENP-NC heteroaggregation then the eco-corona formed via NOM adsorption would dictate the outcome of particle-particle interactions. Focusing on the raw WRW, this would suggest that at early times immediately after introducing the model ENPs there are, in essence, two types of particles in the system—ENPs with low fractional NOM surface coverage and NCs with the maximum fractional NOM surface coverage for the conditions of the WRW. The latter particle type is likely since the adsorption/desorption of NOM to the surface of the NCs is expected to be at equilibrium. It is hypothesized that homoaggregation between two ENPs partially-coated with NOM is more favorable than heteroaggregation between an ENP partially-

coated with NOM and an NC fully-coated with NOM. This hypothesis is supported by comparing $t_{char,homo}$ and $t_{char,hetero}$, wherein it was found that within the range of $10^2 < d_{NC} < 10^3$ nm, $t_{char,homo}$ was consistently less than $t_{char,hetero}$ whenever $\alpha_{homo} \geq \alpha_{hetero}$ (Figure B6). This phenomena may reflect the increasing importance of steric interactions that arise as the NOM surface coverage increases, especially under relatively low ionic strengths.^{32,52}

In light of these aspects, it is hypothesized that the combined ratio of $[NOM]:N_{NP}:N_{NC}$ dictates both particle stability and the mode of aggregation in natural aquatic mediums. For ENPs that readily adsorb NOM, variations in the $[NOM]:[ENP]$ ratio (functionally equivalent to $[NOM]:N_{NP}$) have been shown to either stabilize the ENPs via overcoating by NOM or to promote their aggregation.⁸⁵ This phenomena is likely a function of the total surface area available for NOM adsorption, with changes in $[NOM]$, NOM composition and N_{NP} (which is tied to d_{NP}) affecting the amount of NOM adsorbed to the surface of the ENPs. The impact of $[NOM]:N_{NP}$ can be interpreted as altering α_{homo} and α_{hetero} , which the current work demonstrates can favor one aggregation process over the other. Likewise, the number concentration ratio of $N_{NP}:N_{NC}$ will also dictate the dominant mode of aggregation. If homoaggregation and heteroaggregation are both favorable and $N_{NP} \ll N_{NC}$, then heteroaggregation will be more relevant whereas if $N_{NP} \approx N_{NC}$ or $N_{NP} \gg N_{NC}$, then homoaggregation will be increasingly important.

The conceptual relationship between $[NOM]:N_{NP}:N_{NC}$ is shown in Figures 3.4 and 3.5. When ENPs enter an aquatic system containing NOM and NCs, there are several possible outcomes (Figure 3.4). In cases where there are favorable interactions between NOM and the ENPs (e.g., positively-charged ENPs), a competition is set-up between (1) eco-corona formation on the ENPs via NOM adsorption and (2) aggregation (homo- or heteroaggregation). Whether homo- or heteroaggregation will be dominant is dependent on $N_{NP}:N_{NC}$ and their associated attachment efficiencies (α). When NOM concentrations are high relative to the available ENP and NC concentrations/surface areas, the system is driven towards fully coated ENPs and α_{homo} and α_{hetero} tend toward zero (Figure 3.5).

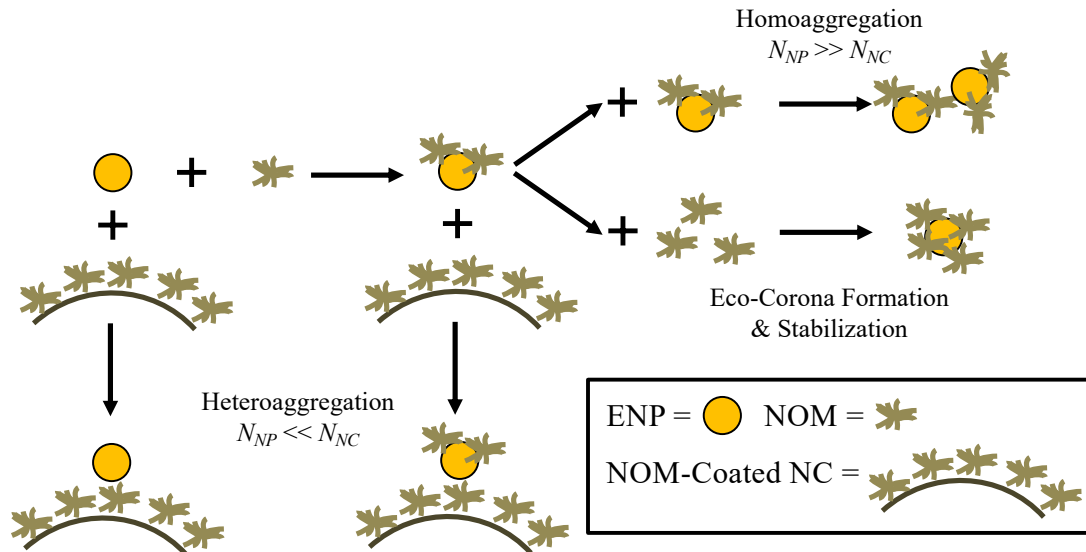


Figure 3.4. Conceptual reactions taking place upon addition of an ENP to an aquatic system containing NOM and NCs. In this illustrative example, NOM-NP interactions are assumed to be favorable, while ENP-ENP interactions are unfavorable.

Furthermore, if NOM interactions are relatively fast, as was reported in Nason et al. (2012)³², it is these initial interactions with NOM that ultimately dictate α .

In the current work we found that the $[\text{NOM}]:N_{NP}:N_{NC}$ employed resulted in a system that favored homoaggregation of model ENPs that readily adsorbed NOM while the model ENPs that did not form an eco-corona or for which interactions with NOM did not promote aggregation were stable. This finding highlights the importance of considering all three factors during experimental design. As all three components are linked, altering one factor can affect both ENP colloidal stability and the dominant mode of aggregation. Clearly, there are challenges that limit the extent to which $[\text{NOM}]:N_{NP}:N_{NC}$ can match realistic environmental conditions. Namely, N_{NP} is often much higher than is expected in the environment. While this is currently difficult to avoid due to analytical limitations, the findings from the current work illustrate the importance of considering this factor, along with $[\text{NOM}]$ and N_{NC} , in interpreting experimental results.

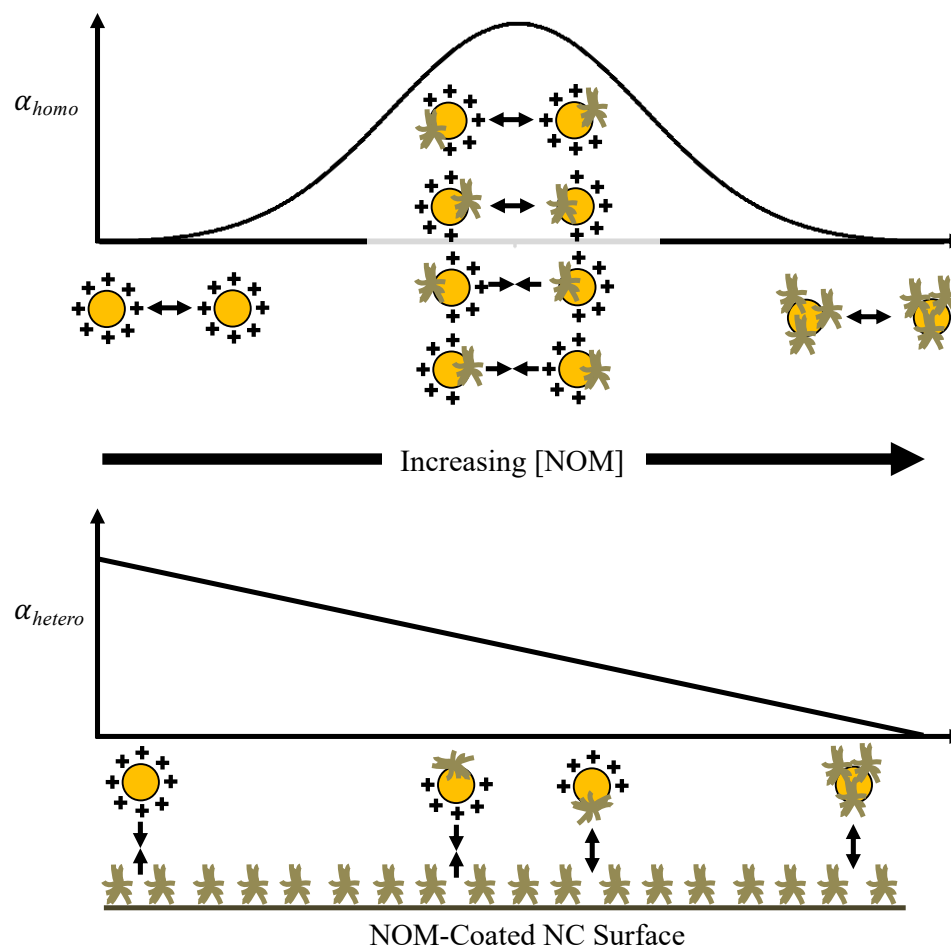


Figure 3.5. Conceptual variation of α_{homo} and α_{hetero} for a positively-charged ENP as a function of $[NOM]$ at fixed N_{NP} and N_{NC} .

Overall, the batch experiments using the raw WRW reveal that variations in the properties of the engineered surface coatings continue to influence particle-particle interactions in a complex aquatic medium. The PEG- and PEG-COOH-AuNPs were stable in both the filtered and raw WRW while the PEG-Amine-, bPEI-, and Cit-AuNPs were unstable and aggregated. Comparing the results of the filtered and raw WRW batch experiments helps highlight the importance of two competing processes—eco-corona formation and aggregation. The results using the filtered WRW show that the former process is dictated by an ENP's engineered surface coatings. Once destabilized, the dominant mode of aggregation affecting the ENPs is dependent on the relative amounts of ENPs and NCs, as

well as the rate and extent of eco-corona formation. Taken as a whole, it is hypothesized that a combination of factors, expressed through the combined ratio of $[\text{NOM}]:N_{NP}:N_{NC}$, will dictate particle stability and the dominant aggregation process affecting the fate and transport of the ENPs.

3.4.3 Surface Affinity Functional Assay

To aid the modelling of ENP aggregation in complex aquatic mediums, we attempted to translate the results from the batch experiments into estimates of α_{homo} and α_{hetero} . To achieve this, the surface affinity functional assay developed by Wiesner and colleagues was evaluated.^{15,16,86–88} According to Hendren et al. (2015)⁹⁸, functional assays are defined as “procedures for quantifying parameters that describe a specific process (or function) occurring within a given (often complex) system”. Functional assays are intended to serve as a bridge between simplified model systems and complex environmental systems. The surface affinity functional assay relies on measuring the number concentration of ENPs remaining in suspension ($N_{NP,i}$) as a function of time.^{15,16} The overall slope determined via linear regression can then be used to extract the value of α_{hetero} (Equation 4).

$$\ln\left(\frac{N_{NP,0}}{N_{NP,i}}\right) = -\alpha_{hetero}^{TOT}(\alpha\beta)_{NP-NC}N_{NC}t \quad (4)$$

In Equation 4, $N_{NP,0}$ is the initial ENP number concentration, while the other terms have been previously defined.

The process of estimating α_{hetero} using the surface affinity functional assay is accomplished through certain assumptions and specific components of the experimental design. First, the method assumes that the loss of ENPs via homoaggregation is negligible. Within certain mediums this assumption is reasonable, such as investigating ENP aggregation within activated sludge where N_{NP} is known to be much less than N_{NC} .^{44,45} Alternatively, this requirement can be achieved by using background colloid concentrations much higher than those expected in the environment or by selecting ENPs that are stable with respect to homoaggregation.^{16,86–88} Using this assumption, α_{hetero} can then be extracted from the slope

of the linear regression by two approaches—dividing by estimated values of $^{TOT}(\alpha\beta)_{NP-NC}$ N_{NC} or normalizing the slope by that measured when aggregation is favorable (i.e., $\alpha_{hetero} \rightarrow 1$). The former can be realized if the properties and number concentration of the colloids are known (e.g., monodisperse and homogeneous model colloids) or are accurately measured. Otherwise, in cases where either $^{TOT}(\alpha\beta)_{NP-NC}$ is difficult to calculate and/or N_{NC} is unknown, the latter approach can be used to derive ‘relative’ surface affinities.

In designing the current research, we chose to work with the experimental conditions presented by an actual environmental medium. While higher than is expected in the environment, N_{NP} in the current work was significantly lower than in previous tests using the surface affinity functional assay.^{15,16,86,87} Likewise, the NC mass concentration (3.9 ± 0.4 mg/L) of the WRW was orders of magnitude lower than previous research applying the surface affinity functional assay. Under these conditions, we found that removal via homoaggregation alone was comparable to the combined effect of homo- and heteroaggregation (Figure 3.1a). This finding indicates that the main assumption underlying the surface affinity functional assay was not valid for our experimental system. Specifically, the method requires that the loss of AuNPs is attributable to heteroaggregation alone. Ignoring this finding and deriving values of α_{hetero} according to the approach would not have served the purpose of refining ENP environmental fate modelling and thus was not attempted.

Even if the assumption that homoaggregation was negligible was valid, incorporating an actual environmental medium into the experimental design generated significant uncertainties when estimating the value of α_{hetero} . First, both N_{NC} and d_{NC} of the native NCs must be measured. Currently, there is no analytical technique that can provide a particle size distribution (PSD) spanning the low-nanometer-to-high-micrometer size range. Overlaying the PSDs from multiple techniques, such as combining the PSD measured via single-particle inductively-coupled plasma mass spectrometry (sp-ICP-MS) or nanoparticle tracking analysis (NTA) with the PSD measured via Coulter Counter presents numerous challenges, the least of which is identifying and quantifying NCs that are an

assemblage of particles from myriad biogenic and geogenic origins. Second, as the derivation of α_{hetero} is dependent upon the estimation of $^{TOT}(\alpha\beta)_{NP-NC}$ and N_{NC} , errors in either of these parameters directly transfer to the estimated value of α_{hetero} . This concern was addressed in Geitner et al. (2017)¹⁶ by calculating the ‘relative surface affinity’ and eliminating the need to calculate $^{TOT}(\alpha\beta)_{NP-NC}$ and N_{NC} . Unfortunately, such a condition may not be realized or even feasible when working with actual environmental systems. Complicating matters is the dependence of $^{TOT}(\alpha\beta)_{NP-NC}$ on an accurate estimation of d_{NC} , which is linked to the issues noted previously. These challenges help to highlight some of the current limitations associated with the surface affinity functional assay.

The surface affinity functional assay does provide a method to calculate α_{hetero} and has been useful under conditions where the above issues are negligible or can be mitigated. The results from the current study simply suggest that this assay may not be readily applicable to all environmental systems of interest. More importantly, the current work highlights the care that must be taken during experimental design to consider how relative changes in [NOM], N_{NP} , and N_{NC} can significantly alter the experimental outcomes. Attempts to simplify the assay or employing conditions that are amenable to the experimental objectives may have unintended (and potentially unknown) consequences and prevent important insights. Referring back to Figures 3.4 and 3.5, it is clear that if N_{NP} and N_{NC} are manipulated independently from [NOM], the system may be biased towards a condition not representative of the actual system under study. For example, if N_{NP} were increased relative to [NOM] (equivalent to reducing [NOM] in Figure 3.5) the result would be increases in both α_{homo} and α_{hetero} . To our knowledge, this potential unintended consequence of the design of the surface affinity functional assay has not yet been explored and deserves additional attention. For example, strategies are needed to guide the appropriate selection of relative [NOM] in instances where it is desirable to employ elevated N_{NP} and N_{NC} .

Under the conditions employed in the current work, it was deemed inappropriate to estimate α_{hetero} . While this prevented us from achieving our second objective, the findings nonetheless serve to demonstrate the relevance of engineered surface coatings through their

influence on ENP aggregation within an actual aquatic medium. Working within a complex natural medium presents various complications. Yet, it remains important to move investigations of relevant processes and factors affecting ENP environmental fate from simplistic model systems to more complex environmental systems to fully capture the interrelated and dynamic processes inherent in the latter.

3.5 Implications on ENP Environmental Fate

In spite of the complications in applying the surface affinity functional assay, this work demonstrated the role engineered surface coatings play in influencing ENP aggregation behavior. More specifically, they show that certain engineered surface coatings have the ability to stabilize ENPs against both homo- and heteroaggregation in a complex aquatic medium while other surface coatings can promote aggregation through eco-corona formation. Furthermore, comparing trends between the filtered and raw WRW provides further evidence that the interaction between natural macromolecules and ENPs can strongly influence ENP colloidal stability.

In modelling the environmental fate of ENPs, Sani-Kast et al. (2015)⁶² found that the properties of the local environment near the point where ENPs are released (e.g., waters receiving the effluent from a wastewater treatment plant) is a strong predictor of environmental fate. If conditions favor aggregation, then the ENPs are more likely to end up in the local sediments where their environmental fate is linked to sediment transport processes.²⁶ Conversely, if the ENPs are stable near the point of discharge then they can remain mobile and be transported further downstream. With this in mind, the results from the batch experiments suggest that the PEG- and PEG-COOH-AuNPs are likely to remain mobile upon their discharge to a natural freshwater environment, whereas the PEG-Amine-, bPEI-, and Cit-AuNPs would aggregate and become associated with the localized sediments.

3.6 Conclusions

The primary aim of this research was to determine if an ENP's engineered surface coating can influence their colloidal stability in a complex aquatic medium. Of the five model ENPs tested, two were colloidally stable (PEG- and PEG-COOH-AuNPs) while the other three were destabilized and removed to varying degrees via aggregation and settling (PEG-Amine-, bPEI-, and Cit-AuNPs). By employing a combination of techniques, we found that various properties of the engineered surface coatings can influence ENP colloidal stability. These include their surface charge, stabilization mechanism, and core-coating binding mechanism. The surface charge of the engineered surface coating was shown to influence eco-corona formation. In cases where NOM adsorption is not favorable and the engineered surface coating is strongly bound to the ENP core (e.g., neutral- or negatively-charged and covalently-bound), the stabilization mechanism can dictate ENP colloidal stability. If the engineered surface coating is weakly bound (e.g., electrostatics), then surface coating displacement via NOM adsorption can occur. Finally, when NOM adsorption is favorable (or the surface coating is displaceable via NOM), the eco-corona formed on the ENP can result in their aggregation through a variety of mechanisms, including interparticle bridging, divalent cation bridging, and localized charge neutralization. However, it should be noted that whether eco-corona formation destabilizes or stabilizes the ENPs is also linked to the ratio of $[\text{NOM}]:N_{NP}$ as well as the aquatic chemistry (i.e., ionic strength and composition).

The second intent of this work was to refine the modelling of ENP aggregation by applying the surface affinity functional assay to derive estimates of α_{hetero} . However, a number of limitations were identified that hindered this goal. Homoaggregation was not negligible at the experimental conditions of the current work, a key assumption of the assay. Furthermore, the method relies upon the accurate measurement of N_{NC} and d_{NC} , which are difficult to estimate in a complex environmental medium. Although these limitations have been circumvented through the use of elevated concentrations of model NCs in natural systems^{16,86-88}, we suggest that the use of elevated N_{NP} and N_{NC} must be carefully considered relative to the role of NOM in controlling NC and ENP surface properties and

attachment efficiencies. We hypothesize that the relative concentrations of [NOM]: N_{NP} : N_{NC} will dictate both colloidal stability and the dominant mode of aggregation. In general, it is recommended that the relative ratios of these three components be considered during experimental design. Ideally, these factors should mimic the expected environmental conditions for the system under investigation. When that is not feasible, consideration should be given to adjusting the experimental design in a way that allows [NOM]: N_{NP} : N_{NC} to reasonably match realistic environmental conditions. Through additional work it is expected that these challenges can be minimized so that the functional assay can be applied to a broader range of environmental systems.

While the research presented here utilized an actual environmental medium to investigate ENP aggregation, there is additional progress to be made in the push towards ‘true’ environmental relevancy. In particular, it is unlikely that ‘pristine’ ENPs, as used in this research, will be directly released to the environment. Instead, recent research has emphasized the importance of considering an ENP’s life-cycle to fully capture the various transformations (termed ‘aging’) that might alter an ENP’s properties during its production, use, and eventual release.^{99–101} Recent investigations also suggest that seasonal variations in the chemistry of the aquatic medium may have surface coating-specific effects.⁸⁴ Thus, future research will need to shift towards utilizing aged ENPs and investigating the role of changing aquatic chemistry to fully define the dominant factors controlling ENP environmental fate.

3.7 Acknowledgements

This research was supported by the National Science Foundation (NSF) Graduate Research Fellowship Program under Grant No. DGE-1314109 and NSF Grant No. 1255020. Any opinions, findings, and conclusions or recommendations expressed in this material are those of the author(s) and do not necessarily reflect the views of the NSF. Special thanks to A. Ungerer (W.M. Keck Collaboratory) for assistance with the ICP-OES measurements; K. Motter (IWW Collaboratory) for assistance with TOC/DOC measurements; A. Deline,

J. Fiest, and A. Bernstein Livne for assistance during the batch experiments; and J. Laurance for assistance with the TR-DLS and EPM measurements.

3.8 Supplementary Information

The Supplementary Information for this manuscript is located in Appendix B.

THE INFLUENCE OF SURFACE COATING FUNCTIONALITY ON
THE AGING OF NANOPARTICLES IN WASTEWATER

Mark C. Surette, Jeffrey A. Nason, and Ralf Kägi

Environmental Science: Nano

Royal Society of Chemistry
1050 Connecticut Ave NW
Suite 500
Washington, D.C. 20036

In-Review

4. THE INFLUENCE OF SURFACE COATING FUNCTIONALITY ON THE AGING OF NANOPARTICLES IN WASTEWATER

4.1 Abstract

Efforts to predict the environmental fate of engineered nanomaterials (ENMs) are frequently based on the physiochemical properties and behavior of the ENMs in their pristine, “as-produced” state. However, it is well-established that ENMs can be physically, biologically, and chemically transformed, resulting in altered physiochemical properties and behavior. Wastewater treatment plants (WWTPs) represent an important stage in an ENM’s life-cycle where they can be transformed. To better understand the properties of ENMs discharged from WWTPs into surface waters, we investigated how the transformation processes of aggregation and corona formation are influenced by the surface coating applied to ENMs during their manufacture. Using 40 nm gold nanoparticles coated with polyethylene glycol, lipoic acid, or branched polyethylenimine as model ENMs, batch experiments were performed to investigate aggregation and corona formation during the primary clarification and activated sludge treatment stages. A tangential flow filtration system was used to evaluate if the initial transformations were altered as the aquatic chemistry of the background matrix was changed, mimicking the varying conditions ENMs would experience during transport through a WWTP. Using a combination of corroborative techniques including dynamic light scattering, phase analysis light scattering, ultraviolet-visible light spectroscopy, and transmission electron microscopy, we find that the model ENMs aggregated in each wastewater matrix, regardless of the initial surface coating. Differences in the UV-Vis spectra indicate that the nature of the corona acquired by the ENMs differed as a function of the surface coating of the pristine ENMs. In addition, initial ENM transformations during exposure to the influent wastewater persisted even as the background matrix changed. These results support the finding that ENMs discharged from WWTPs will not resemble their pristine analogs. Furthermore, the corona acquired by ENMs in WWTPs may vary in relation to their pristine properties and be dictated by conditions during early stage exposures.

4.2 Introduction

To assess the implications posed by the increased use of engineered nanomaterials (ENMs), environmental fate models have been developed to identify the dominant exposure pathways and estimate exposure concentrations.¹⁰⁻¹² A fundamental concept underlying these models is that the physiochemical properties of ENMs can be used to predict their environmental behavior. Extensive research has been conducted to estimate the various input parameters used in these models.^{27,29,80} Yet, much of this research inherently assumes that ENMs released to the environment will resemble their pristine, “as-produced” state. As discussed by Lowry et al. (2012)⁴², ENMs are likely to be transformed within natural environments, resulting in materials that have significantly different physiochemical properties than their pristine analogs. These transformation processes will also occur within engineered systems, such as sewers or wastewater treatment plants (WWTPs).

Transformations of colloids occur in natural and engineered environments through physical, chemical, and biological processes.³⁹⁻⁴² In the context of ENMs, significant attention has been given to investigating physical transformations via homo- and heteroaggregation^{14-16,30} and chemical transformations via reduction-oxidation processes and dissolution¹⁷⁻¹⁹. In addition, the adsorption of organic macromolecules including proteins, humic and fulvic substances to ENMs has been extensively investigated.²⁰⁻²²

Material Flow Analysis (MFA) modelling performed by various research groups have shown that WWTPs represent a common ‘life stage’ for many ENMs following their production and use.^{1-3,5,102-106} While the majority of ENMs entering WWTPs are expected to heteroaggregate with suspended particulate matter (SPM),^{45,107} the complete heteroaggregation and removal of all ENMs entering WWTPs is unlikely. Thus, WWTP effluent is one pathway through which ENMs are released to the environment. Indeed, numerous studies have detected ENMs in WWTP effluent.^{44,47-50} To predict the environmental fate of ENMs and to assess the exposure to relevant forms of ENMs, the key factors and processes that drive ENM transformations have to be understood.

Various studies have investigated the transformations occurring to ENMs entering these engineered systems. Particular emphasis has been placed on the aggregation, sulfidation, and dissolution of AgNPs^{44,45,47} and various metal oxide NPs, including, TiO₂^{49,50}, CeO₂¹⁰⁸, and SiO₂ NPs.^{109,110} A common finding amongst these studies is that the ENMs that pass the WWTP and are discharged to surface waters possess properties that differ from their pristine state. As discussed by Salieri et al. (2018)¹¹¹, this observation has substantial implications for models that attempt to link ENM physiochemical properties to the processes affecting their environmental fate. Recent MFA modelling performed by Adam et al. (2018)¹¹² included data on the transformations of the ENM core material to estimate the form and annual release of two ENM types (AgNPs and TiO₂ NPs) to the environment. However, these authors noted the “almost complete lack of data” regarding transformations to the surface coatings applied to ENMs.

Continuing this line of inquiry, the surface coatings applied to ENMs during their manufacture, herein referred to as “engineered surface coatings”, have been shown to influence the aggregation behavior of ENMs in both simulated and actual aquatic environments by mediating ‘eco-corona’ formation (i.e., the adsorption of natural organic macromolecules).^{20,60,85,113} The focus of the current research was to investigate the role of engineered surface coatings in controlling aggregation and corona formation during conventional wastewater treatment (i.e., activated sludge process) and to understand the links, if any, between the properties of ‘aged’ ENMs and their pristine analogs in this context.

To accomplish this, three different 40 nm gold nanoparticles with covalently-bound engineered surface coatings were selected as model ENMs. Differently functionalized gold nanoparticles with well-defined particle sizes and functionalities provide an ideal platform to probe the impact of surface coating properties on ENM transformations while avoiding transformations to the core material, such as dissolution or sulfidation, that would confound such analysis. Corona formation and aggregation during individual WWTP stages were investigated using batch experiments containing filtered wastewater matrices from either

the raw influent, nitrification, or denitrification stages of a pilot WWTP. Filtering these waters focused our assessment on the fraction of ENMs not removed via heteroaggregation with SPM. Corona formation and (homo)aggregation were assessed using a suite of complementary and corroborative techniques, including ultraviolet-visible light spectroscopy (UV-Vis), dynamic light scattering (DLS), phase analysis light scattering (PALS), and transmission electron microscopy (TEM). These techniques probed changes related to the engineered surface coating including conformational changes or the adsorption of organic macromolecules, indicated whether the model ENMs aggregated, and revealed the resulting aggregate structure.

To simulate the effect of sequential wastewater treatment processes, a tangential flow filtration (TFF) system was used to exchange the wastewater matrix while keeping the model ENMs in the system. A combination of in-line UV-Vis and DLS detectors and off-line TEM analysis were used to assess corona formation and aggregation occurring over time as the composition of the wastewater medium changed. Results from these matrix exchange experiments were compared to the results of the batch experiments to assess whether subsequent exposures to different media affect the transformation processes.

4.3 Materials and Methods

4.3.1 Engineered Nanomaterials

40 nm gold nanoparticles (AuNPs) with three different covalently-bound (thiol) engineered surface coatings were chosen as model ENMs: 5 kiloDalton (kDa) polyethylene glycol (PEG), lipoic acid (COOH), and 25 kDa branched polyethylenimine (bPEI). All the AuNPs were purchased from nanoComposix, Inc. (NanoXact 0.05 mg/mL). The measured and manufacturer reported characteristics of the pristine AuNPs are provided in Table 4.1. Further details regarding their characterization, including the conversion of the measured electrophoretic mobility (EPM) to the modelled zeta potential (ζ) values, are provided in Appendix C.

Table 4.1. Measured and manufacturer reported properties of pristine AuNPs.

Surface Coating	Core Diameter D_c (nm)	Intensity-Weighted Hydrodynamic Diameter $D_{h,initial}$ (nm)	Electrophoretic Mobility μ_E ($[\mu\text{m}/\text{S}] / [\text{V}/\text{cm}]$)	Zeta Potential ζ (mV)	Surface Plasmon Resonance λ_{SPR} (nm)
PEG	40 ± 3	48.7 ± 0.6	-2.27 ± 0.4 (pH 5.5 ± 0.9)	-45.9 ± 8.1	523.3 ± 1.9
COOH	40 ± 5	50.0 ± 2.2	-2.06 ± 0.3 (pH 5.6 ± 0.5)	-41.7 ± 6.1	524.0 ± 0.0
bPEI	42 ± 5	51.7 ± 1.2	2.21 ± 0.4 (pH 5.3 ± 0.3)	44.6 ± 8.1	524.3 ± 0.7

Error bars indicate \pm 95% confidence interval (D_c : N/A; $D_{h,initial}$: $n = 34$; μ_E/ζ : $n = 9$; λ_{SPR} : $n = 3$).

4.3.2 Preparation of Wastewater Matrices

Samples from the primary clarifier, denitrification, and nitrification stages were obtained from a pilot WWTP located at Eawag (Dübendorf, Switzerland). One liter of sample from a given reactor was collected prior to use each day between 9:00 – 10:00 a.m. It was found that the AuNPs readily heteroaggregated with SPM (Figure C1). To focus our assessment on the transformations caused by the aquatic chemistry of the wastewater matrix and represent the fraction of ENMs passing the WWTP, the SPM in the wastewater/mixed liquor samples was removed via centrifugation at 3,000 rpm ($\approx 1,800g$ RCF) for 30 minutes (estimated particle size cutoff of ≈ 575 nm at $\rho_{particle} = 1.2$ g/cm³) followed by sequential filtration of the supernatant (≈ 900 mL) through 1 μm and 0.45 μm cellulose-acetate and 0.2 μm polycarbonate membrane filters (Sartorius). Details regarding the layout and operation of the pilot WWTP are discussed in Kägi et al. (2011)⁴⁴, with additional details regarding the properties of the wastewater matrices in Table C2.

4.3.3 Batch Experiments (Single Wastewater Matrix)

The colloidal stability of each AuNP type in the wastewater matrices was tracked using time-resolved dynamic light scattering (TR-DLS). Samples ($V_{TOT} = 1$ mL) containing a given filtered wastewater matrix ($V_{WW} = 980$ μL) were prepared in polystyrene micro-cuvettes (VWR) and dosed with 20 μL of a given AuNP type to a mass concentration (C_{NP}) of 1 mg Au/L. Upon dosing, the intensity-weighted hydrodynamic diameter (D_h) was recorded over an ≈ 45 minute period (160 measurements, each 15 seconds long) using a

ZetaSizer Nano ZS (Malvern Panalytical). Using the TR-DLS data, the colloidal stability of the AuNPs was assessed by calculating the extent of aggregation ($D_{h,final}/D_{h,initial}$) according to the procedure described previously.⁸⁵

Conformational changes to the engineered surface coating and/or the adsorption of organic macromolecules to the surface coating, as well as the aggregate structure, were investigated via time-resolved UV-Vis (TR-UV-Vis) using a Cary 60 UV-Vis Spectrophotometer (Agilent Technologies). Prior to sample analysis, the UV-Vis instrument was blank-corrected using 0.2 μm filtered, 18.2 M Ω -cm Nanopure water (DDI; Barnstead). Then, the blank-corrected background spectrum of the wastewater matrix was measured by adding 9.8 mL ($V_{TOT} = 10$ mL) of the selected filtered wastewater matrix to a 50 mm light-path Quartz Suprasil[®] cuvette (Hellma Analytics) and measuring the absorbance (A) from $\lambda = 400 - 800$ nm at a rate of 10 nm/s. The wastewater matrix sample was then dosed with 0.2 mL of a given AuNP type to $C_{NP} = 1$ mg Au/L, gently mixed, and the absorbance of the sample was measured at 20-minute intervals over a period of 120 minutes. For each measurement, a background-corrected UV-Vis spectra and a background-corrected and normalized (A/A_{max}) UV-Vis spectra were generated (see Appendix C for details; Figure C2).

The surface charge of the AuNPs in the various wastewater matrices were investigated using phase analysis light scattering (PALS). Briefly, the electrophoretic mobility (EPM) of the model ENMs was measured using PALS and the resulting zeta potential (ζ) estimated as described in Appendix C. Samples ($V_{TOT} = 1$ mL) containing a given filtered wastewater matrix ($V_{WW} = 980$ μL) were prepared in polystyrene micro-cuvettes (VWR) and dosed with 20 μL of a given AuNP type to $C_{NP} = 1$ mg Au/L. After incubating for 30 minutes, ≈ 0.8 mL was transferred via sterile syringe to a Folded Capillary Zeta Cell (Malvern Panalytical) and the EPM of the sample was measured (5 measurements of 30 cycles each) using a ZetaSizer Nano ZS (Malvern Panalytical).

Finally, the size and structure of AuNP-containing aggregates was analyzed via transmission electron microscopy (TEM) using a scanning transmission electron microscope (STEM; HD2700Cs, Hitachi). The microscope was operated at an acceleration voltage of 200 kV. The secondary electron (SE) and high angular annular dark field (HAADF) signals were used to assess the structure of the aggregates and the spatial arrangements of the primary particles within individual aggregates. Samples ($V_{TOT} = 2$ mL) containing a given filtered wastewater matrix ($V_{WW} = 1.96$ mL) were prepared in polystyrene micro-centrifuge tubes (VWR) and dosed with 0.04 mL of a given AuNP type to $C_{NP} = 1$ mg Au/L. The samples were then allowed to rest for 120 minutes. For the PEG- and COOH-AuNPs, 1 mL of the sample was then centrifuged onto a poly-L-lysine (0.1% w/v; Sigma-Aldrich) functionalized carbon grid (Cu 200 mesh, carbon coated, Plano GmbH) at 14,000 rpm ($\approx 26,000g$ RCF) for 45 minutes. For the bPEI-AuNPs, 1 mL of the sample was centrifuged onto a glow discharged (ELMO, Cordouan Technologies) carbon grid (Cu 200 mesh, carbon coated, Plano GmbH) at the same conditions as the PEG- and COOH-AuNPs.

4.3.4 TFF Experiments (Changing Wastewater Matrices)

A wastewater matrix exchange process was developed to investigate the transformations occurring to a given AuNP type as the background wastewater matrix was changed, mimicking the varying aquatic chemistry ENMs would experience while transiting through a WWTP. To achieve this, a tangential-flow filtration (TFF) system equipped with a single-stage filtration unit was used (MMS Membrane Systems). The AuNPs were retained and continually cycled within the TFF system using a polyethersulfone (PES) membrane with a nominal pore size of 40 nm (GE Life Sciences), which was found to trap the AuNPs within the retentate while allowing sufficient flux of the background wastewater matrix through the membrane. Details regarding the operation and testing of the TFF system are provided in Appendix C (Figures C3 – C4 and Table C3).

Two sets of experiments were performed for each AuNP type using the TFF system—one wherein only the filtered influent wastewater matrix was used (baseline) and another

wherein the background wastewater matrix was steadily changed to a mixture of influent, denitrification, and nitrification matrices (double matrix exchange). For each set of experiments, the same initial procedure was followed: (1) a 588 mL sample of filtered influent wastewater ($V_{TOT} = 600$ mL) was dosed with 12 mL of a given AuNP type to $C_{NP} = 1$ mg Au/L; (2) the sample was gently mixed and added to the TFF system reservoir; and (3) the TFF system was purged of air before continually operating with a transmembrane pressure (TMP) of 2-3 bar, a cross-flow velocity (V_s) of ≈ 1.4 cm/s, and at $T = 19 - 20$ °C. Samples of the retentate were continually removed from the TFF system at a rate of ≈ 2 mL/minute (F_R), while the flowrate of the permeate through the filter membrane varied between $\approx 0.4 - 0.6$ mL/minute (F_P).

During the double matrix exchange, filtered wastewater from the denitrification reactor was added to the TFF system reservoir from $t = 20 - 140$ minutes at a rate of ≈ 2.5 mL/minute, matching the combined outflow from the system ($F_R + F_P$). From $t = 40 - 240$ minutes, filtered wastewater from the nitrification reactor was added to the TFF system reservoir. When both denitrification and nitrification wastewater were added to the TFF system (i.e., $t = 40 - 140$ minutes), the rate of addition of each matrix was reduced to ≈ 1.25 mL/minute so that the combined addition of the denitrification and nitrification wastewater matrices matched the combined outflow from the TFF system ($F_R + F_P$). From $t = 140 - 240$ minutes, only the nitrification wastewater was added to the TFF system, at a rate of ≈ 2.5 mL/minute. This process, while not exactly mimicking the transport processes occurring in a full-scale WWTP, was deemed an appropriate compromise that both exposed the AuNPs to changing wastewater matrices over a reasonable amount of time and avoided excessive concentration or dilution of the AuNPs in the retentate.

The retentate removed from the TFF system, which contained the transformed ENMs, was pumped to a mixing cell that was continuously stirred via a magnetic stirrer. From there, samples were analyzed at 5-minute intervals via in-line DLS and UV-Vis detectors. The intensity-weighted hydrodynamic diameter (D_h) was measured via 3 measurements, each 20 seconds long using a ZetaSizer Nano ZS (Malvern Panalytical), while the UV-Vis

spectrum was measured at $\lambda = 400 - 800$ nm at a rate of 1 nm/s using a Cary 60 UV-Vis equipped with a 40 mm light-path Torlon fiber-optic dip probe (Agilent Technologies). For each UV-Vis measurement, a background-corrected and normalized (A/A_{max}) UV-Vis spectra was generated (see Appendix C for details; Figure C5). The pH of the retentate was continuously monitored for the duration of the experiment. Upon completion of the experiment, ≈ 15 mL of the retentate was collected and analyzed via TEM according to the procedures described previously.

4.4 Results and Discussion

4.4.1 Transformations in Single Wastewater Matrices

4.4.1.1 PEG-AuNPs.

The extent of aggregation ($D_{h,final}/D_{h,initial}$) calculated from the TR-DLS measurements was used to determine if the ENMs aggregated in each wastewater matrix. Values of $D_{h,final}/D_{h,initial} \approx 1$ denote particle stability whereas $D_{h,final}/D_{h,initial} > 1$ indicates that particles are aggregating, with $1.3D_h$ indicative of doublet formation.¹¹⁴ The PEG-AuNPs aggregated in each wastewater matrix, as $D_{h,final}/D_{h,initial}$ was consistently > 1 (Figure 4.1). The TEM micrographs corroborate this finding and reveal that the PEG-AuNPs formed aggregates as large as a micrometer after incubating in each of the wastewater matrices for 120 minutes (Figures 4.2a-c).

The TR-UV-Vis spectra that were obtained after dispersing the PEG-AuNPs in each of the wastewater matrices possess several consistent features, illustrated in the example spectra shown in Figures 4.3a-c and the replicate spectra shown in Figures C11 – C13. First, there are two distinct peaks in the UV-Vis measurements collected at $t \geq 20$ minutes: a primary peak located in proximity to λ_{SPR} (≈ 523 nm, Table 4.1, herein referred to as λ_{max}) and a secondary peak at longer wavelengths (λ'_{max}). The peak at λ_{max} was red-shifted relative to λ_{SPR} (Figure C10), although the amount was not statistically significant in the nitrification wastewater matrix.

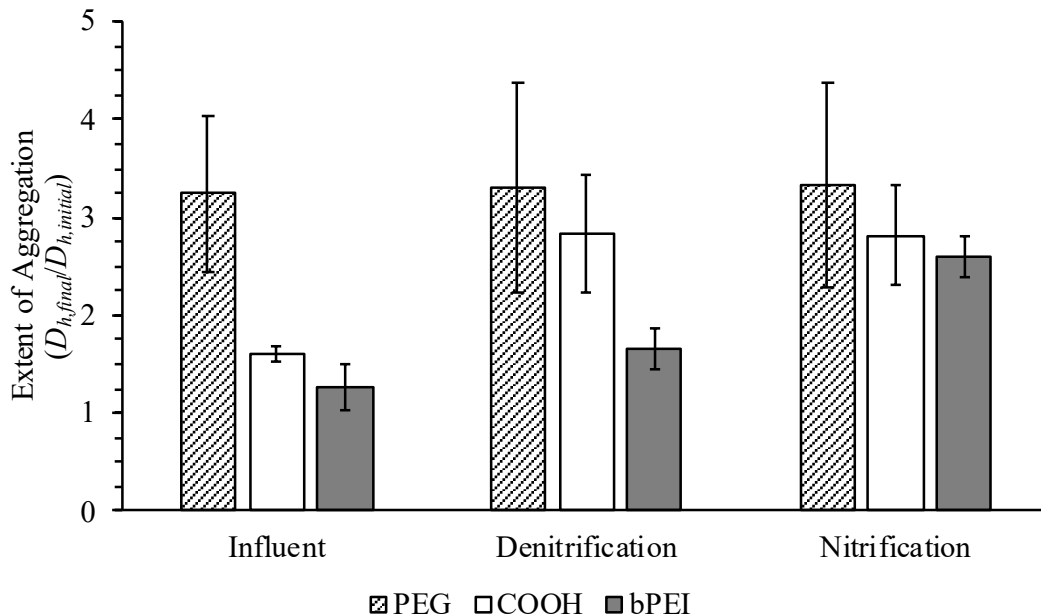


Figure 4.1. Extent of aggregation ($D_{h,final}/D_{h,initial}$) of each AuNP type in each matrix after ≈ 45 minutes. Error bars indicate $\pm 95\%$ confidence interval ($n = 3$).

With the exception of one replicate measurement (Figure C12), the peak height at λ_{max} consistently decreased (see background-corrected spectra in Figures C11 – C13). Indications of the secondary peak are first evident within ≤ 20 seconds after the PEG-AuNPs were initially dispersed in each of the wastewater matrices, demonstrated by the “shoulder” occurring at $\lambda'_{max} \approx 620$ nm. At $t \geq 20$ minutes, this secondary peak was more pronounced, having higher absorbance than that measured at λ_{max} , and was located at $\lambda'_{max} \approx 750$ nm.

The quenching and red-shift observed at λ_{max} are characteristic patterns attributed to a change in the local dielectric permittivity (ϵ_r) near the AuNP surface. This change can occur through a number of mechanisms, including conformational changes to the molecular structure of the engineered surface coating and the adsorption of organic macromolecules to either the surface coating (overcoating) or directly to the AuNP surface (displacement).^{115,116} These features are also produced when AuNPs aggregate such that very short center-to-center separation distances (d_s) occur and enable plasmon coupling

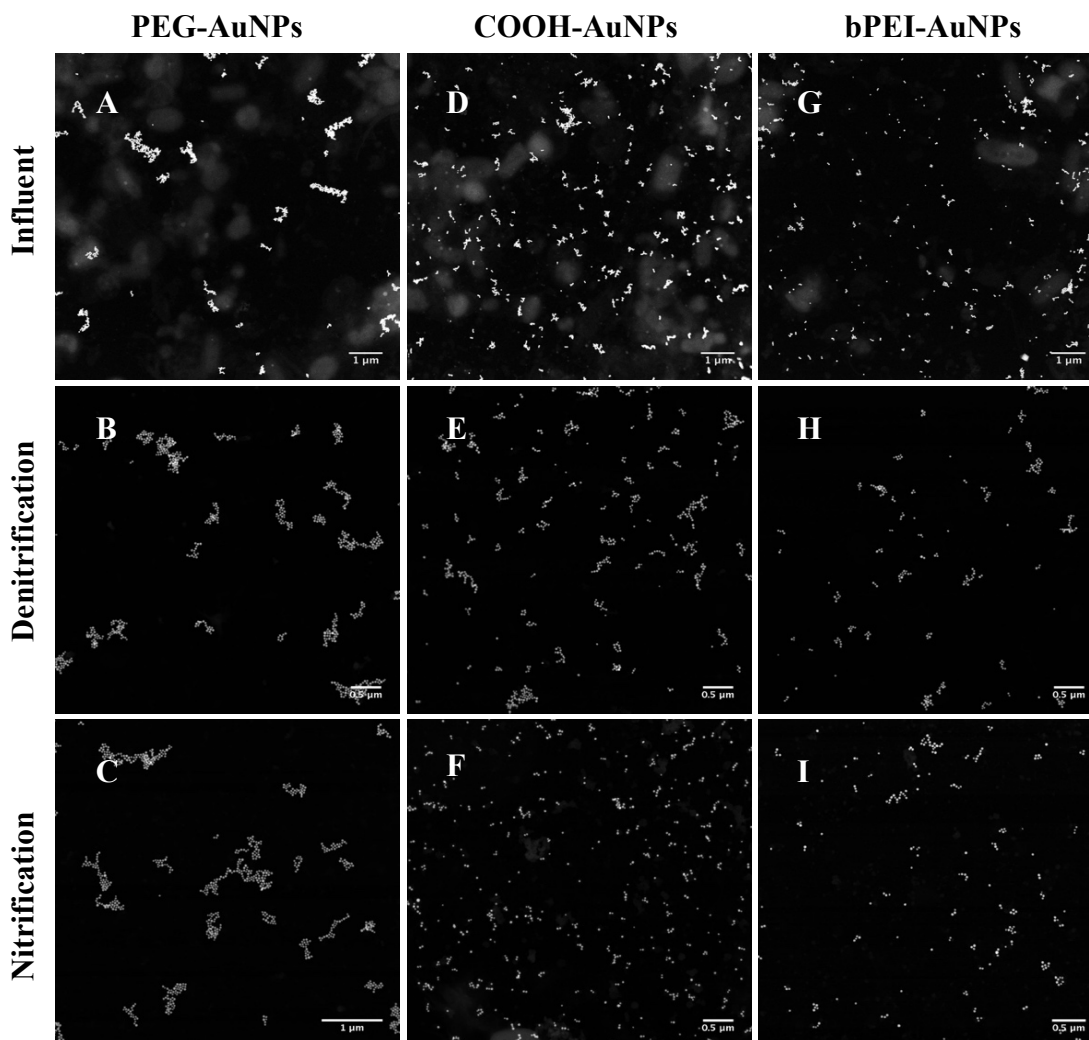


Figure 4.2. TEM-HAADF micrographs of (a-c) PEG-AuNPs, (d-f) COOH-AuNPs, and (g-i) bPEI-AuNPs in (top) influent (middle) denitrification and (bottom) nitrification wastewater matrices after incubating for ≈ 120 minutes.

between adjacent AuNPs.^{117–119} The presence of the secondary peak at λ'_{max} , however, is unique to the latter process. As d_s decreases, the surface plasmon resonance peak increasingly red-shifts to longer wavelengths (λ_{max}) until it “devolves” into two distinct peaks—the transverse surface plasmon resonance peak occurring in proximity to λ_{SPR} (i.e., λ_{max}) and the longitudinal surface plasmon resonance peak found at longer wavelengths (i.e., λ'_{max}).¹¹⁸ These two distinct peaks are a characteristic feature of anisotropic metallic

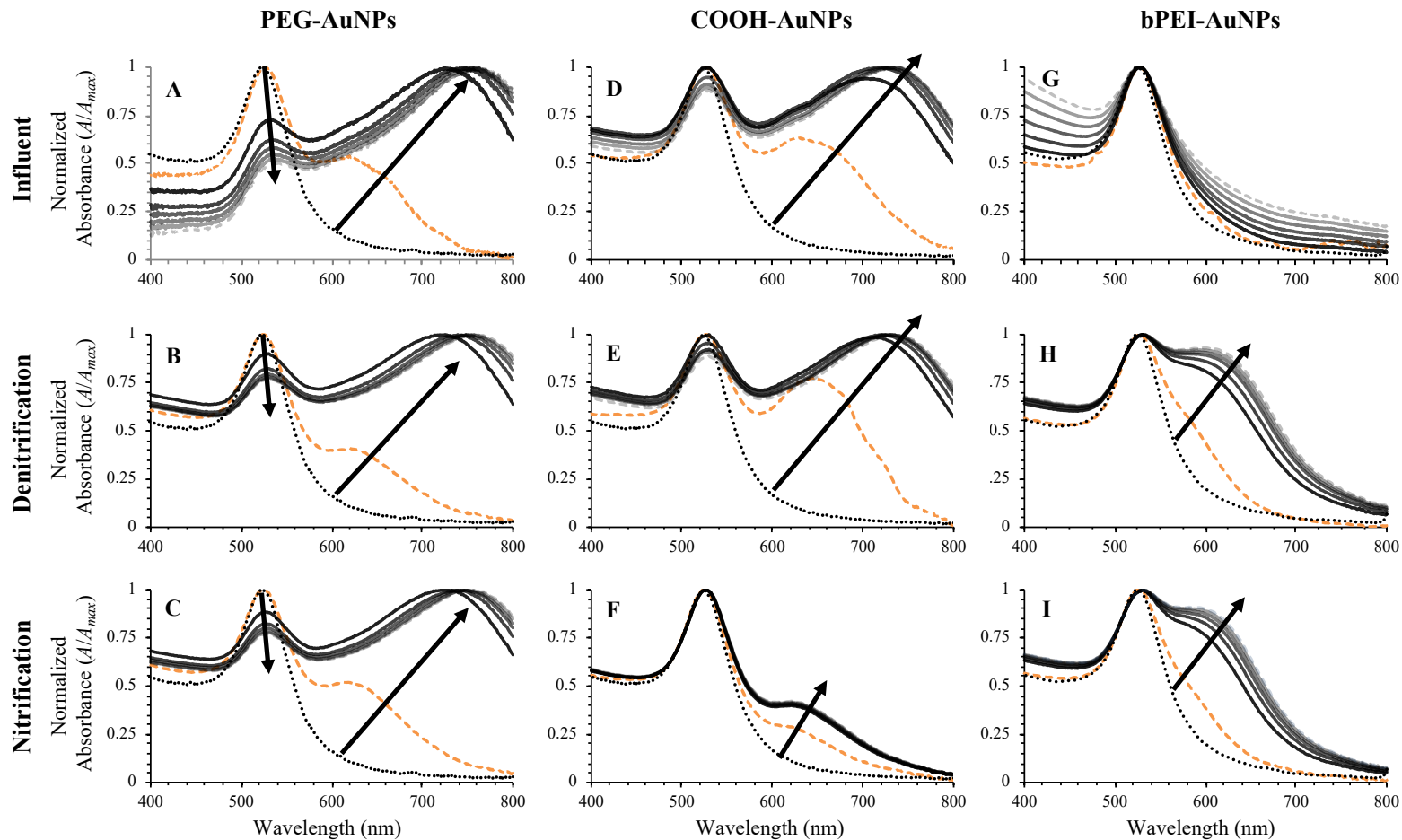


Figure 4.3. Background-corrected and normalized (A/A_{max}) UV-Vis spectra for (a-c) PEG-AuNPs, (d-f) COOH-AuNPs, and (g-i) bPEI-AuNPs in (top) influent (middle) denitrification and (bottom) nitrification wastewater matrices. Orange dashed-line depicts the UV-Vis spectra collected immediately upon addition of AuNPs ($t \leq 20$ seconds), grey dashed-line depicts spectra at $t = 120$ minutes, and grey-scale depicts spectra at 20-minute intervals in between (black-to-grey). For reference, the black dotted-line depicts the UV-Vis spectra in DDI.

ENMs with high aspect ratios, such as gold nanorods.¹²⁰ With respect to spherical AuNPs, these peaks are a function of the orientation of the incident light path relative to the long-axis of two adjacent AuNPs and d_s .^{118,119}

This phenomena was explored by Rechberger et al. (2003)¹¹⁸ and Sendroiu et al. (2006)¹¹⁹, who investigated the relation of the spectral aggregation shift ($\Delta\lambda_{agg} = \lambda'_{max} - \lambda_{max}$) to the ratio of d_s to nanoparticle diameter ($d_s/2r_c$) for particle pairs in well-controlled systems. According to Sendroiu et al. (2006)¹¹⁹, $\Delta\lambda_{agg}$ was found to exponentially increase with decreasing d_s , with $\Delta\lambda_{agg} \approx 100$ nm indicative of $d_s/2r_c \approx 1.0$ for doublets in suspension.¹¹⁹ In the present study, we find $\Delta\lambda_{agg}$ for the PEG-AuNPs varied between ≈ 203 nm (nitrification) and ≈ 225 nm (influent and denitrification). By analyzing the TEM micrographs to measure d_s between neighboring primary particle pairs within each aggregate assemblage and using the reported value of D_c (Table 4.1), the ratio of $d_s/2r_c$ was calculated (see Appendix C for details). For the PEG-AuNPs in each wastewater matrix, $d_s/2r_c$ was consistently ≈ 1.07 (Table 4.2), with the primary particles separated by a few nanometers in each aggregate assemblage.

Table 4.2. Average center-to-center separation distance (d_s) and its ratio to nanoparticle diameter ($d_s/2r_c$) calculated for each AuNP type in each wastewater matrix.

Surface Coating	Core Diameter, D_c (nm)	Influent		Denitrification		Nitrification	
		d_s (nm)	$d_s/2r_c$	d_s (nm)	$d_s/2r_c$	d_s (nm)	$d_s/2r_c$
PEG	40 ± 3	42.6 ± 0.4	1.06 ± 0.01	42.8 ± 0.3	1.07 ± 0.01	42.6 ± 0.2	1.07 ± 0.004
COOH	40 ± 5	41.4 ± 0.7	1.04 ± 0.02	43.2 ± 0.4	1.08 ± 0.01	42.7 ± 0.5	1.07 ± 0.01
bPEI	42 ± 5	44.0 ± 0.6	1.05 ± 0.01	42.8 ± 0.4	1.02 ± 0.01	44.4 ± 0.6	1.06 ± 0.01

Error bars indicate $\pm 95\%$ confidence interval (n varies; see Figures C21 – C23).

The overall TR-UV-Vis and TEM patterns reported herein are in line with the findings observed by Rechberger et al. (2003)¹¹⁸ and Sendroiu et al. (2006)¹¹⁹. Our finding that $\Delta\lambda_{agg} \approx 200 - 225$ nm corresponds with $d_s/2r_c \approx 1.07$ differs from the results reported previously and is likely an effect of analyzing large aggregate assemblages as opposed to carefully

patterned AuNPs fixed on a surface. These differences highlight the limitations of utilizing UV-Vis measurements alone to assess the structure of ENM aggregates in complex matrices. The TEM results, which clearly indicate that the PEG-AuNPs formed large aggregates consisting of primary particles separated by a few nanometers, are consistent with both the TR-DLS measurements and general UV-Vis spectral trends and demonstrate the benefit of using multiple, corroborative techniques.

The UV-Vis results further suggest that as the PEG-AuNPs aggregated, either the structure of PEG surface coating underwent significant conformational changes or an organic matter corona formed via adsorption of organic macromolecules to the surface coating (overcoating) or directly to the AuNP surface (displacement). It is not possible to distinguish between these processes with the current experimental approach. However, the electrophoretic mobility (EPM) of the PEG-AuNPs measured after incubation in each filtered wastewater matrix was less negative than that measured in the 1 mM NaCl and was comparable across each matrix (Figure 4.4). Previous research indicates that the background organic matter in wastewater matrices is mainly comprised of extracellular polymeric substances (EPS), which typically possess a negative surface charge due to the presence of various charged functional groups, such as carboxyl, phenolic and hydroxyl groups.^{121–123} Based on the UV-Vis results and the trends in the EPM data it is hypothesized that upon dispersion in the wastewater matrices, the PEG-AuNPs acquired a corona comprised of these organic macromolecules from the surrounding matrix. This corona clearly negates the stabilization provided by the PEG coating, allowing the PEG-AuNPs to form closely-spaced particle aggregates.

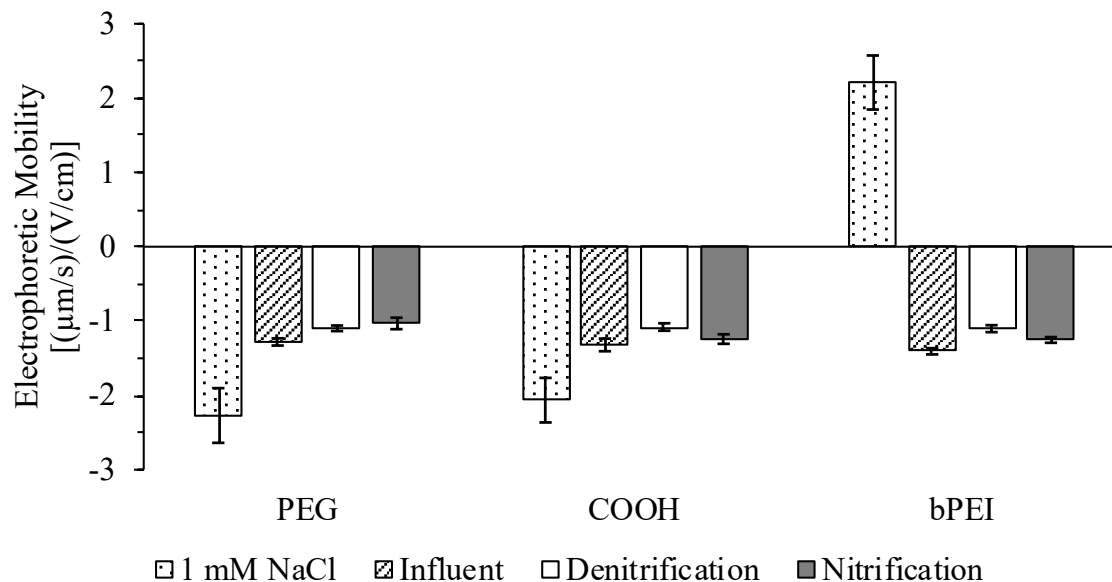


Figure 4.4: Electrophoretic mobility (EPM) of each AuNP type in each wastewater matrix at $\text{pH } 8.0 \pm 0.04$ and in 1 mM NaCl (see Table 4.1). Error bars indicate $\pm 95\%$ confidence interval ($n = 3$).

Previous research has demonstrated that the PEG surface coating electrosterically stabilizes the PEG-AuNPs across a range of conditions, including up to very high ionic strengths (up to 1.5 M) and various mass concentration ratios of natural organic matter to AuNPs (i.e. $[\text{NOM}]:[\text{NP}]$).^{85,113} For the current work, the ionic strength of the wastewater matrices varied between 18.4 – 21.7 mM and $[\text{NOM}]:[\text{NP}]$ was between 16.4 – 168.0 mg C/mg Au (Table C2). The ionic strength of the wastewater matrices is significantly lower than the conditions of the prior work, indicating that electric double layer (EDL) compression is not a relevant mechanism causing the PEG-AuNPs to aggregate.

While NOM has not been found to affect the aggregation behavior of the PEG-AuNPs, it appears that the organic matter in the wastewater matrices interacts with the PEG-AuNPs differently than NOM from freshwater sources. The composition of organic matter in WWTPs has been found to differ in relation to the aquatic chemistry and microbial community of different WW treatment processes.^{121–123} Characterization of the organic matter in the wastewater matrices was beyond the scope of this work. However, previous

research has shown that wastewater-derived EPS is predominately comprised of carbohydrates and proteins, although humic substances are also a major component in activated sludge treatment processes.^{121–123} For a detailed discussion regarding the composition of EPS in wastewater treatment systems, the reader is referred to the review by Sheng et al. (2010)¹²¹ and the references contained therein. Variations in organic matter composition have been shown to influence the formation of microbial aggregates in wastewater treatment processes, particularly in the presence of divalent cations.^{122,124–126} It is hypothesized that the EPS produced from the microbial communities in the WWTP interacts and alters the aggregation behavior of the PEG-AuNPs differently than freshwater-derived NOM. These interactions may also be facilitated by the presence of high concentrations of divalent cations (Table S2) as well as other solutes not typically found in freshwater environments, such as the nitrogenous species ammonia (NH_4^+), nitrite (NO_2^-) and nitrate (NO_3^- ; Table C2). These species could interact with the PEG surface coating through specific interactions (i.e., the terminal hydroxyl [OH] moiety exhibits zwitterionic behavior) or non-specific interactions with the polyethyleneoxide chain.¹²⁷

4.4.1.2 COOH-AuNPs.

With some exceptions, similar trends to those noted with the PEG-AuNPs were observed for the COOH-AuNPs. The TR-DLS measurements demonstrate that the COOH-AuNPs aggregated in each wastewater matrix, although $D_{h,final}/D_{h,initial}$ was lower in the influent wastewater compared to the filtered mixed liquor matrices from the activated sludge process (Figure 4.1 and Figure C7). The TEM micrographs also indicate that the COOH-AuNPs aggregated in each wastewater matrix (Figures 4.2d-f) but not to the extent observed for the PEG-AuNPs, indicated by the larger number of smaller ($<1 \mu\text{m}$) aggregates.

Where the COOH- and PEG-AuNPs notably differ is in their respective TR-UV-Vis spectra. With the exception of one replicate (Figure C16), quenching of the primary peak at λ_{max} was not observed for the COOH-AuNPs (background-correct spectrum in Figures C14 – C16). Instead, the peak height at λ_{max} was generally greater at $t = 120$ minutes than

that measured at $t \approx 0$ minutes (Figures C14 – C16), which is attributed to small variations in the background UV-Vis spectra measured in the absence of the AuNPs (Figure C2e). The red-shift at λ_{max} (Figure C10) as well as the distinct secondary peak at $\lambda'_{max} \approx 740$ nm (Figures 4.3d-e) were observed for the COOH-AuNPs in the influent and denitrification wastewater matrices, although the red-shift was not statistically significant in the influent wastewater matrix. In the nitrification wastewater matrix, the red-shift at λ_{max} was less pronounced than that observed in the denitrification matrix (Figure C10) while the secondary peak at λ'_{max} occurs at a shorter wavelength ($\lambda'_{max} \approx 630$ nm) and reaches a lower absorbance compared to λ_{max} (Figure 4.3f), resembling the “shoulder” observed in the initial PEG-AuNP TR-UV-Vis spectra.

These differences suggest that the structure of the COOH-AuNP aggregates formed in each matrix was slightly different. The $\Delta\lambda_{agg}$ was much lower in the nitrification wastewater (≈ 106 nm) compared to the influent and denitrification wastewater matrices (≈ 206 and ≈ 211 nm, respectively). Based on the trends previously reported^{118,119}, the TR-UV-Vis data suggests that d_s between adjacent COOH-AuNPs would be greater in the nitrification wastewater than the influent or denitrification wastewater. However, analysis of the TEM micrographs reveal that d_s was lowest in the influent wastewater matrix and was comparable in the denitrification and nitrification wastewater matrices (Table 4.2). As noted previously, the divergence between the UV-Vis and TEM measurements likely reflects the heterogenous nature of the aggregates formed. Overall, the finding that $d_s/2r_c$ in the various matrices was $\approx 1.04 - 1.08$ reveals that the COOH-AuNPs, like the PEG-AuNPs, formed aggregates containing closely-spaced primary particles separated by a few nanometers.

With similar trends as the PEG-AuNPs, UV-vis and EPM data (Figures 4.3 and 4.4) suggest that the COOH-AuNPs also acquire a corona of organic macromolecules via specific interactions with the carboxylic (COOH) moiety or non-specific interactions with the polyethyleneoxide chain. The relatively higher $d_s/2r_c$ in the denitrification and nitrification wastewater matrices may indicate that the composition of this corona is different than those

formed on the COOH-AuNPs dispersed in the influent wastewater matrix. As such, the combination of varying organic matter composition and aquatic chemistry may have altered the aggregation behavior and the resulting aggregate structure of the COOH-AuNPs in each wastewater treatment stage.

4.4.1.3 bPEI-AuNPs.

The bPEI-AuNPs experienced different extents of aggregation in the three matrices: $D_{h,final}/D_{h,initial}$ was lowest in the influent matrix and highest in the nitrification matrix (Figure 4.1). A distinct feature observed during the bPEI-AuNP TR-DLS measurements was a near-instantaneous increase in D_h of $\approx 20 - 30$ nm that was common across the wastewater matrices (Figure C8). After this initial increase in D_h , the bPEI-AuNPs appear resistant to further aggregation in the influent wastewater matrix. However, TR-DLS measurements performed over a much longer time period reveal that after ≈ 50 minutes (coinciding with the end of the ‘shorter’ TR-DLS measurement period), the bPEI-AuNPs begin to aggregate in the influent matrix (Figure C9). After ≈ 120 minutes, the D_h of the bPEI-AuNPs approaches 200 nm and was comparable to that measured for the PEG-AuNPs over the same period. In general, the TEM micrographs support the finding that the bPEI-AuNPs were physically transformed via aggregation (Figures 4.2g-i). In all three wastewater matrices, the bPEI-AuNPs formed some large aggregates (Figures 4.2g-i), although a considerable amount of smaller aggregates (e.g., dimers and trimers) formed in the influent wastewater matrix (Figure 4.2g).

While sharing some similarities to the TR-UV-Vis spectra obtained with the PEG- and COOH-AuNPs, there are notable differences in the measurements of the bPEI-AuNPs. First, the peak height at λ_{max} was consistently greater at $t = 120$ minutes versus $t \approx 0$ minutes (background-corrected spectrum in Figures C17 – C19). Again, we believe this to be an artifact of small variations in the background UV-Vis spectra measured in the absence of the AuNPs (Figure C2e). λ_{max} was red-shifted relative to λ_{SPR} in this case (Figure C10). Unlike the PEG- and COOH-AuNPs, no secondary peak was noted when the bPEI-AuNPs were dispersed in the influent wastewater matrix (Figure 4.3g). In the denitrification and

nitrification wastewater matrices, a “shoulder” at $\lambda'_{max} \approx 600$ nm consistently appeared at a slightly lower peak height compared to λ_{max} (Figures 4.3h-i and Figures C18 – C19). Compared to the PEG- and COOH-AuNPs, $\Delta\lambda_{agg}$ was much lower in the denitrification and nitrification wastewater matrices (≈ 71 nm) and negligible in the influent wastewater matrix. However, analysis of the TEM micrographs reveals that $d_s/2r_c$ for the bPEI-AuNPs was comparable to the other AuNP types (Table 4.2).

For the bPEI-AuNPs, there is a clear indication that the surface coatings underwent charge reversal in each wastewater matrix, changing from highly positive in the 1 mM NaCl to negative in all three wastewater matrices (Figure 4.4). In combination with the near-instantaneous increase in D_h observed via TR-DLS (Figure C8) and the features observed during the TR-UV-Vis measurements (Figures 4.3g-i), it can be inferred that the bPEI-AuNPs acquired a corona from the surrounding wastewater matrices. It is hypothesized that the corona acquired by the bPEI-AuNPs occurred through adsorption of the organic macromolecules to the amine moieties. Given the initial positive charge of the bPEI-AuNPs, this coating would favor interactions with the negatively-charged organic macromolecules that are ubiquitous in wastewater matrices.^{121–123} This behavior has been observed previously in simulated and real freshwater media when NOM was present.^{85,113} In the simulated freshwater medium at pH 8.0 (comparable to the pH of the wastewater matrices [Table C2]), it was found that $[\text{NOM}]:[\text{NP}] \geq \approx 0.3$ mg C/mg Au resulted in charge reversal of the bPEI-AuNPs via NOM adsorption.⁸⁵ Based on this, it is expected that the $[\text{NOM}]:[\text{NP}]$ in the current work, which varied between 16.4 – 168.0 mg C/mg Au (Table C2), would result in an organic matter corona extensively overcoating the bPEI-AuNPs. This hypothesis is also supported by the spectral trends (e.g., red-shift) in the TR-UV-Vis data at λ_{max} (Figures 4.3g-i and C10). Like the other AuNPs investigated, the bPEI-AuNPs aggregated upon dispersion in the wastewater matrices, mostly likely via the formation of an organic matter corona and interparticle bridging similar to previous observations.^{85,113}

4.4.1.4 Summary.

Each AuNP type underwent somewhat different transformations in each of the wastewater matrices investigated; yet, several overarching trends emerged. First, all three AuNPs were found to aggregate, which we hypothesize is linked to the corona they acquired upon dispersion in the wastewater matrices. Evidence that the AuNPs acquired an organic matter corona is based on the features observed during the TR-UV-Vis measurements and the finding that the EPM of each AuNP type was comparable in the three wastewater matrices (Figure 4.4). For the bPEI-AuNPs, reversal of the surface charge was a clear indicator that organic macromolecules had adsorbed and facilitated aggregation.^{85,113} The mechanisms resulting in the formation of an organic matter corona on the PEG- and COOH-AuNPs are not clear. However, their formation may have been influenced by the nature of the organic matter and the high concentration of divalent cations and other solutes in the wastewater matrices (Table C2) that are not common in natural freshwater environments. Previous work with these AuNP types indicate that the PEG- and COOH-AuNPs are not destabilized by charge screening or charge neutralization,^{85,113} suggesting that specific interactions between components of the wastewater organic matter and the engineered surface coatings (e.g. bridging) are facilitating aggregation. While beyond the scope of the current work, variations in the composition of the corona layer formed on the AuNPs are hypothesized to affect the structure of the ENM aggregates that formed in each of the wastewater matrices.

Second, the timescale of the transformations was relatively fast. For example, changes in the PEG- and COOH-AuNPs UV-Vis spectra (e.g., presence of secondary peak at λ'_{max}) are first evident during the initial measurement immediately following the addition of the AuNPs to the wastewater matrices (estimated to be ≤ 20 seconds). For the bPEI-AuNPs, changes in the UV-Vis spectra are also initially apparent but were more pronounced by the second measurement at $t = 20$ minutes, while an initial increase in D_h during the TR-DLS measurements was noted within the first minute.

4.4.2 Transformations during Changing Wastewater Matrices

4.4.2.1 Batch Experiments vs. Baseline Matrix Exchange.

For each AuNP type, the $D_{h,final}/D_{h,initial}$ calculated during the baseline matrix exchange procedure after ≈ 45 minutes is slightly higher than that measured during the batch experiments over the same period of time (Figure 4.5). This is attributed to increased particle-particle collisions via fluid shear occurring in the TFF system, which were absent in the batch measurements. Nonetheless, the relative trend in $D_{h,final}/D_{h,initial}$ between the two methods is comparable, with PEG > COOH \approx bPEI.

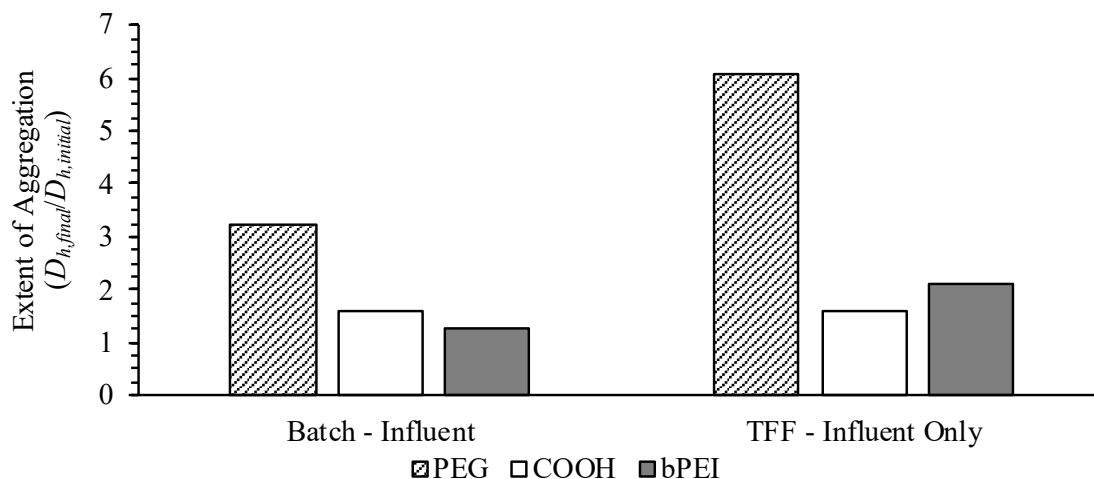


Figure 4.5. Extent of aggregation ($D_{h,final}/D_{h,initial}$) of each AuNP type during (left) batch experiments and (right) the wastewater matrix exchange procedure with only the influent wastewater matrix after ≈ 45 minutes.

During the baseline matrix exchange procedure, the UV-Vis spectra recorded for the PEG-AuNPs indicates the presence of two peaks, one in proximity to λ_{SPR} (i.e., λ_{max}) and another at $\lambda \approx 725$ nm (λ'_{max} , Figure 4.6a). The signal attributed to the PEG-AuNPs is obscured by the background wastewater matrix at $t \geq 60$ min., indicated by the highest absorbance at $\lambda \leq 400$ nm that gradually decreases as λ increases. This indicates that over time the signal

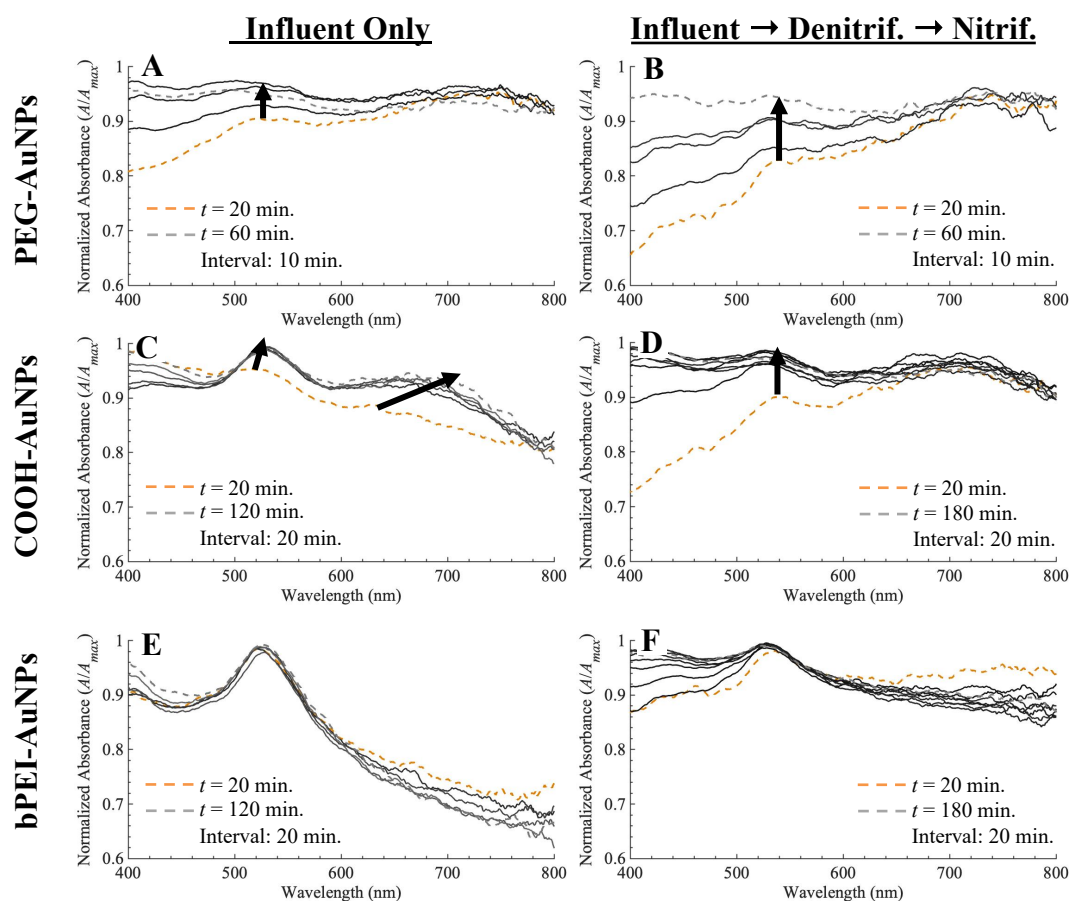


Figure 4.6. Background-corrected and normalized (A/A_{max}) UV-Vis spectra for (a,b) PEG-AuNPs, (c,d) COOH-AuNPs, and (e,f) bPEI-AuNPs during wastewater matrix exchange testing.

attributable to the PEG-AuNPs is lost, which could be from the loss of the PEG-AuNPs via attachment to the PES membrane or from their aggregation and subsequent extraction within the retentate for DLS and UV-Vis analysis. The UV-Vis spectra for the COOH-AuNPs measured during the baseline matrix exchange procedure has similar features to those observed with the PEG-AuNPs. Initially, only a single peak is evident at λ_{max} but over time a secondary peak appears (λ'_{max} , Figure 4.6c), initially at $\lambda'_{max} \approx 630$ nm before red-shifting to $\lambda'_{max} \approx 680$ nm. Unlike the PEG- and COOH-AuNPs, only a single peak is evident in the bPEI-AuNP UV-Vis spectra (Figure 4.6e), consistently appearing in proximity to λ_{SPR} . As with the DLS data, the relative trends in the UV-Vis spectra for each AuNP type during the baseline matrix exchange procedure are comparable to those

observed during the batch experiments using the influent wastewater matrix. These features include the secondary peak at λ'_{max} for the PEG- (Figures 4.3a and 4.6a) and COOH-AuNPs (Figures 4.3d and 4.6c) and the absence of secondary peak at λ'_{max} for the bPEI-AuNPs (Figures 4.3g and 4.6e).

In general, the similarity in the trends observed with the two methods indicates that the transformations occurring to the AuNPs during the two experimental methods are comparable. From this, we can assess how changing the background wastewater matrix affects the transformations occurring to the AuNPs by comparing the results to those obtained during the batch measurements.

4.4.2.2 Baseline vs. Double Matrix Exchange.

The extent of aggregation ($D_{h,final}/D_{h,initial}$) calculated for each AuNP type after ≈ 120 minutes exposure to only the influent wastewater (baseline) and after sequential exposure to the influent, denitrification, and nitrification matrices (double matrix exchange) are shown in Figure 4.7. During both experiments, the trends in $D_{h,final}/D_{h,initial}$ were the same and comparable to those observed during the batch experiments (Figure 4.1), with PEG > COOH \approx bPEI. The D_h of the PEG-AuNPs increased to ≈ 390 nm and ≈ 590 nm (baseline and double matrix exchange, respectively). In contrast, the D_h of the COOH-AuNPs only increased to ≈ 125 nm and ≈ 320 nm while D_h of the bPEI-AuNPs increased to ≈ 100 nm and ≈ 230 nm (baseline and double matrix exchange, respectively). These trends were confirmed via TEM, which indicated the presence of few but large PEG-AuNP aggregates upwards of 1 μm , a large number of moderately-sized COOH-AuNPs aggregates, and many lower-order bPEI-AuNP aggregates, such as dimers and trimers (Figure C24).

The higher $D_{h,final}/D_{h,initial}$ observed during the double matrix exchange experiments may reflect changes in the composition of the background matrix. During the batch measurements, $D_{h,final}/D_{h,initial}$ of the COOH- and bPEI-AuNPs was greater in both the denitrification and nitrification wastewater matrices relative to that measured in the influent wastewater matrix (Figure 4.1). However, this behavior was not observed with the PEG-

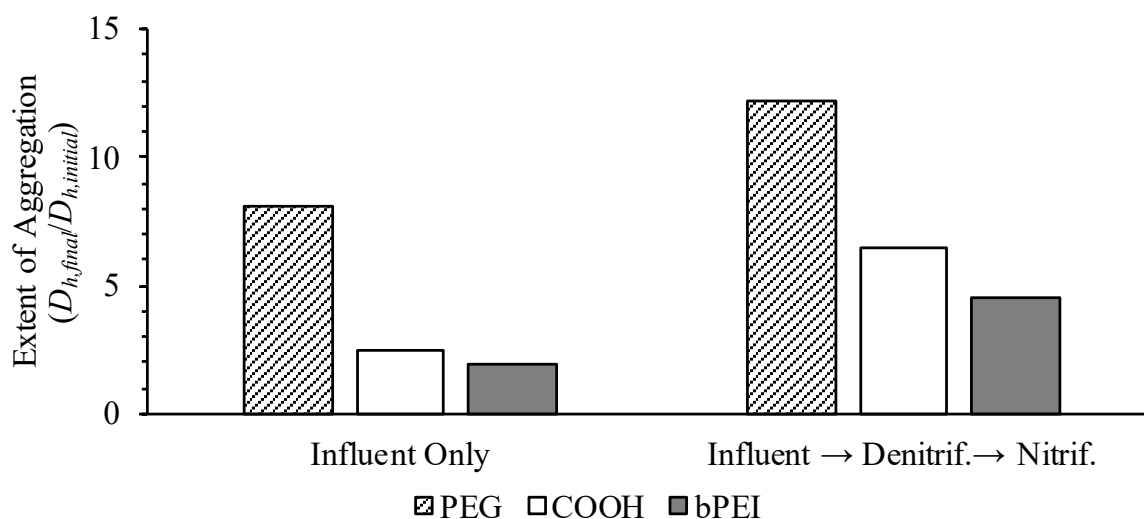


Figure 4.7. Extent of aggregation ($D_{h,final}/D_{h,initial}$) of each AuNP type during the wastewater matrix exchange procedure after ≈ 120 minutes.

AuNPs, which aggregated to similar extents in each of the wastewater matrices during the batch experiments (Figure 4.1). Nonetheless, the increased $D_{h,final}/D_{h,initial}$ during the double matrix exchange experiments suggests that changing the composition of the background matrix may influence the aggregation behavior of the AuNPs. It may have been that the AuNPs, after initially acquiring an organic matter corona from the influent wastewater matrix, continued aggregating due to the presence of some constituent that was absent from the influent wastewater matrix. This may reflect changes in the aquatic chemistry within each of the wastewater matrices, such as the reduction-oxidation reactions that change the relative amounts of the nitrogenous species ammonia (NH_4^+), nitrite (NO_2^-) and nitrate (NO_3^-) between each of the wastewater treatment stages.

The TR-UV-Vis spectra measured for each AuNP type during the double matrix exchange experiments are also shown in Figure 4.6. In general, the spectral patterns mimic those obtained during the baseline matrix exchange experiment. The location of secondary peaks for the PEG- and COOH-AuNPs were found at comparable wavelengths as those during the baseline measurements. Likewise, only a single peak in proximity to λ_{SPR} was observed for the bPEI-AuNPs during the double matrix exchange experiment. The similarity in the UV-Vis spectra between the baseline and double matrix exchange procedures for all the

AuNPs reveals that similar transformations to the AuNPs are likely occurring, even as the background matrix changes. Stated another way, these results indicate that the initial transformations occurring to the AuNPs upon their exposure to the influent matrix, which are specific to the engineered surface coating, continue to persist even as the composition of the background matrix changes to that of the subsequent biological treatment stages. The formation of a persistent organic matter corona would have been promoted by the relatively higher amount of organic matter in the influent wastewater ([NOM]:[NP] = 168 mg C/mg Au) compared to that of the biological treatment stages ([NOM]:[NP] = 16.4 and 45.9 mg C/mg Au, respectively; Table C2). As with the batch experiments, the mechanisms behind the transformations of the AuNPs appear to be influenced by their initial engineered surface coating. However, all the AuNPs were observed to aggregate, a processes we believe is facilitated by the acquisition of an organic matter corona. As noted previously, the aggregation behavior of the PEG- and COOH-AuNPs was found to be unaffected by the presence of organic matter in simulated and actual freshwater media.^{85,113} The results reported herein indicate that the composition and properties of the organic matter within the wastewater matrices was able to interact with and destabilize each of the model AuNPs investigated. This process may have been facilitated by the aquatic chemistry of the wastewater media, which is substantially different than that of freshwater environments.

4.5 Implications for Modelling ENM Environmental Fate

These results highlight the importance of colloid surface properties in influencing the aggregation of ENMs and the formation of organic matter coronas. In the context of ENMs, these results have significant implications when attempting to model environmental fate and exposure on the basis of pristine properties. Each of the model ENMs investigated underwent transformations when exposed to the wastewater matrices that were specific to the matrix and the initial surface coating of the ENMs. The interaction of the surface coating with constituents in the surrounding matrix were found to alter ENM aggregation and affect the structure of the aggregates. Furthermore, these transformations occurred over very short timescales (i.e., seconds-to-minutes). In a moderate-sized city (e.g., Zürich, Switzerland), the average residence time for untreated wastewater to reach a treatment

facility and the hydraulic residence time (HRT) within a typical wastewater treatment plant (WWTP) are each on the order of several hours.^{128,129} Thus, ENMs discharged to surface waters via WWTPs will certainly not retain their initial, pristine properties nor resemble their “engineered” analogs. Finally, the transformations that occurred to the model ENMs during their exposure to the influent wastewater, which are expected to occur as ENMs are transported in sewer systems en route to a treatment facility, were found to persist even as the background matrix changed.

Recognizing that a majority of ENMs entering WWTPs are removed via aggregation with suspended particulate matter, it is hypothesized that the fraction of ENMs not removed and discharged to surface waters will most likely be present in aggregates >100 nm and possess an organic corona composed of exudates from the microbial community in raw wastewater. In combination, these findings complicate attempts to link the physiochemical properties of pristine ENMs to the processes affecting their environmental fate. Instead, the properties of the ENMs after ‘aging’ will dictate their environmental fate and will be relevant for accurate exposure assessments. To investigate this further, additional work is aimed at comparing the aggregation behavior of aged ENMs versus their pristine counterparts upon dispersion in samples from a natural, freshwater river. Furthermore, the nature of the corona acquired by the model ENMs used in the current study will be further investigated via surface sensitive techniques to explore the kinetics of organic matter adsorption, the mechanisms of corona formation and the composition/structure of the adsorbed layer.

4.6 Acknowledgements

This research was supported by the National Science Foundation (NSF) Graduate Research Fellowship Program under Grant No. DGE-1314109 and NSF Grant No. 1255020, and through the NSF Graduate Research Opportunities Worldwide (GROW) Program. Any opinions, findings, and conclusions or recommendations expressed in this material are those of the author(s) and do not necessarily reflect the views of the NSF. Additional support was provided by the Swiss National Science Foundation (SNF) under Project No. 177090. We acknowledge the Scientific Center for Optical and Electron Microscopy

(ScopeM) of the ETH Zürich for providing access to their microscopes. Special thanks to B. Sinnet for assistance throughout the project, J. Traber for assistance with the TFF system, and D. Mitrano for suggestions during the experimental design.

4.7 Supplementary Information

The Supplementary Information for this manuscript is located in Appendix C.

THE INFLUENCE OF SURFACE COATING FUNCTIONALITY
ON THE FATE OF PRISTINE AND WASTEWATER-AGED GOLD
NANOPARTICLES IN FRESHWATER

Mark C. Surette and Jeffrey A. Nason

In-Preparation

5. THE INFLUENCE OF SURFACE COATING FUNCTIONALITY ON THE FATE OF PRISTINE AND WASTEWATER-AGED GOLD NANOPARTICLES IN FRESHWATER

5.1 Abstract

The environmental fate of engineered nanomaterials (ENMs) can be affected by the surface coatings applied during their manufacture (termed “engineered surface coatings”). This phenomena is often examined using ENMs in their ‘as-produced’ form. However, the physiochemical properties of ENMs are likely to be altered during their life-cycle. Engineered systems, such as sewers and wastewater treatment plants (WWTPs), represent a life-cycle stage where ENM properties can be transformed before being released to the environment. The focus of the current study was to compare the aggregation behavior of ‘pristine’ and ‘aged’ ENMs in samples of raw and filtered freshwater. Gold nanoparticles (AuNPs) coated with polyethylene glycol (PEG), lipoic acid (COOH) and branched polyethylenimine (bPEI) were selected as model ENMs. Pristine AuNPs were aged through suspension and subsequent recovery from filtered primary wastewater using a previously reported technique. Aside from two cases (PEG-AuNPs in raw river water and COOH-AuNPs in filtered river water), pristine AuNPs were removed to a negligible extent. These results indicate that the physiochemical properties of the pristine AuNPs influence ENM aggregation behavior in river water, often preventing their homo- and/or heteroaggregation. Yet, regardless of the initial surface coating, AuNPs aggregated and acquired an organic matter corona during wastewater aging. In contrast with their pristine counterpart, aged AuNPs were consistently lost from suspension in both raw and filtered river water. Higher removal was observed in the raw river water compared to filtered river water, demonstrating that the aged AuNPs undergo heteroaggregation in addition to homoaggregation, while negligible removal of the aged AuNPs was observed in ultrapure water. This reveals that the aging of ENMs in wastewater can stimulate their aggregation and subsequent removal in natural aquatic systems. With regards to the engineered surface coatings, their effect on ENM fate in natural aquatic media is negligible after the properties of the ENMs have been altered in wastewater treatment systems.

5.2 Introduction

Engineered nanomaterials (ENMs) are being increasingly incorporated into a variety of consumer and industrial products.^{1,2} While toxicological effects have been linked to some ENMs, the environmental risks they pose are not clear.^{7,8} One challenge hindering ENM risk assessments is uncertainty regarding the concentration of ENMs in the environment. Due to analytical limitations, it is necessary to rely on environmental fate models to estimate exposure concentrations.¹⁰⁻¹² However, the predicted environmental concentrations (PECs) generated by these models vary over several orders of magnitude.¹² To reduce variability in these estimates, further refinement of ENM environmental fate models is necessary.

As noted by Garner et al. (2017)¹², a key aspect of refining ENM environmental fate models is reducing the uncertainty of parameter values describing medium-dependent processes. One medium-dependent process that has received significant attention is the aggregation of ENMs in aquatic environments.²³ This process can be affected by the surface coating applied to ENMs during their manufacture (herein referred to as “engineered surface coatings”) through a number of mechanisms, including electrostatic and/or steric forces.^{20,23,38,43} The aggregation of ENMs can also be impacted by the adsorption of naturally-occurring organic macromolecules to the surface of the ENM, such as proteins, humic and fulvic substances.²⁰⁻²²

The aggregation of ENMs is typically investigated using simulated aquatic media. While often yielding important mechanistic insights, there is growing recognition that the aggregation behavior of ENMs in simulated aquatic media, and the parameters describing this process, may diverge from their behavior in complex, natural aquatic media.^{16,23,87} In these latter systems, a number of additional, interrelated processes can occur and simultaneously influence ENM aggregation. Recent studies examining ENM aggregation behavior in complex aquatic media demonstrate the potential for engineered surface coatings to impact ENM environmental fate.^{16,113,130}

While engineered surface coatings may influence ENM aggregation behavior in environmentally-relevant systems, this phenomena has nonetheless been examined using ‘pristine’ ENMs. It is generally recognized that ENMs will be transformed during their life-cycle, resulting in materials that have significantly different physiochemical properties than their pristine analogs.⁴² These transformation processes can occur at various stages in an ENM’s life-cycle and through a number of physical, chemical, and biological processes.^{39–42} This raises the question of whether the aggregation behavior of ‘aged’ ENMs differs from the behavior of their more often studied pristine analogs, particularly within actual aquatic media. When considering the life-cycle of ENMs, engineered systems such as sewers and wastewater treatment plants (WWTPs) represent an important stage where an ENM’s physiochemical properties can be altered.^{44,45,47–50,108–110} These engineered systems also represent one pathway through which ENMs are released to the environment.^{44,47–50,131} Thus, it is critical to understand the properties and aggregation behavior of aged ENMs. With regards to engineered surface coatings, it is unknown if they remain a relevant factor influencing ENM aggregation after the ENMs are transformed in wastewater treatment systems.

The focus of the current work was to examine the impact of wastewater aging using three different 15 nm gold nanoparticles (AuNPs) with covalently-bound (thiol) engineered surface coatings as model ENMs. These engineered surface coatings were previously found to alter ENM aggregation in simulated and actual freshwater media, as well as the ENM transformations during conventional wastewater treatment processes.^{85,113,132} These AuNP types were also shown to undergo rapid transformations in wastewater and the organic matter corona acquired during exposure to the influent wastewater persisted even as the aquatic chemistry of the matrix changed.¹²⁶ Based on these findings, filtered effluent from the primary clarifier of a full-scale WWTP was used to age the AuNPs in this work. Using ‘pristine’ and ‘aged’ variants of each AuNP type, a suite of batch experiments were performed to compare changes in the suspended AuNP concentration over time. Samples of raw and filtered river water were used to explore the effect of homoaggregation alone (filtered) and the combined effects of homo- and heteroaggregation (raw). A suite of

complementary techniques were used to characterize the pristine and aged AuNPs and to further examine their aggregation behavior in the various media used.

In building on the previous investigations, the results from the current research will help establish the capacity for engineered surface coatings to alter ENM environmental fate under highly-realistic conditions. Ultimately, this work will help identify the dominant factors influencing ENM aggregation behavior and accelerate the refinement of ENM environmental fate models.

5.3 Materials and Methods

5.3.1 Engineered Nanomaterials

15 nm gold nanoparticles (AuNPs) with three different covalently-bound (thiol) engineered surface coatings were chosen as model ENMs: 5 kiloDalton (kDa) polyethylene glycol (PEG), lipoic acid (COOH), and 25 kDa branched polyethylenimine (bPEI). All the AuNPs were purchased from nanoComposix, Inc. (NanoXact 0.05 mg/mL). The measured and manufacturer reported characteristics of the pristine AuNPs are provided in Table 5.1. Further details regarding their characterization, including the conversion of the measured electrophoretic mobility (μ_E) to the modelled zeta potential (ζ) values, are provided in Appendix D.

Table 5.1. Measured and manufacturer reported properties of pristine AuNPs.

Surface Coating	Core Diameter (D_c) [nm]	Intensity-Weighted Hydrodynamic Diameter ($D_{h,initial}$) [nm]	Electrophoretic Mobility (μ_E) [($\mu\text{m/s}$) / (V/cm)]	Zeta Potential (ζ) [mV]	Surface Plasmon Resonance (λ_{SPR}) [nm]
PEG	15.4 \pm 1.1	40.0 \pm 1.76	-0.28 \pm 0.17	-5.9 \pm 3.6	519.2 \pm 1.9
COOH	15.4 \pm 1.2	16.8 \pm 4.9	-0.98 \pm 0.2	-20.6 \pm 4.2	518.5 \pm 5.4
bPEI	15.3 \pm 1.1	26.1 \pm 3.6	0.56 \pm 0.13	11.8 \pm 2.7	521.5 \pm 2.2

Error bars indicate \pm 95% confidence interval (D_c : $n = \text{N/A}$; $D_{h,initial}$: $n = 3$; μ_E/ζ : $n = 15$; λ_{SPR} : $n = 3$).

Electrophoretic mobility measured at pH \approx 7.4 in pH-adjusted 1 mM KCl.

D_c : Manufacturer reported; $D_{h,initial}$, μ_E , and λ : measured. See Appendix D for details.

5.3.2. River Water

Samples were collected from the Willamette River (Oregon, USA) as described previously.¹¹³ The approach for collecting, preparing, and analyzing the river water is briefly summarized here. Additional details are provided in Appendix D. Approximately 2 L samples of river water were collected from the intake line to the City of Corvallis' municipal drinking water treatment facility (H.D. Taylor Water Treatment Plant, Corvallis, OR) using acid-washed 1 L high-density polyethylene (HDPE) containers (Nalgene®). The samples were collected between 8:30 – 9:30 a.m. on the day of the batch experiments (detailed below). Shortly after collection, half of the sample was sequentially filtered through pre-rinsed 0.45 μm and 0.2 μm Supor® membrane filters (Pall Corporation) and stored in the dark at 4 °C until use (referred to herein as filtered river water). Each filter was pre-washed with >125 mL of 18.2 M Ω -cm distilled, deionized (DDI) water (EGLA Purelab) prior to use and the initial (>25 mL) filtrate was discarded. The remainder of the river water was unaltered (referred to herein as raw river water). The filtered river water was used to examine the impact of homoaggregation in isolation while the raw river water was used to assess the combined impact when both homo- and heteroaggregation can occur. A summary of the water quality characteristics of the river water used in each group of batch experiments is provided in Table 5.2 (see Appendix D Table D2 for details).

Table 5.2. Water quality characteristics of Willamette River water used in batch tests.

Parameter	Value			Units
	Feb. 25 th (PEG)	March 5 th (bPEI)	March 15 th (COOH)	
Dissolved Organic Carbon (DOC)	2.47 ± 0.04	1.63 ± 0.04	1.49 ± 0.06	mg C/L
Ionic Strength	0.81	0.96	0.92	mM
pH	7.39	7.32	7.22	
Total Suspended Solids (TSS)	104.6 ± 5.2	13.7 ± 11.2	11.3 ± 6.3	mg/L
Conductivity	184.0	125.0	74.6	$\mu\text{S}/\text{cm}$
Total Alkalinity	20.31	23.20	23.95	mg/L as CaCO ₃
Total Hardness	18.06 ± 0.87	22.26 ± 0.54	21.3 ± 2.22	mg/L as CaCO ₃

Error bars indicate \pm 95% confidence interval ($n = 3$).

5.3.3. Engineered Nanomaterial Aging

The model ENMs were aged in effluent from the primary clarifier of a full-scale municipal wastewater treatment facility based on a procedure outlined previously.¹²⁶ Approximately 2 L of primary clarifier effluent was collected using acid-washed 1 L high-density polyethylene (HDPE) containers (Nalgene®). The samples were collected between 8:45 – 9:30 a.m. on the day of the batch experiments (detailed below). To remove the suspended solids, the wastewater samples were first centrifuged at $\approx 1,800g$ RCF for 30 minutes. The supernatant (≈ 1.8 L) was then decanted and sequentially filtered through pre-rinsed and ashed $1.2 \mu\text{m}$ glass microfiber filters (GF/C Whatman) followed by pre-rinsed $0.45 \mu\text{m}$ and $0.2 \mu\text{m}$ Supor® membrane filters (Pall Corporation). Each filter was pre-washed with >125 mL of DDI prior to use and the initial (>25 mL) filtrate was discarded. The filtered wastewater samples were stored in the dark at 4°C until use. A summary of the water quality characteristics of the wastewater samples used in each group of batch experiments is provided in Table 5.3 (see Appendix D Table D3 for details).

To generate the aged ENMs, 245 mL of filtered wastewater was dosed with 5 mL of a given pristine AuNP type to an initial concentration of 1 mg Au/L. The AuNPs were allowed to incubate in the wastewater matrix for ≈ 30 minutes before the AuNP/wastewater dispersion was concentrated using a VivaFlow 50R 100 kDa molecular weight cut-off (MWCO) tangential-flow filtration (TFF) cartridge (Sartorius). Based on initial testing, the 100 kDa MWCO membrane was found to maintain the AuNPs within the retentate while allowing the excess wastewater matrix to pass through the membrane (see Appendix D for details; Table D4). During the concentration/separation process, the AuNP/wastewater dispersion was continuously circulated through the TFF cartridge at a flowrate of 100 mL/min and a transmembrane pressure (TMP) of ≈ 2 bar. This process was continued until the permeate volume, which was tracked gravimetrically, was $\geq \approx 225$ mL (corresponding to a concentration factor of $\geq 10\times$). A portion of the concentrated aged AuNP dispersion was immediately used in the batch experiments (detailed below). The remainder was stored at 4°C in the dark and used the following day (<12 hours later). During this storage period,

the size of the aged AuNPs did not substantially change (Table D5). Additional details regarding the testing and storage of the TFF cartridge are provided in Appendix D.

Table 5.3. Water quality characteristics of primary clarifier effluent used in batch tests.

Parameter	Value			Units
	Feb. 26 th (PEG)	March 6 th (bPEI)	March 16 th (COOH)	
Dissolved Organic Carbon (DOC)	10.2 ± 0.87	16.42 ± 0.61	17.66 ± 0.48	mg C/L
Ionic Strength ^a	8.4	9.2	9.1	mM
pH	6.87	7.08	7.61	
Conductivity	523.0	574.0	570.0	μS/cm

Error bars indicate ± 95% confidence interval ($n = 3$).

^a Calculated per $I = 1.6 \times 10^{-5} \times \text{Specific Conductance (S.C.)}^{133}$

5.3.4. Batch Experiments

Batch experiments were performed using an approach similar to that reported previously.¹¹³ An illustration depicting the experimental approach is shown in Figure 5.1. For each AuNP type, four different groups of batch experiments were performed: pristine AuNPs in raw river water, aged AuNPs in raw river water, aged AuNPs in filtered river water, and pristine AuNPs in filtered river water. Each group included six replicates of the selected AuNP type/matrix combination, as well as two controls—raw river water centrifuged at 3,500 rpm ($\approx 2,200g$ RCF) for 5 minutes (referred to herein as centrifuged river water) and DDI water. The first control was added to examine the impact of small naturally-occurring colloids (NCs; $d_{NC} < \approx 300$ nm) in the river water. The second control was used to assess vessel interactions and the loss of the AuNPs during the centrifugation step.

Using 50-mL polypropylene centrifuge tubes (VWR International), each group of eight vials (i.e., six replicates and two controls) were prepared by dosing the selected matrix to a target initial concentration of $C_{NP,initial} = 250 \mu\text{g Au/L}$. After dosing, each vessel was briefly vortexed and a 5 mL aliquot was collected to measure $C_{NP,initial}$. The vials were then

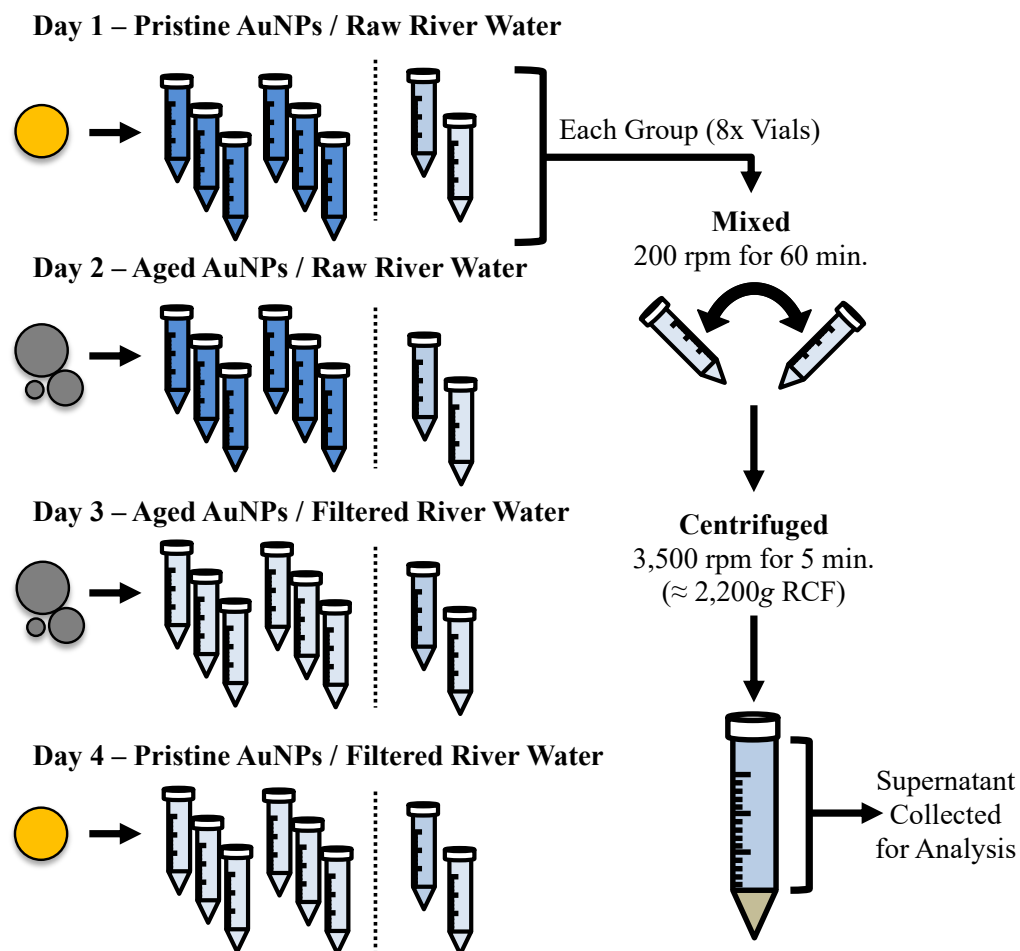


Figure 5.1. Illustrative example of experimental approach.

placed horizontally on a shaker table and continuously mixed at 200 rpm for 60 minutes. After mixing, the vessels were immediately centrifuged at 3,500 rpm ($\approx 2,200g$ RCF) for 5 minutes and the supernatant ($V_{TOT} = 30$ mL) was collected via three sequential withdrawals of 10-mL aliquots collected ≈ 1 cm below the surface. Each 30-mL sample was digested using *aqua regia* (3:1 ultrapure HCl:HNO₃) and the final AuNP concentration ($C_{NP,final}$) was measured using an Agilent 7900 inductively-coupled plasma mass spectrometer (ICP-MS; Agilent Technologies). Additional details regarding the digestion technique are provided in Appendix D.

5.3.5 Supporting Analytics

Time-resolved dynamic light scattering (TR-DLS) was used to assess the colloidal stability of the pristine AuNPs in filtered river water. The intensity-weighted hydrodynamic diameter (D_h) of the AuNPs was measured for ≈ 30 minutes at $C_{NP} = 1$ mg Au/L and the extent of aggregation ($D_{h,final}/D_{h,initial}$) was calculated. Values of $D_{h,final}/D_{h,initial} \approx 1.0$ denote particle stability whereas $D_{h,final}/D_{h,initial} > 1.0$ indicates aggregation. Phase analysis light scattering (PALS) was used to measure the electrophoretic mobility (μ_E) of the pristine AuNPs in filtered river water at $C_{NP} = 5$ mg Au/L. Conformational changes to the pristine engineered surface coating and/or the adsorption of organic macromolecules to the surface coating were examined at $C_{NP} = 5$ mg Au/L using ultraviolet-visible light spectroscopy (UV-Vis). The pristine AuNP concentrations used during the PALS and UV-Vis measurements were chosen to generate adequate signals using these techniques. The aged AuNPs were also characterized via DLS, PALS, and UV-Vis in filtered river water and the wastewater permeate generated during each aging procedure (TFF permeate). Due to the lower concentration of the aged AuNP/wastewater dispersion (≈ 5 mg Au/L; see Appendix D Table D4), the DLS, PALS, and UV-Vis measurements of the aged AuNPs were performed at ≈ 1 mg Au/L. Details regarding the preparation and analysis of the samples via these methods have been discussed previously and are summarized in Appendix D.^{113,132}

5.4 Results and Discussion

The loss of the AuNPs in the filtered and raw river water was evaluated by comparing the initial and final AuNP concentrations ($C_{NP,initial}$ and $C_{NP,final}$, respectively) using a one-way paired t -test ($\alpha = 0.05$). The results were also compared to a previous study that examined the aggregation behavior of pristine AuNPs in filtered and raw river water obtained from the same source.¹¹³ This comparison allowed for verification of the previous results and provided a foundation for comparing the aggregation behavior of pristine and aged AuNPs in the same aquatic media.

5.4.1 Pristine AuNPs in Filtered River Water

Removal of the pristine AuNPs in the batch tests using filtered river water is presumed to be attributable to the effects of organic macromolecule adsorption (termed ‘eco-corona’ formation) and/or homoaggregation due to the absence of naturally-occurring colloids (NCs). The pristine PEG-AuNPs were not removed to a significant extent (paired t -test(6), $p = 0.49$; Figure 5.2) and the TR-DLS measurements show no change in D_h (Figure 5.3). Removal of the pristine PEG-AuNPs in the DDI control was also negligible (Figure D2), indicating minimal losses to either the vessel walls or from the centrifugation step. In combination, these results indicate that the PEG-AuNPs were stable in the filtered river water and did not undergo homoaggregation. The μ_E of the PEG-AuNPs was found to be negative in both pH-adjusted 1 mM KCl and filtered river water (Figure 5.4). In the latter, the negative μ_E likely prevented the formation of an eco-corona due to electrostatic repulsion between the negatively-charged PEG-AuNPs and natural organic matter (NOM) macromolecules. The UV-Vis spectra (Figure 5.5) were evaluated for changes in λ_{SPR} and an increase in the full-width at half-max (FWHM) of the peak at λ_{SPR} (see Appendix D for details). These features are typically observed when AuNPs aggregate and/or the local dielectric permittivity (ϵ_r) near the AuNP surface is altered, which occurs following changes to the molecular structure of the engineered surface coating or the adsorption of NOM.^{115,116} These features are notably absent in the UV-Vis spectra measured in the filtered river water relative to that measured in DDI (Appendix D Tables D7 and D8), confirming that the PEG-AuNPs did not adsorb NOM. These results are consistent with previous research where steric interactions between PEG-AuNPs prevented their homoaggregation in simulated freshwater and filtered river water.^{85,113}

The pristine bPEI-AuNPs were also not removed to a significant extent in the filtered river water (paired t -test(6), $p = 0.3$; Figure 5.2). While the TR-DLS measurements indicate an increase in D_h , with $D_{h,final}/D_{h,initial} = 1.82 \pm 0.18$ (\pm standard deviation; $n = 2$; Figure 5.3), this near-instantaneous increase was observed when the bPEI-AuNPs were initially dispersed in the filtered river water, after which no significant change in D_h occurred (Appendix D Figure D1). The PALS measurements show that the bPEI-AuNPs underwent

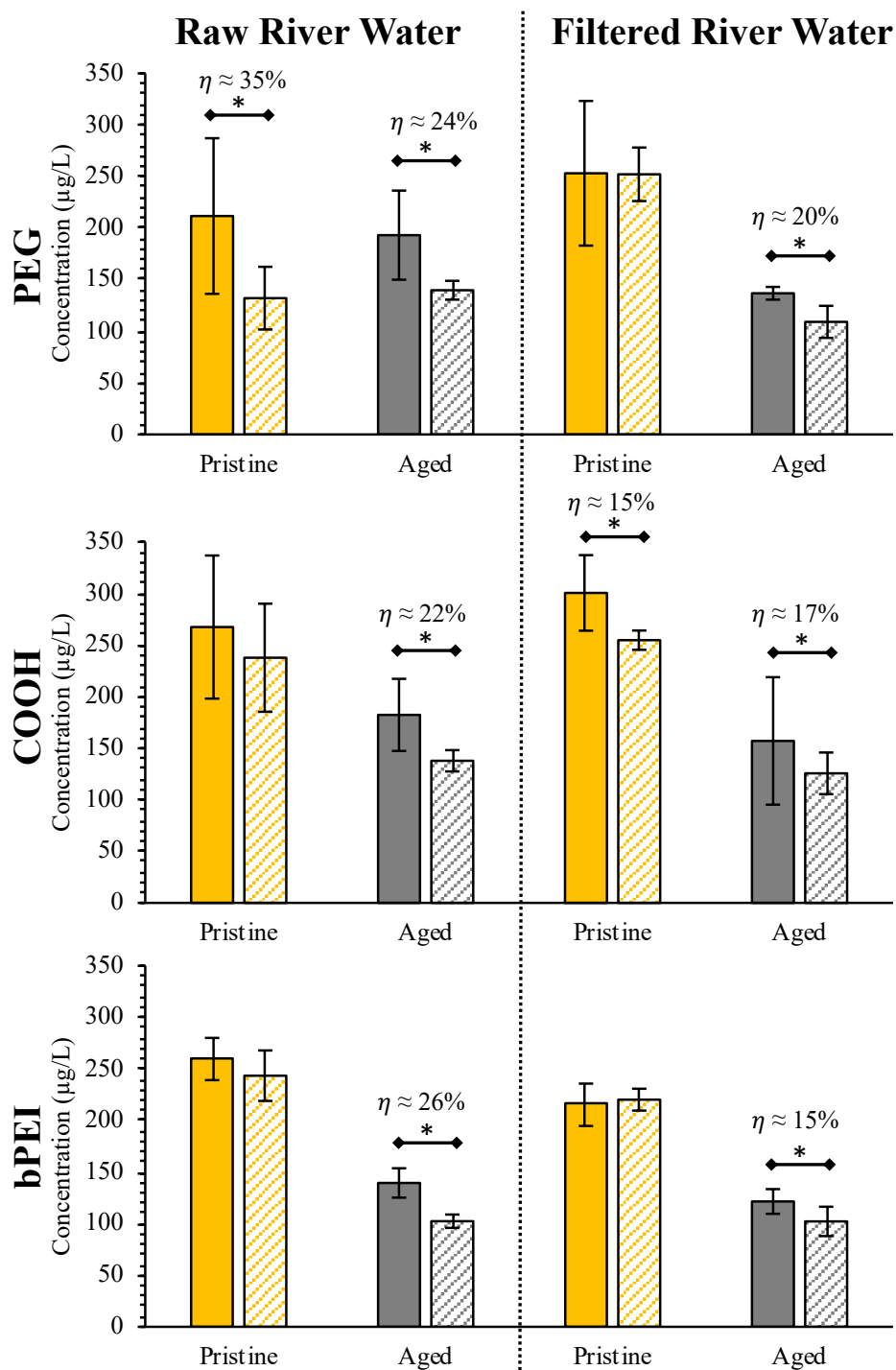


Figure 5.2. $C_{NP,initial}$ (solid) and $C_{NP,final}$ (hashed) for each AuNP type/form in raw and filtered river water. Error bars indicate \pm 95% confidence interval ($n = 4 - 6$). Asterisk indicates significant decrease in concentration (one-way paired t -test; $\alpha = 0.05$).

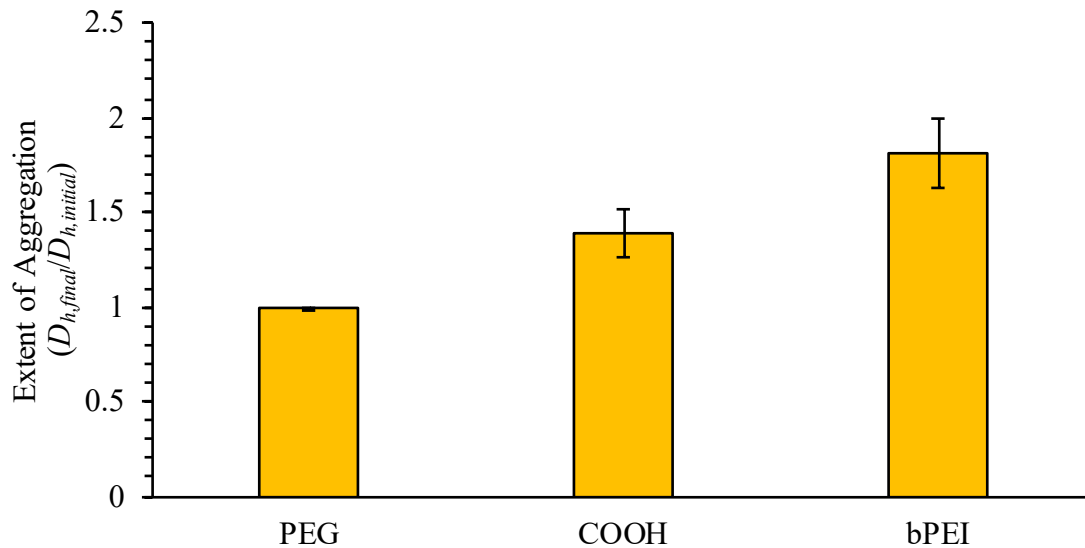


Figure 5.3. Extent of aggregation ($D_{h,final}/D_{h,initial}$) of pristine AuNPs in filtered river water. Error bars indicate \pm standard deviation ($n = 2$).

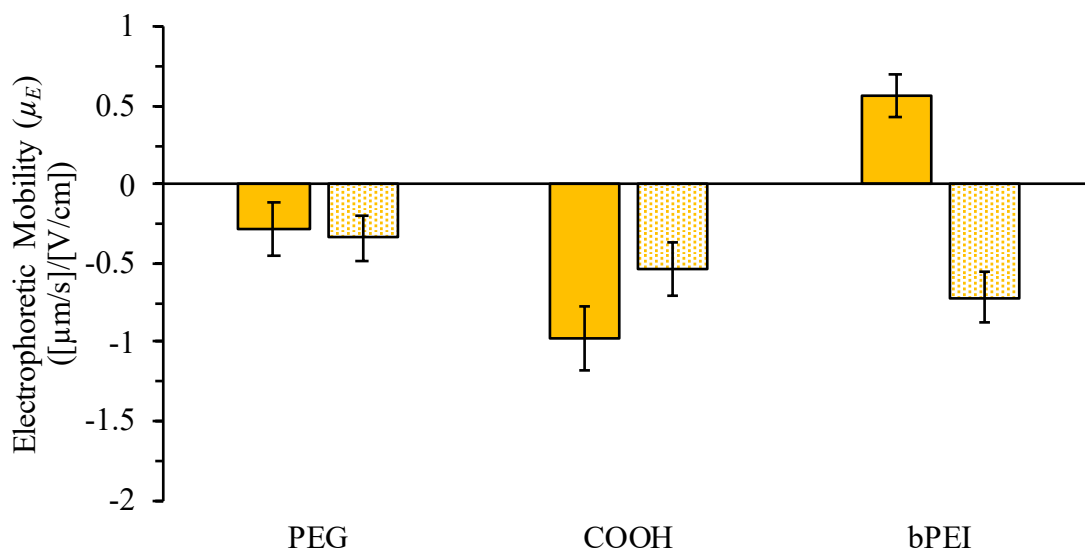


Figure 5.4. Electrophoretic mobility (μ_E) of each pristine AuNP type in pH-adjusted 1 mM KCl ($\text{pH} \approx 7.4$) (solid) and filtered river water ($\text{pH} 7.2 - 7.4$; see Table 5.2) (dotted). Error bars indicate \pm 95% confidence interval ($n = 15$).

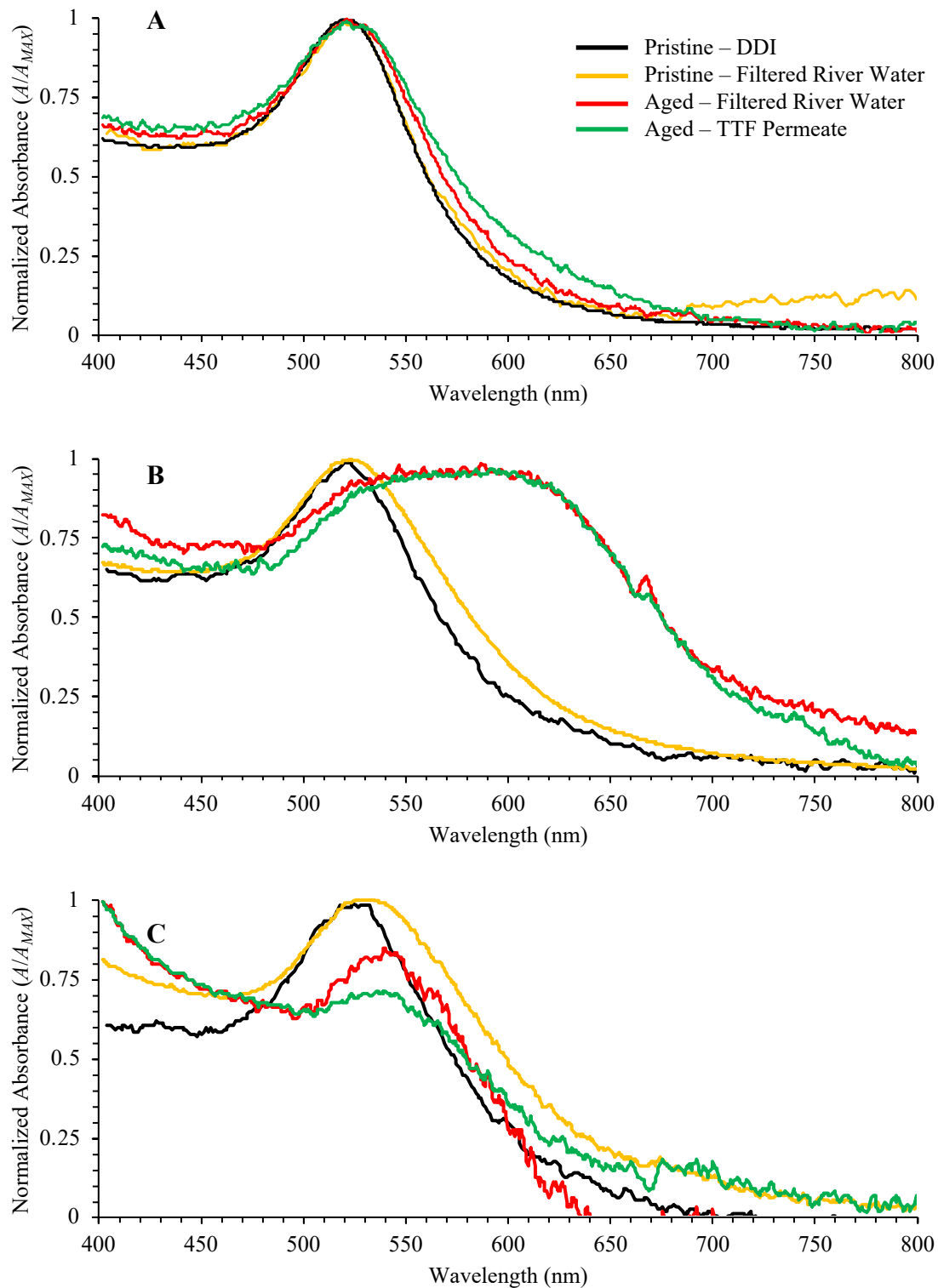


Figure 5.5. Average background-corrected and normalized (A/A_{max}) UV-Vis spectra of (a) PEG-AuNPs, (b) COOH-AuNPs, and (c) bPEI-AuNPs in various media.

charge reversal in the filtered river water (Figure 5.4), which has been observed previously and is attributed to the rapid adsorption of NOM to the cationic bPEI surface coating.^{85,113} This is supported by the UV-Vis measurements in the filtered river water (Figure 5.5), indicating a red-shift in λ_{SPR} relative to that measured in DDI and an increase in the FWHM (see Appendix D Tables D7 and D8). At the NOM-to-AuNP mass concentration ratio ([NOM]:[NP]) of the batch experiments (≈ 6.5 mg C/mg Au) and TR-DLS measurements (≈ 1.7 mg C/mg Au), this eco-corona is expected to sufficiently cover the bPEI-AuNPs and prevent their homoaggregation.^{85,113} Indeed, significant losses of the pristine bPEI-AuNPs were observed in the DDI control (Appendix D Figure D2), indicating that the absence of NOM enabled the attachment of the bPEI-AuNPs to the vessel walls. Based on the current results, it is hypothesized that the bPEI-AuNPs either underwent a brief period of homoaggregation (evidenced by $D_{h,final}/D_{h,initial}$) as NOM was adsorbing to the AuNP surface (evidenced by μ_E and UV-Vis) and/or rapidly acquired an eco-corona. In either case, once the fractional surface coverage of adsorbed NOM became sufficiently high, homoaggregation was prevented due to electrosteric interactions between NOM-coated bPEI-AuNPs. This process, occurring over less than a minute, resulted in NOM-coated bPEI-AuNPs and/or relatively small bPEI-AuNPs aggregates that were not removed during centrifugation. These findings demonstrate the importance of the [NOM]:[NP] ratio on ENM aggregation behavior and the kinetics of NOM adsorption versus aggregation.^{32,113}

Contrary to the other AuNP types, the pristine COOH-AuNPs were removed to a significant extent in the filtered river water (paired t -test(4), $p = 0.02$; Figure 5.2). The average percent removal (η) was slightly greater than that measured in the centrifuged river water and DDI controls ($\eta \approx 15\%$, 9% and 7% , respectively; Appendix D Figure D2). The TR-DLS measurements indicate a small initial increase in D_h , with $D_{h,final}/D_{h,initial} = 1.39 \pm 0.13$ (\pm standard deviation; $n = 2$; Figure 5.3), after which no change in D_h occurred (Appendix D Figure D1). One explanation for the removal of the COOH-AuNPs and their increased D_h is that the COOH-AuNPs homoaggregated in the filtered river water. However, the mechanism for this is unclear, as electrosteric interactions between the COOH-AuNPs have been previously shown to prevent their homoaggregation in simulated

freshwater and filtered river water.^{85,113} Furthermore, if the COOH-AuNPs did homoaggregate, the relatively small aggregates formed per the TR-DLS measurements would not be removed during centrifugation. As such, the cause of their removal during the batch experiments is unknown. The increase in D_h could also be due to the adsorption of NOM; however, their negative μ_E (Figure 5.4) is expected to hinder the formation of an eco-corona in the filtered river water. The UV-Vis measurements indicate no significant change in the λ_{SPR} measured in the filtered river water relative to that measured in DDI (Figure 5.5; see Appendix D Table D7) but do show an increase in the FWHM (see Appendix D Table D8). Based on these contradictory results, it is unclear whether if the COOH-AuNPs homoaggregated and/or if NOM adsorbed to the surface of the COOH-AuNPs.

5.4.2 *Pristine AuNPs in Raw River Water*

Batch experiments in the raw river water contained NCs and the accompanying possibility of heteroaggregation. As such, additional removal of the AuNPs in the raw versus filtered river water is presumably attributable to heteroaggregation. In the raw river water, the pristine PEG-AuNPs were removed to a significant extent (paired t -test(5), $p < 0.01$; Figure 5.2). The PEG-AuNPs were previously found to be resistant to homo- and heteroaggregation in raw river water.¹¹³ The current results are contradictory and suggest that the PEG-AuNPs heteroaggregated with the background NCs. As the total suspended solids (TSS) concentration in the current work (Table 5.2) is considerably higher than the previous study (104.6 ± 5.2 mg/L vs. 3.9 ± 0.4 mg/L, respectively), the increased removal is reasonable as the rate of aggregation is second-order with respect to particle number concentration. This conclusion is supported by the observed removal of the pristine PEG-AuNPs in the centrifuged river water (Appendix D Figure D2), which occurred to a lesser extent than that found in the raw river water ($\eta \approx 29\%$ vs. 35% , respectively) but higher than that observed in the DDI control ($\eta \approx 6\%$). These findings demonstrate the impact that the number concentration ratio of ENMs-to-NCs ($N_{NP}:N_{NC}$) has on the aggregation behavior of ENMs.

In contrast, the pristine COOH- and bPEI-AuNPs were not removed to a significant extent in the raw river water (COOH: paired t -test(4), $p = 0.22$; bPEI: paired t -test(6), $p = 0.17$; Figure 5.2), indicating that they did not undergo heteroaggregation. The behavior of the COOH-AuNPs in the raw river water differs from that observed with the filtered river water. Interestingly, this trend is similar to that observed in the previous study, where η of the COOH-AuNPs was higher in the filtered river water compared to the raw river water.¹¹³ This suggests that the COOH-AuNPs are more susceptible to homoaggregation as opposed to heteroaggregation. As for the bPEI-AuNPs, their behavior in the raw river water is attributed to the same mechanisms affecting their stability in the filtered river water. Namely, the rapid formation of an eco-corona that stabilizes the bPEI-AuNPs and prevents significant aggregation.

In general, the behavior of the pristine AuNPs in both the filtered and raw river water is reasonable given our previous findings.^{85,113} Removal of the PEG-AuNPs in the raw river water is attributed to the relatively high TSS concentration (Table 5.2), the behavior of the COOH-AuNPs is consistent with that observed previously, and the colloidal stability of the bPEI-AuNPs is linked to eco-corona formation and the [NOM]:[NP] ratio. The results using the filtered river water highlight the impact of eco-corona formation on ENM aggregation behavior and demonstrate the importance of the [NOM]:[NP] ratio. Likewise, the results using the raw river water highlight the impact that the $N_{NP}:N_{NC}$ ratio has on ENM aggregation behavior. More importantly, however, these results serve as a foundation for examining the aggregation behavior of the aged AuNPs in the same aquatic media.

5.4.3 Aged AuNPs in Filtered River Water

After aging in the wastewater media, all three AuNP types were removed to a significant extent in the filtered river water (PEG: paired t -test(6), $p < 0.01$; COOH: paired t -test(4), $p = 0.049$; bPEI: paired t -test(6), $p = 0.04$; Figure 5.2). By the completion of the aging procedure, the D_h of the aged AuNPs had significantly increased relative to their pristine analogs (Figure 5.6 and Appendix D Figure D3), indicating that all three AuNP types homoaggregated during the aging process. The exact mechanisms causing the AuNPs to

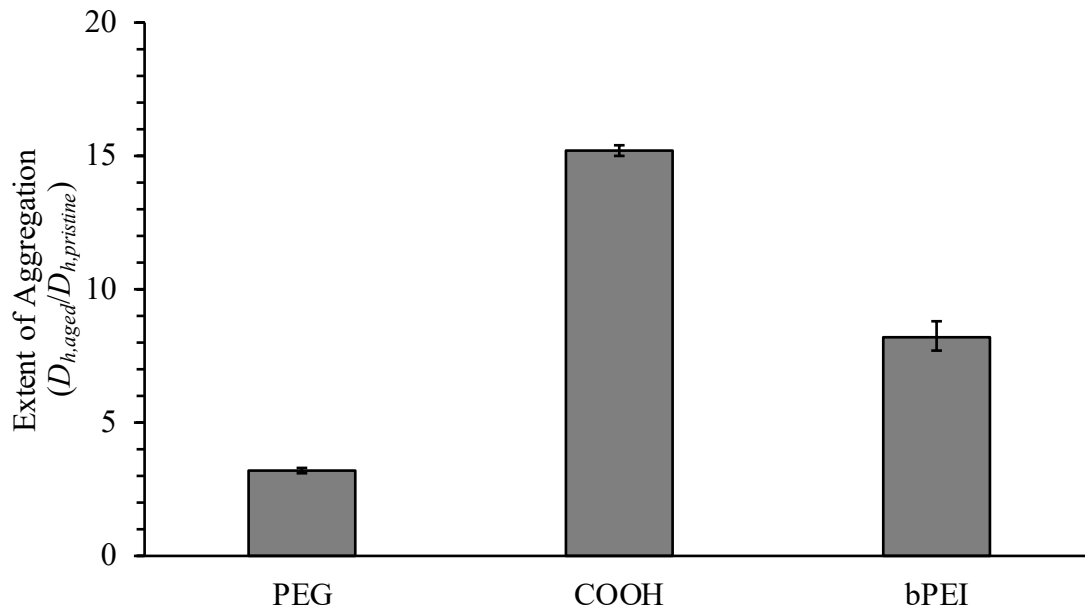


Figure 5.6. Increase in D_h of aged AuNPs relative to D_h of pristine AuNPs ($D_{h,aged}/D_{h,pristine}$) measured in DDI. Error bars indicate $\pm 95\%$ confidence interval ($n = 3$).

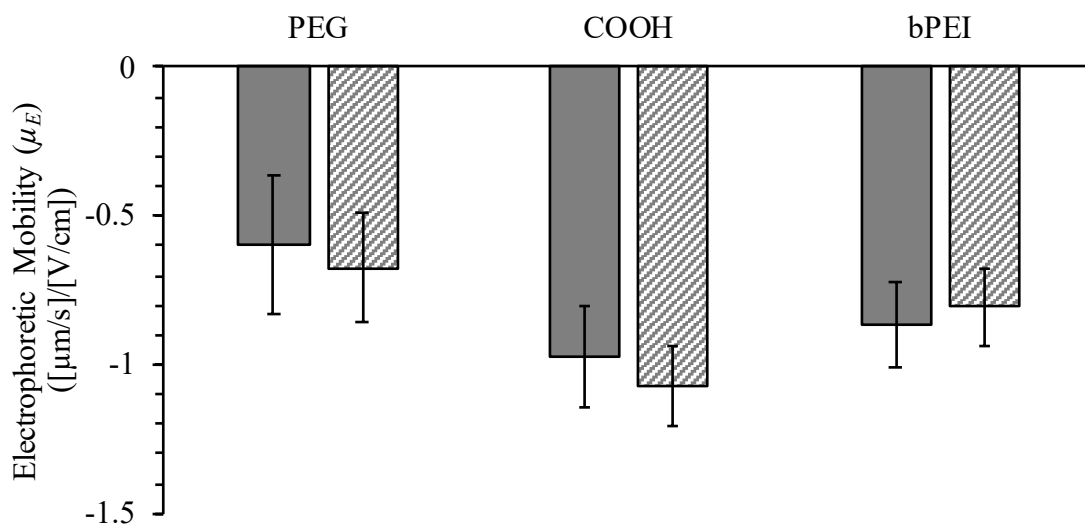


Figure 5.7. Electrophoretic mobility (μ_E) of each aged AuNP type in wastewater permeate (pH 6.9 – 7.6; see Table 5.3) (solid) and filtered river water (pH 7.2 – 7.4; see Table 5.2) (hashed). Error bars indicate $\pm 95\%$ confidence interval ($n = 15$).

homoaggregate in the wastewater media are unclear, however, previous research examining these same AuNP types in filtered primary clarifier effluent reported similar behavior.¹³² In that work, it was hypothesized that the homoaggregation of the AuNPs was linked to the formation of an organic matter corona comprised of extracellular polymeric substances (EPS) produced by the microbial community in wastewater treatment systems and the aquatic chemistry of those environments.¹³² The UV-Vis spectra and μ_E of the aged AuNPs collected in the current work further support this hypothesis (Figures 5.5 and 5.7). In both the TFF permeate and in filtered river water, the λ_{SPR} of each aged AuNP type was red-shifted relative to that measured in DDI (see Appendix D Table D7) and the FWHM of the UV-Vis spectra increased (Figure 5.5 and Appendix D Table D8). The aged COOH-AuNPs show a substantial increase in the FWHM and an accompanying broadening of the peak at λ_{SPR} . This may indicate the presence of a ‘secondary’ peak from the transverse surface plasmon resonance (TSPR) overlapping with the ‘primary’ peak from the longitudinal surface plasmon resonance (LSPR).^{118,119} The presence of the LSPR and TSPR was observed previously with the COOH-AuNPs and was attributed to very short center-to-center separation distances (d_s) between adjacent AuNPs in each aggregate assemblage such that plasmon coupling occurred.¹³² Finally, the μ_E of the aged AuNPs measured in the TFF permeate and filtered river water were comparable and consistently negative (Figure 5.7). Overall, these findings are similar to those observed previously and indicate that of each AuNP type was transformed in the filtered wastewater media.¹³²

Slight removal of the aged AuNPs was measured in the DDI controls (see Appendix D Figure D2), however, the amount was consistently less than that observed for each aged AuNP type in the filtered river water (Figure 5.2). This indicates that removal of the aged AuNPs in the filtered river water was not primarily from interactions with the vessel walls nor from the centrifugation process alone. Instead, the loss of the aged AuNPs is attributed to their continued homoaggregation upon dispersion and mixing in the filtered river water, followed by their sedimentation during the centrifugation process. Given the negative μ_E (Figure 5.7) and the organic matter corona formed on the aged AuNPs, it is unlikely that they would favorably interact with one another due to electrosteric forces. Indeed, the

relatively negligible removal observed in the DDI controls supports this (see Appendix D Figure D2). This indicates that the aquatic chemistry of the filtered river water and/or the presence of NOM caused the aged AuNPs to continue homoaggregating.

There are a number of possible mechanisms that might explain this behavior. First, the presence of divalent cations in the filtered river water (see Appendix D Table D2) would facilitate homoaggregation via divalent cation bridging (DCB). This mechanism is potentially enhanced by the presence of divalent cations already bound to the aged AuNP corona that were acquired in the wastewater matrix, where divalent cation concentrations were much higher than those measured in the filtered river water (see Appendix D Tables D2 and D3). Second, the presence of NOM in the filtered river water would also promote homoaggregation via NOM-facilitated interparticle bridging. Here, the NOM in the river water may adsorb directly to the aged AuNP corona and/or to divalent cations bound to the corona. In any case, it is not possible to distinguish between these mechanisms with the current experimental approach but it is likely that both are relevant. The absence of these constituents in the DDI controls points to their impact on the colloidal stability of the aged AuNPs.

It is worth noting that no change in D_h of the aged AuNPs was observed during the initial DLS measurements performed in filtered river water (see Appendix D Figure D3). Consequently, longer duration TR-DLS measurements were not performed concurrently with the batch experiments. The discrepancy between the results of the batch experiments and DLS measurements is likely due to the relatively short measurement period (≈ 9 minutes) and reduced particle-particle interactions occurring during the DLS measurements compared to the batch experiments. When the aged AuNPs are first dispersed in the filtered river water, their D_h is on the order of 100 – 250 nm (Figure 5.6 and Appendix D Figure D3). In this size range, particle-particle interactions between the aged AuNPs are predominantly from Brownian motion.^{96,134} In the batch experiments, however, the aged AuNPs undergo continuous mixing and thus experience additional collisions from fluid shear. As the aged AuNPs homoaggregate and their D_h increases,

shear-induced collisions would become the predominant collision mechanism.^{96,134} Over the course of the batch experiments, the higher number of particle interactions that the aged AuNPs experience relative to those in the DLS sample cuvette would result in a higher aggregation rate, and thus may account for the removal observed in the batch experiments.

5.4.4 Aged AuNPs in Raw River Water

In the raw river water, all three AuNP types were also removed to a significant extent after aging (PEG: paired *t*-test(6), $p = 0.02$; COOH: paired *t*-test(6), $p = 0.01$; bPEI: paired *t*-test(6), $p < 0.01$; Figure 5.2). Removal of each aged AuNP type was also observed in the centrifuged river water to a comparable extent (see Appendix D Figure D2). In combination, these results indicate that the aged AuNPs underwent heteroaggregation, in addition to homoaggregation, in the raw river water. The η of the aged AuNPs in the raw river water were consistently higher than those measured in filtered river water (Figure 5.2). Given the dependence of the aggregation rate on the particle number concentration, the higher η in the raw and centrifuged river water relative to that observed in the filtered river water is reasonable and demonstrates the combined effect of homo- and heteroaggregation.

The exact mechanisms causing the aged AuNPs to heteroaggregate are again unclear but likely similar to those resulting in their homoaggregation, namely DCB and NOM-facilitated interparticle bridging. Here, divalent cation bridges are hypothesized to have formed between the negatively-charged aged AuNPs and NCs, resulting in the heteroaggregation of these two particle types. As noted previously, the source of the adsorbed divalent cations could be either the raw river water or previously bound divalent cations acquired by the AuNPs while aging in the wastewater matrix. In addition, NOM bridges between the aged AuNP corona and/or adsorbed divalent cations and the background NCs may have also formed. Again, distinguishing between these two mechanisms is not possible with the current experimental approach but it is likely that both mechanisms are relevant.

In their pristine form, removal of the COOH-AuNPs was only observed in the filtered river water while removal of the PEG-AuNPs was only observed in the raw river water. No removal of the bPEI-AuNPs was observed in either the filtered or raw river water. In contrast, after aging in the wastewater media, significant removal of each aged AuNP type was observed in both the filtered and raw river water. This finding demonstrates the impact that ENM transformations during wastewater treatment have on the aggregation behavior of the model ENMs in an actual aquatic media. Specifically, the properties of the aged ENMs, in particular the organic matter corona acquired by the ENMs during exposure to the wastewater media, dictate their aggregation behavior. Finally, both the previous research and the current work indicate that the initial properties of the ENM surface coatings alter the transformations occurring during wastewater treatment. Functionally, the impact of these transformations is consistent across the AuNP types investigated (i.e., increased removal in river water). However, it is unclear whether the composition of organic matter corona acquired by the different AuNP types is similar or varies due to differences in the initial physiochemical properties of the engineered surface coatings.

5.5 Implications for ENM Environmental Fate

In-light of previous research and the results of the current work, two main conclusions can be reached. First, the properties of the pristine engineered surface coatings impact ENM aggregation behavior in an actual aquatic media. While some studies have reported that heteroaggregation and sedimentation will drive ENM environmental fate^{130,135}, both the previous study and the current work demonstrate that engineered surface coatings can, in some cases, prevent pristine ENMs from homo- and heteroaggregating. Furthermore, this study provides additional evidence that the aggregation behavior of pristine ENMs in the environment is linked to the relative concentrations of NOM, ENMs and background NCs (i.e., $[NOM]:N_{NP}:N_{NC}$).

Second, ENM transformations prior to their release to the environment and the properties that result will dictate ENM aggregation behavior. With regards to engineered surface coatings, their influence on ENM fate in natural aquatic media is negligible after the

properties of the ENM have been altered. Instead, the organic matter corona acquired by the ENMs in wastewater treatment systems will dictate ENM interactions in natural aquatic environments. It remains to be determined whether the aged ENMs will undergo additional transformations once released to the environment, such as replacement or overcoating of the wastewater-derived corona layer by NOM in the receiving water.

Finally, numerous studies have noted that within WWTPs, ENMs are likely to heteroaggregate with suspended particulate matter (SPM) and/or undergo various chemical transformations, such as sulfidation or dissolution.^{44,45,47,49,50,108–110} Thus, while the complete removal of all ENMs entering WWTPs is unlikely, the small fraction that is released to the environment will certainly not resemble, nor behave, as pristine ENMs. With the intent of refining ENM environmental fate models, it is recommended that future research focus on further elucidating the behavior of aged ENMs in actual aquatic media. Ultimately, this line of inquiry should work towards establishing the factors that dictate the outcome of medium-dependent processes, such as aggregation, and how those factors are incorporated in ENM environmental fate models.

5.6 Acknowledgements

This research was supported by the National Science Foundation (NSF) Graduate Research Fellowship Program under Grant No. DGE-1314109 and NSF Grant No. 1255020. Any opinions, findings, and conclusions or recommendations expressed in this material are those of the author(s) and do not necessarily reflect the views of the NSF. Special thanks to A. Franco (Portland State University) for assistance with the ICP-MS measurements; K. Motter (IWW Collaboratory) for assistance with TOC/DOC measurements; and I. Ramirez-Aguilar for assistance with the DLS, PALS, and UV-Vis measurements.

5.7 Supplementary Information

The Supplementary Information for this manuscript is located in Appendix D.

6. CONCLUSIONS

6.1 Summary

The dominant processes impacting ENM fate need to be identified and examined such that they can be appropriately reflected in ENM environmental fate models. Focusing on surface water environments, aggregation is recognized as an important process influencing ENM environmental fate. Through the application of well-controlled model systems, a number of factors have been shown to impact this process. A significant advantage of using synthetic aquatic media and simplified experimental systems is the ability to isolate specific components affecting ENM aggregation behavior. In addition, examinations utilizing model systems lend themselves to the development of mechanistic models that are readily incorporated into ENM environmental fate models.

While recognizing the advantages to such an approach, a major drawback of only examining ENM aggregation behavior in well-controlled model systems is that the factors and mechanisms identified in such systems may not accurately reflect ENM behavior in actual environmental systems. Model aquatic systems inherently lack the complexity of actual aquatic media wherein dynamic and interrelated processes can occur simultaneously. Furthermore, investigations in these systems are typically performed using ‘pristine’ ENMs, which do not reflect the physiochemical properties that ‘aged’ ENMs possess following myriad transformation processes. For these reasons, it is critical that highly-realistic systems are also utilized to identify the factors influencing ENM aggregation behavior in the environment and aid the refinement of ENM environmental fate models.

The motivation behind the current research was to work across these two experimental spaces, focusing on whether engineered surface coatings are an important factor affecting the fate of ENMs in surface water environments. A series of experimental phases were conducted that spanned simulated-to-actual aquatic media and incorporated the use of ‘pristine’ and ‘aged’ ENMs. First, the aggregation behavior of a suite of model ENMs possessing different surface coating functionalities was examined in simulated freshwater media of varying aquatic chemistry. Then, the aggregation behavior of those same model

ENMs was assessed in samples from a freshwater river. Behavior in this “real” system was compared to the results from the work in the simulated system to identify the mechanisms affecting ENM colloidal stability in the more complex media. The research then transitioned to examining the environmental fate of ENMs ‘aged’ during wastewater treatment. Here, the focus shifted to examining a more environmentally-relevant form of ENMs being released to the environment. Transformations of the model ENMs during exposure to wastewater media were first investigated and a method was developed to simulate the aging of ENMs during wastewater treatment. Then, the aggregation behavior of ‘pristine’ and ‘aged’ ENMs were assessed in samples from a freshwater river. This final phase was used to identify whether engineered surface coatings are a relevant factor influencing the environmental fate of ENMs after considering the transformations ENMs undergo during their life-cycle.

An important aspect underlying the experimental framework detailed above is that it incorporates experimental systems of differing complexity to examine the hypotheses motivating this research, referred to herein as “bottom-up” and “top-down” approaches (Figure 6.1). In the “bottom-up” approach, progressively more complex experimental designs were employed to transition from mechanistic studies using well-controlled conditions to more realistic investigations using actual environmental conditions. In the “top-down” approach, the reverse was applied, breaking down and explaining the observations made using actual environmental systems with less-complex, mechanistically-driven investigations. By combining both approaches, where the results of one research phase were used to inform the other phases, important mechanistic insights were gained as well as the identification of specific factors influencing the environmental fate of ENMs.

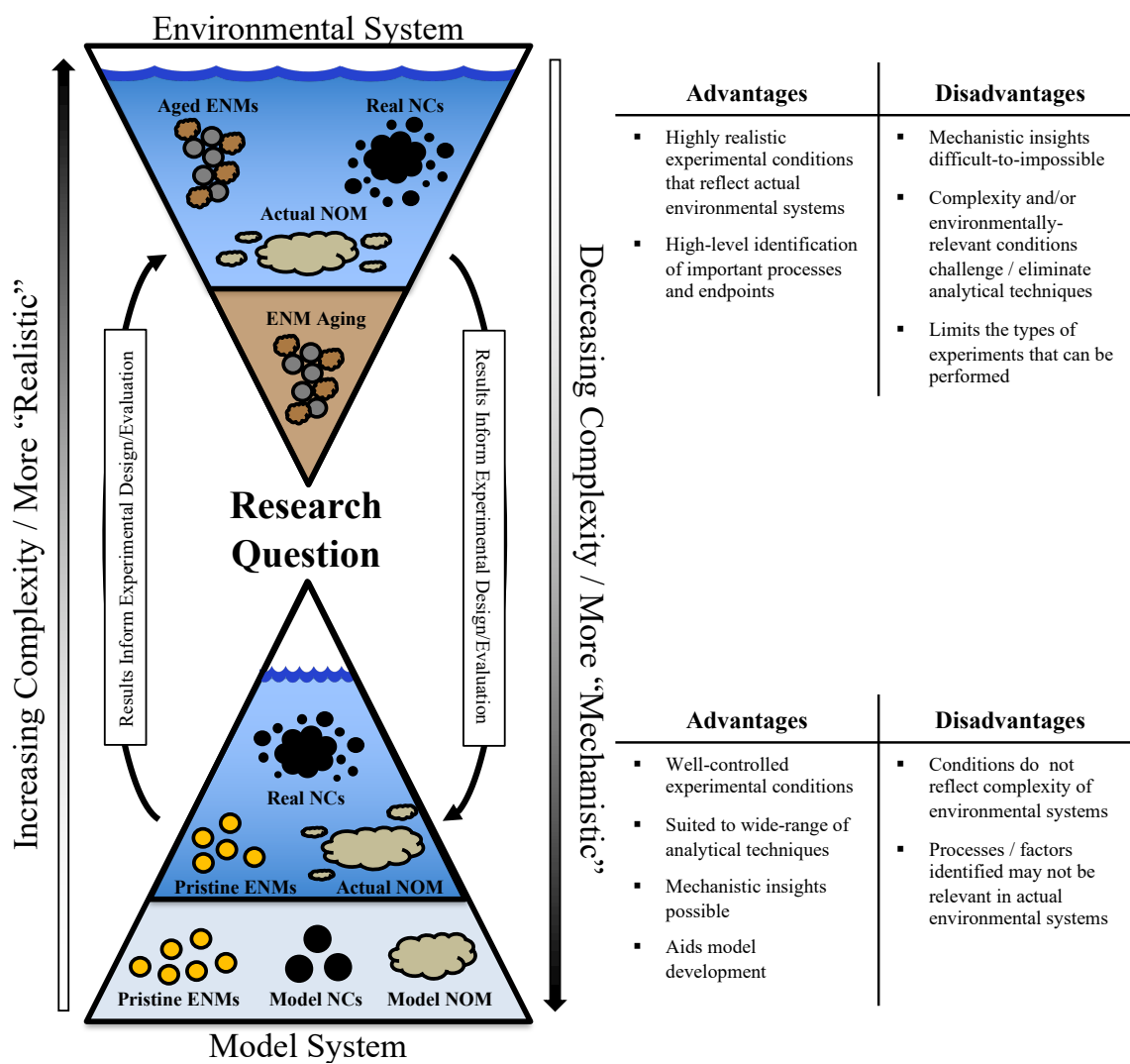


Figure 6.1. Illustrative example comparing advantages and disadvantages of working in model and actual environmental systems.

6.2 Conclusions

From this body of work, the following conclusions can be drawn:

1. In their pristine form, the PEG and PEG-COOH engineered surface coatings prevented ENM aggregation in simulated and actual aquatic media via steric (PEG) or electrosteric (PEG-COOH) stabilization.

2. In their pristine form and in the absence of natural organic matter (NOM), the bPEI and PEG-Amine engineered surface coatings prevented ENM aggregation in simulated and actual aquatic media via electrosteric stabilization.
3. In their pristine form and in the presence of NOM, the bPEI and PEG-Amine engineered surface coatings enabled ENM aggregation via NOM-facilitated interparticle bridging; however, this process was dependent on the relative concentration ratio of NOM-to-ENMs (expressed as $[\text{NOM}]:N_{NP}$).
4. The relative concentrations of NOM, ENMs, and background natural colloids (NCs), expressed as $[\text{NOM}]:N_{NP}:N_{NC}$, dictates the aggregation behavior of pristine ENMs with bPEI and PEG-Amine engineered surface coatings and determines the dominant mode of aggregation (i.e., homo- vs. heteroaggregation).
5. In the absence of background suspended particulate matter (SPM), the PEG, COOH, and bPEI engineered surface coatings altered ENM aggregation and corona formation during exposure to media representative of conventional wastewater treatment processes.
6. Engineered nanomaterials discharged to surface waters via WWTP effluent will not retain their initial, pristine properties nor resemble their “engineered” analogs due to the rapid formation of an organic matter corona on the ENMs that enables their aggregation.
7. After exposure to wastewater media and the transformations that occur therein, the effect of engineered surface coatings on the aggregation behavior of aged ENMs in a natural aquatic media is masked. Instead, the properties of the aged ENMs and their ‘acquired’ organic matter corona will dictate ENM aggregation behavior in the environment.

In synthesizing the above conclusions, there are two overarching findings stemming from this work. The first is the fundamental relationship expressed by $[\text{NOM}]:N_{NP}:N_{NC}$. Here, variations among these three factors were consistently found to dictate both the aggregation behavior of the model ENMs and the dominant mode of aggregation (i.e., homo- vs. heteroaggregation). The other is the fundamental role that adsorbed organic matter plays

in mediating the aggregation behavior and environmental fate of ENMs, including both ‘eco-coronas’ formed in natural systems and the corona acquired in engineered systems. In both instances, the concentration and composition of the organic matter as well as the initial physiochemical properties of the ENM’s surface coating will dictate corona formation. When interactions between ENMs and organic matter are unfavorable, a corona layer is unlikely to form and the impact on ENM environmental fate is negligible. However, when the interactions are favorable, the impact of the corona layer on ENM environmental fate will vary in relation to the corona layer surface coverage and its resulting impact on ENM aggregation behavior.

6.3 Significance

Based on the conclusions stated above, the overarching objective of this research was met: engineered surface coatings influence the aggregation behavior, and thus environmental fate, of ENMs in their pristine form; however, following the transformations that occur to ENMs during wastewater treatment, the impact of the engineered surface coatings is minimized. Instead, the properties of the aged ENMs, particularly the organic matter corona acquired during wastewater treatment, will dictate ENM aggregation in the environment. To further the refinement of ENM environmental fate models, emphasis should be placed on elucidating the behavior of aged ENMs under environmentally-relevant conditions. Simultaneously, the importance given to the engineered surface coating during experimental design should be shifted towards understanding how the surface coatings drive and shape corona formation on ENMs.

6.4 Recommendations for Future Work

While this study advances our knowledge of the dominant factors influencing ENM environmental fate, there are a number of questions that remain. For one, little is known regarding the composition of the organic matter corona acquired by ENMs during wastewater treatment. Recent research by Armanious et al. (2014, 2016)^{136,137} utilizing quartz crystal microbalance with dissipation monitoring (QCM-D) has shown the utility of this tool to explore NOM adsorption to model ENM surfaces. This technique could be

adapted to examine both the kinetics and composition of organic matter adsorbed to ENMs during wastewater treatment. While the current research indicates that the initial corona acquired by ENMs en-route to a WWTP would likely persist during sequential wastewater treatment stages, this hypothesis should be confirmed. Moreover, it is unknown how the corona acquired during wastewater treatment evolves after the ENMs are introduced to a freshwater environment containing NOM of different character and concentration. This latter phenomena has broad implications when trying to identify the dominant processes altering ENM environmental fate. The techniques applied in the current research should be expanded to explore the aggregation behavior of aged ENMs in samples from a variety of freshwater rivers. While the behavior of the aged ENMs was explored under varying aquatic chemistry in the current study, river water samples were only collected from a single source. Extending this research to other freshwater rivers may help elucidate the importance of NOM composition on the behavior of the aged ENMs. Finally, all of these aspects could be supported by a number of mechanistically-driven studies. In particular, the nuanced relationship between the relative concentration ratios of NOM, ENMs, and NCs ($[NOM]:N_{NP}:N_{NC}$) on ENM aggregation behavior should be explored. The current work can serve as a guide to identify existing knowledge gaps and prioritize the relevant aspects to examine.

During this research, there were several lessons-learned that should be considered during future experimental designs. In particular, an early goal of this research was to aid the refinement of ENM environmental fate models by quantifying homo- and heteroaggregation attachment efficiency factors (α_{homo} and α_{hetero} , respectively) under environmentally-relevant and highly realistic conditions. This was not accomplished for several reasons but most significantly due to the challenges of working in complex, environmental systems. Research focused on quantifying α_{homo} and α_{hetero} using simulated freshwater media of varying complexity would likely yield important insights and provide a much stronger foundation to further examine ENM aggregation in more complex systems. Ultimately, while there is benefit in working in both well-controlled, simplistic systems and poorly-controlled, complex systems, emphasis should be placed on one or the

other depending on the underlying research objective. Ideally, a balance can be reached that provides detailed, mechanistic insights into processes that remain relevant in actual environmental systems. It is envisioned that with carefully constructed experimental designs, the two approaches could be run in parallel to provide deeper insights into important and environmentally-relevant phenomena.

7. REFERENCES

- 1 A. A. Keller, S. McFerran, A. Lazareva and S. Suh, Global life cycle releases of engineered nanomaterials, *J. Nanoparticle Res.*, 2013, **15**, 1692.
- 2 A. A. Keller, W. Vosti, H. Wang and A. Lazareva, Release of engineered nanomaterials from personal care products throughout their life cycle, *J. Nanoparticle Res.*, 2014, **16**, 2489.
- 3 T. Y. Sun, N. A. Bornhöft, K. Hungerbühler and B. Nowack, Dynamic Probabilistic Modeling of Environmental Emissions of Engineered Nanomaterials, *Environ. Sci. Technol.*, 2016, **50**, 4701–4711.
- 4 B. Nowack and T. D. Bucheli, Occurrence, behavior and effects of nanoparticles in the environment, *Environ. Pollut.*, 2007, **150**, 5–22.
- 5 F. Gottschalk, T. Y. Sun and B. Nowack, Environmental concentrations of engineered nanomaterials: Review of modeling and analytical studies, *Environ. Pollut.*, 2013, **181**, 287–300.
- 6 F. Gottschalk, T. Sonderer, R. W. Scholz and B. Nowack, Modeled Environmental Concentrations of Engineered Nanomaterials (TiO₂, ZnO, Ag, CNT, Fullerenes) for Different Regions, *Environ. Sci. Technol.*, 2009, **43**, 9216–9222.
- 7 S. J. Klaine, P. J. J. Alvarez, G. E. Batley, T. F. Fernandes, R. D. Handy, D. Y. Lyon, S. Mahendra, M. J. McLaughlin and J. R. Lead, Nanomaterials in the Environment: Behavior, Fate, Bioavailability, and Effects, *Environ. Toxicol. Chem.*, 2008, **27**, 1825.
- 8 N. Mahaye, M. Thwala, D. A. Cowan and N. Musee, Genotoxicity of metal based engineered nanoparticles in aquatic organisms: A review, *Mutat. Res. Mutat. Res.*, 2017, **773**, 134–160.
- 9 S. Wagner, A. Gondikas, E. Neubauer, T. Hofmann and F. von der Kammer, Spot the Difference: Engineered and Natural Nanoparticles in the Environment-Release, Behavior, and Fate, *Angew. Chemie Int. Ed.*, 2014, **53**, 12399–12419.
- 10 H. H. Liu and Y. Cohen, Multimedia environmental distribution of engineered nanomaterials, *Environ. Sci. Technol.*, 2014, **48**, 3281–3292.
- 11 J. Meesters, A. A. Koelmans, J. T. K. Quik, A. J. Hendriks and D. Van De Meent, Multimedia modeling of engineered nanoparticles with simpleBox4nano: Model definition and evaluation, *Environ. Sci. Technol.*, 2014, **48**, 5726–5736.
- 12 K. L. Garner, S. Suh and A. A. Keller, Assessing the Risk of Engineered Nanomaterials in the Environment: Development and Application of the nanoFate Model, *Environ. Sci. Technol.*, 2017, **51**, 5541–5551.

- 13 M. Baalousha, G. Cornelis, T. A. J. Kuhlbusch, I. Lynch, C. Nickel, W. J. G. M. Peijnenburg and N. W. van den Brink, Modeling nanomaterial fate and uptake in the environment: current knowledge and future trends, *Environ. Sci. Nano*, 2016, **3**, 323–345.
- 14 A. Praetorius, J. Labille, M. Scheringer, A. Thill, K. Hungerbühler and J. Bottero, Heteroaggregation of Titanium Dioxide Nanoparticles with Model Natural Colloids under Environmentally Relevant Conditions, *Environ. Sci. Technol.*, 2014, **48**, 10690–10698.
- 15 L. E. Barton, M. Therezien, M. Auffan, J.-Y. Bottero and M. R. Wiesner, Theory and Methodology for Determining Nanoparticle Affinity for Heteroaggregation in Environmental Matrices Using Batch Measurements, *Environ. Eng. Sci.*, 2014, **31**, 421–427.
- 16 N. K. Geitner, N. J. O'Brien, A. A. Turner, E. J. Cummins and M. R. Wiesner, Measuring Nanoparticle Attachment Efficiency in Complex Systems, *Environ. Sci. Technol.*, 2017, **51**, 13288–13294.
- 17 G. V. Lowry, B. P. Espinasse, A. R. Badireddy, C. J. Richardson, B. C. Reinsch, L. D. Bryant, A. J. Bone, A. Deonarine, S. Chae, M. Therezien, B. P. Colman, H. Hsu-Kim, E. S. Bernhardt, C. W. Matson and M. R. Wiesner, Long-Term Transformation and Fate of Manufactured Ag Nanoparticles in a Simulated Large Scale Freshwater Emergent Wetland, *Environ. Sci. Technol.*, 2012, **46**, 7027–7036.
- 18 A. L. Dale, G. V. Lowry and E. A. Casman, Modeling Nanosilver Transformations in Freshwater Sediments, *Environ. Sci. Technol.*, 2013, **47**, 12920–12928.
- 19 X. Feng, Y. Yan, B. Wan, W. Li, D. P. Jaisi, L. Zheng, J. Zhang and F. Liu, Enhanced Dissolution and Transformation of ZnO Nanoparticles: The Role of Inositol Hexakisphosphate, *Environ. Sci. Technol.*, 2016, **50**, 5651–5660.
- 20 S. M. Louie, R. D. Tilton and G. V. Lowry, Critical review: impacts of macromolecular coatings on critical physicochemical processes controlling environmental fate of nanomaterials, *Environ. Sci. Nano*, 2016, **3**, 283–310.
- 21 S. M. Louie, R. D. Tilton and G. V. Lowry, Effects of molecular weight distribution and chemical properties of natural organic matter on gold nanoparticle aggregation., *Environ. Sci. Technol.*, 2013, **47**, 4245–54.
- 22 S. Jayalath, S. C. Larsen and V. H. Grassian, Surface adsorption of Nordic aquatic fulvic acid on amine-functionalized and non-functionalized mesoporous silica nanoparticles, *Environ. Sci. Nano*, 2018, **5**, 2162–2171.
- 23 W. J. G. M. Peijnenburg, M. Baalousha, J. Chen, Q. Chaudry, F. Von der kammer, T. A. J. Kuhlbusch, J. R. Lead, C. Nickel, J. T. K. Quik, M. Renker, Z. Wang and A. a. Koelmans, A Review of the Properties and Processes Determining the Fate of Engineered Nanomaterials in the Aquatic Environment, *Crit. Rev. Environ. Sci.*

- Technol.*, 2015, **45**, 2084–2134.
- 24 M. Baalousha, F. Von der Kammer, M. Motelica-Heino, M. Baborowski, C. Hofmeister and P. Le Coustumer, Size-Based Speciation of Natural Colloidal Particles by Flow Field Flow Fractionation, Inductively Coupled Plasma-Mass Spectroscopy, and Transmission Electron Microscopy/X-ray Energy Dispersive Spectroscopy: Colloids–Trace Element Interaction, *Environ. Sci. Technol.*, 2006, **40**, 2156–2162.
 - 25 J. T. K. Quik, M. C. Stuart, M. Wouterse, W. J. G. M. Peijnenburg, A. J. Hendriks and D. van de Meent, Natural colloids are the dominant factor in the sedimentation of nanoparticles, *Environ. Toxicol. Chem.*, 2012, **31**, 1019–1022.
 - 26 A. L. Dale, G. V. Lowry and E. A. Casman, Stream Dynamics and Chemical Transformations Control the Environmental Fate of Silver and Zinc Oxide Nanoparticles in a Watershed-Scale Model, *Environ. Sci. Technol.*, 2015, **49**, 7285–7293.
 - 27 A. L. Dale, E. A. Casman, G. V. Lowry, J. R. Lead, E. Viparelli and M. Baalousha, Modeling Nanomaterial Environmental Fate in Aquatic Systems, *Environ. Sci. Technol.*, 2015, **49**, 2587–2593.
 - 28 A. Praetorius, N. Tufenkji, K.-U. Goss, M. Scheringer, F. von der Kammer and M. Elimelech, The road to nowhere: equilibrium partition coefficients for nanoparticles, *Environ. Sci. Nano*, 2014, **1**, 317.
 - 29 G. Raza, M. Amjad, I. Kaur, M. Baalousha, J. R. Lead and D. Wen, Stability and Aggregation Kinetics of Titania Nanomaterials under Environmentally Realistic Conditions, *Environ. Sci. Technol.*, 2016, **50**, 12525–12525.
 - 30 J. A. Gallego-Urrea, J. Hammes, G. Cornelis and M. Hassellöv, Coagulation and sedimentation of gold nanoparticles and illite in model natural waters: Influence of initial particle concentration, *NanoImpact*, 2016, **3–4**, 67–74.
 - 31 B. M. Smith, D. J. Pike, M. O. Kelly and J. A. Nason, Quantification of Heteroaggregation between Citrate-Stabilized Gold Nanoparticles and Hematite Colloids, *Environ. Sci. Technol.*, 2015, **49**, 12789–12797.
 - 32 J. A. Nason, S. A. McDowell and T. W. Callahan, Effects of natural organic matter type and concentration on the aggregation of citrate-stabilized gold nanoparticles, *J. Environ. Monit.*, 2012, **14**, 1885.
 - 33 C. Sun, J. S. H. Lee and M. Zhang, Magnetic nanoparticles in MR imaging and drug delivery, *Adv. Drug Deliv. Rev.*, 2008, **60**, 1252–1265.
 - 34 C. Fang, N. Bhattarai, C. Sun and M. Zhang, Functionalized Nanoparticles with Long-Term Stability in Biological Media, *Small*, 2009, **5**, 1637–1641.

- 35 T. Phenrat, N. B. Saleh, K. Sirk, H. J. Kim, R. D. Tilton and G. V. Lowry, Stabilization of aqueous nanoscale zerovalent iron dispersions by anionic polyelectrolytes: Adsorbed anionic polyelectrolyte layer properties and their effect on aggregation and sedimentation, *J. Nanoparticle Res.*, 2008, **10**, 795–814.
- 36 A. M. El Badawy, K. G. Scheckel, M. Suidan and T. Tolaymat, The impact of stabilization mechanism on the aggregation kinetics of silver nanoparticles, *Sci. Total Environ.*, 2012, **429**, 325–331.
- 37 A. R. Petosa, D. P. Jaisi, I. R. Quevedo, M. Elimelech and N. Tufenkji, Aggregation and deposition of engineered nanomaterials in aquatic environments: Role of physicochemical interactions, *Environ. Sci. Technol.*, 2010, **44**, 6532–6549.
- 38 M. Baalousha, Effect of nanomaterial and media physicochemical properties on nanomaterial aggregation kinetics, *NanoImpact*, 2017, **6**, 55–68.
- 39 U. Weilenmann, C. R. O'Melia and W. Stumm, Particle transport in lakes: Models and measurements, *Limnol. Oceanogr.*, 1989, **34**, 1–18.
- 40 J. Buffle and G. G. Leppard, Characterization of Aquatic Colloids and Macromolecules. 1. Structure and Behavior of Colloidal Material, *Environ. Sci. Technol.*, 1995, **29**, 2169–2175.
- 41 J. Buffle, K. J. Wilkinson, S. Stoll, M. Filella and J. Zhang, A Generalized Description of Aquatic Colloidal Interactions: The Three-colloidal Component Approach, *Environ. Sci. Technol.*, 1998, **32**, 2887–2899.
- 42 G. V. Lowry, K. B. Gregory, S. C. Apte and J. R. Lead, Transformations of Nanomaterials in the Environment, *Environ. Sci. Technol.*, 2012, **46**, 6893–6899.
- 43 E. M. Hotze, T. Phenrat and G. V. Lowry, Nanoparticle Aggregation: Challenges to Understanding Transport and Reactivity in the Environment, *J. Environ. Qual.*, 2010, **39**, 1909.
- 44 R. Kägi, A. Voegelin, B. Sinnet, S. Zuleeg, H. Hagendorfer, M. Burkhardt and H. Siegrist, Behavior of Metallic Silver Nanoparticles in a Pilot Wastewater Treatment Plant, *Environ. Sci. Technol.*, 2011, **45**, 3902–3908.
- 45 R. Kägi, A. Voegelin, C. Ort, B. Sinnet, B. Thalmann, J. Krismer, H. Hagendorfer, M. Elumelu and E. Mueller, Fate and transformation of silver nanoparticles in urban wastewater systems, *Water Res.*, 2013, **47**, 3866–3877.
- 46 R. Kägi, A. Voegelin, B. Sinnet, S. Zuleeg, H. Siegrist and M. Burkhardt, Transformation of AgCl nanoparticles in a sewer system - A field study, *Sci. Total Environ.*, 2015, **535**, 20–27.
- 47 B. Kim, C.-S. Park, M. Murayama and M. F. Hochella, Discovery and Characterization of Silver Sulfide Nanoparticles in Final Sewage Sludge Products,

- Environ. Sci. Technol.*, 2010, **44**, 7509–7514.
- 48 L. Li, M. Stoiber, A. Wimmer, Z. Xu, C. Lindenblatt, B. Helmreich and M. Schuster, To What Extent Can Full-Scale Wastewater Treatment Plant Effluent Influence the Occurrence of Silver-Based Nanoparticles in Surface Waters?, *Environ. Sci. Technol.*, 2016, **50**, 6327–6333.
- 49 M. A. Kiser, P. Westerhoff, T. Benn, Y. Wang, J. Pérez-Rivera and K. Hristovski, Titanium nanomaterial removal and release from wastewater treatment plants, *Environ. Sci. Technol.*, 2009, **43**, 6757–6763.
- 50 P. Westerhoff, G. Song, K. Hristovski and M. A. Kiser, Occurrence and removal of titanium at full scale wastewater treatment plants: Implications for TiO₂ nanomaterials, *J. Environ. Monit.*, 2011, **13**, 1195–1203.
- 51 P. Christian, F. von der Kammer, M. Baalousha and T. Hofmann, Nanoparticles: structure, properties, preparation and behaviour in environmental media, *Ecotoxicology*, 2008, **17**, 326–343.
- 52 L. M. Mosley, K. A. Hunter and W. A. Ducker, Forces between Colloid Particles in Natural Waters, *Environ. Sci. Technol.*, 2003, **37**, 3303–3308.
- 53 J. R. Lead and K. J. Wilkinson, Aquatic Colloids and Nanoparticles: Current Knowledge and Future Trends, *Environ. Chem.*, 2006, **3**, 159.
- 54 K. L. Chen, S. E. Mylon and M. Elimelech, Enhanced aggregation of alginate-coated iron oxide (Hematite) nanoparticles in the presence of calcium, strontium, and barium cations, *Langmuir*, 2007, **23**, 5920–5928.
- 55 M. Therezien, A. Thill and M. R. Wiesner, Importance of heterogeneous aggregation for NP fate in natural and engineered systems, *Sci. Total Environ.*, 2014, **485–486**, 309–318.
- 56 A. Praetorius, M. Scheringer and K. Hungerbühler, Development of Environmental Fate Models for Engineered Nanoparticles - A Case Study of TiO₂ Nanoparticles in the Rhine River, *Environ. Sci. Technol.*, 2012, **46**, 6705–6713.
- 57 J. Gao, S. Youn, A. Hovsepian, V. L. Llaneza, Y. Wang, G. Bitton and J. C. J. Bonzongo, Dispersion and toxicity of selected manufactured nanomaterials in Natural River water samples: Effects of water chemical composition, *Environ. Sci. Technol.*, 2009, **43**, 3322–3328.
- 58 K. Luyts, D. Napierska, B. Nemery and P. H. M. Hoet, How physico-chemical characteristics of nanoparticles cause their toxicity: complex and unresolved interrelations, *Environ. Sci. Process. Impacts*, 2013, **15**, 23–38.
- 59 Z. Wang, L. Zhang, J. Zhao and B. Xing, Environmental processes and toxicity of metallic nanoparticles in aquatic systems as affected by natural organic matter,

- Environ. Sci. Nano*, 2016, **3**, 240–255.
- 60 D. P. Stankus, S. E. Lohse, J. E. Hutchison and J. A. Nason, Interactions between Natural Organic Matter and Gold Nanoparticles Stabilized with Different Organic Capping Agents, *Environ. Sci. Technol.*, 2011, **45**, 3238–3244.
- 61 L. Li, Y. Wang, Q. Liu and G. Jiang, Rethinking Stability of Silver Sulfide Nanoparticles (Ag₂S-NPs) in the Aquatic Environment: Photoinduced Transformation of Ag₂S-NPs in the Presence of Fe(III), *Environ. Sci. Technol.*, 2016, **50**, 188–196.
- 62 N. Sani-Kast, M. Scheringer, D. Slomberg, J. Labille, A. Praetorius, P. Ollivier and K. Hungerbühler, Addressing the complexity of water chemistry in environmental fate modeling for engineered nanoparticles., *Sci. Total Environ.*, 2015, **535**, 150–159.
- 63 T. Abe, S. Kobayashi and M. Kobayashi, Aggregation of colloidal silica particles in the presence of fulvic acid, humic acid, or alginate: Effects of ionic composition, *Colloids Surfaces A Physicochem. Eng. Asp.*, 2011, **379**, 21–26.
- 64 K. L. Chen and M. Elimelech, Influence of humic acid on the aggregation kinetics of fullerene (C60) nanoparticles in monovalent and divalent electrolyte solutions, *J. Colloid Interface Sci.*, 2007, **309**, 126–134.
- 65 K. L. Chen and M. Elimelech, Aggregation and Deposition Kinetics of Fullerene (C60) Nanoparticles, *Langmuir*, 2006, **22**, 10994–11001.
- 66 S. E. Mylon, K. L. Chen and M. Elimelech, Influence of natural organic matter and ionic composition on the kinetics and structure of hematite colloid aggregation: Implications to iron depletion in estuaries, *Langmuir*, 2004, **20**, 9000–9006.
- 67 W. Stumm and J. J. Morgan, *Aquatic Chemistry: Chemical Equilibria and Rates in Natural Waters*, John Wiley & Sons, Inc., 3rd edn., 1995.
- 68 E. M. Thurman, in *Organic Geochemistry of Natural Waters*, Springer Netherlands, Dordrecht, 1985, pp. 7–65.
- 69 International Humic Substances Society (IHSS) - Source Materials for IHSS Samples, <http://www.humicsubstances.org/sources.html>, (accessed 10 August 2016).
- 70 H. K. Hall, Sterically Hindered Phenolic Buffers. Application to Determination of Rates of Amidation of Ethyl Chloroformate 1, *J. Am. Chem. Soc.*, 1957, **79**, 5439–5441.
- 71 F. Benyettou, J. Hardouin, M. Lecouvey, H. Jouni and L. Motte, PEGylated Versus Non-PEGylated γ -Fe₂O₃@Alendronate Nanoparticles, *J. Bioanal. Biomed.*, 2012, **04**, 39–44.

- 72 R. M. C. Dawson, D. C. Elliott, W. H. Elliott and K. M. Jones, *Data for biochemical research*, 1986.
- 73 I. Willner, Y. Eichen, A. J. Frank and M. A. Fox, Photoinduced Electron-Transfer Processes Using Organized Redox-Functionalized Bipyridinium Polyethylenimine TiO₂ Colloids and Particulate Assemblies, *J. Phys. Chem.*, 1993, **97**, 7264–7271.
- 74 B. M. Smith, D. J. Pike, M. O. Kelly and J. A. Nason, Quantification of Heteroaggregation between Citrate-Stabilized Gold Nanoparticles and Hematite Colloids, *Environ. Sci. Technol.*, 2015, **49**, 12789–12797.
- 75 K. L. Chen, S. E. Mylon and M. Elimelech, Aggregation Kinetics of Alginate-Coated Hematite Nanoparticles in Monovalent and Divalent Electrolytes, *Environ. Sci. Technol.*, 2006, **40**, 1516–1523.
- 76 S. M. Ansar, F. S. Ameer, W. Hu, S. Zou, C. U. Pittman and D. Zhang, Removal of Molecular Adsorbates on Gold Nanoparticles Using Sodium Borohydride in Water, *Nano Lett.*, 2013, **13**, 1226–1229.
- 77 Y. Huang, W. Liu, H. Cheng, T. Yao, L. Yang, J. Bao, T. Huang, Z. Sun, Y. Jiang and S. Wei, Solvent-induced desorption of alkanethiol ligands from Au nanoparticles, *Phys Chem Chem Phys*, 2016, **18**, 15927–15933.
- 78 G. Cornelis, Fate descriptors for engineered nanoparticles: the good, the bad, and the ugly, *Environ. Sci. Nano*, 2015, **2**, 19–26.
- 79 A. L. Dale, G. V. Lowry and E. A. Casman, Much ado about α : reframing the debate over appropriate fate descriptors in nanoparticle environmental risk modeling, *Environ. Sci. Nano*, 2015, **2**, 27–32.
- 80 A. Praetorius, R. Arvidsson, S. Molander and M. Scheringer, Facing complexity through informed simplifications: a research agenda for aquatic exposure assessment of nanoparticles, *Environ. Sci. Process. Impacts*, 2013, **15**, 161–168.
- 81 A. Philippe and G. E. Schaumann, Interactions of dissolved organic matter with natural and engineered inorganic colloids: A review, *Environ. Sci. Technol.*, 2014, **48**, 8946–8962.
- 82 S. M. Louie, E. R. Spielman-Sun, M. J. Small, R. D. Tilton and G. V. Lowry, Correlation of the Physicochemical Properties of Natural Organic Matter Samples from Different Sources to Their Effects on Gold Nanoparticle Aggregation in Monovalent Electrolyte, *Environ. Sci. Technol.*, 2015, **49**, 2188–2198.
- 83 F. Loosli and S. Stoll, Effect of surfactants, pH and water hardness on the surface properties and agglomeration behavior of engineered TiO₂ nanoparticles, *Environ. Sci. Nano*, 2016, **4**, 203–211.
- 84 L.-J. A. Ellis, M. Baalousha, E. Valsami-Jones and J. R. Lead, Seasonal variability

- of natural water chemistry affects the fate and behaviour of silver nanoparticles, *Chemosphere*, 2018, **191**, 616–625.
- 85 M. C. Surette and J. A. Nason, Effects of surface coating character and interactions with natural organic matter on the colloidal stability of gold nanoparticles, *Environ. Sci. Nano*, 2016, **3**, 1144–1152.
- 86 N. K. Geitner, S. M. Marinakos, C. Guo, N. O'Brien and M. R. Wiesner, Nanoparticle Surface Affinity as a Predictor of Trophic Transfer, *Environ. Sci. Technol.*, 2016, **50**, 6663–6669.
- 87 B. P. Espinasse, N. K. Geitner, A. Schierz, M. Therezien, C. J. Richardson, G. V. Lowry, L. Ferguson and M. R. Wiesner, Comparative Persistence of Engineered Nanoparticles in a Complex Aquatic Ecosystem, *Environ. Sci. Technol.*, 2018, **52**, 4072–4078.
- 88 N. K. Geitner, J. L. Cooper, A. Avellan, B. T. Castellon, B. G. Perrotta, N. Bossa, M. Simonin, S. M. Anderson, S. Inoue, M. F. Hochella, C. J. Richardson, E. S. Bernhardt, G. V. Lowry, P. L. Ferguson, C. W. Matson, R. S. King, J. M. Unrine, M. R. Wiesner and H. Hsu-Kim, Size-Based Differential Transport, Uptake, and Mass Distribution of Ceria (CeO₂) Nanoparticles in Wetland Mesocosms, *Environ. Sci. Technol.*, 2018, **52**, 9768–9776.
- 89 T. Karanfil, I. Erdogan and M. A. Schlautman, Selecting filter membranes DOC and SUVA₂₅₄, *J. Am. Water Work. Assoc.*, 2003, **95**, 86–100.
- 90 M. S. Croughan, J.-F. Hamel and D. I. C. Wang, Hydrodynamic effects on animal cells grown in microcarrier cultures, *Biotechnol. Bioeng.*, 1987, **29**, 130–141.
- 91 K. L. Chen, B. A. Smith, W. P. Ball and D. H. Fairbrother, Assessing the colloidal properties of engineered nanoparticles in water: case studies from fullerene C 60 nanoparticles and carbon nanotubes, *Environ. Chem.*, 2010, **7**, 10.
- 92 S. A. McDowell, The Effects of Engineered Coatings and Natural Organic Matter on Nanoparticle Aggregation, *M.S. Thesis Oregon State Univ.*
- 93 G. S. Perera, S. A. Athukorale, F. Perez, C. U. Pittman and D. Zhang, Facile displacement of citrate residues from gold nanoparticle surfaces, *J. Colloid Interface Sci.*, 2018, **511**, 335–343.
- 94 M. Baalousha, F. von der Kammer, M. Motelica-Heino, H. S. Hilal and P. Le Coustumer, Size fractionation and characterization of natural colloids by flow-field flow fractionation coupled to multi-angle laser light scattering, *J. Chromatogr. A*, 2006, **1104**, 272–281.
- 95 H. P. Jarvie and S. M. King, Small-Angle Neutron Scattering Study of Natural Aquatic Nanocolloids, *Environ. Sci. Technol.*, 2007, **41**, 2868–2873.

- 96 M. Han and D. F. Lawler, The (Relative) Insignificance of G in Flocculation, *J. Am. Water Work. Assoc.*, 1992, **84**, 79–91.
- 97 A. A. Keller, H. Wang, D. Zhou, H. S. Lenihan, G. Cherr, B. J. Cardinale, R. Miller and J. I. Zhaoxia, Stability and aggregation of metal oxide nanoparticles in natural aqueous matrices, *Environ. Sci. Technol.*, 2010, **44**, 1962–1967.
- 98 C. O. Hendren, G. V. Lowry, J. M. Unrine and M. R. Wiesner, A functional assay-based strategy for nanomaterial risk forecasting, *Sci. Total Environ.*, 2015, **536**, 1029–1037.
- 99 D. M. Mitrano, S. Motellier, S. Clavaguera and B. Nowack, Review of nanomaterial aging and transformations through the life cycle of nano-enhanced products, *Environ. Int.*, 2015, **77**, 132–147.
- 100 D. M. Mitrano and B. Nowack, The need for a life-cycle based aging paradigm for nanomaterials: importance of real-world test systems to identify realistic particle transformations, *Nanotechnology*, 2017, **28**, 072001.
- 101 B. Nowack and D. M. Mitrano, Procedures for the production and use of synthetically aged and product released nanomaterials for further environmental and ecotoxicity testing, *NanoImpact*, 2018, **10**, 70–80.
- 102 N. C. Mueller and B. Nowack, Exposure Modeling of Engineered Nanoparticles in the Environment, *Environ. Sci. Technol.*, 2008, **42**, 4447–4453.
- 103 T. Yin, F. Gottschalk, K. Hungerbühler and B. Nowack, Comprehensive probabilistic modelling of environmental emissions of engineered nanomaterials, *Environ. Pollut.*, 2014, **185**, 69–76.
- 104 N. A. Bornhöft, T. Y. Sun, L. M. Hilty and B. Nowack, A dynamic probabilistic material flow modeling method, *Environ. Model. Softw.*, 2016, **76**, 69–80.
- 105 T. Y. Sun, D. M. Mitrano, N. A. Bornhöft, M. Scheringer, K. Hungerbühler and B. Nowack, Envisioning Nano Release Dynamics in a Changing World: Using Dynamic Probabilistic Modeling to Assess Future Environmental Emissions of Engineered Nanomaterials, *Environ. Sci. Technol.*, 2017, **51**, 2854–2863.
- 106 A. Lazareva and A. A. Keller, Estimating potential life cycle releases of engineered nanomaterials from wastewater treatment plants, *ACS Sustain. Chem. Eng.*, 2014, **2**, 1656–1665.
- 107 M. A. Kiser, H. Ryu, H. Jang, K. Hristovski and P. Westerhoff, Biosorption of nanoparticles to heterotrophic wastewater biomass, *Water Res.*, 2010, **44**, 4105–4114.
- 108 L. K. Limbach, R. Bereiter, E. Muller, R. Krebs, R. Galli and W. J. Srtark, Removal of Oxide Nanoparticles in a Model Wastewater Treatment Plant: Influence of

- Agglomeration and Surfactants on Clearing Efficiency, *Environmental Sci. Technol.*, 2008, **42**, 5828–5833.
- 109 H. P. Jarvie, H. Al-Obaidi, S. M. King, M. J. Bowes, M. J. Lawrence, A. F. Drake, M. A. Green and P. J. Dobson, Fate of silica nanoparticles in simulated primary wastewater treatment, *Environ. Sci. Technol.*, 2009, **43**, 8622–8628.
- 110 L. Otero-González, J. A. Field, I. A. C. Calderon, C. A. Aspinwall, F. Shadman, C. Zeng and R. Sierra-Alvarez, Fate of fluorescent core-shell silica nanoparticles during simulated secondary wastewater treatment, *Water Res.*, 2015, **77**, 170–178.
- 111 B. Salieri, D. A. Turner, B. Nowack and R. Hirsch, Life cycle assessment of manufactured nanomaterials: Where are we?, *NanoImpact*, 2018, **10**, 108–120.
- 112 V. Adam, A. Caballero-Guzman and B. Nowack, Considering the forms of released engineered nanomaterials in probabilistic material flow analysis, *Environ. Pollut.*, 2018, **243**, 17–27.
- 113 M. C. Surette and J. A. Nason, Nanoparticle aggregation in a freshwater river: the role of engineered surface coatings, *Environ. Sci. Nano*, 2019, **6**, 540–553.
- 114 H. Holthoff, S. U. Egelhaaf, M. Borkovec, P. Schurtenberger and H. Sticher, Coagulation Rate Measurements of Colloidal Particles by Simultaneous Static and Dynamic Light Scattering, *Langmuir*, 1996, **12**, 5541–5549.
- 115 S. Diegoli, A. L. Manciuola, S. Begum, I. P. Jones, J. R. Lead and J. A. Preece, Interaction between manufactured gold nanoparticles and naturally occurring organic macromolecules, *Sci. Total Environ.*, 2008, **402**, 51–61.
- 116 V. L. Pallem, H. A. Stretz and M. J. M. Wells, Evaluating Aggregation of Gold Nanoparticles and Humic Substances Using Fluorescence Spectroscopy, *Environ. Sci. Technol.*, 2009, **43**, 7531–7535.
- 117 F. Frederix, J.-M. Friedt, K.-H. Choi, W. Laureyn, A. Campitelli, D. Mondelaers, G. Maes and G. Borghs, Biosensing Based on Light Absorption of Nanoscaled Gold and Silver Particles, *Anal. Chem.*, 2003, **75**, 6894–6900.
- 118 W. Rechberger, A. Hohenau, A. Leitner, J. R. Krenn, B. Lamprecht and F. R. Aussenegg, Optical properties of two interacting gold nanoparticles, *Opt. Commun.*, 2003, **220**, 137–141.
- 119 I. E. Sendroui, S. F. L. L. Mertens and D. J. Schiffrin, Plasmon interactions between gold nanoparticles in aqueous solution with controlled spatial separation, *Phys. Chem. Chem. Phys.*, 2006, **8**, 1430.
- 120 C. J. Murphy, T. K. Sau, A. M. Gole, C. J. Orendorff, J. Gao, L. Gou, S. E. Hunyadi and T. Li, Anisotropic metal nanoparticles: Synthesis, assembly, and optical applications, *J. Phys. Chem. B*, 2005, **109**, 13857–13870.

- 121 G.-P. Sheng, H.-Q. Yu and X.-Y. Li, Extracellular polymeric substances (EPS) of microbial aggregates in biological wastewater treatment systems: A review, *Biotechnol. Adv.*, 2010, **28**, 882–894.
- 122 M. F. Dignac, V. Urbain, D. Rybacki, A. Bruchet, D. Snidaro and P. Scribe, Chemical Description of Extracellular Polymers: Implications on Activated Sludge Floc Structure, *Water Sci. Technol.*, 1998, **38**, 45–53.
- 123 J. Zeng, J. M. Gao, Y. P. Chen, P. Yan, Y. Dong, Y. Shen, J. S. Guo, N. Zeng and P. Zhang, Composition and aggregation of extracellular polymeric substances (EPS) in hyperhaline and municipal wastewater treatment plants, *Sci. Rep.*, 2016, **6**, 1–9.
- 124 M. Esparza-Soto and P. Westerhoff, Biosorption of humic and fulvic acids to live activated sludge biomass, *Water Res.*, 2003, **37**, 2301–2310.
- 125 X.-M. Liu, H.-W. Luo, F. Zhang, S.-J. Yuan, J. Xu, J.-G. Wu and H.-Q. Yu, Contribution of Extracellular Polymeric Substances (EPS) to the Sludge Aggregation, *Environ. Sci. Technol.*, 2010, **44**, 4355–4360.
- 126 D. C. Sobock and M. J. Higgins, Examination of three theories for mechanisms of cation-induced bioflocculation, *Water Res.*, 2002, **36**, 527–538.
- 127 R. P. Schwarzenbach, P. M. Gschwend and D. M. Imboden, *Environmental Organic Chemistry*, John Wiley & Sons, Inc., 3rd Ed., 2016.
- 128 C. Ort, A. L. N. van Nuijs, J. D. Berset, L. Bijlsma, S. Castiglioni, A. Covaci, P. de Voogt, E. Emke, D. Fatta-Kassinos, P. Griffiths, F. Hernández, I. González-Mariño, R. Grabic, B. Kasprzyk-Hordern, N. Mastroianni, A. Meierjohann, T. Nefau, M. Östman, Y. Pico, I. Racamonde, M. Reid, J. Slobodnik, S. Terzic, N. Thomaidis and K. V. Thomas, Spatial differences and temporal changes in illicit drug use in Europe quantified by wastewater analysis, *Addiction*, 2014, **109**, 1338–1352.
- 129 A. K. McCall, R. Palmitessa, F. Blumensaat, E. Morgenroth and C. Ort, Modeling in-sewer transformations at catchment scale – implications on drug consumption estimates in wastewater-based epidemiology, *Water Res.*, 2017, **122**, 655–668.
- 130 J. T. K. Quik, I. Velzeboer, M. Wouterse, A. A. Koelmans and D. van de Meent, Heteroaggregation and sedimentation rates for nanomaterials in natural waters, *Water Res.*, 2014, **48**, 269–279.
- 131 F. Loosli, J. Wang, S. Rothenberg, M. Bizimis, C. Winkler, O. Borovinskaya, L. Flamigni and M. Baalousha, Sewage spills are a major source of titanium dioxide engineered (nano)-particle release into the environment, *Environ. Sci. Nano*, 2019, **6**, 763–777.
- 132 M. C. Surette, J. A. Nason and R. Kägi, Influence of Surface Coatings on Corona Formation and Aggregation of Engineered Nanomaterials During Conventional Wastewater Treatment Processes, *Rev.*

- 133 F. N. Ponnamparuma, E. M. Tianco and T. A. Loy, Ionic strengths of the solutions of flooded soils and other natural aqueous solutions from specific conductance, *Soil Sci.*, , DOI:10.1097/00010694-196612000-00009.
- 134 M. Han and D. F. Lawler, Interactions of Two Settling Spheres: Settling Rates and Collision Efficiency, *J. Hydraul. Eng.*, 1991, **117**, 1269–1289.
- 135 I. Velzeboer, J. T. K. Quik, D. van de Meent and A. A. Koelmans, Rapid settling of nanoparticles due to heteroaggregation with suspended sediment, *Environ. Toxicol. Chem.*, 2014, **33**, 1766–1773.
- 136 A. Armanious, M. Aeppli and M. Sander, Dissolved organic matter adsorption to model surfaces: Adlayer formation, properties, and dynamics at the nanoscale, *Environ. Sci. Technol.*, 2014, **48**, 9420–9429.
- 137 A. Armanious, M. Münch, T. Kohn and M. Sander, Competitive Coadsorption Dynamics of Viruses and Dissolved Organic Matter to Positively Charged Sorbent Surfaces, *Environ. Sci. Technol.*, 2016, **50**, 3597–3606.

APPENDICES

A. SUPPLEMENTARY INFORMATION – FIRST MANUSCRIPT

A1. Investigation into Reagent Order of Additions

To verify that the aggregation observed via time-resolved dynamic light scattering (TR-DLS) was not an artifact of the method employed when combining the components of each sample, an investigation was performed utilizing two different methods for adding each component to the sample. Since the most significant aggregation (i.e., highest extent of aggregation) was observed with the bPEI-AuNPs and the presence of Suwannee River Natural Organic Matter (SRNOM), the following methods were focused to assessing whether or not aggregation of the bPEI-AuNPs could be observed using the two methods outlined below. The only variation between the two methods is related to the order in which the AuNPs and SRNOM are added. This intent of testing these two methods was to compare the standard method utilized throughout this research with a set of experimental conditions that more closely matches what is expected to occur in the environment (i.e., NOM macromolecules would already be dispersed within an aquatic environment, with ENMs being ‘released’ to that environment from a source).

1. **Standard Method:** The standard method used throughout the research presented in the main text:
 - (1) Preparation of a 3.5 mL distilled, deionized (DDI) particle-free blank;
 - (2) Removal of DDI for the required volume of AuNPs and electrolyte;
 - (3) Addition of the electrolyte (1 mM KCl);
 - (4) Addition of the AuNPs (1 mg Au/L);
 - (5) Initial size verification via DLS (3 DLS measurements, each 3 minutes long);
 - (6) Addition of SRNOM (1.0 mg C/L); and
 - (7) The cuvette was inverted and immediately analyzed via TR-DLS (120 DLS measurements, each 15 seconds long).
2. **Modified Method:** A modified method that added the SRNOM to the solution prior to the AuNPs:
 - (1) Preparation of a 3.5 mL DDI particle-free blank;
 - (2) Removal of DDI for the required volume of AuNPs and electrolyte;
 - (3) Addition of the electrolyte (1 mM KCl);

- (4) Addition of SRNOM (1.0 mg C/L);
- (5) Initial size verification via DLS (3 DLS measurements, each 3 minutes long);
- (6) Addition of the AuNPs (1.0 mg Au/L); and
- (7) The cuvette was inverted and immediately analyzed via TR-DLS (120 DLS measurements, each 15 seconds long).

The results, shown in Figure A1, indicate that using either method results in the same general extent of aggregation. It is worth noting that these results also match prior results reported in Figure A1f that tested these same general conditions.

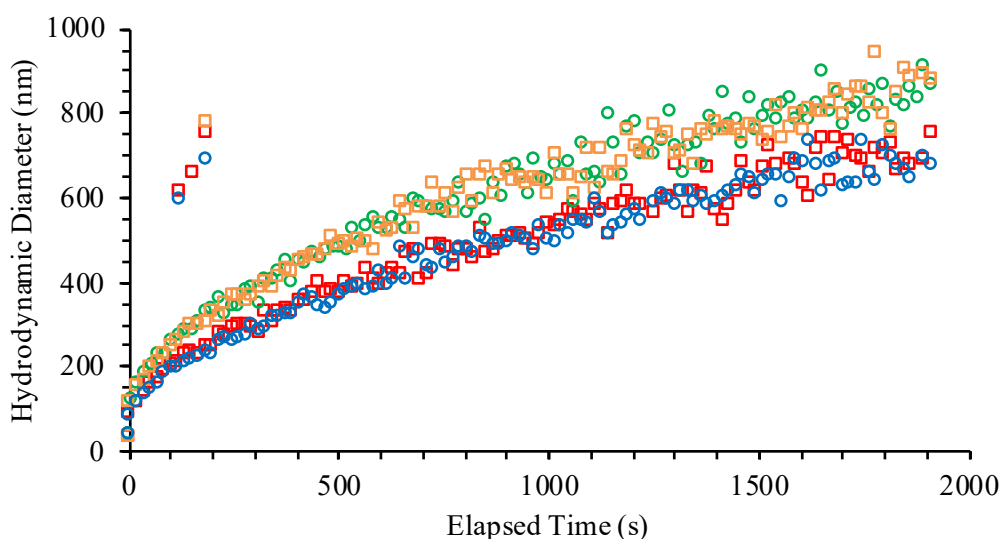


Figure A1. Intensity-weighted hydrodynamic diameter (D_h) as a function of time for 1 mg/L bPEI-AuNPs in the presence of 1 mM KCl and 1.0 mg C/L SRNOM. Standard method at (○) pH 5.79 and (○) pH 5.81; modified method at (□) pH 6.0 and (□) pH 6.01.

A2. Effects of Surface Coating Molecular Weight on PEG-AuNP Stability

As can be seen in Figure A2, there is an increase in the hydrodynamic diameter (D_h) of the PEG-AuNPs with respect to the increasing surface coating molecular weight—from approximately 28.6 ± 8.3 nm to 68.7 ± 8.2 nm for the 2 kDa and 30 kDa PEG-AuNPs, respectively. The increase in the hydrodynamic diameter is attributable to the longer PEG polymer chains present on the higher molecular weight PEG surface coatings, as the core

diameter was unchanged between the different PEG-AuNPs (approximately 10.5 ± 0.9 ; Table 2.1 in main text).

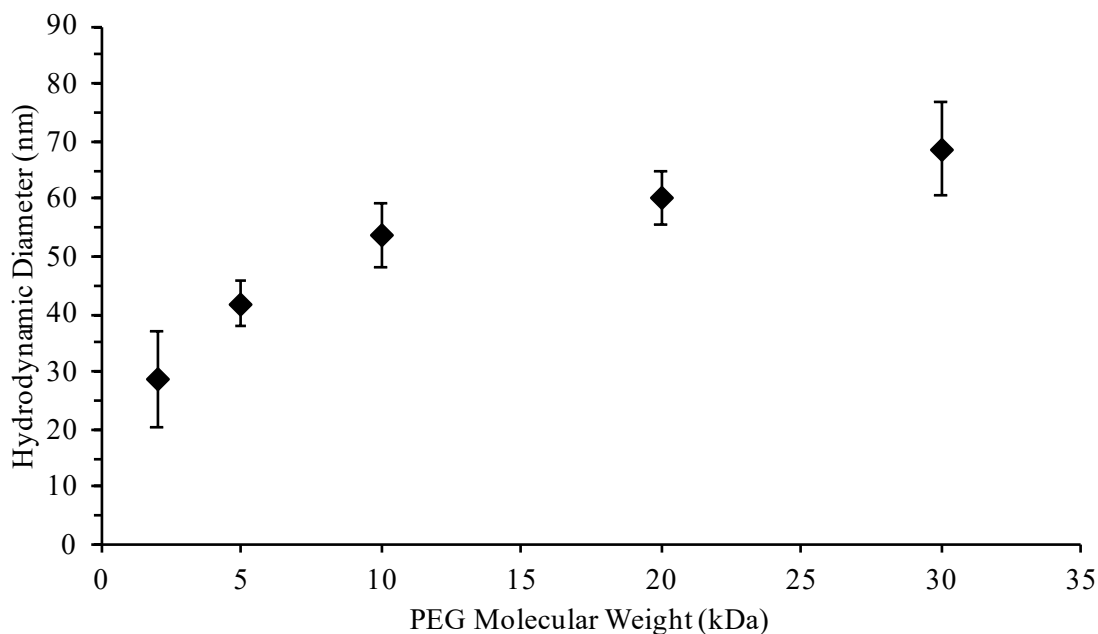


Figure A2. Hydrodynamic diameter (D_h) as a function of PEG surface coating molecular weight (kDa) for the PEG-AuNPs at pH 5.9 ± 0.1 . Error bars equal ± 1 S.D.

An initial series of TR-DLS measurements were performed to assess the stability of the PEG-AuNPs in high ionic strength solutions. Each of the PEG-AuNPs were added to solutions containing either 1 M KCl or 1 M CaCl₂, following the procedures described in the main text, and monitored via TR-DLS. The results, shown in Figure A3, indicate that no aggregation occurs for the various molecular weight PEG-AuNPs in either the 1:1 KCl or 2:1 CaCl₂. These results are consistent with the measurements focused on assessing the 2 kDa PEG-AuNPs (detailed in the main text).

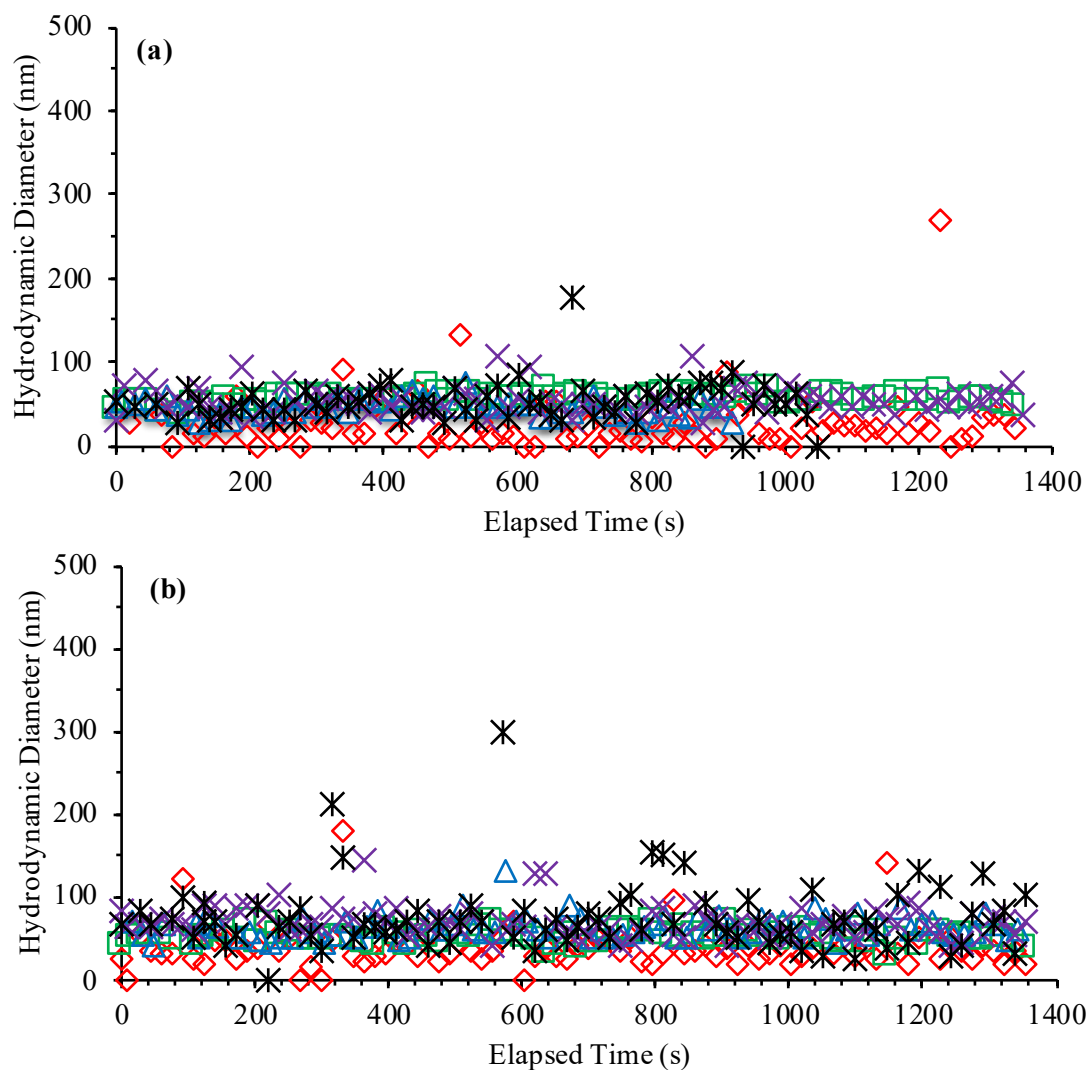


Figure A3. Hydrodynamic diameter (D_h) as a function of time for PEG-AuNPs with different molecular weight coatings in the presence of (a) 1 M KCl at $\text{pH } 5.6 \pm 0.1$ (b) 1 M CaCl_2 at $\text{pH } 7.8 \pm 0.1$ at various molecular weight: (\diamond) 2 kDa; (\square) 5 kDa; (\triangle) 10 kDa; (\times) 20 kDa; and ($*$) 30 kDa.

Finally, TR-DLS measurements of the 30 kDa PEG-AuNPs in the presence of varying concentrations of SRNOM were performed. As shown in Figure A4, no aggregation of the 30 kDa PEG-AuNPs was noted regardless of the mass concentration ratio of [SRNOM]:[AuNPs]. These results are consistent with the testing performed for the 2 kDa PEG-AuNPs that also showed no aggregation in the presence of SRNOM.

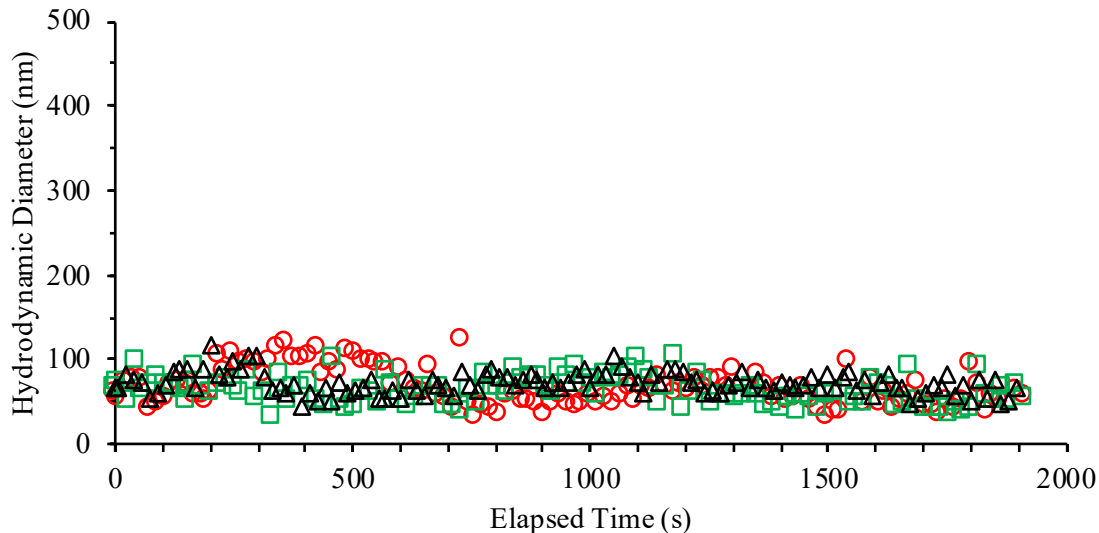


Figure A4. Hydrodynamic diameter (D_h) as a function of time for the 30 kDa PEG-AuNPs in the presence of 1 mM KCl and at varying mass concentration ratios of [SRNOM]:[AuNPs]—(○) 0.007; (□) 0.07; and (△) 0.66 mg C/mg AuNPs at pH 5.3 ± 0.1 .

In summary, the additional experiments presented here suggest little difference in the stability of the PEG-AuNPs with respect to changes in the molecular weight of the PEG surface coating, illustrating that this parameter is a minor factor influencing PEG-AuNPs aggregation under the conditions tested.

A3. TR-DLS of AuNPs with Varying Electrolyte Concentrations and Valence

Figures A5 – A8 indicate no change in D_h over time for the four AuNP types in the presence of both 1:1 KCl and 2:1 CaCl_2 at concentrations between 40 and 500 mM.

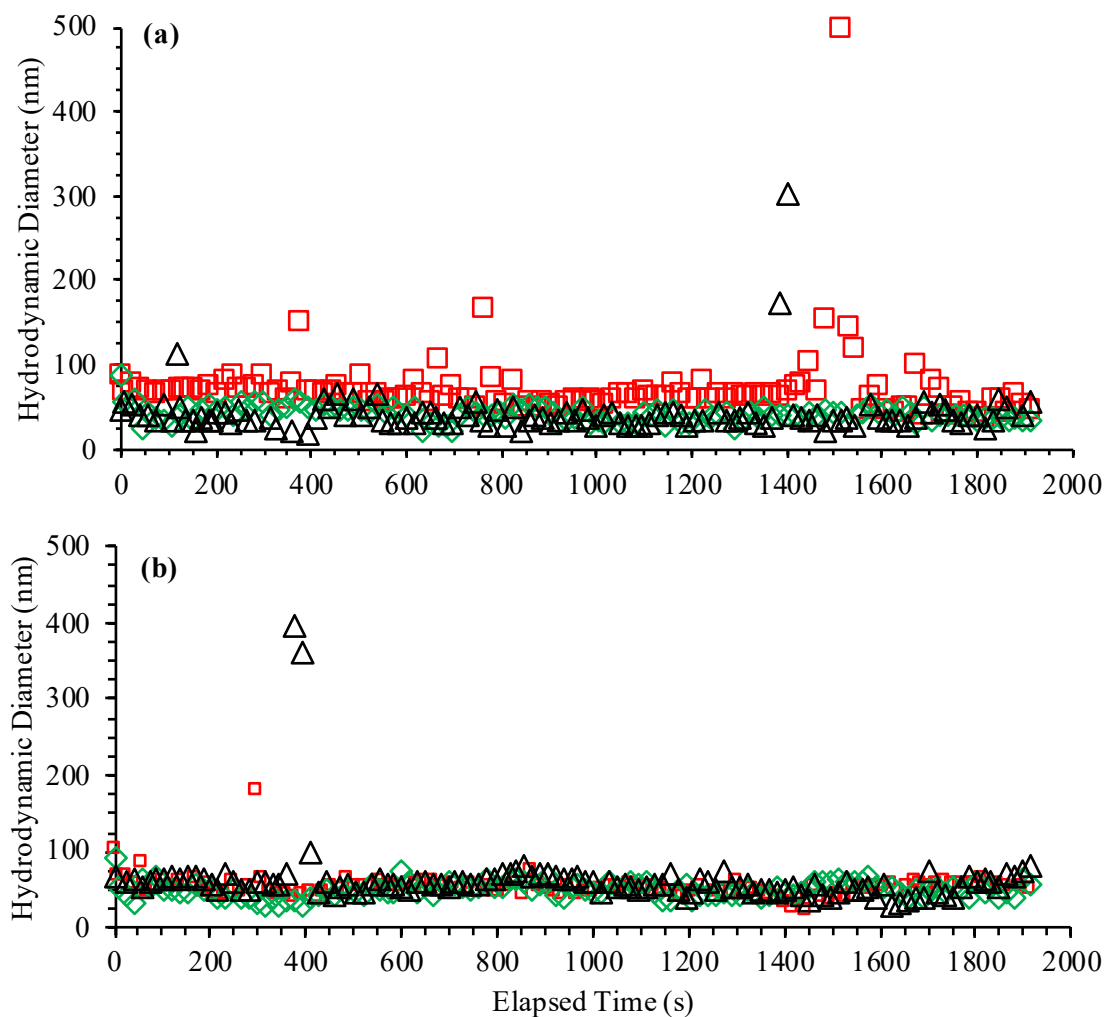


Figure A5. Intensity-weighted hydrodynamic diameter (D_h) of 3 kDa PEG-Amine-AuNP as a function of time in the presence of (a) KCl and (b) CaCl₂ at (□) 40 mM; (◇) 120 mM; and (△) 500 mM and pH 5.9 ± 0.9 .

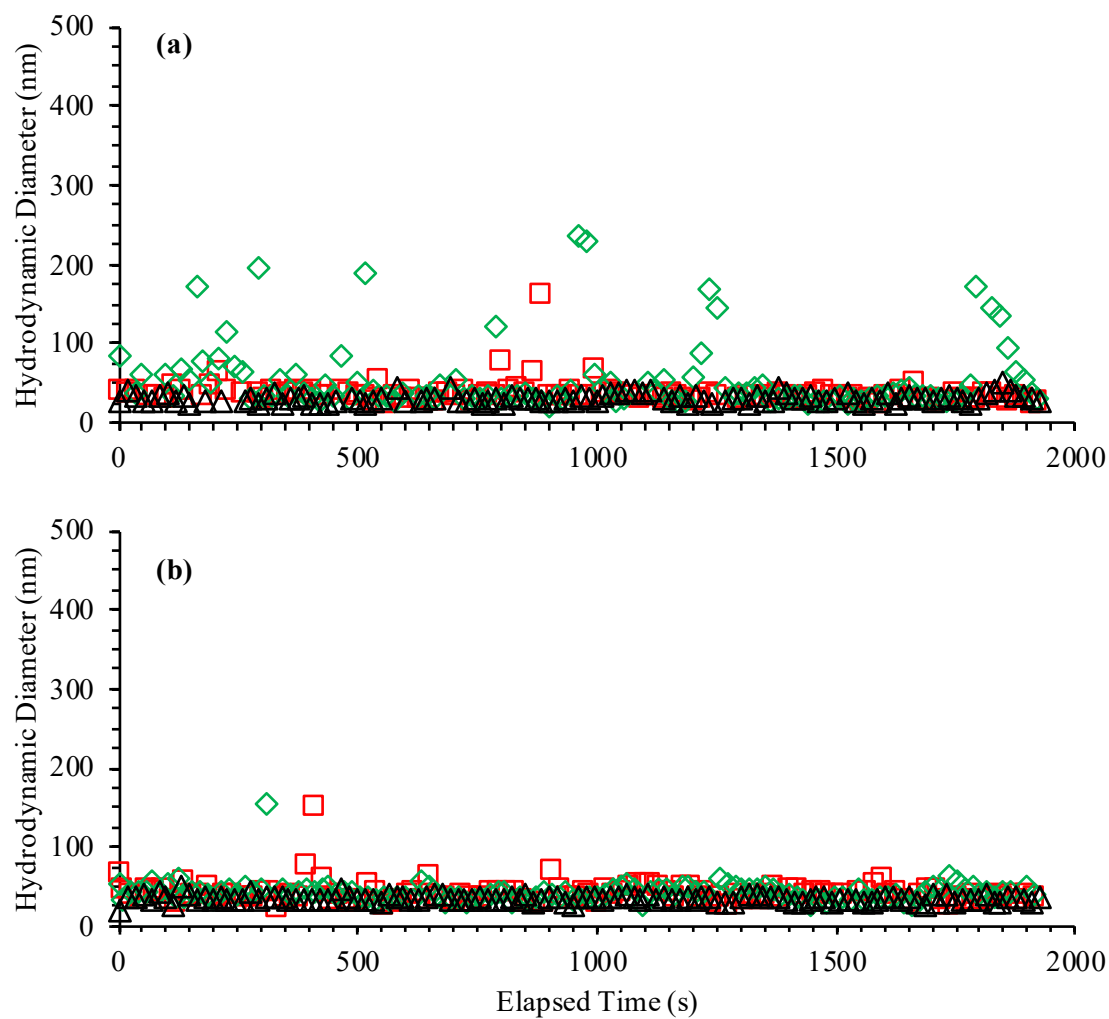


Figure A6. Intensity-weighted hydrodynamic diameter (D_h) of 3 kDa PEG-COOH-AuNP as a function of time in the presence of (a) KCl and (b) CaCl₂ at (□) 40 mM; (◇) 120 mM; and (△) 500 mM and pH 6.6 ± 1.2 .

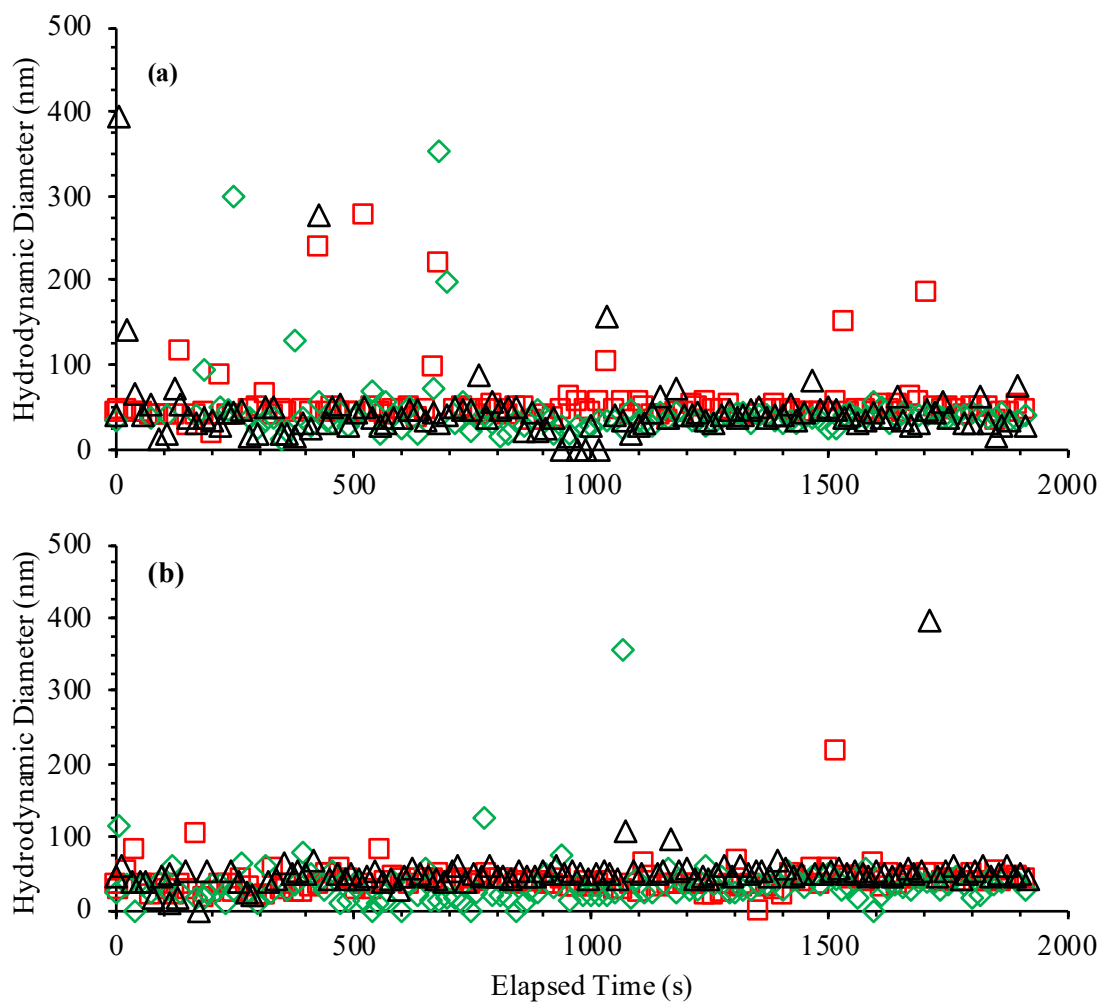


Figure A7. Intensity-weighted hydrodynamic diameter (D_h) of 2 kDa PEG-AuNPs as a function of time in the presence of (a) KCl and (b) CaCl_2 at (\square) 40 mM; (\diamond) 120 mM; and (\triangle) 500 mM and pH 5.9 ± 1.0 .

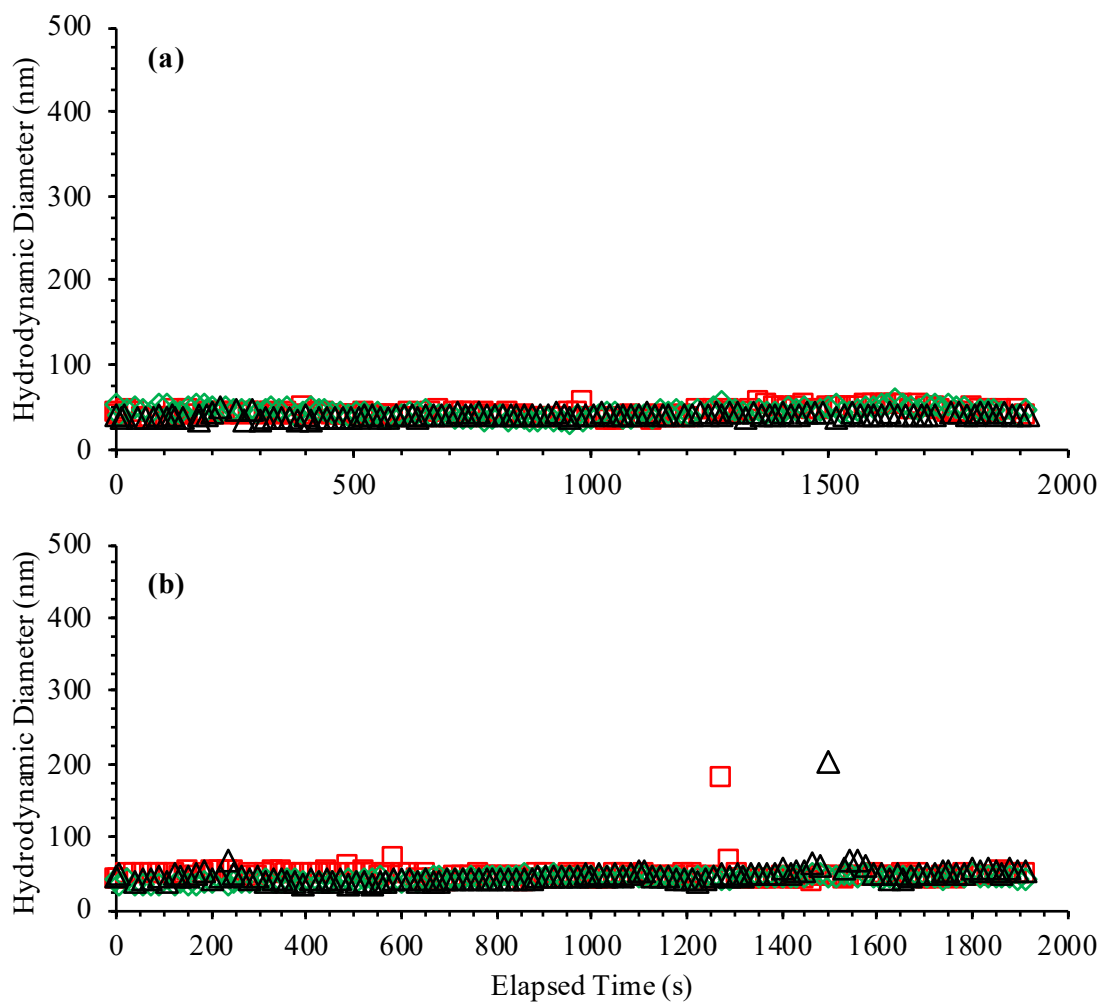


Figure A8. Intensity-weighted hydrodynamic diameter (D_h) of bPEI-AuNPs as a function of time in the presence of (a) KCl and (b) CaCl₂ at (□) 40 mM; (◇) 120 mM; and (△) 500 mM and pH 6.0 ± 1.1 .

A4. TR-DLS of 3 kDa PEG-Amine-AuNPs and bPEI-AuNPs at High I and pH_{IEP}

TR-DLS measurements were conducted to verify the stability of the 3 kDa PEG-Amine-AuNPs and bPEI-AuNPs near their isoelectric point (IEP) and at high ionic strength. Samples were prepared using the methods outlined in the main text and adjusted to approximately the pH_{IEP} measured during the EPM titrations (pH_{IEP} 9.7 and pH_{IEP} 10.3 for 3 kDa PEG-Amine-AuNPs and bPEI-AuNPs, respectively). Then, 500 mM KCl was added to the dispersions and D_h was measured over time. The results, shown in Figure A9, indicate that both these AuNP types are stable in the presence of high ionic strength and at pH_{IEP} .

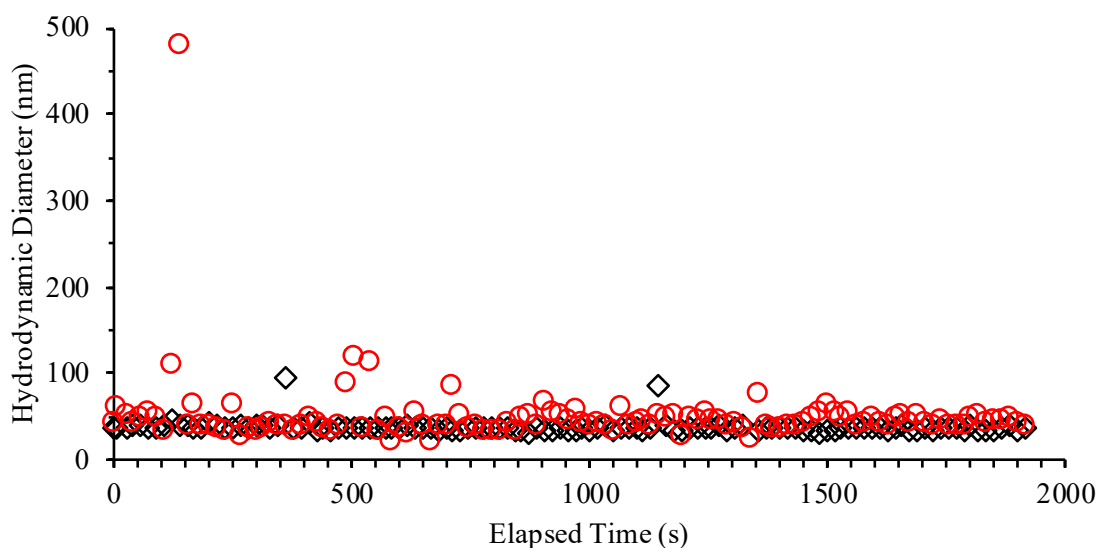


Figure A9. Intensity-weighted hydrodynamic diameter (D_h) as a function of time for the (○) 3 kDa PEG-Amine-AuNPs at pH 10.0 and (◇) bPEI-AuNPs at pH 10.5 in the presence of 500 mM KCl.

A5. Variation of D_h vs. pH for bPEI-AuNPs

The initial size measurements performed during the SRNOM testing (Step 4, main text) are presented in Figure A10. These measurement steps involve 3 DLS measurements, with each measurement lasting 3 minutes. Regardless of the solution pH, the D_h of the bPEI-AuNPs does not substantially vary from the value reported in Table 2.1 of the main text ($D_h = 47.6$ nm).

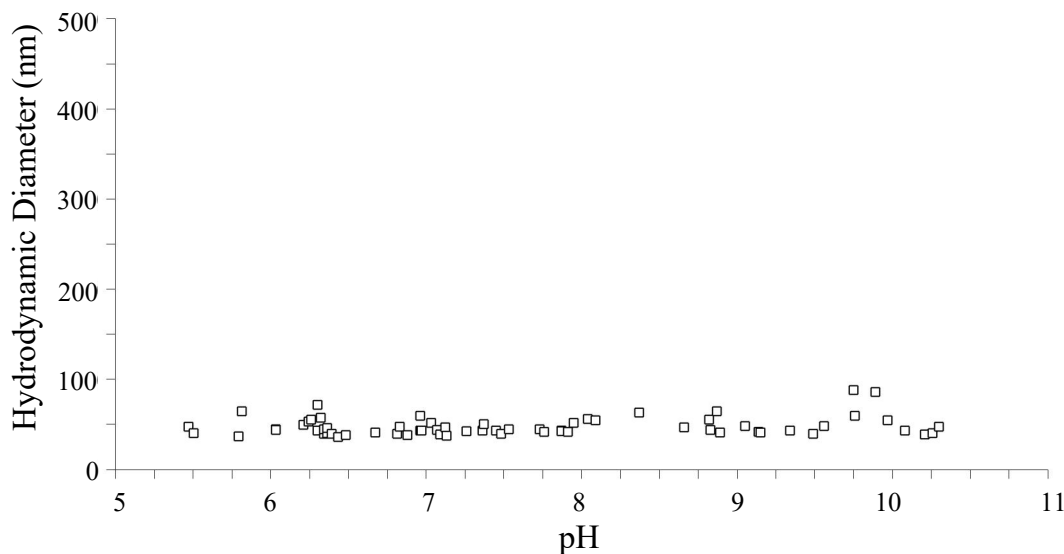


Figure A10. Intensity-weighted hydrodynamic diameter (D_h) as a function of pH for the bPEI-AuNPs in the presence of 1 mM KCl.

A6. TR-DLS of bPEI-AuNPs at Varying pH and [SRNOM]:[AuNPs]

Figure A11 presents the raw TR-DLS data for bPEI-AuNPs dispersed in DDI at varying [SRNOM]:[AuNPs] ratios (0.007-1.7) and pH (6-10). At low [SRNOM]:[AuNPs] (Figures A11a-b) no aggregation was observed across the range of pH tested. As the [SRNOM]:[AuNPs] ratio is increased (Figures A11c-g), homoaggregation occurred, but only over a certain range of pH. For example, at pH 6.3 no aggregation was noted at [SRNOM]:[AuNPs] = 0.2 but significant aggregation was observed at this pH when [SRNOM]:[AuNPs] = 0.66 (Figures A11c and A11e, respectively). As the [SRNOM]:[AuNPs] continued to increase further (Figure A11h), no significant aggregation was observed across the range of pH tested. As noted in the main text, it is hypothesized that a combination of charge reversal (due to the adsorption of NOM macromolecules to the bPEI-AuNPs at low pH) and electrosteric interactions (at high pH) resulted in the stability of the bPEI-AuNPs at the high [SRNOM]:[AuNPs].

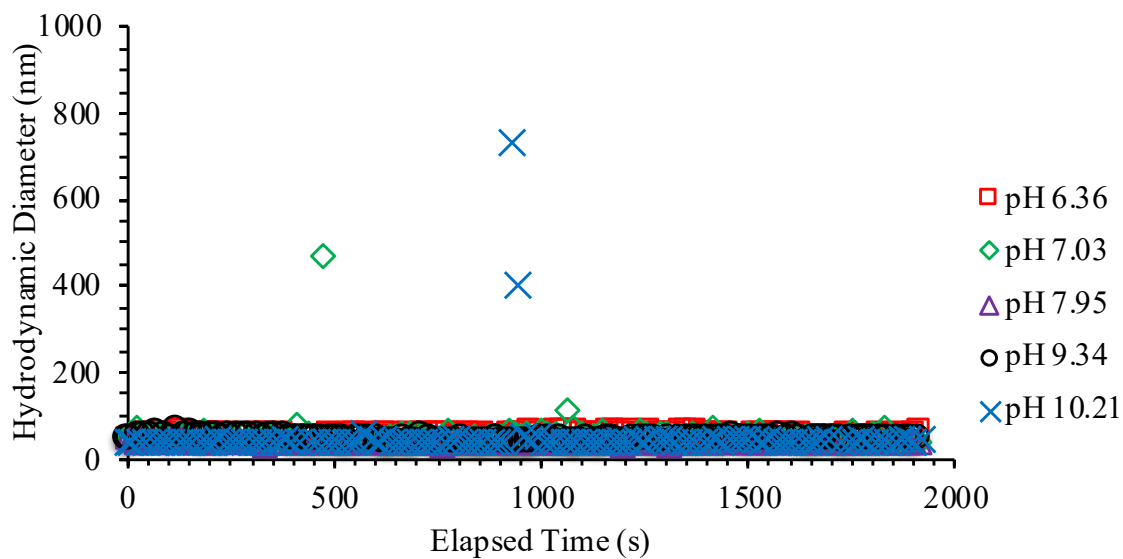


Figure A11a. Intensity-weighted hydrodynamic diameter (D_h) as a function of time for bPEI-AuNPs at varying pH and [SRNOM]:[AuNPs] = 0.007 mg C / mg AuNPs. $I = 1$ mM KCl.

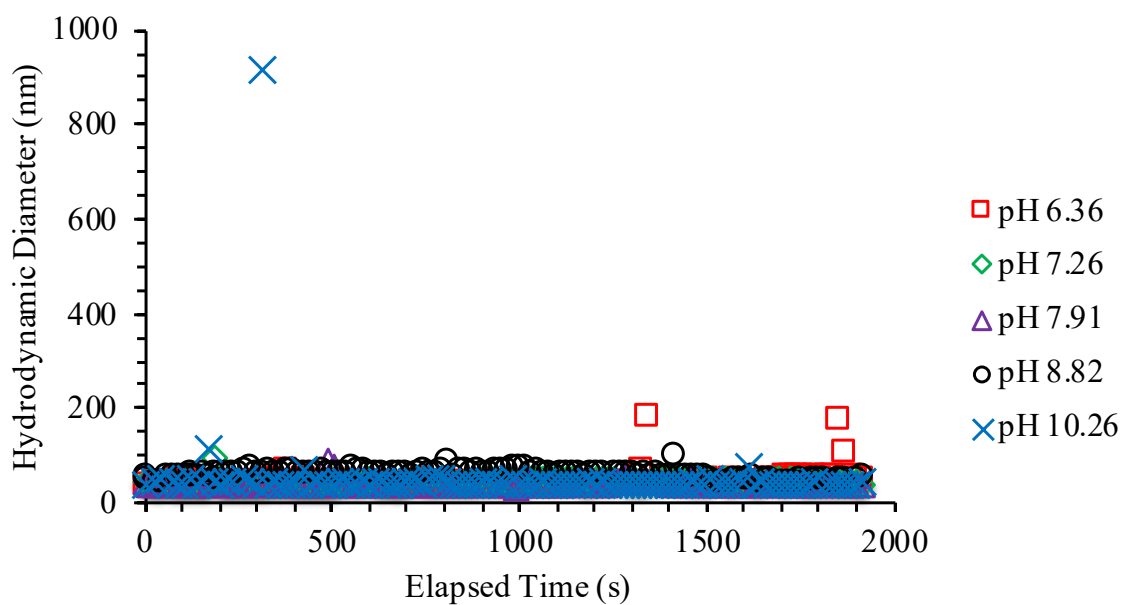


Figure A11b. Intensity-weighted hydrodynamic diameter (D_h) as a function of time for bPEI-AuNPs at varying pH and [SRNOM]:[AuNPs] = 0.07 mg C / mg AuNPs. $I = 1$ mM KCl.

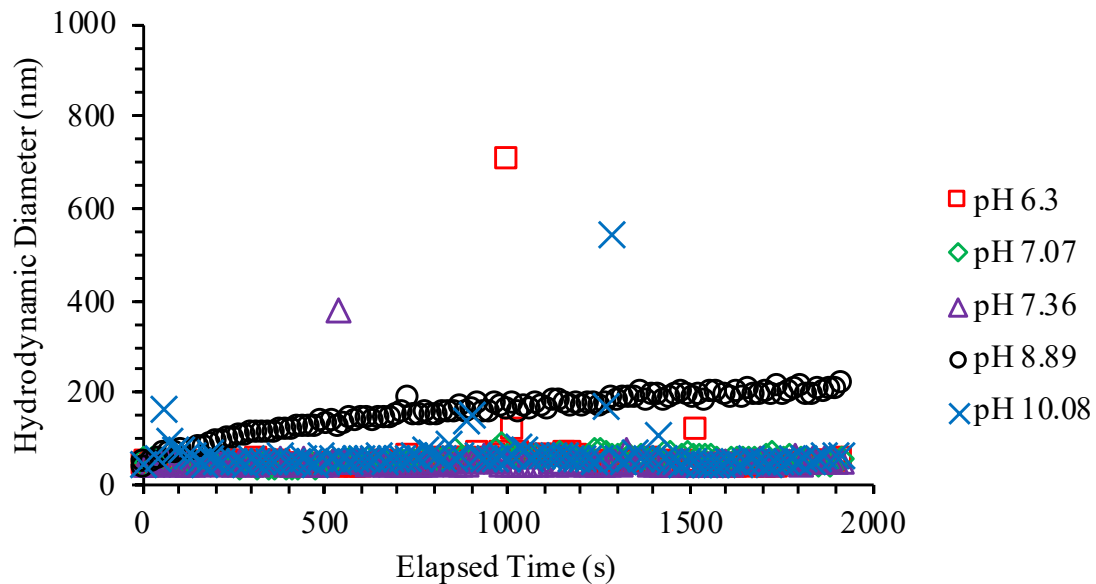


Figure A11c. Intensity-weighted hydrodynamic diameter (D_h) as a function of time for bPEI-AuNPs at varying pH and $[\text{SRNOM}]:[\text{AuNPs}] = 0.2 \text{ mg C} / \text{mg AuNPs}$. $I = 1 \text{ mM KCl}$.

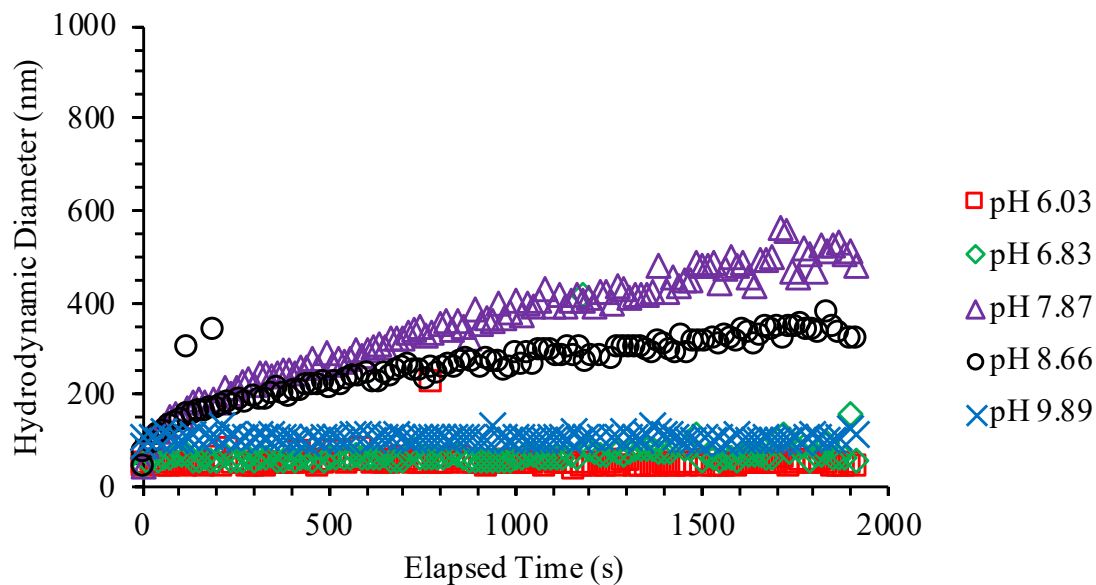


Figure A11d. Intensity-weighted hydrodynamic diameter (D_h) as a function of time for bPEI-AuNPs at varying pH and $[\text{SRNOM}]:[\text{AuNPs}] = 0.4 \text{ mg C} / \text{mg AuNPs}$. $I = 1 \text{ mM KCl}$.

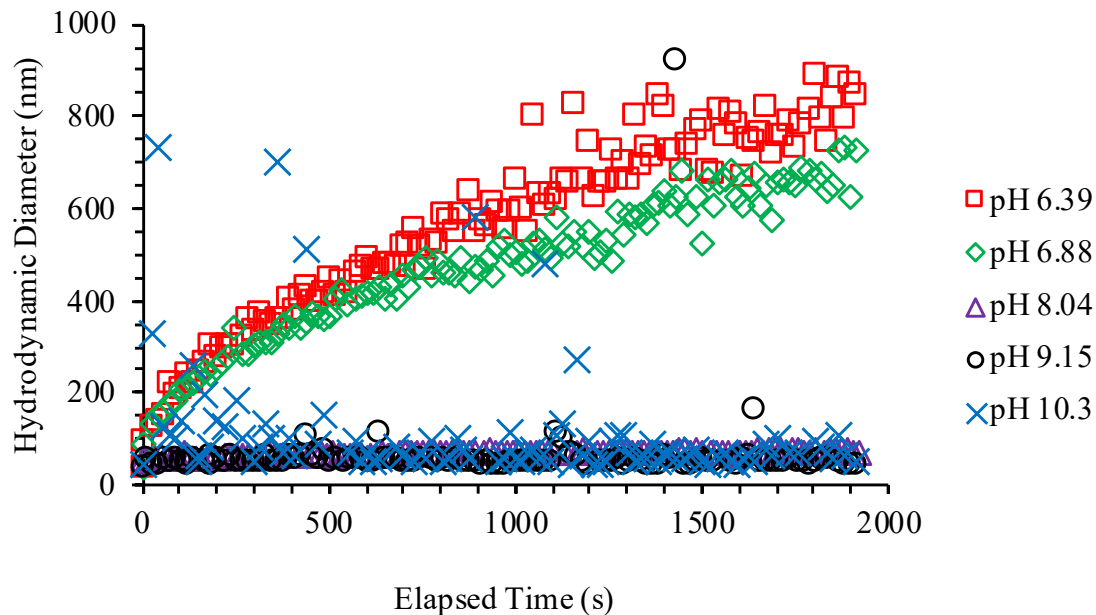


Figure A11e. Intensity-weighted hydrodynamic diameter (D_h) as a function of time for bPEI-AuNPs at varying pH and $[\text{SRNOM}]:[\text{AuNPs}] = 0.66 \text{ mg C} / \text{mg AuNPs}$. $I = 1 \text{ mM KCl}$.

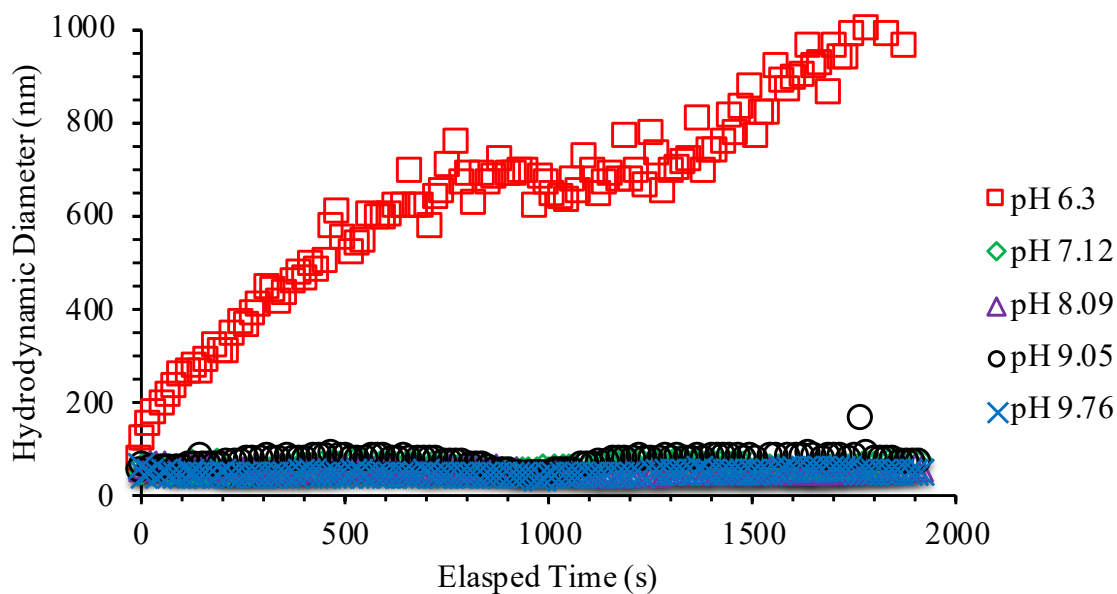


Figure A11f. Intensity-weighted hydrodynamic diameter (D_h) as a function of time for bPEI-AuNPs at varying pH and $[\text{SRNOM}]:[\text{AuNPs}] = 1.0 \text{ mg C} / \text{mg AuNPs}$. $I = 1 \text{ mM KCl}$.

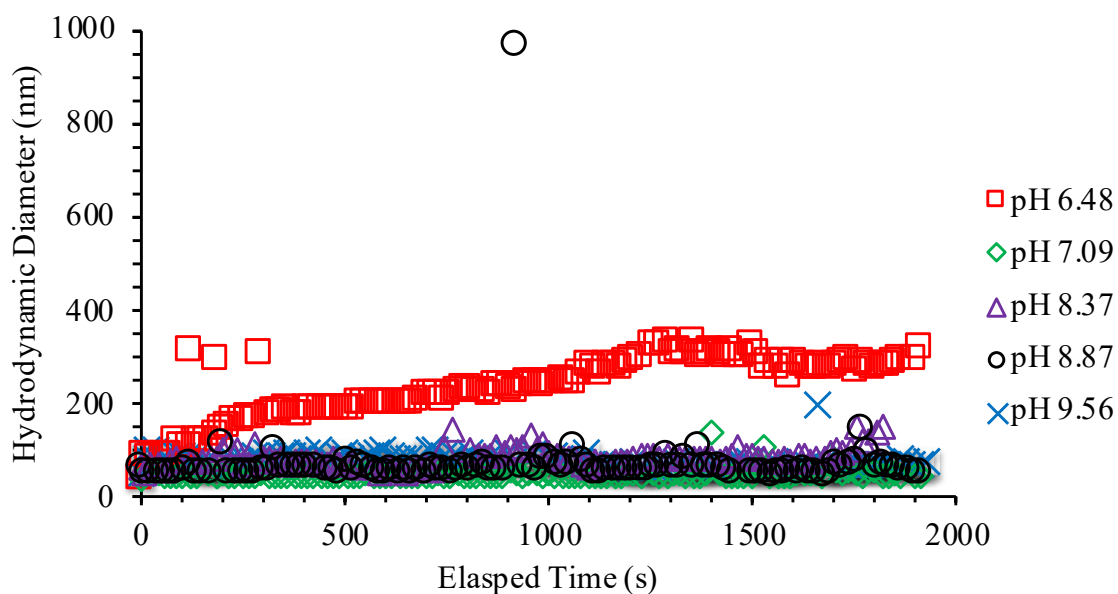


Figure A11g. Intensity-weighted hydrodynamic diameter (D_h) as a function of time for bPEI-AuNPs at varying pH and $[\text{SRNOM}]:[\text{AuNPs}] = 1.3 \text{ mg C} / \text{mg AuNPs}$. $I = 1 \text{ mM KCl}$.

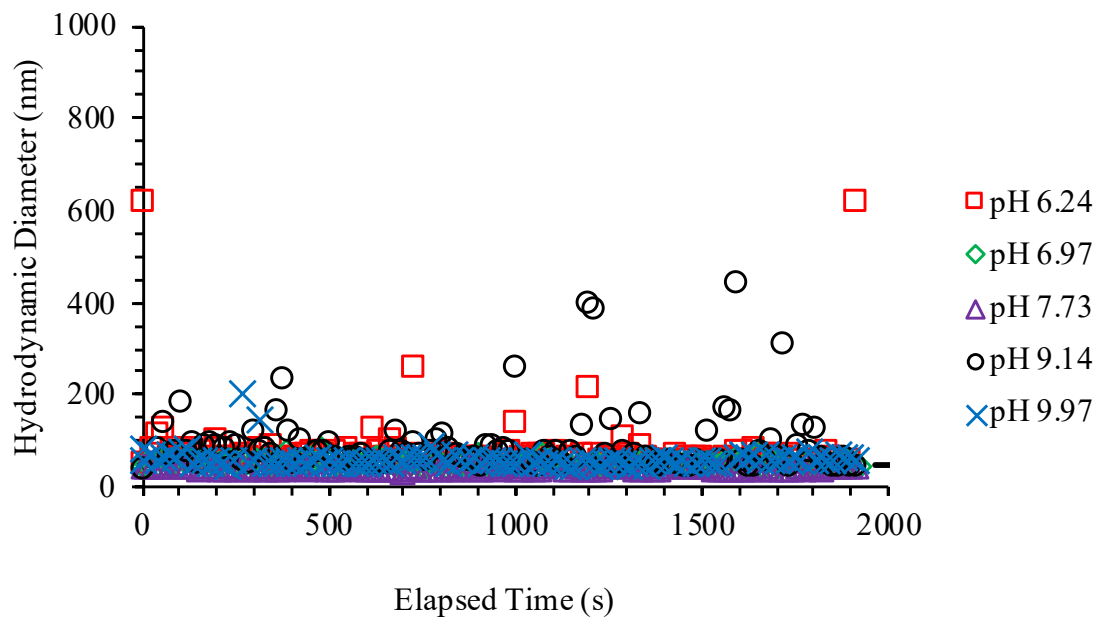


Figure A11h. Intensity-weighted hydrodynamic diameter (D_h) as a function of time for bPEI-AuNPs at varying pH and $[\text{SRNOM}]:[\text{AuNPs}] = 1.7 \text{ mg C} / \text{mg AuNPs}$. $I = 1 \text{ mM KCl}$.

A7. Development of Extent of Aggregation Contour Plots for bPEI-AuNPs

The contour plot depicting the extent of aggregation ($D_{h,30} / D_{h,0}$) as a function of pH and [SRNOM]:[AuNPs] (Figure 2.4 in main text) was created by applying a combination of extrapolation and interpolation techniques to the numerous TR-DLS datasets. Using the procedures outlined in the main text, the value of $D_{h,30} / D_{h,0}$ was determined for each TR-DLS measurement, representing a distinct pH and [SRNOM]:[AuNPs] combination. The results from these calculations are shown by the white markers in Figure A12.

To perform the interpolation/extrapolation analysis, a grid was created that was comprised of grid cells at 0.25 pH unit increments and 0.125 [SRNOM]:[AuNPs] increments, creating a total of 336 grid cells (24 x 14). Using Delaunay triangulation, the value of $D_{h,30} / D_{h,0}$ was determined at each grid cell via a combination natural-neighbor interpolation (for grid cells falling between existing data points) and nearest-neighbor extrapolation (for grid cells beyond the extent of the existing data points).

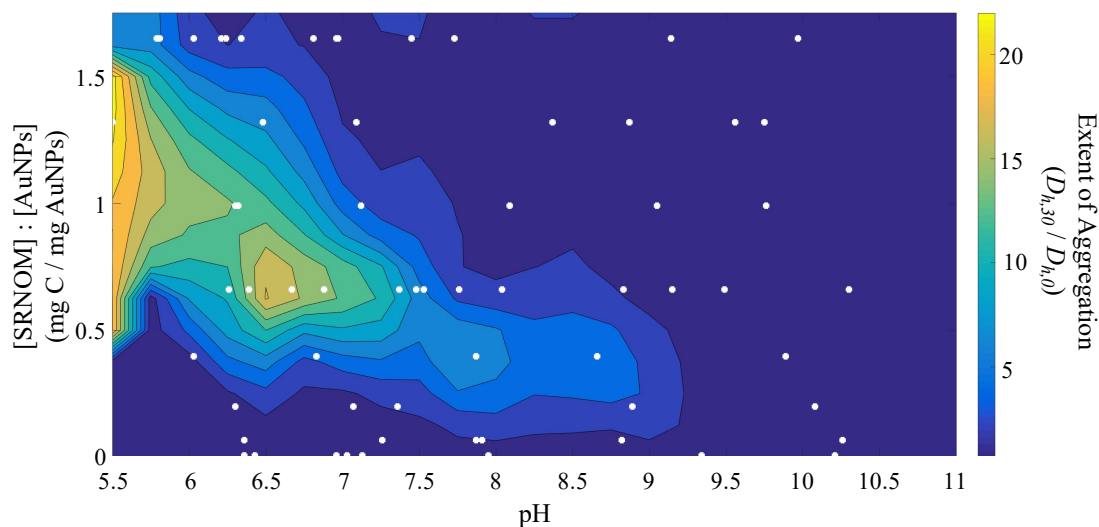


Figure A12. Extent of aggregation ($D_{h,30} / D_{h,0}$) for the bPEI-AuNPs as a function of pH and [SRNOM]:[AuNPs] in the presence of 1 mM KCl. Individual points represent the conditions (pH and [SRNOM]:[AuNPs]) for each TR-DLS measurement sequences used to generate contour plot.

A8. Assessment of bPEI-AuNP Destabilization Mechanisms

To determine whether or not adsorption and charge neutralization versus adsorption and interparticle bridging was the dominant mechanism resulting in the destabilization of the bPEI-AuNPs, an evaluation was performed that combined the EPM titrations with the TR-DLS measurements. Using the combination of pH and [SRNOM]:[AuNPs] that resulted in charge neutralization (Figure 2.3 in main text), these data points were plotted on the contour plots depicting the change in the initial rate of aggregation (dD_h/dt) and the extent of aggregation ($D_{h,30}/D_{h,0}$) as a function of pH and [SRNOM]:[AuNPs]. Using these data points, a linear regression ($R^2 = 0.92$) was performed to identify how the point of adsorption and charge neutralization changes in response to variations in pH and [SRNOM]:[AuNPs]. This regression, which approximates where adsorption and charge neutralization is expected, indicates that the highest values for dD_h/dt and $D_{h,30}/D_{h,0}$ both occur at conditions where the SRNOM-decorated bPEI-AuNPs have an overall negative surface charge (i.e., at pH and [SRNOM]:[AuNPs] that were found to have a negative surface charge per Figure 2.3 in the main text). As the maximum values for dD_h/dt and $D_{h,30}/D_{h,0}$ do not coincide with the charge neutralization region, the results indicate that adsorption and interparticle bridging is the dominant mechanism destabilizing the bPEI-AuNPs.

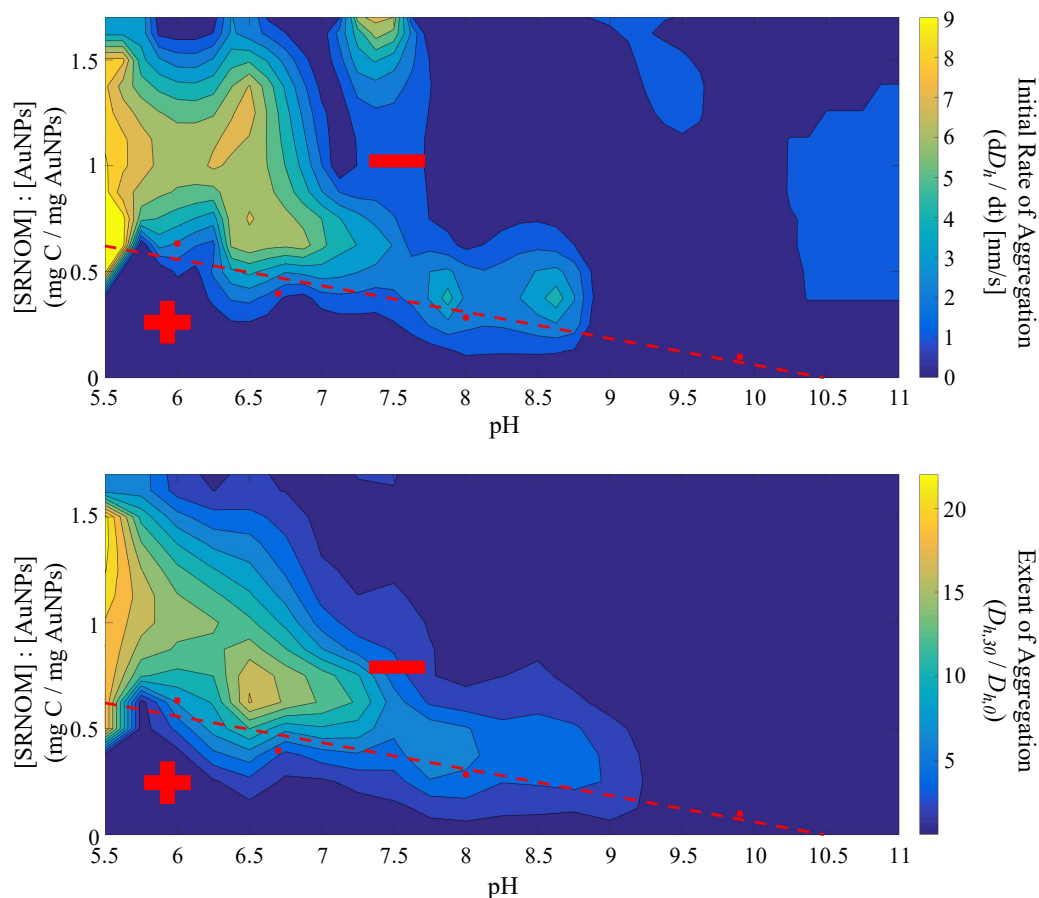


Figure A13. Initial aggregation rate (dD_h/dt ; top) and extent of aggregation ($D_{h,30}/D_{h,0}$; bottom) for bPEI-AuNPs in the presence of 1 mM KCl as a function of both pH and the ratio of [SRNOM]:[AuNPs]. Data points represent combination of pH and [SRNOM]:[AuNPs] where charge neutralization occurs (Figure 2.3 in main text).

A9. SRNOM Control Study

To verify that aggregation observed via TR-DLS was attributable to ENM-ENM aggregation (via the various processes discussed in the main text) and not NOM-NOM interaction, a control study was performed. In this study, 0.66 mg C/L SRNOM was mixed with standard synthetic hard freshwater (*i.e.*, a mixture of monovalent and divalent electrolytes) at relevant pH and then monitored via TR-DLS for approximately 30 minutes. As is evidenced in Figure A14, no significant aggregation occurred ($D_{h,0} = D_{h,30}$), indicating that NOM-NOM aggregates are not forming. Thus, any changes in D_h with time during the TR-DLS testing for each AuNP type can be attributed to ENM-ENM aggregation.

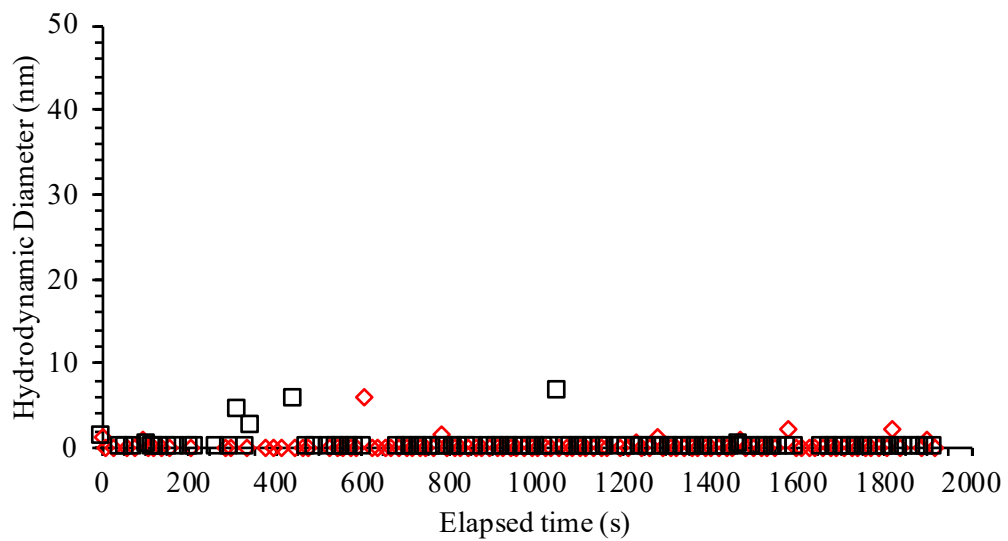


Figure A14. Intensity-weighted hydrodynamic diameter (D_h) as a function of time for 0.66 mg C/L SRNOM in standard synthetic hard freshwater ($I \approx 0.02\text{M}$) at (◇) pH 8.0 and (□) pH 8.4.

B. SUPPLEMENTARY INFORMATION – SECOND MANUSCRIPT

B1. Intensity- vs. Number-Weighted Hydrodynamic Diameter

Inspection of the multi-modal size distribution (MSD) generated during the initial sizing of the model engineered nanoparticles (ENPs) indicates the presence of few, small aggregates and/or particle contaminants in the samples. As noted in Table B1, intensity-weighted hydrodynamic diameter (D_h) reported by the manufacturer was generally consistent with the ‘initial peak’ calculated by the MSD analysis (i.e., the peak expected to be representative of the model ENPs). Likewise, the number-weighted D_h measured for the entire sample (also reported in Table B1) was similar to the intensity-weighted, ‘initial peak’ D_h . Overall, these various measurements indicate that the primary particles were in the range of $\approx 20 - 30$ nm, which is within expectations given the engineered surface coatings possessed by the model ENPs.

Table B1. Manufacturer reported intensity-weighted D_h and ‘as-received’ intensity- and number-weighted D_h of model ENPs.

Surface Coating	Intensity-Weighted D_h (nm)		Number-Weighted D_h (nm)
	Manufacturer-Reported	MSD Initial Peak	
2 kDa PEG	N/A	20.3 ± 10.4	19.8 ± 10.2
3 kDa PEG-COOH	35	29.1 ± 12.4	22.5 ± 13.8
3 kDa PEG-Amine	31	32.0 ± 7.7	31.0 ± 7.4
25 kDa bPEI	47.6	15.1 ± 42.6	14.1 ± 40.7
Citrate	18	20.4 ± 3.2	8.0 ± 9.2

Error bars indicate $\pm 95\%$ confidence interval; (PEG) $n = 4$; (PEG-COOH) $n = 7$; (PEG-Amine) $n = 7$; (bPEI) $n = 2$; (Cit) $n = 4$.

B2. Electrophoretic Mobility/Zeta Potential of Model Engineered Nanoparticles

The electrophoretic mobility (EPM) of the model ENPs were measured in pH-adjusted 1 mM KCl at 10 mg Au/L (Table B2) according to the procedures detailed in Surette and Nason (2016).

Table B2. Electrophoretic mobility (EPM) of model ENPs.

Surface Coating	Electrophoretic Mobility ([$\mu\text{m}/\text{S}$] / [V/cm])
2 kDa PEG	-1.22 ± 0.2 (pH 6.8 ± 0.03)
3 kDa PEG-COOH	-1.23 ± 0.2 (pH 7.1 ± 0.1)
3 kDa PEG-Amine	-0.71 ± 0.1 (pH 7.0 ± 0.1)
25 kDa bPEI	1.20 ± 0.1 (pH 6.8 ± 0.1)
Citrate	-2.26 ± 0.2 (pH 7.4 ± 0.1)

Error bars indicate \pm 95% confidence interval ($n = 15$).

The measured EPM (μ_E) were then converted to zeta potential (ζ) according to Henry (1931) with the correction $f_1(\kappa a)$ applied according to Ohshima (1994), resulting in the following equation:

$$\zeta = \frac{3\mu_E\eta}{2\epsilon_w f_1(\kappa a)} = \frac{3\mu_E\eta}{2\epsilon_w \left(1 + \frac{1}{2\left[1 + \frac{\delta}{\kappa a}\right]^3}\right)} \quad (\text{B1})$$

Where:

$$\delta = \frac{2.5}{1 + 2e^{-\kappa a}} \quad (\text{B2})$$

The definition of the variables in Equations B1 and B2, along with their corresponding values, are shown in Table B3. The calculated value of ζ for each model ENP is shown in the main text (Table 3.1).

Table B3. Inputs used to calculate ζ from μ_E .

Input	Value	Source
Permittivity in Water (ϵ_w)	$6.95 \times 10^{-10} \text{ C}^2/\text{J}\cdot\text{m}$	Known – H ₂ O
Medium Dynamic Viscosity (η)	$1 \times 10^{-3} \text{ N}\cdot\text{s}/\text{m}^2$	Known – H ₂ O
Ohshima Fitting Parameter (δ)	1.2 – 1.3	Hunter (2001)
Inverse Debye Length (κ)	0.104 nm^{-1}	Calculated per Benjamin & Lawler (2013)
Particle Radius (a)	5.25 – 7.5 nm	Measured (Table 3.1)

All values at 25 °C.

B3. River Water Characteristics

Samples of the Willamette River water (WRW) obtained on June 30, 2017 were characterized according to the methods described in the American Water Works Association (AWWA) *Standard Methods for the Examination of Water and Wastewater, 22nd Edition* (American Public Health Association, 2012). All analyses were performed in triplicate and were completed within 21-days of sample collection according to their method-specific holding times. All samples that were collected for analysis of the dissolved fraction were filtered within 3 hours after collection. Samples that were collected for total metals analysis were acid-preserved immediately upon collection. Samples that were collected for dissolved metals analysis were first filtered (using pre-washed filters) and then acid-preserved immediately following filtration. A summary of the results and the associated *Standard Methods* are provided in Table B4.

The particle size distribution (PSD) of the background natural colloids was determined via Coulter Counter according to Method 2560-B. Three separate samples were analyzed in triplicate ($n = 9$), with all runs performed at 5% v/v raw WRW dispersed in 0.45 μm filtered ISOTON II® (Beckman Coulter) as the background electrolyte solution. The Coulter Counter was operated in total-count mode ($\geq 10,000$ total counts) using a 30 μm aperture with the current at $-400 \mu\text{A}$, flow at 3.5 $\mu\text{L}/\text{s}$, gain at 8, and resistivity at 54.4 k Ω . The detection range was between 0.746 – 30 μm (lower- and upper-limits, respectively). The

PSD (Figure B1) was generated by averaging the number of particles within each size ‘bin’ across the replicate measurements.

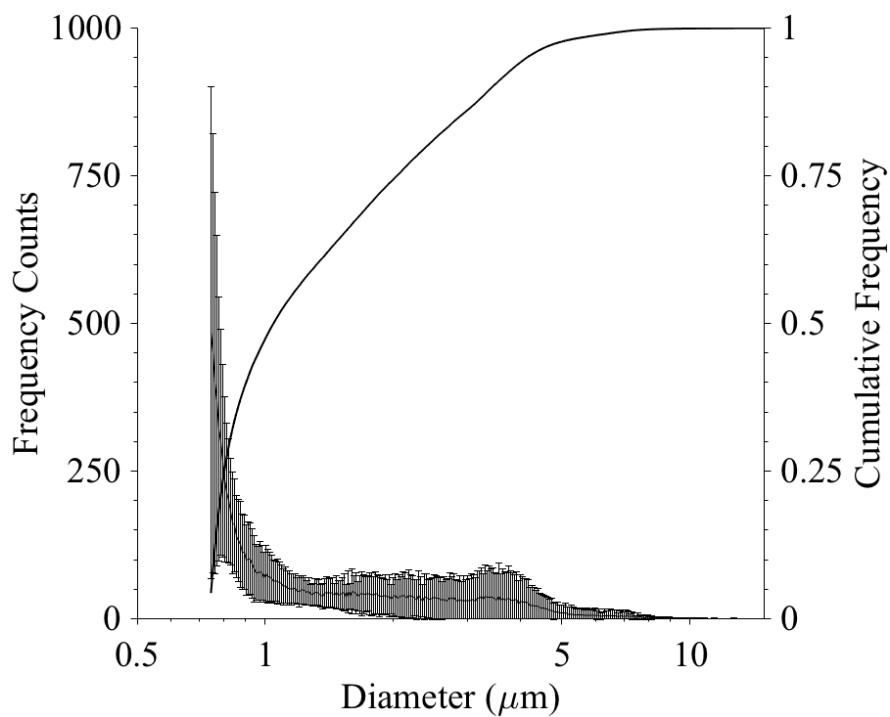


Figure B1: Particle size distribution of natural colloids in raw WRW measured via Coulter Counter. Error bars indicate $\pm 95\%$ confidence interval ($n = 9$).

Table B4. Summary of Willamette River water quality parameters/characteristics.

Parameter	Value	Unit	Method
Total Organic Carbon (TOC)	0.80 ± 0.0	mg C/L	Method 5310-B
Dissolved Organic Carbon (DOC)	0.83 ± 0.1	mg C/L	
<u>Dissolved Cations:</u>			
Ca ²⁺	4.85 ± 0.43	mg/L	Method 3125
Mg ²⁺	1.58 ± 0.38	mg/L	
Na ⁺	4.04 ± 0.13	mg/L	
K ⁺	0.63 ± 0.23	mg/L	
Fe ³⁺	N/D	mg/L	
<u>Dissolved Anions:</u>			
F ⁻	N/D	mg/L	Method 4110-C
Cl ⁻	1.83 ± 0.04	mg/L	
NO ₂ ⁻	N/D	mg/L	
NO ₃ ⁻	0.51 ± 0.0	mg/L	
SO ₄ ²⁻	2.71 ± 0.01	mg/L	
pH	7.9 ± 0.10		Probe Measurement
Total Suspended Solids (TSS)	3.9 ± 0.4	mg/L	Method 2540-D
Total Alkalinity	25.0	mg/L as CaCO ₃	Method 2320
Total Hardness	18.6	mg/L as CaCO ₃	Method 2340-B

Error bars indicate ± one standard deviation on the mean ($n = 3$).

B4. Filter Washing Procedure

To prepare the filtered WRW, the procedures recommended by Karanfil et al. (2003) were followed. Prior to use, the filters were washed with approximately 1L (0.45 µm PES filters) or 0.5 L (0.02 µm syringe filters) of 18.2 MΩ-cm distilled, deionized (DDI) water (EGLA Purelab). After washing and upon initiation of sample filtration, the first 50 mL of the filtrate was discarded. This process was repeated at each sequential filtration stage (i.e., decreasing pore size).

To verify whether organics were leached from the filter material, the organic carbon (OC) concentration was measured at three points along the sequential filtration steps. The total organic carbon (TOC) was measured for the raw WRW to provide a baseline OC

concentration. Samples were then collected and analyzed following 0.45 μm filtration (operationally defined as DOC) and again following the 0.02 μm filtration.

The results, summarized in Table B5, show that there was no statistically significant difference in the measured OC concentration following each filtration step (unfiltered to 0.45 μm : paired t -test(1) = 4.25, p = 0.15; 0.45 μm to 0.02 μm : paired t -test(1), = 2.32 p = 0.26; unfiltered to 0.02 μm : paired t -test(2) = 4.39, p = 0.05).

Table B5. Measured organic carbon concentration following each filtration step.

Parameter	Value	
Total Organic Carbon (TOC)	0.80 \pm 0.01	mg C/L
Dissolved Organic Carbon – 0.45 μm Filtration	0.83 \pm 0.05	mg C/L
Dissolved Organic Carbon – 0.02 μm Filtration	0.95 \pm 0.15	mg C/L

Error bars indicate \pm 95% confidence interval ($n = 2 - 3$).

B5. Calculation of Average Shear Rate

The average shear-rate was calculated according to the equations provided in Croughan et al. (1987), which are summarized below, and the inputs provided in Table B6.

$$G = \frac{112.8Nr_i^{1.8}(r_t^{0.2}-r_i^{0.2})(r_c/r_i)^{1.8}}{r_t^2-r_i^2} \quad (\text{B3})$$

$$\frac{r_c}{r_i} = \frac{Re}{(1000+1.6Re)} \quad (\text{B4})$$

$$Re = \frac{ND_i^2\rho}{\mu} \quad (\text{B5})$$

Table B6. Inputs used to calculate the average shear rate (G).

Parameter	Value	Units
Impeller Speed (N)	400	rpm
Impeller Radius (r_i)	11	mm
Impeller Diameter (D_i)	22	mm
Mixing Vessel Radius (r_v)	17.5	mm
Radius of Forced Vortex Zone (r_c)	5.9	mm
Medium Dynamic Viscosity (μ)	0.0089	g/cm-s
Medium Density (ρ)	0.997	g/cm ³

B7. Centrifugation Testing – Removal Natural Colloids

The intent of this test was to optimize the removal of the background natural colloids (NCs) within the river water sample (as well as any attached model ENPs, when present), while minimizing the removal of any unaggregated model ENPs (tested separately; details below).

1. Three 15-mL polypropylene centrifugation vials (Falcon™, BD Biosciences) were each filled with 6 mL of raw WRW.
2. The triplicate samples were then centrifuged at 3,500 rpm ($\approx 2,200\times g$ RCF) for various durations—2, 5, and 10 minutes.
3. After centrifugation, 3 mL of the supernatant was removed and analyzed via dynamic light scattering (DLS) via 3 measurement runs, each 3 minutes long to measure the post-centrifugation z -average hydrodynamic diameter (D_h).

Using the medium density ($\rho = 0.998$ g/cm³), viscosity ($\mu = 0.01$ g/cm-s), and an assumed value for the density of the NCs ($\rho_{NC} = 2.65$ g/cm³) in combination with the experimental conditions (i.e., centrifugation speed/duration), a theoretical particle size threshold was established. For the given system at 3,500 rpm ($\approx 2,200\times g$ RCF) and 5 minutes centrifugation, NCs with $D_h \geq \approx 300$ nm should be removed. The results of the post-

centrifugation D_h measurements obtained via DLS, provided in Table B7, closely match the predicted particle size threshold.

Table B7. Measurement of D_h of the background natural colloids following centrifugation.

Duration of Centrifugation	Post-Centrifugation (D_h) (nm)
2 Minutes	313.5 ± 17.2
5 Minutes	303.3 ± 28.3
10 Minutes	252.9 ± 16.9

Error bars indicate \pm one standard deviation on the mean ($n = 3$).

The gauge the extent of NC removal via centrifugation, the turbidity of the unaltered WRW was measured before and after centrifugation (at 3,500 rpm for 2 minutes). The results, shown in Table B8, indicate the turbidity decreased by $\approx 66\%$, demonstrating that a fraction of the background NCs remained in suspension following centrifugation.

Table B8. Pre- and post-centrifugation turbidity of unaltered WRW.

Sample	Turbidity (NTU)
Pre-Centrifugation	3.41 ± 0.69
Post-Centrifugation	1.17 ± 0.25

Error bars indicate \pm one standard deviation on the mean ($n = 3$).

To extend this analysis further, we applied the Random Sequential Adsorption (RSA) model detailed by Sadowska et al. (2014) to determine if very small NCs (i.e. $d_{NC} < 300$ nm) that had heteroaggregated with the model ENPs could remain in suspension following centrifugation. To accomplish this, we calculated the maximum fractional surface coverage (θ_{max}) of a model NC that could be “occupied” by model ENPs. From this, we estimated the total number of model ENPs that could attach to a single model NC and estimated the spherical-equivalent density and size of the ENP-NC heteroaggregate. We then determined whether such an ENP-NC heteroaggregate would be removed via centrifugation at the

speed and duration used in our experimental method (i.e., 3,500 rpm for 2 minutes). There are a number of assumptions that are required to perform this analysis. For the model NC, we assume it is a monodisperse spherical collector with the density of SiO₂ ($\rho = 2.65 \text{ g/cm}^3$). Furthermore, we assume that the model ENPs are present on the model NC at θ_{max} . Although θ_{max} is calculated by incorporating electrostatic interactions between adjacent model ENPs, it ignores steric interactions that are known to be occurring.

The results indicate that a model NC covered with model ENPs to the extent estimated by θ_{max} would remain in suspension following centrifugation up to $d_{NC} \leq 280 \text{ nm}$. This cut-off is slightly lower than that estimated previously. While confirming that this phenomena is possible within our experimental system, the impacts on our experimental results are much harder to estimate. Furthermore, this analysis represents a worst-case scenario by ignoring the presence of large NCs (i.e., $d_{NC} > \approx 300 \text{ nm}$), assuming that homoaggregation does not occur (i.e., $\alpha_{homo} = 0$), ignoring particle transport processes (β), and assuming that $\alpha_{hetero} = 1.0$.

B8. Centrifugation Testing – Removal of AuNPs

The intent of this test was to assess and quantify the losses of the model ENPs that may be attributed to the centrifugation process. Based upon previous testing, each model ENP was known to be stable when dispersed in 0.02 μm filtered 18.2 M Ω -cm distilled, deionized water (DDI; EGLA Purelab). Thus, following dispersion into DDI and following centrifugation, any difference in the AuNP concentration before and after centrifugation could be quantified and attributed to loss during the centrifugation process. A preliminary test was first performed at 3,500 rpm ($\approx 2,200\times\text{g RCF}$) for 5 minutes using the following procedure.

1. Five 15-mL polypropylene centrifugation vials (Falcon™, BD Biosciences) were each filled with 7.2 mL of 0.02 μm filtered DDI and well-mixed with 0.8 mL of a given model ENP type ($C_{NP} = 5 \text{ mg/L}$). One replicate for each model ENP type was prepared.

2. Prior to centrifugation, 3 mL was removed from each sample, transferred to a quartz cuvette, and analyzed via UV-Vis at $\lambda = 520$ nm to measure the pre-centrifugation concentration.
3. The remaining 5 mL was centrifuged at 3,500 rpm ($\approx 2,200\times$ g RCF) for 5 minutes.
4. After centrifugation, the top 3 mL was removed, transferred to a quartz cuvette, and analyzed via UV-Vis at $\lambda = 520$ nm to measure the post-centrifugation absorbance.

The results of the preliminary test are provided in Table B9. Based upon the results, it was decided that a shorter duration centrifugation time should be tested to see if the percent loss could be reduced. The same approach detailed above was followed, except that triplicate samples of each model ENP were prepared and were centrifuged at 3,500 rpm ($\approx 2,200\times$ g RCF) for 2 minutes.

Table B9. Measurement of AuNP concentration before and after centrifugation (5-minute duration).

Model ENP	Pre-Centrifugation C_{NP} (mg/L)	Post-Centrifugation C_{NP} (mg/L)	Percent Change
bPEI	4.81	4.58	-4.7%
Cit	4.37	3.12	-28.6%
PEG-COOH	4.11	2.81	-31.7%
PEG-Amine	5.05	4.63	-8.2%
PEG	4.98	1.66	-66.7%

The results for the additional testing, shown in Table B10, indicate that for all model ENPs tested, the losses due to centrifugation were reduced when centrifuging for 2 minutes versus 5 minutes (Table B9). The combination of 3,500 rpm ($\approx 2,200\times$ g RCF) for 2 minutes was selected for use in the batch experiments, based upon these results and the results indicating only a minimal decrease in the size of NCs removed (Table B7) using the shorter centrifugation duration.

Even when using the shorter centrifugation duration, there were still measurable losses for the Cit-, PEG-COOH-, and PEG-AuNPs. To account for this, the AuNP concentrations measured via ICP-OES during the batch experiments were increased by multiplying the ‘as-measured/undiluted’ Au concentration by a correction factor (Cit: 1.085; PEG-COOH: 1.206; PEG: 1.190).

Table B10. Measurement of AuNP concentration before and after centrifugation (2-minute duration).

Model ENP	Pre-Centrifugation C_{NP} (mg/L) ^a	Post-Centrifugation C_{NP} (mg/L) ^a	Percent Change
bPEI	4.8 ± 0.1	4.9 ± 0.1	+2.3%
Cit	3.9 ± 0.2	3.5 ± 0.2	-8.5%
PEG-COOH	3.8 ± 0.1	3.0 ± 0.1	-20.6%
PEG-Amine	5.0 ± 0.1	5.0 ± 0.1	<1.0%
PEG	4.8 ± 0.1	3.9 ± 0.1	-19.0%

Error bars indicate ± one standard deviation on the mean ($n = 3$).

B9. Vial Interactions – Loss of AuNPs to Centrifugation Vials

The results from the centrifugation testing (Table B10) indicated that significant losses were still observed for the PEG-COOH- and PEG-AuNPs (-20.6% and -19.0%, respectively), even at the shorter centrifugation duration. Based upon this, it was decided to further explore these losses to determine if they were associated with interactions between the model ENPs and the centrifugation vials. The following procedure was applied:

1. Six 15-mL polypropylene centrifugation vials (Falcon™, BD Biosciences) were each filled with 8.1 mL of 0.02 μm filtered DDI and well-mixed with 0.9 mL of a given model ENP type ($C_{NP} = 5$ mg/L). Triplicate samples for PEG-COOH- and PEG-AuNPs were prepared.
2. Immediately upon combination, 3 mL was removed from each sample, transferred to a quartz cuvette, and analyzed via UV-Vis at $\lambda = 520$ nm to measure the absorbance.

- Additional samples were removed and analyzed at $t = 10$ and 30 minutes from each replicate and analyzed according to the same procedures.

The results, shown in Figure B2, indicate that no statistically significant difference in the absorbance occurred over the 30-minute period (PEG-COOH: paired t -test(2) = 0.74 $p = 0.54$; PEG: paired t -test(2) = 3.01 $p = 0.09$). These results show that the losses noted during the centrifugation testing (Table B10) were associated with the centrifugation process.

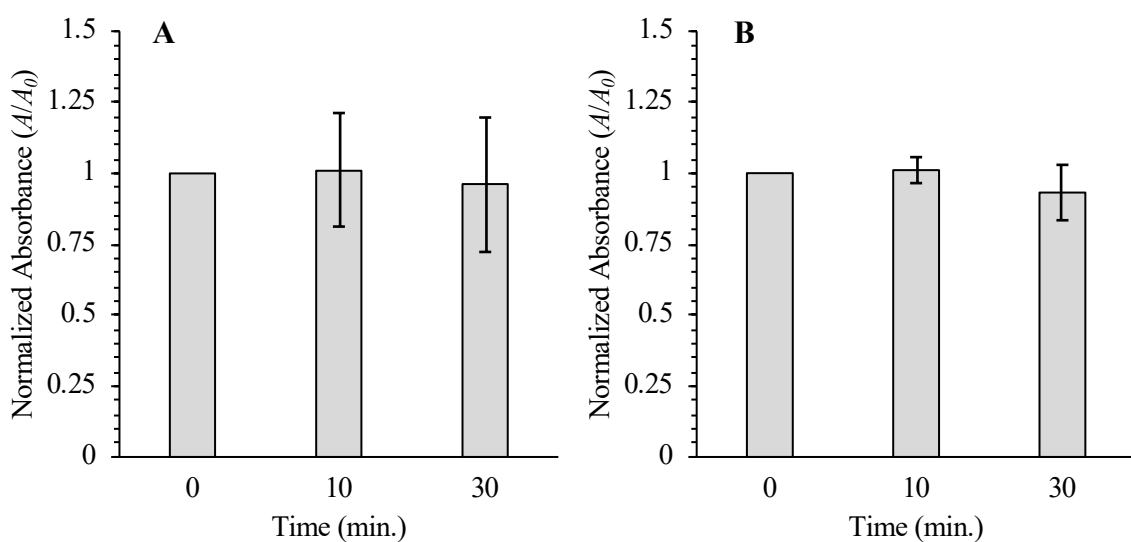


Figure B2: Normalized absorbance (A/A_0) over time for (a) PEG-COOH- and (b) PEG-AuNPs. Error bars indicate $\pm 95\%$ confidence interval ($n = 3$).

B10. Digestion Technique

Once all sample aliquots were generated for a given batch ($n = 42$ per batch), each aliquot was acid-digested according to the following procedure:

- Each aliquot, contained within a perfluoroalkoxy alkane (PFA) vial, was placed on a heat plate, uncapped, and heated to 200 °C to evaporate off the water.
- Once a small amount of residue remained ($\approx 25 \mu\text{L}$), 2.5 mL of freshly-prepared *aqua regia* (3:1 ultrapure HCl:HNO₃) was added to each PFA vial and heated at 200 °C to evaporate off the *aqua regia*.

3. When a small drop of aqua regia/residue remained, the PFA vials were removed from the heat plate and 1 mL of 3+1 *aqua regia* (3:1 DDI:*aqua regia*) was added to each PFA vial. The vials were then allowed to cool to room temperature.
4. After cooling to room temperature, 1 mL from each PFA vial was transferred, via calibrated pipette, to a 50-mL polypropylene centrifuge tube (Falcon™, BD Biosciences) containing 10 mL of DDI. After this first transfer, a series of five additional wash/transfer steps were performed as follows: 1 mL of 3+1 *aqua regia* (3:1 DDI:*aqua regia*) was added to each PFA vial, being careful to rinse down the sidewalls of the vials, and then 1 mL from each PFA vial was transferred, via calibrated pipette, to their respective 50-mL polypropylene centrifuge tube.
5. The total, final volume of each polypropylene vial was recorded and the tubes were stored at 4 °C until ready for analysis via ICP-OES.

B11. Digestion Technique – Spike/Recovery Testing

To verify that the digestion technique resulted in adequate recovery (i.e., >90%) of the model ENPs upon their introduction to the river water, a spike/recovery test was performed. The intent of the spike/recovery test was to mimic the experimental procedure used in the batch experiments but generate a ‘worst-case’ scenario where no model ENPs are removed via centrifugation following interactions with the natural colloids. To do this, the model ENPs were spiked into the samples following the centrifugation step.

1. Six 15-mL polypropylene centrifugation vials (Falcon™, BD Biosciences) were each filled with 5 mL of raw WRW and centrifuged at 3,500 rpm ($\approx 2,200\times g$ RCF) for 2 minutes.
2. Immediately following sample centrifugation, a 4-mL sample of the supernatant was collected from each 15-mL vial and transferred to a separate 7-mL PFA vial. Each sample was preserved via addition of 10 μ L of concentrated (70% w/w) ultra-pure HNO₃.
3. Two sets of samples, prepared in triplicate, were created as follows:

4. Three of the PFA vials were each spiked PEG-Amine-AuNPs to $C_{NP} = 500 \mu\text{g/L}$ by removing and discarding 0.04 mL of the preserved river water and then replacing this volume with 0.04 mL of the model ENP.
5. The remaining three PFA vials were designated as a background sample to measure the Au concentration within the WRW.
6. All six PFA vials were then acid digested according to the procedure outlined above and analyzed via ICP-OES.
7. Following analysis, the percent recovery of each vial spiked with AuNPs was calculated, accounting for the Au mass present within the WRW.

As was expected, the background Au concentration within the WRW was below the analytical detection limit ($< 2 \mu\text{g/L}$). Therefore, the Au concentration measured in the samples collected during the control testing, as well as the batch experiments, can be solely attributed to the model ENPs introduced into the system. The results for the sample spiked with the AuNPs, summarized in Table B11, indicate good recovery was obtained ($103\% \pm 11\%$). Thus, the digestion technique was considered adequate to digest the model ENPs within the samples collected during the batch experiments.

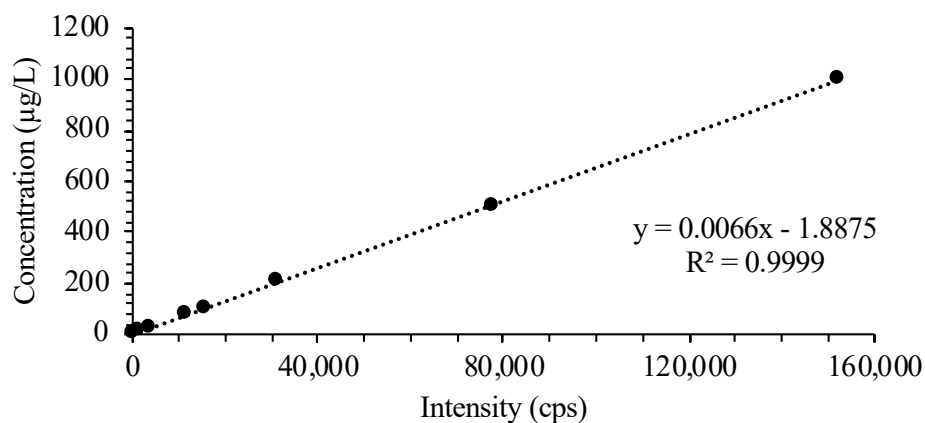


Figure B3: Standard curve generated during spike/recovery testing.

Table B11. Measured AuNP concentration and percent recovery.

Sample	Undiluted Au Concentration ($\mu\text{g/L}$)	Percent Recovery
Spiked #1	573.13	114.6%
Spiked #2	473.09	94.6%
Spiked #3	495.30	99.1%
Average \pm S.D.	513.84 \pm 52.53	103% \pm 11%

B13. Synthetic Willamette River Water

The synthetic WRW was made by dissolving the salts listed in Table B12 into 1 L of 18.2 M Ω -cm distilled, deionized water (DDI; EGLA Purelab). Upon mixing, the synthetic WRW was adjusted to pH 7.69 and stored at 4 °C in Nalgene® containers. Prior to use, the synthetic WRW was filtered through a 0.02 μm syringe filter (Anotop®, Whatman). After 24-hours following preparation, the pH of the synthetic WRW was measured again and found to have stabilized at pH 7.48.

Table B12. Composition of synthetic Willamette River water.

Compound	Mass Added to 1 L (mg)	Final Concentration (mM)
MgCl ₂ ·6H ₂ O	6.7	0.033
CaCO ₃	13.1	0.131
MgSO ₄	3.6	0.030
KNO ₃	0.8	0.0079

B14. Time-Resolved Dynamic Light Scattering (TR-DLS) Measurements

The results of duplicate TR-DLS measurements for each model ENP are shown in Figure B4. Initial aggregation rates ($dD_h/dt|_{t \rightarrow 0}$) were calculated from the TR-DLS data according to the method presented by Chen et al. (2010). Briefly, the initial aggregation rate was calculated from the slope of a linear regression fitted to the data from $D_{h,initial}$ to $1.3D_{h,initial}$, encompassing the region dominated by doublet formation. The slope calculated via the linear regression was then evaluated to determine if it was statistically different than zero (Students t -test, $\alpha = 0.05$).

For the PEG- and PEG-COOH-AuNPs, the initial aggregation rates were not statistically different than zero (PEG: $t\text{-test}(50) = -0.80$, $p = 0.43$ and $t\text{-test}(106) = -1.13$, $p = 0.26$; PEG-COOH: $t\text{-test}(115) = 1.65$, $p = 0.10$ and $t\text{-test}(54) = 0.05$, $p = 0.96$), thus demonstrating that the PEG- and PEG-COOH-AuNPs were colloiddally stable during the TR-DLS measurement period.

For the PEG-Amine and bPEI-AuNPs, there was a near-instantaneous increase in D_h such that the linear regression would be fit to only two data points. As such, an alternative method was used to calculate $dD_h/dt|_{t \rightarrow 0}$ where the $1.3D_{h,initial}$ criterion was adjusted such that the first data-point after $D_{h,initial}$ was used in-lieu of $D_{h,initial}$ to define the region that was regressed (i.e., $D_{h,initial+1}$ to $1.3D_{h,initial+1}$ instead of $D_{h,initial}$ to $1.3D_{h,initial}$). While the results for the PEG-Amine-AuNPs were both statistically different than zero ($t\text{-test}(9) = 7.29$, $p \ll 0.001$ and $t\text{-test}(9) = 5.98$, $p \ll 0.001$), only one of the linear regression slopes for the bPEI-AuNPs was statistically significant ($t\text{-test}(3) = 2.38$, $p = 0.14$ and $t\text{-test}(2) = 14.84$, $p = 0.04$). This is likely due to the limited amount of data included in the regression and the resulting sensitivity to variability between the D_h measured at each time point. Since the TR-DLS measurement profiles for the bPEI-AuNPs, as well as the PEG-Amine-AuNPs, clearly demonstrate that these model ENPs aggregated, both of the calculated $dD_h/dt|_{t \rightarrow 0}$ were retained to determine the average $dD_h/dt|_{t \rightarrow 0}$.

Finally, the Cit-AuNPs required a combination of the two approaches, as one of the replicate measurements saw a near-instantaneous increase in D_h while the other did not. In both cases, the calculated $dD_h/dt|_{t \rightarrow 0}$ were not statistically different than zero ($t\text{-test}(116) = 1.37$, $p = 0.17$ and $t\text{-test}(9) = 0.62$, $p = 0.55$).

The calculated $dD_h/dt|_{t \rightarrow 0}$ for each model ENP are reported in Table B13.

Table B13. Initial aggregation rates ($dD_h/dt|_{t \rightarrow 0}$) of model ENPs in filtered WRW.

Surface Coating	Average $dD_h/dt _{t \rightarrow 0}$ (nm/s)
PEG-COOH	0.004 ± 0.005
PEG	-0.015 ± 0.008
PEG-Amine	$0.285 \pm 0.008^*$
bPEI	$1.104 \pm 0.180^*$
Cit	0.063 ± 0.080

Error bars indicate \pm one standard deviation ($n = 2$).

* Indicates average $dD_h/dt|_{t \rightarrow 0}$ is statistically different than zero.

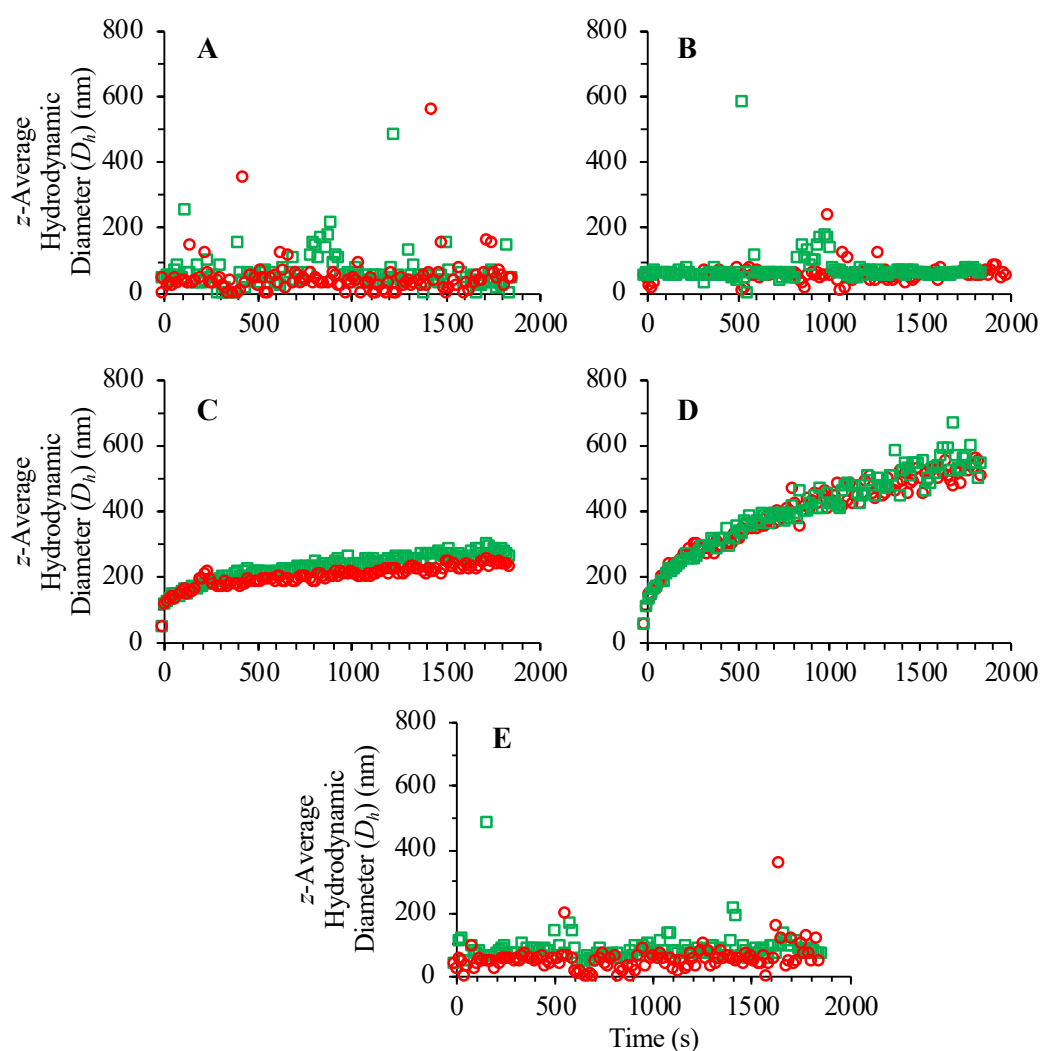


Figure B4. Z-average hydrodynamic diameter (D_h) as a function of time for (a) PEG; (b) PEG-COOH; (c) PEG-Amine; (d) bPEI; and (e) Cit-AuNPs dispersed in filtered WRW.

B15. Modelling of Collision Frequency Functions

In the Rectilinear Model detailed by Benjamin & Lawler (2013), the initial collision frequency between two dissimilar particle types (i.e., heteroaggregation of an ENP with a natural colloid [NC]) can be determined by evaluating the mechanisms producing collisions between them. These mechanisms include Brownian motion ($^{BR}\beta_{NP-NC}$), differential sedimentation ($^{DS}\beta_{NP-NC}$), and fluid shear ($^{SH}\beta_{NP-NC}$). Each of these is determined according to Equations B6 – B8 below:

$$^{BR}\beta_{NP-NC} = \frac{2k_B T}{3\mu} \left[\left(\frac{1}{d_{NP}} + \frac{1}{d_{NC}} \right) (d_{NP} + d_{NC}) \right] \quad (\text{B6})$$

$$^{DS}\beta_{NP-NC} = \frac{\pi}{4} |v_{NP} - v_{NC}| (d_{NP} + d_{NC})^3 \quad (\text{B7})$$

$$^{SH}\beta_{NP-NC} = \frac{G}{6} (d_{NP} + d_{NC})^3 \quad (\text{B8})$$

Where:

$$v_{NP,NC} = \frac{g(\rho_{NP,NC} - \rho_w)(d_{NP,NC})^2}{18\mu} \quad (\text{B9})$$

When the colliding particles are the same type (i.e., homoaggregation of two ENPs), Equations B6 – B8 simplify to:

$$^{BR}\beta_{NP-NP} = \frac{8k_B T}{3\mu} \quad (\text{B10})$$

$$^{SH}\beta_{NP-NP} = \frac{4G}{3} (d_{NP})^3 \quad (\text{B11})$$

Where $^{DS}\beta_{NP-NP} = 0$, as two particles with the same characteristics (e.g., ρ_{NP} and d_{NP}) will have the same settling rates and will not undergo collisions due to differential sedimentation.

Using the inputs shown in Table B14, the collision frequency function for each transport mechanism (i.e., $^{BR}\beta$, $^{DS}\beta$, and $^{SH}\beta$) and type of particle interaction (i.e., homo- and

heteroaggregation) were modelled. For ENP-NC interactions (heteroaggregation), the collision frequency functions were modelled by varying d_{NC} from $1 - 10^4$ nm while fixing d_{NP} at 15 nm (representative of the core diameter measured for the model ENPs). For ENP-ENP interactions (homoaggregation), the collision frequency functions were simplified as only one particle size was necessary to consider (i.e., d_{NP}).

The replicate Coulter Counter measurements performed on the raw WRW indicate an approximate median NC diameter (d_{NC}) of $1.34 \pm 0.8 \mu\text{m}$ (Figure B1). However, considering the size detection limits of the Coulter Counter ($d_{NC} \geq 0.746 \mu\text{m}$) and the trend in the PSD indicating the number frequency rapidly increases as d_{NC} decreases, it is expected that the ‘true’ median value of d_{NC} in the raw WRW is well below the instrument detection limits. This expectation is supported by previous research indicating that the majority of NCs (on a number-weighted basis) will have diameters $\ll 1 \mu\text{m}$.^{11,12} Regardless, for ENP-ENP and ENP-NC interactions with $d_{NC} \leq 5 \mu\text{m}$, Brownian motion ($^{BR}\beta$) is the dominant collision mechanism owing to the small size of the model ENPs (Figure B5).

Table B14. Inputs used to calculate β for each transport mechanism.

Parameter	Value	Units	Source
Boltzmann Constant (k_B)	1.38×10^{-16}	$\text{g cm}^2/\text{s}^2 \text{K}$	Constant
Standard Gravity (g)	9.81	m/s^2	Constant
Density of NC (ρ_{NC})	2.65	g/cm^3	Assumed – SiO ₂
Density of AuNP (ρ_{NP})	19.3	g/cm^3	Assumed – Au
Diameter of NC (d_{NC})	$1 - 10^4$	nm	Assumed
Diameter of AuNP (d_{NP})	15	nm	Measured (TEM)
NC Mass Conc. (C_{NC})	3.9	mg/L	Measured
NP Mass Conc. (C_{NP})	500	$\mu\text{g/L}$	Measured
Temperature (T)	298	K	Measured
Medium Dynamic Viscosity (μ)	0.0089	g/cm-s	Known – H ₂ O
Medium Density (ρ_w)	0.997	g/cm^3	Known – H ₂ O
Time-Averaged Shear Rate (G)	15.6	s^{-1}	Calculated

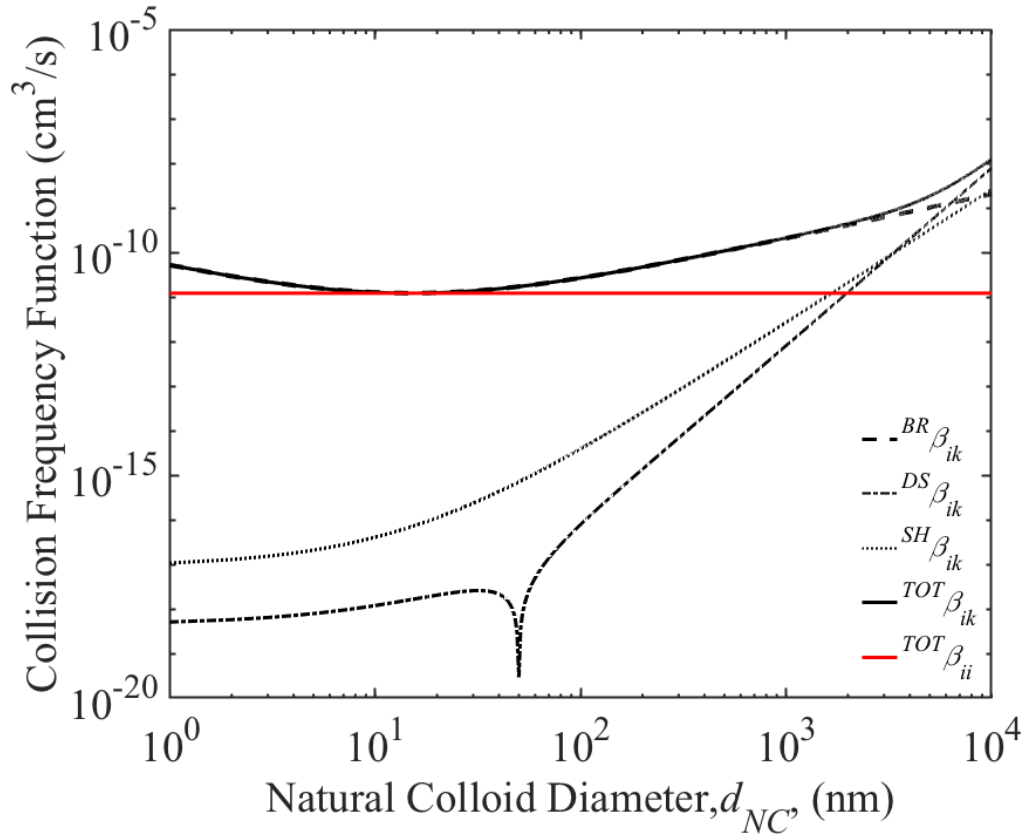


Figure B5. Collision frequency function for each transport mechanism during heteroaggregation (β_{NP-NC}) and the total collision frequency function during (solid black) heteroaggregation ($^{TOT}\beta_{NP-NC}$) and (red) homoaggregation ($^{TOT}\beta_{NP-NP}$).

B16. Modelling of Initial Aggregation Rates

Initial aggregation rates describing the loss of ENPs via aggregation were modelled using the Smoluchowski Aggregation Equation (Equation B12). For a detailed discussion regarding this equation, the reader is referred to Benjamin and Lawler (2013).

$$\frac{dN_k}{dt} = \frac{1}{2} \alpha_{emp} \sum_{\substack{\text{all } i \text{ and } j \\ \text{such that} \\ V_i + V_j = V_k}} ^{TOT} (\alpha_{ij} \beta_{ij}) N_i N_j - \alpha_{emp} N_k \sum_{\text{all } i} ^{TOT} (\alpha_{ik} \beta_{ik}) N_i \quad (\text{B12})$$

Using Equation B12, the initial rate of change in the number concentration of unaggregated ENPs ($dN_{NP}/dt|_{t \rightarrow 0}$) can be modelled. This is accomplished by assuming that ENPs are not formed within the system (i.e., the first set of terms on the right-hand side of Equation B12

is negligible), only collisions from Brownian motion ($^{BR}\beta$) need to be considered since the other transport mechanisms were found to be negligible within the expected range of d_{NC} (Figure B5), and short-range correction factors (Curvilinear Model) for Brownian motion ($^{BR}\alpha$) were included to account for the forces arising as two particles approach one another closely.

From this, Equation B12 can be used to describe the loss of ENPs via homoaggregation with other ENPs or via heteroaggregation with the NCs in the system. The former process is realized by recognizing that at early times (i.e., $t \rightarrow 0$) the ENPs are represented by a single particle size-class, hence $N_i = N_k = N_{NP}$ with $d_i = d_{NP}$ (fixed at 15 nm). The latter process is realized by assuming that all the NCs are represented by a single particle size-class, resulting in two particle size-classes in the system at early times, i.e., $N_i = N_{NC}$ with $d_i = d_{NC}$ (varying from 0.01 – 1 μm) and $N_k = N_{NP}$ with $d_k = d_{NP}$ (fixed at 15 nm).

$$\left(\frac{dN_{NP}}{dt}\right)_{t \rightarrow 0}^{homo} = -\alpha_{homo}^{BR}(\alpha\beta)_{NP-NP}N_{NP}^2 \quad (\text{B13})$$

$$\left(\frac{dN_{NP}}{dt}\right)_{t \rightarrow 0}^{hetero} = -\alpha_{hetero}^{BR}(\alpha\beta)_{NP-NC}N_{NP}N_{NC} \quad (\text{B14})$$

The relative importance of either mechanism can then be assessed across a range of values for α_{hetero} and α_{homo} , as presented in Figure 3.3 in the main text.

B17. Characteristic Time for Homo- and Heteroaggregation

Using the modelled initial aggregation rates ($dN_{NP}/dt|_{t \rightarrow 0}$) for homo- and heteroaggregation, the characteristic time for the loss of the model ENPs via homo- and heteroaggregation ($t_{char,homo}$ and $t_{char,hetero}$, respectively) can be calculated according to Equations B15 and B16:

$$t_{char,homo} = \frac{N_{NP}}{-\left(\frac{dN_{NP}}{dt}\right)_{t \rightarrow 0}_{homo}} = \frac{1}{\alpha_{homo}^{BR(\alpha\beta)_{NP-NP}N_{NP}}} \quad (\text{B15})$$

$$t_{char,hetero} = \frac{N_{NP}}{-\left(\frac{dN_{NP}}{dt}\right)_{t \rightarrow 0}_{hetero}} = \frac{1}{\alpha_{hetero}^{BR(\alpha\beta)_{NP-NC}N_{NC}}} \quad (\text{B16})$$

Using the same inputs presented in Table B14 and discussed in the previous sections, $t_{char,homo}$ and $t_{char,hetero}$ were calculated across a range of d_{NC} and for various values of α_{homo} and α_{hetero} . The results are shown in Figure B6.

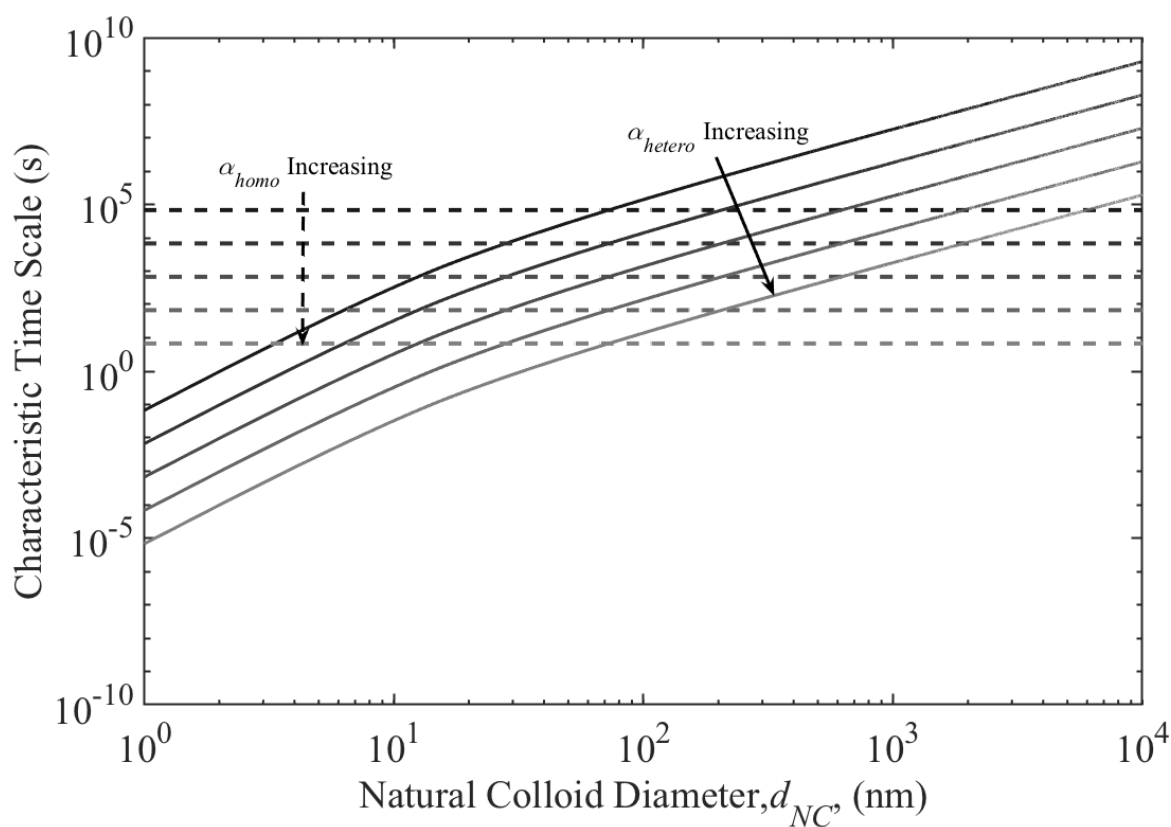


Figure B6. Characteristic time (τ) for (dashed) homoaggregation and (solid) heteroaggregation as a function of d_{NC} , with α_{homo} and α_{hetero} varying between $[10^{-4} - 10^0]$.

B18. References

- 1 Surette, M. C.; Nason, J. A. Effects of surface coating character and interactions with natural organic matter on the colloidal stability of gold nanoparticles. *Environ. Sci. Nano* 2016, **3** (5), 1144–1152.
- 2 Henry, D. C. The cataphoresis of suspended particles. Part I. – The equation of cataphoresis. *Proc. Roy. Soc. A* 1931, **133** (821), 106.
- 3 Ohshima, H. A simple expression for Henry's function for the retardation effect in electrophoresis of spherical colloidal particles. *J. Colloid Interface Sci.* 1994, **11** (1), 269 – 271.
- 4 Hunter, R.J. *Foundations of Colloid Science, 2nd Edition* 2002. Oxford University Press, London, United Kingdom.
- 5 Benjamin, M. M.; Lawler, D.F. *Water Quality Engineering – Physical/Chemical Treatment Processes* 2013. John Wiley & Sons, Inc., Hoboken, New Jersey.
- 6 American Water Works Association (AWWA) *Standard Methods for the Examination of Water and Wastewater, 22nd Edition* 2012. American Public Health Association.
- 7 Karanfil, T.; Erdogan, I.; Schlautman, M. A. Selecting filter membranes DOC and SUVA₂₅₄. *J. Am. Water Work. Assoc.* 2003, **95** (3), 86–100.
- 8 Croughan, M. S.; Hamel, J.-F.; Wang, D. I. C. Hydrodynamic effects on animal cells grown in microcarrier cultures. *Biotechnol. Bioeng.* 1987, **29** (1), 130–141.
- 9 M. Sadowska, Z. Adamczyk, and M. Nattich-Rak, Mechanism of nanoparticle deposition on polystyrene latex particles, *Langmuir*, 2014, **30**, 692-699.
- 10 Chen, K. L.; Smith, B. A.; Ball, W. P.; Fairbrother, D. H. Assessing the colloidal properties of engineered nanoparticles in water: case studies from fullerene C 60 nanoparticles and carbon nanotubes. *Environ. Chem.* 2010, **7** (1), 10.

C. SUPPLEMENTARY INFORMATION – THIRD MANUSCRIPT

C1. Characterization of Pristine Model Engineered Nanoparticles

The manufacturer reported specifications and measured characteristics of the model engineered nanomaterials (ENMs) are provided in Table 4.1 (main text). The values were determined as follows:

Core Diameter (D_c): Manufacturer reported specification. Measured via transmission electron microscopy (TEM) using a JEM-1010 TEM (JEOL).

Intensity-weighted hydrodynamic diameter ($D_{h,initial}$): Measured via dynamic light scattering (DLS) at 1 mg Au/L in 0.02 μm filtered 18.2 M Ω -cm Nanopure water (DDI; Barnstead) using a ZetaSizer Nano ZS (Malvern Panalytical). Each replicate measurement ($n = 34$) was performed for 1-minute.

Electrophoretic mobility (μ_E): Measured at 5 mg Au/L in pH-adjusted (pH 5.3 – 5.6) 1 mM NaCl (prepared in 0.02 μm filtered DDI) using a Folded Capillary Zeta Cell with a ZetaSizer Nano ZS (Malvern Panalytical). Each replicate measurement ($n = 9$) was performed for 30 cycles. Details on the conversion of the measured EPM to modelled zeta potential (ζ) are provided in the next section.

Surface Plasmon Resonance (λ_{SPR}): Measured via ultraviolet-visible light spectroscopy (UV-Vis) at 5 mg Au/L in 0.02 μm filtered DDI using a Cary-60 UV-Vis (Agilent Technologies). Each replicate measurement ($n = 3$) was performed at $\lambda = 400 - 800$ nm at a scan rate of 2 nm/s using a 10 mm light-path Quartz Suprasil[®] micro-cuvette (Hellma Analytics).

C2. Zeta Potential Calculation in Simple Electrolyte Solution (1 mM NaCl)

The measured EPM (μ_E), reported in Table 4.1 (main text), were converted to zeta potential (ζ) according to Henry (1931) with the correction $f_1(\kappa a)$ applied according to Ohshima (1994), resulting in the following equation:

$$\zeta = \frac{3\mu_E\eta}{2\epsilon_w f_1(\kappa a)} = \frac{3\mu_E\eta}{2\epsilon_w \left(1 + \frac{1}{2 \left[1 + \frac{\delta}{\kappa a} \right]^3} \right)} \quad (\text{C1})$$

Where:

$$\delta = \frac{2.5}{1+2e^{-\kappa a}} \quad (\text{C2})$$

The definition of the variables in Equations C1 and C2, along with their corresponding values, are shown in Table C1.

Table C1. Inputs used to calculate ζ from μ_E .

Input	Value ^a	Source
Permittivity in Water (ϵ_w)	$6.95 \times 10^{-10} \text{ C}^2/\text{J}\cdot\text{m}$	Known – H ₂ O
Medium Dynamic Viscosity (η)	$1 \times 10^{-3} \text{ N}\cdot\text{s}/\text{m}^2$	Known – H ₂ O
Ohshima Fitting Parameter (δ)	2 – 2.04	Calculated per Hunter (2001)
Debye Length (κ)	0.104 nm ⁻¹	Calculated per Benjamin & Lawler (2013)
Particle Radius (a)	20 – 21 nm	Measured (Table 4.1)

^a All values at 25 °C.

C3. Removal of Gold Nanoparticles in Unaltered Wastewater Matrices

The removal of the gold nanoparticles (AuNPs) via heteroaggregation with the suspended particulate matter (SPM) in all three unaltered wastewater matrix was verified. Batch experiments were performed by dosing samples ($V_{TOT} = 75 \text{ mL}$) of each unaltered wastewater matrix to $C_{NP} = 1 \text{ mg Au/L}$. Upon dosing, each batch was continuously mixed for ≈ 45 minutes (comparable to the measurement period of the time resolved dynamic light scattering [TR-DLS] experiments), after which the mixing was stopped and a settling period of ≈ 30 minutes was used to remove the bulk of the SPM and any associated ENMs. Then, 15 mL of the supernatant was removed and digested using a combination of H₂O₂ (to remove organics) and fresh *aqua regia* (3:1 ultrapure HCl:HNO₃; to dissolve AuNPs) via microwave digestion. Triplicate samples of the digestate were prepared and analyzed via inductively-coupled plasmas mass spectroscopy (ICP-MS) using a 7500-CE ICP-MS (Agilent Technologies, Inc.) to quantify the concentration of AuNPs remaining in suspension (Figure C1).

Significantly less removal was noted in the influent wastewater matrix relative to that measured in the denitrification and nitrification matrices. This likely reflects the lower number concentration of suspended solids in the influent wastewater compared to the biological treatment stages where suspended solids are both concentrated and created during biological growth. The increased concentration of suspended solids would increase both the aggregation rate and the total surface area for the AuNPs to attach to.

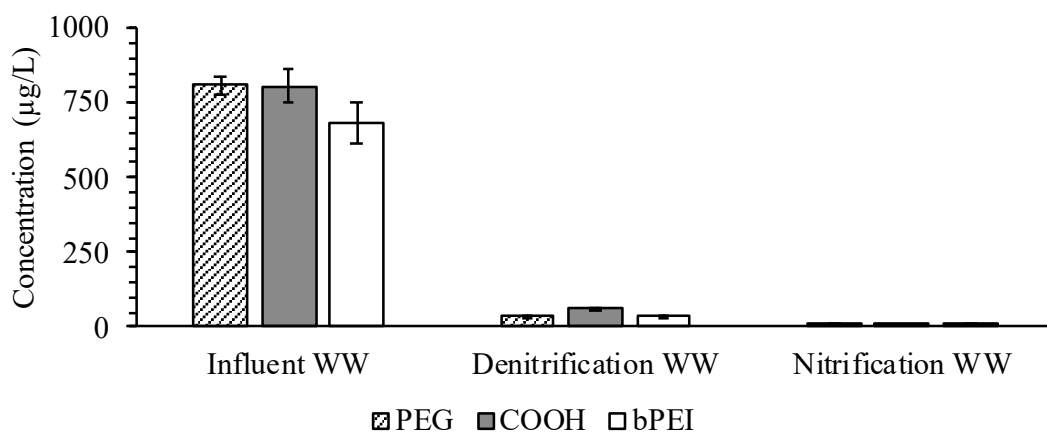


Figure C1: Concentration of each AuNP remaining in suspension in unaltered wastewater matrices after ≈ 45 minutes. Error bars indicate $\pm 95\%$ confidence interval ($n = 3 - 5$).

C4. Properties of Wastewater Matrices

The aquatic chemistry of the influent, denitrification, and nitrification wastewater matrices was measured by collecting a 1L sample from the primary clarifier and activated sludge treatment stage (anoxic and aerobic tanks), respectively, between 9:00-10:00 a.m. The samples were immediately centrifuged at 3,000 rpm ($\approx 1,860g$ RCF) for 30 minutes and the supernatant (≈ 900 mL) was sequentially filtered through $1 \mu\text{m}$ and $0.45 \mu\text{m}$ cellulose-acetate filters using a stainless steel pressure filtration unit (Sartorius). The filtered samples were then analyzed according to the methods described in the American Water Works Association (AWWA) *Standard Methods for the Examination of Water and Wastewater, 22nd Edition* (American Public Health Association, 2012). The results are summarized in Table C2.

Table C2. Characteristics of 0.45 μm -filtered wastewater matrices.

	Influent	Denitrification (Anoxic)	Nitrification (Aerobic)
Conductivity ($\mu\text{S}/\text{cm}$)	1,358	1,182	1,151
Ionic Strength (mM) ^a	21.7	18.9	18.4
pH	8.16	7.65	7.76
Dissolved Organic Carbon (mg/L) ^b	168.0	16.4	45.9
<u>Inorganic Non-Metallic Constituents^c</u>			
NH_4^+ (mg/L as N)	17.3	2.1	16.3
NO_2^- (mg/L as N)	0.25	0.58	0.5
NO_3^- (mg/L as N)	1.4	9.2	<0.2
PO_4^{3-} (mg/L as P)	2.5	1.3	1.2
<u>Metals^d</u>			
Ca^{2+} (mg/L)	94.4	87.8	84.2
Mg^{2+} (mg/L)	10.7	11.2	10.4
K^+ (mg/L)	65.3	78.1	68.7
Na^+ (mg/L)	185.6	195.6	193.3

^a Calculated using $I = 1.6 \times 10^{-5} \times \text{S.C.}$ ^c Measured via Method 4110.^b Measured via Method 5310-B.^d Measured via Method 3120.

C5. Data Treatment of UV-Vis Spectra – Batch Experiments

For each UV-Vis measurement, the background-corrected UV-Vis spectrum was generated by subtracting the blank-corrected background spectrum (measured prior to the addition of the AuNPs) from the UV-Vis spectrum measured at each 20-minute interval after the addition of the AuNPs (Figure C2a-b). The background-corrected and normalized (A/A_{max}) UV-Vis spectrum was generated by dividing the background-corrected absorbance at each wavelength (A) by the maximum absorbance (A_{max}) that was measured (Figure C2c-d).

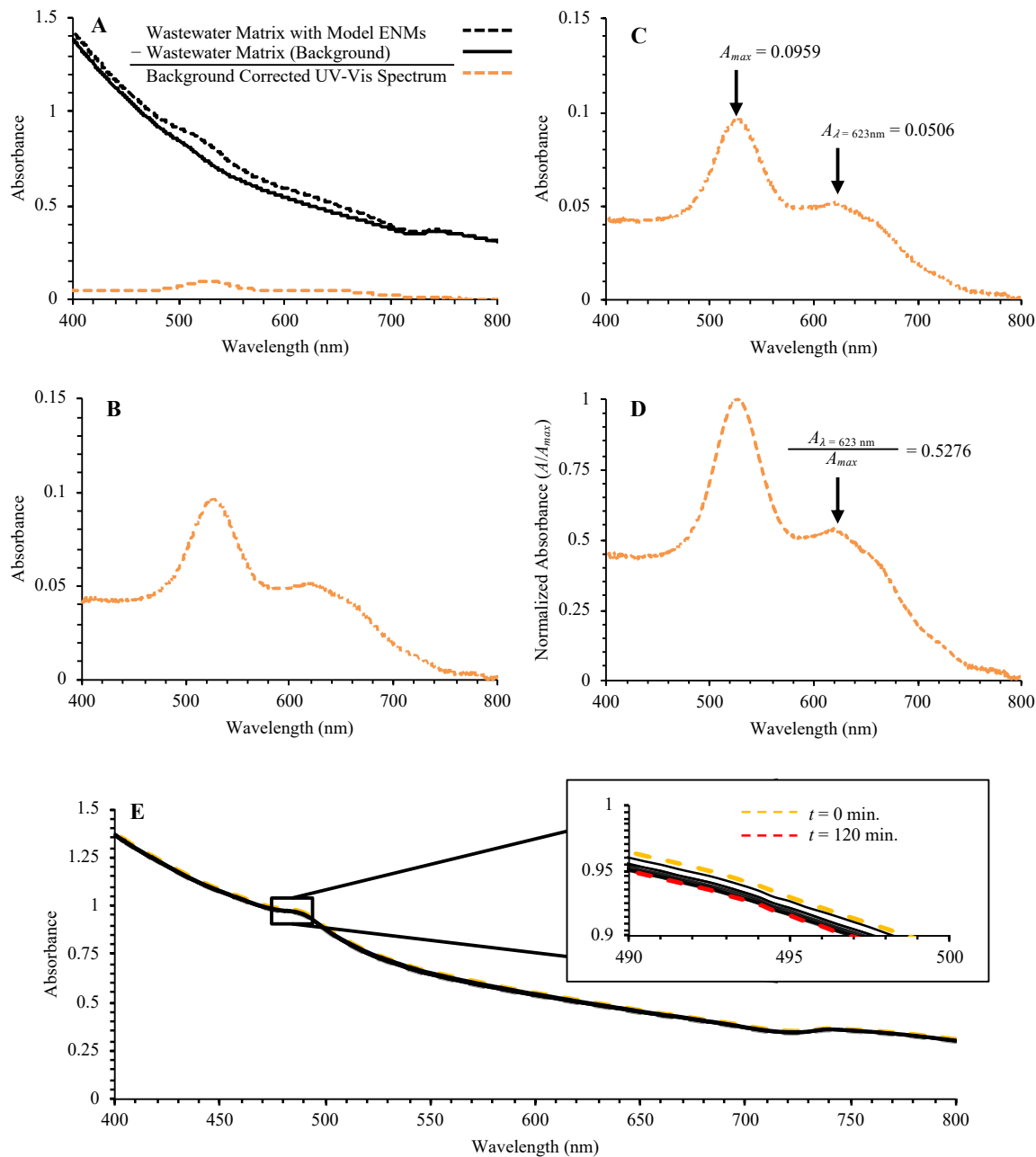


Figure C2. Illustrative example of UV-Vis data treatment steps, shown for PEG-AuNPs in influent wastewater matrix. (a) generation of background-corrected UV-Vis spectrum, (b) enlargement of background-corrected UV-Vis spectrum, (c) identification of λ_{max} , (d) generation of background-corrected and normalized UV-Vis spectrum, and (e) variation in background UV-Vis spectra (influent wastewater matrix).

C6. Matrix Exchange using Tangential-Flow Filtration System

To perform the matrix exchange experiments, a tangential-flow filtration (TFF) system was used. A process flow diagram for the system is shown in Figure C3. Note that during the baseline testing, only the influent wastewater matrix was added to the TFF reservoir. We chose to simultaneously add the denitrification and nitrification wastewater matrices from $t = 40 - 140$ minutes rather than adding them one at a time. Two other alternative approaches were considered, both operating the TFF system like a sequencing batch reactor. The first was to significantly reduce the amount of a given wastewater matrix before adding the next matrix, without continuously drawing and analyzing samples (i.e., $F_R = 0$ mL/minute). This approach would require a significant amount of time for each matrix exchange step (≈ 18 hours to remove $\approx 90\%$ of V_{TOT} via F_P alone) while simultaneously increasing the AuNP concentration in the retentate, thus introducing artifacts that would complicate our analysis. The second approach was to operate the system in a similar manner (i.e., reduce V_{TOT} by $\approx 90\%$) but continuously withdraw and analyze samples. This approach would hinder analysis of the AuNPs after exposure to the denitrification and nitrification wastewater matrices, since the concentration of AuNPs in the TFF system would have been significantly reduced, via withdrawal in F_P , prior to the introduction of the additional matrices. While not exactly mimicking the processes occurring in a full-scale WWTP, our approach is considered a compromise and was intended to serve as a proxy for the transport processes occurring in a WWTP while enabling an investigation of ENM transformations exposed to changing wastewater matrices.

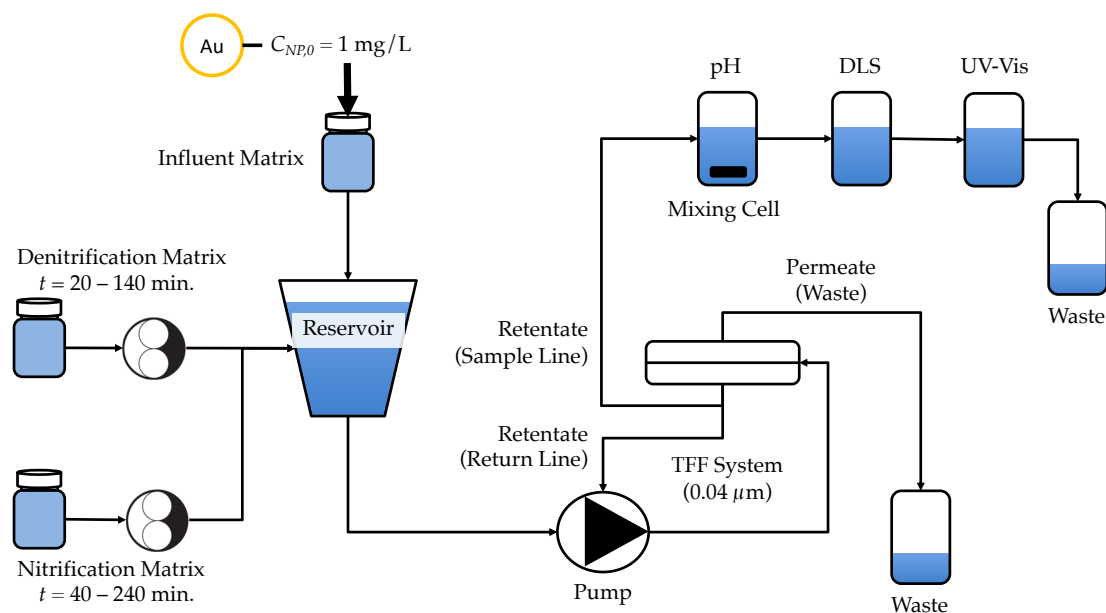


Figure C3. Process flow diagram for TFF system coupled with in-line DLS and UV-Vis detectors.

Figure C4 shows the results of modelling to estimate the volume fraction of each wastewater matrix within the TFF system during the double matrix exchange process, assuming complete mixing. After the initial period when only the influent wastewater matrix is present, the fraction of the denitrification wastewater matrix in the TFF system steadily increases, reaching a maximum of $\approx 25\%$ at $t = 140 \text{ min.}$, at which point the addition of the denitrification wastewater matrix was stopped. The fraction of the nitrification wastewater also steadily increases after $t = 40 \text{ min.}$, reaching a maximum of $\approx 50\%$ at $t = 240 \text{ min.}$, at which point the procedure was stopped.

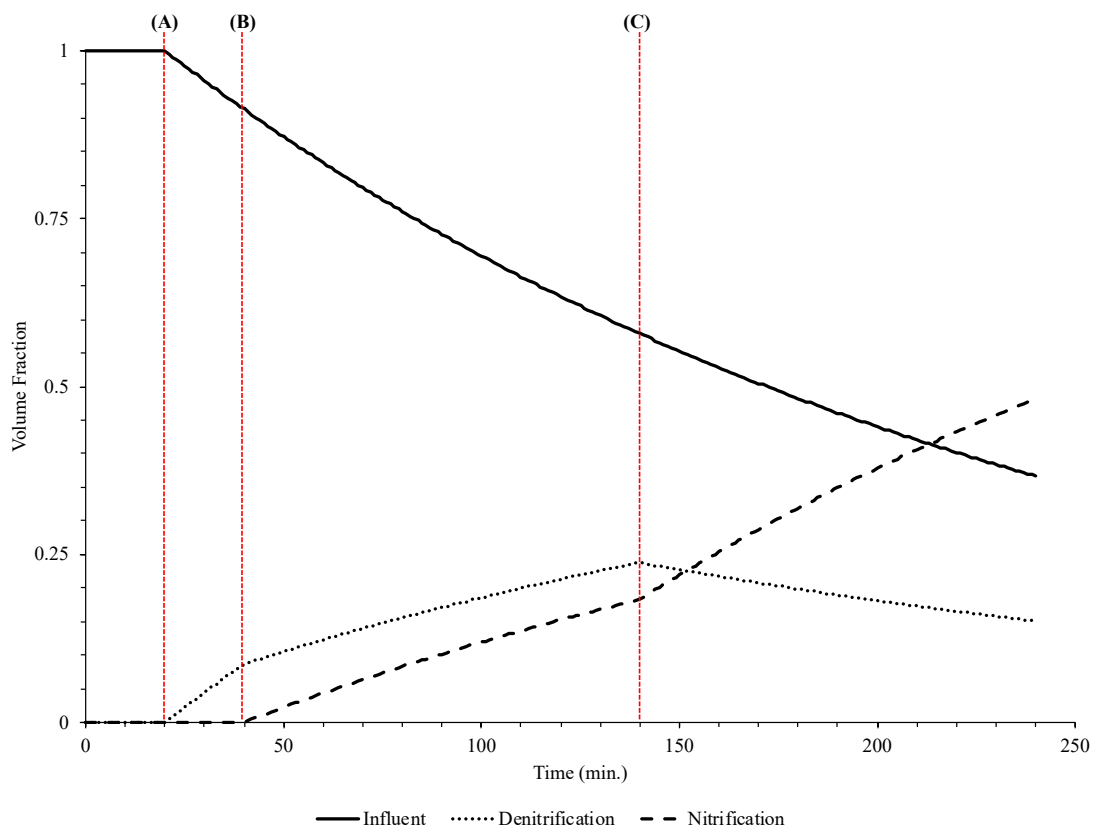


Figure C4. Estimated volume fraction of each wastewater matrix in the TFF system during the double matrix exchange. (a) Commencement of denitrification matrix addition, (b) commencement of nitrification matrix addition, and (c) cessation of denitrification matrix addition while continuing addition of nitrification matrix.

C7. Testing of Tangential-Flow Filtration System

The ability of the TFF membrane to retain the AuNPs was tested by the following procedure:

- 1) A 300 mL sample containing the AuNPs was prepared by dispersing the bPEI-AuNPs in 0.02 μm filtered 18.2 M Ω -cm Nanopure water (DDI; Barnstead) to $C_{NP} = 0.5$ mg/L ($V_{DDI} = 297$ mL; $V_{AuNP} = 3$ mL).
- 2) Upon preparation of the sample, aliquots were collected in triplicate ($V_{TOT} = 10$ mL) via calibrated pipette and transferred to separate 15 mL polypropylene tubes to confirm the initial solution concentration. The remainder of the sample was transferred to the TFF reservoir.
- 3) The TFF system was then operated at a transmembrane pressure (TMP) of 2-3 bar, a cross-flow velocity (V_s) of ≈ 1.4 cm/s, and at $T = 19 - 20$ °C, with a 0.04 μm PES membrane installed in the filter housing.
- 4) The AuNP/DDI matrix was cycled through the TFF system until sufficient volume (≥ 30 mL) had been obtained in the permeate vessel.
- 5) The permeate vessel was briefly mixed via gentle shaking and aliquots were collected in triplicate ($V_{TOT} = 10$ mL) via calibrated pipette and transferred to separate 15 mL polypropylene tubes.
- 6) The samples were then microwave digested in fresh *aqua regia* (3:1 HCl:HNO₃) and analyzed via inductively coupled plasma mass spectrometry (ICP-MS).

The results, shown in Table C3, indicate that $\approx 99\%$ of the AuNP mass was retained within the TFF system.

Table C3. Concentration of bPEI-AuNPs in TFF permeate.

	Average Concentration ($\mu\text{g/L}$)
Initial Solution	525.73 ± 166.9
Permeate	5.50 ± 1.0

Error bars indicate $\pm 95\%$ confidence interval ($n = 3$).

C8. Data Treatment of UV-Vis Spectra – Matrix Exchange

The TR-UV-Vis spectra measured during the matrix exchange procedure were generated following the same overall steps as the batch experiments. Unlike the batch experiments, the background UV-Vis spectra were found to change over time before stabilizing (Figure C5a). This likely reflects an initial change in the composition of the background wastewater matrix as some constituents, such as small organic macromolecules, are selectively removed via filtration through the PES membrane (0.04 μm) of the tangential flow filtration (TFF) system.

To address this, the background spectra was measured over time by operating the TFF system with only with the background matrix (or matrices, in the case of the double matrix exchange) and measuring the UV-Vis spectrum at 5-minute intervals (Figure C5a). The experiment then proceeded as described in the main text, generating the uncorrected UV-Vis spectra for a given AuNP type and wastewater matrix combination. The background-corrected UV-Vis spectra (Figure C5b) were then generated by subtracting the previously measured background spectra (Figure C5a) from the corresponding uncorrected UV-Vis spectra measured at each interval. To account for negative absorbance values, attributed to the ‘blinking’ of the instrument with 18.2 M Ω -cm Nanopure water (DDI; Barnstead) between each experiment, a correction of 0.3 A.U. was applied to all the background-corrected UV-Vis spectra at each wavelength and time interval. Because our analysis focuses on the relative locations and heights of peaks, this offset does not affect the resulting conclusions. The background-corrected and normalized (A/A_{max}) UV-Vis spectra were generated by dividing the background-corrected absorbance at each wavelength (A) by the maximum absorbance (A_{max}) that was measured (Figure C5c). A moving average window ($n = 15$) was then applied to smooth the data (Figure C5d).

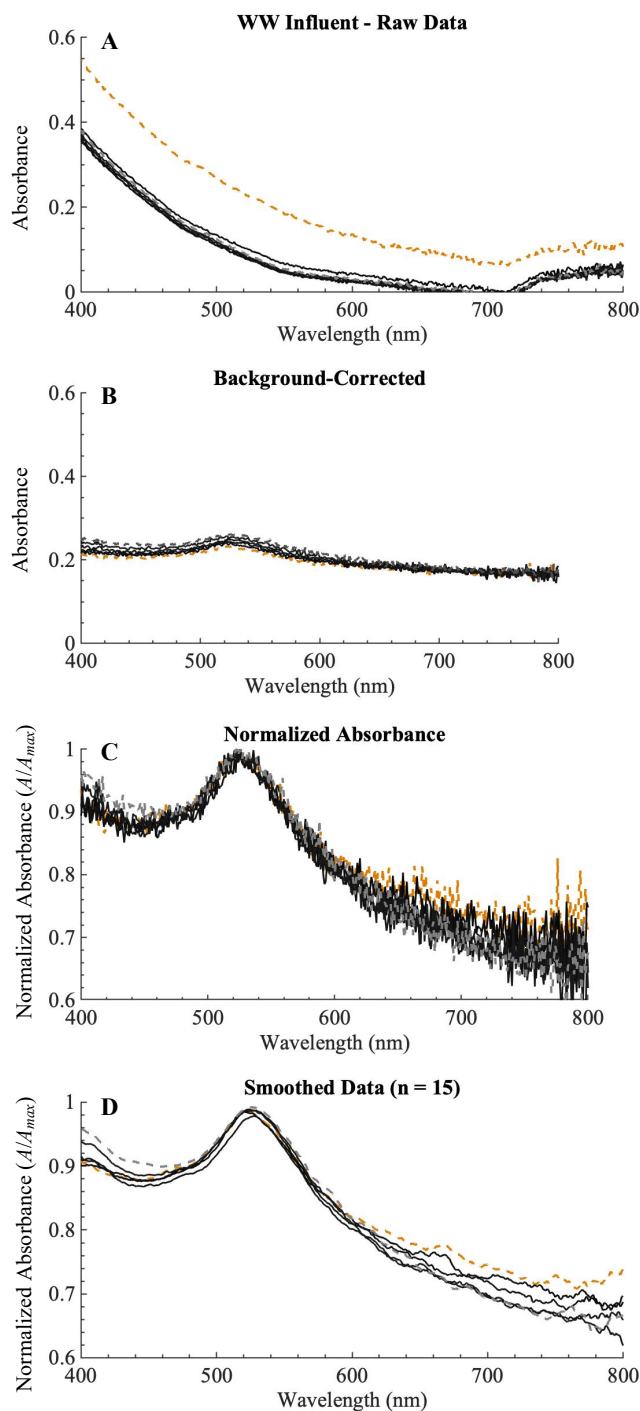


Figure C5. Illustrative example of UV-Vis data treatment steps during matrix exchange procedure, shown for bPEI-AuNPs in influent wastewater matrix (baseline): (a) background wastewater matrix UV-Vis spectra, (b) background-corrected UV-Vis spectra, (c) background-corrected and normalized (A/A_{max}) UV-Vis spectra, and (d) background-corrected, normalized, and smoothed UV-Vis spectra.

C9. Time-Resolved Dynamic Light Scattering

The colloidal stability of each AuNP type upon dispersion in the wastewater matrices was tracked using time-resolved dynamic light scattering (TR-DLS). The samples were prepared and analyzed according to the procedures discussed in the main text. Each AuNP type was measured in each wastewater matrix in triplicate. The results are presented in Figures C6 – C8. In addition, a “long-term” TR-DLS measurement (herein referred to as LT-TR-DLS) was performed to extend the measurement period to ≈ 120 minutes. During the LT-TR-DLS, the same procedure as that outlined for the TR-DLS measurements was followed, except that a 45-second delay occurred between each of the measurements. The results of the LT-TR-DLS are presented in Figure C9.

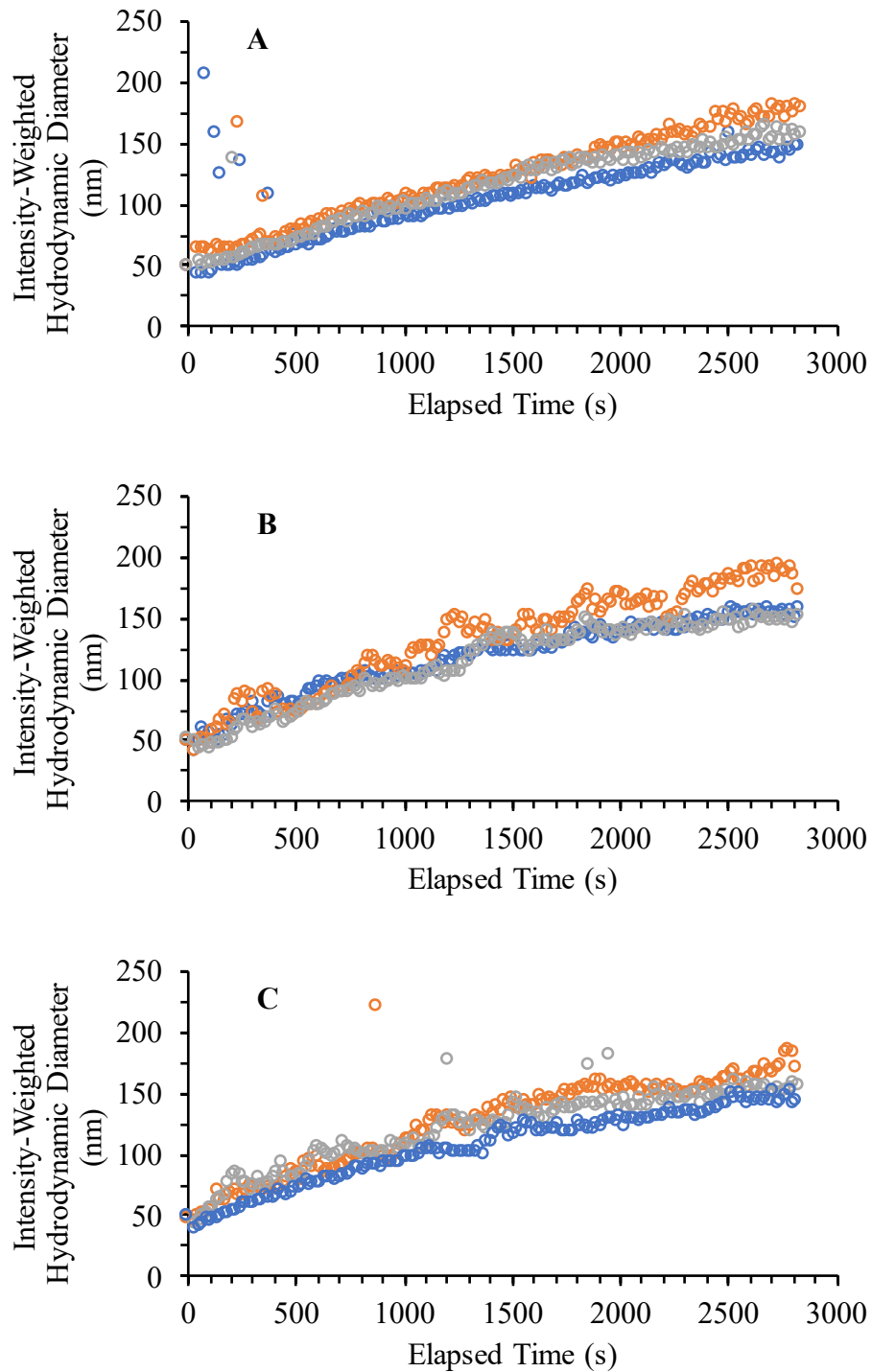


Figure C6: Intensity-weighted hydrodynamic diameter (D_h) over time for PEG-AuNPs in (a) influent, (b) denitrification, and (c) nitrification wastewater matrices.

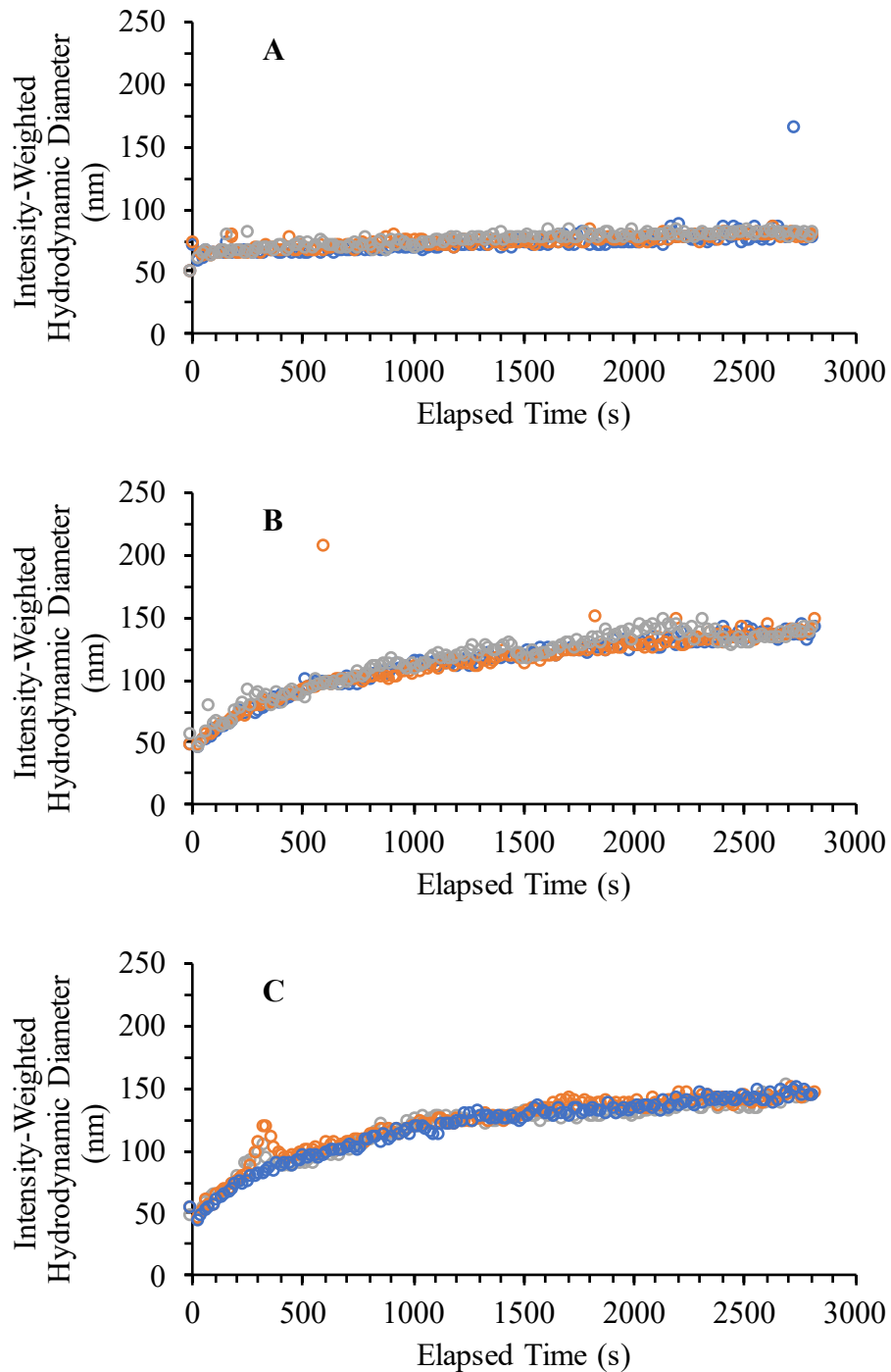


Figure C7: Intensity-weighted hydrodynamic diameter (D_h) over time for COOH-AuNPs in (a) influent, (b) denitrification, and (c) nitrification wastewater matrices.

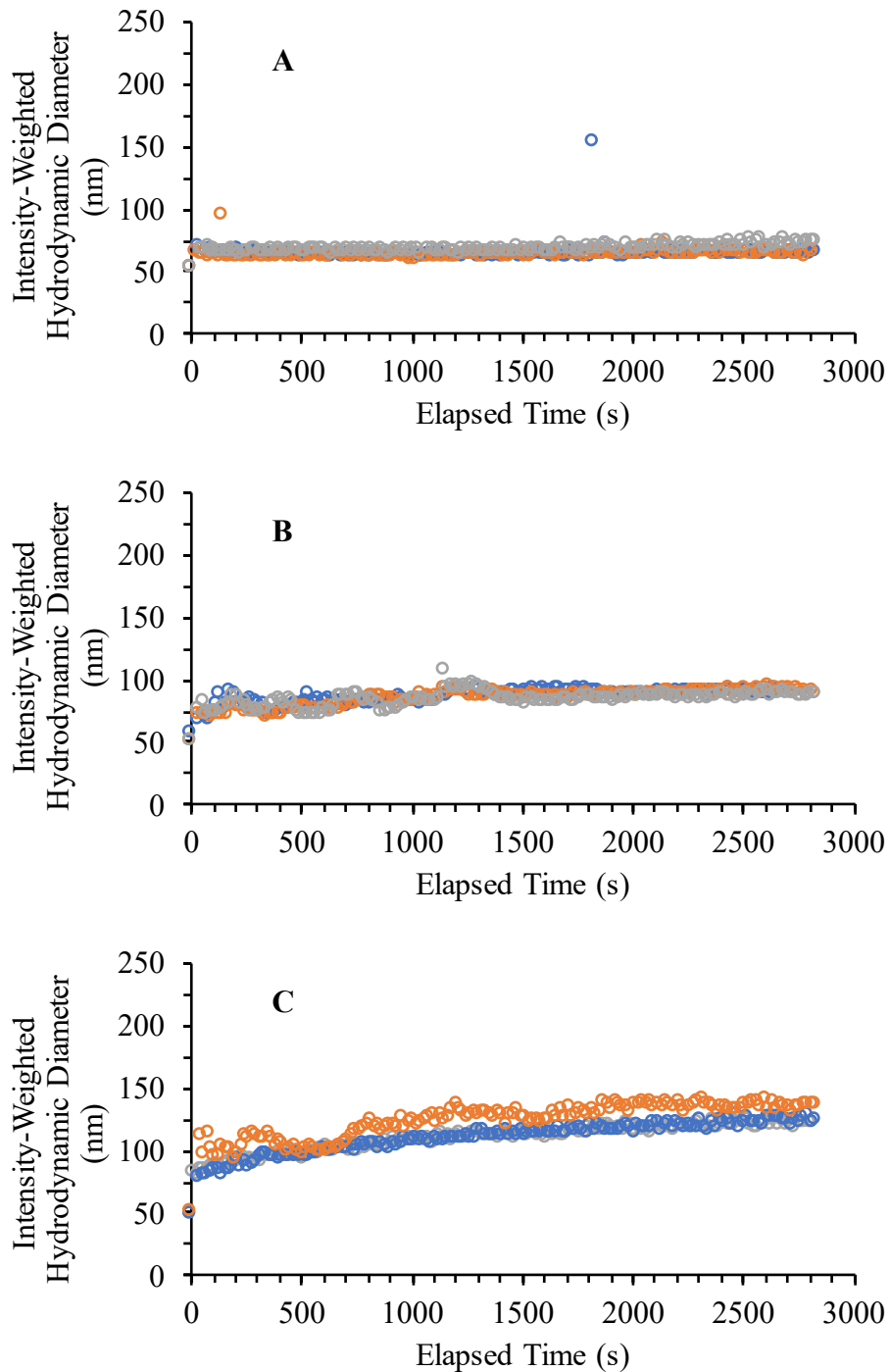


Figure C8: Intensity-weighted hydrodynamic diameter (D_h) over time for bPEI-AuNPs in (a) influent, (b) denitrification, and (c) nitrification wastewater matrices.

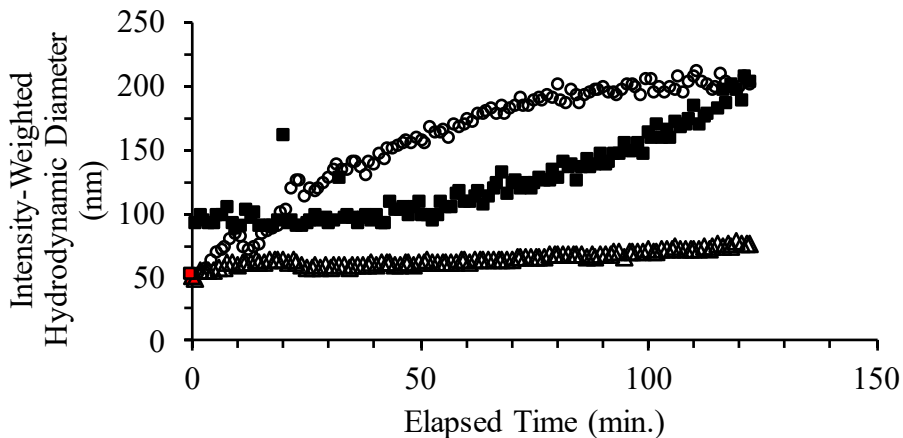


Figure C9: Intensity-weighted hydrodynamic diameter (D_h) over time for (○) PEG-AuNPs, (△) COOH-AuNPs, and (■) bPEI-AuNPs in influent wastewater matrix. $D_{h,initial}$ for each AuNP type is shown in red.

C10. Time-Resolved UV-Vis Spectra – Batch Experiments

Conformational changes of the engineered surface coating and/or adsorption of organic macromolecules to the AuNPs, as well as estimates of the AuNP interparticle separation distance, were assessed using time-resolved ultraviolet-visible light spectroscopy (TR-UV-Vis). The samples were prepared and analyzed according to the procedures discussed in the main text. Each AuNP type was measured in each wastewater matrix in triplicate. The replicate measurements are presented in Figures C11 – C19. From these replicate UV-Vis spectra, the red-shift of the primary peak in proximity to λ_{SPR} (Table 4.1), referred to herein as λ_{max} , was calculated for each AuNP type in each wastewater matrix (Figure C10).

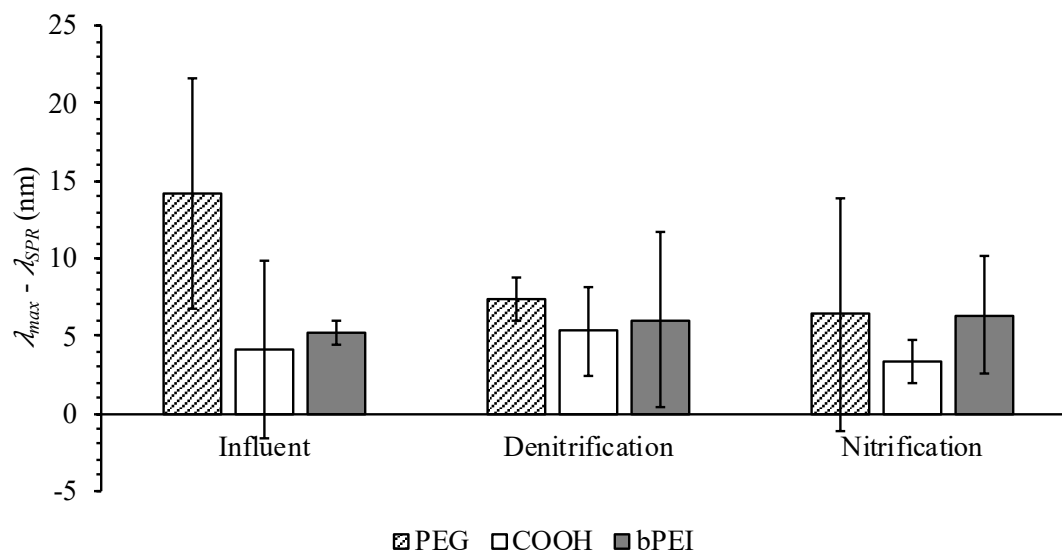


Figure C10. Average red-shift of the primary peak (λ_{max}) in relation to λ_{SPR} for each AuNP type after incubating for 120 minutes in each wastewater matrix. Error bars indicate $\pm 95\%$ confidence interval ($n = 3$).

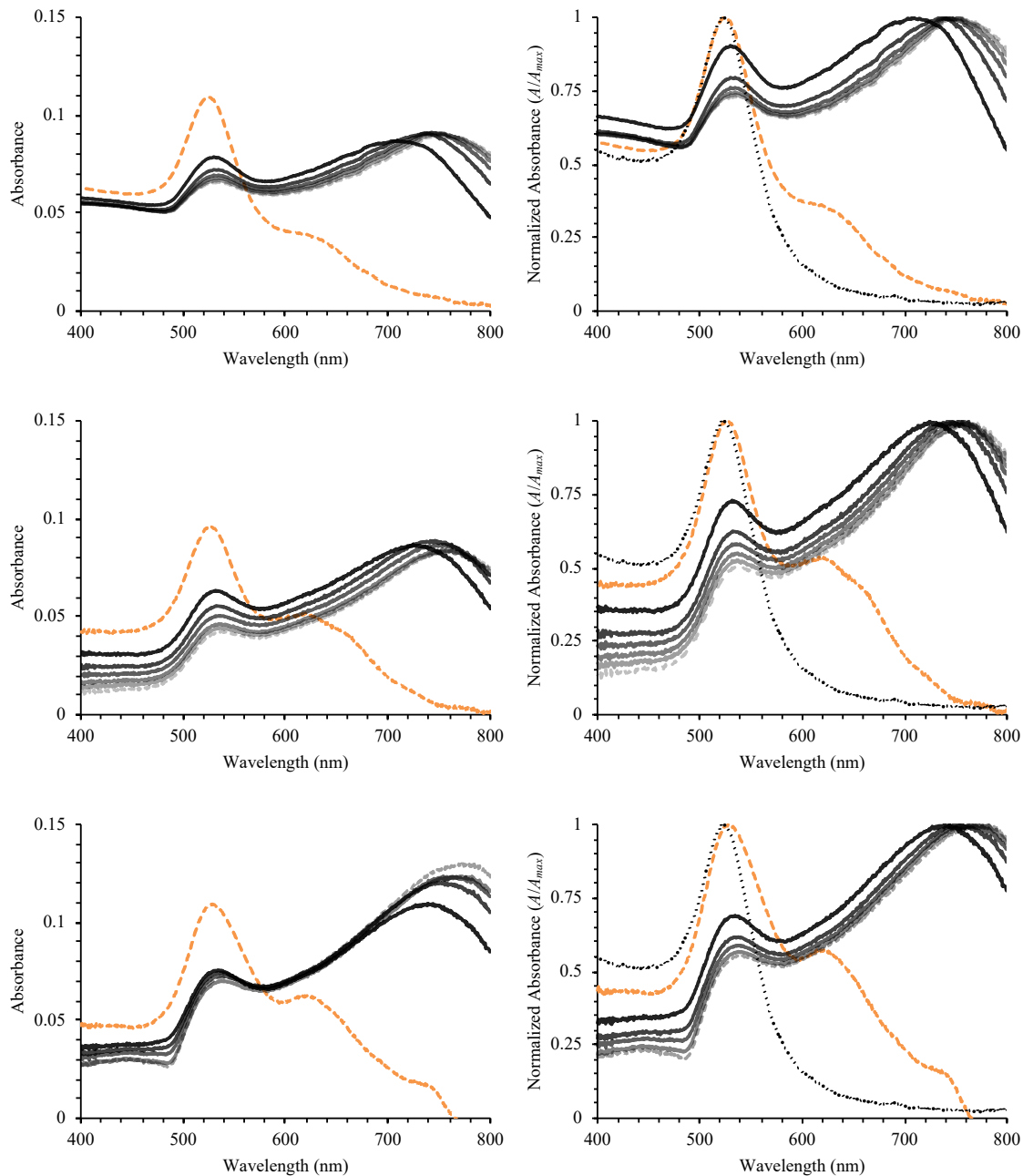


Figure C11. (Left) Background-corrected and (right) background-corrected and normalized (A/A_{max}) UV-Vis spectra for PEG-AuNPs in influent wastewater matrix. Orange dashed-line depicts UV-Vis spectra at $t \approx 0$ minutes, grey dashed-line depicts spectra at $t = 120$ minutes, and grey-scale depicts spectra at 20-minutes intervals in between (black-to-grey). For reference, the black dotted-line depicts the UV-Vis spectra in DDI.

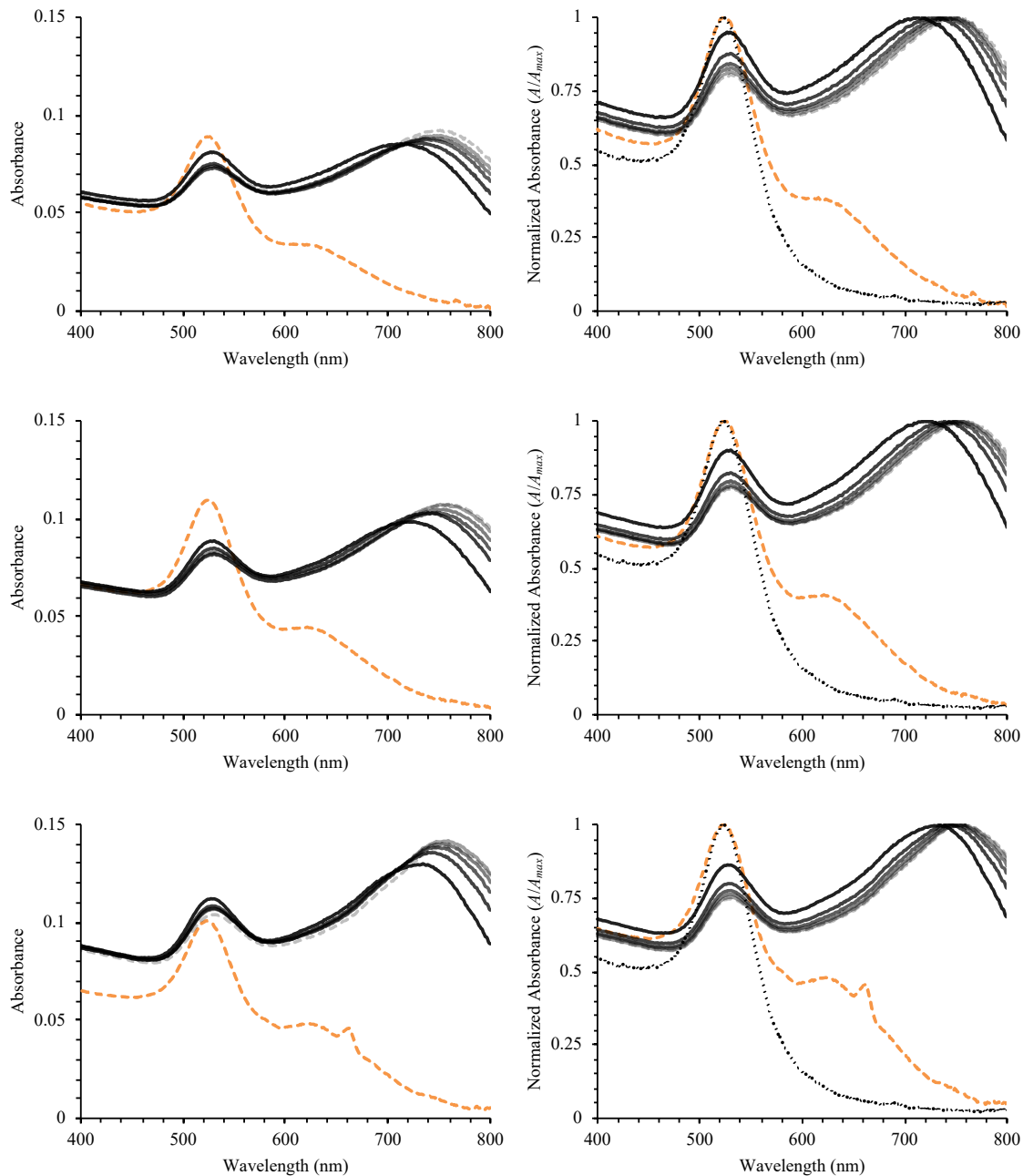


Figure C12. (Left) Background-corrected and (right) background-corrected and normalized (A/A_{max}) UV-Vis spectra for PEG-AuNPs in denitrification wastewater matrix. Orange dashed-line depicts UV-Vis spectra at $t \approx 0$ minutes, grey dashed-line depicts spectra at $t = 120$ minutes, and grey-scale depicts spectra at 20-minutes intervals in between (black-to-grey). For reference, the black dotted-line depicts the UV-Vis spectra in DDI.

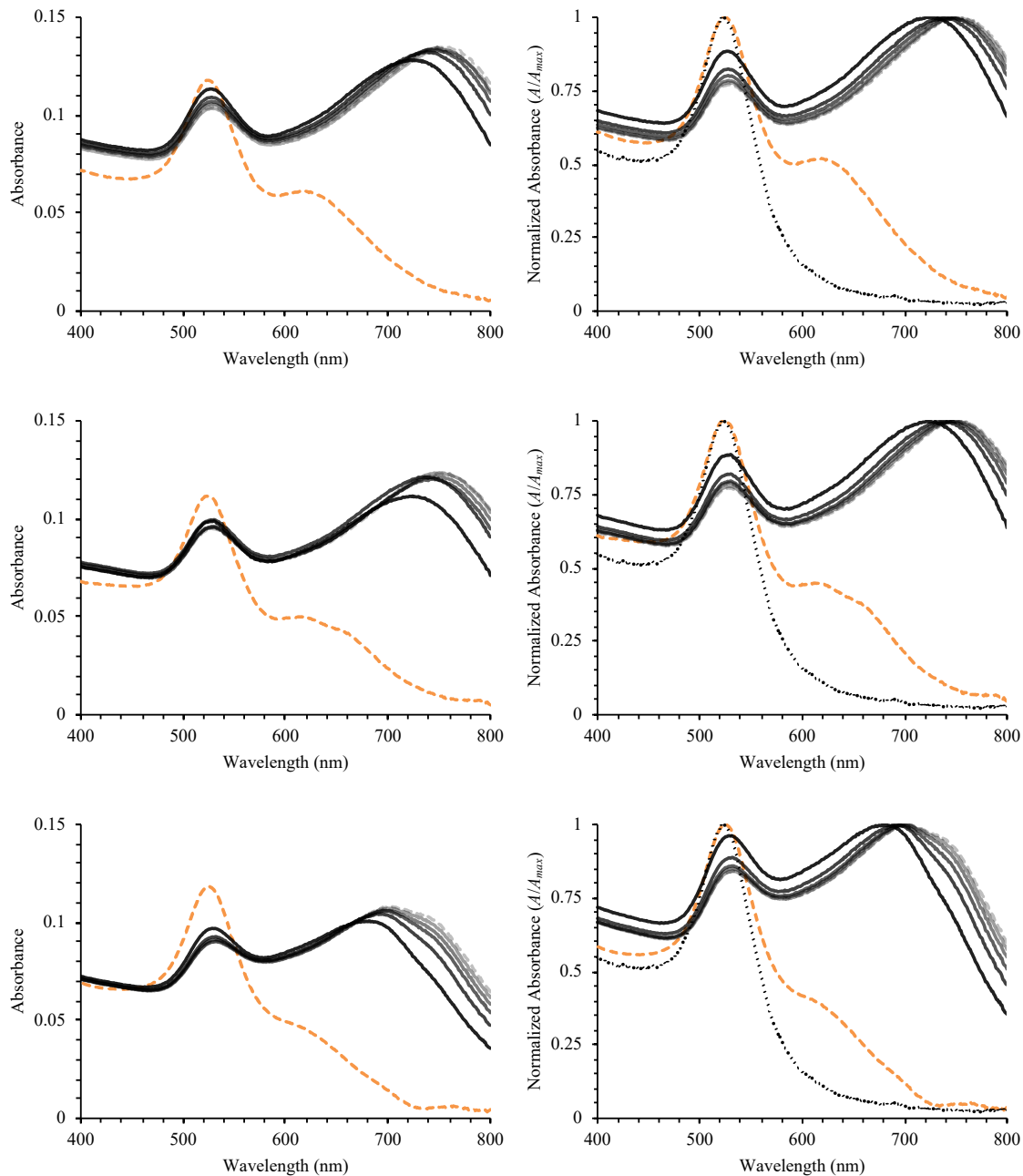


Figure C13. (Left) Background-corrected and (right) background-corrected and normalized (A/A_{max}) UV-Vis spectra for PEG-AuNPs in nitrification wastewater matrix. Orange dashed-line depicts UV-Vis spectra at $t \approx 0$ minutes, grey dashed-line depicts spectra at $t = 120$ minutes, and grey-scale depicts spectra at 20-minutes intervals in between (black-to-grey). For reference, the black dotted-line depicts the UV-Vis spectra in DDI.

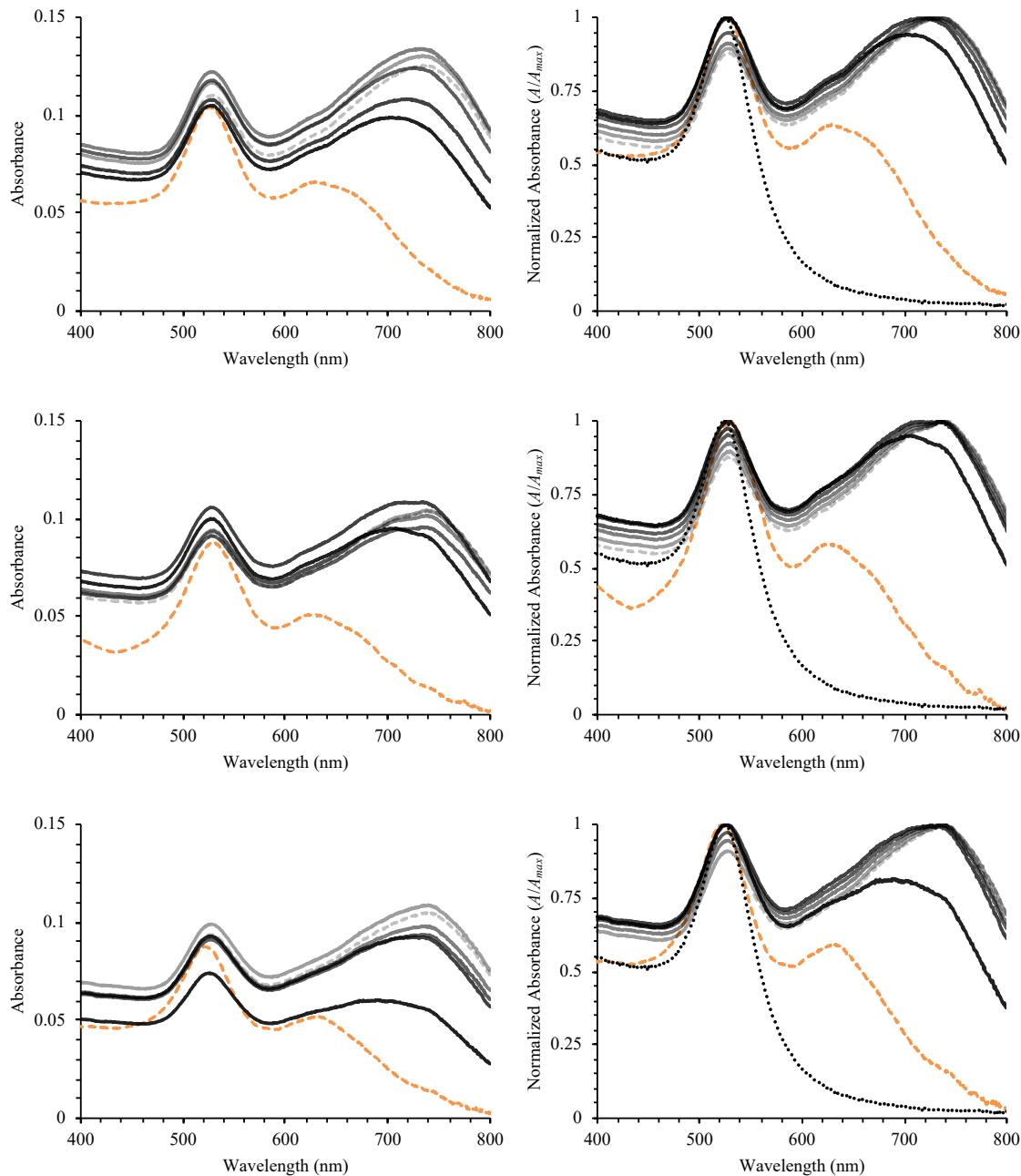


Figure C14. (Left) Background-corrected and (right) background-corrected and normalized (A/A_{max}) UV-Vis spectra for COOH-AuNPs in influent wastewater matrix. Orange dashed-line depicts UV-Vis spectra at $t \approx 0$ minutes, grey dashed-line depicts spectra at $t = 120$ minutes, and grey-scale depicts spectra at 20-minutes intervals in between (black-to-grey). For reference, the black dotted-line depicts the UV-Vis spectra in DDI.

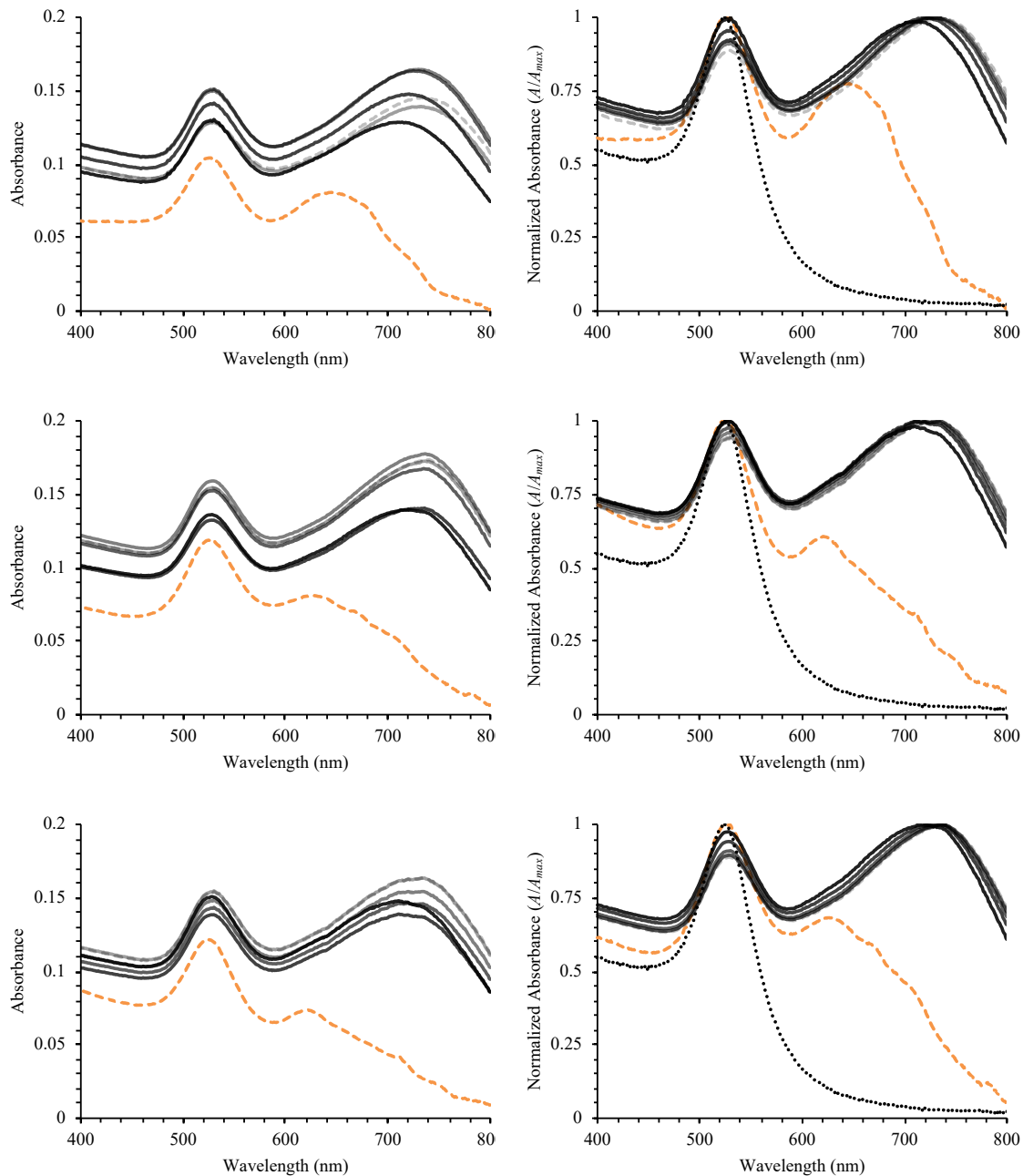


Figure C15. (Left) Background-corrected and (right) background-corrected and normalized (A/A_{max}) UV-Vis spectra for COOH-AuNPs in denitrification wastewater matrix. Orange dashed-line depicts UV-Vis spectra at $t \approx 0$ minutes, grey dashed-line depicts spectra at $t = 120$ minutes, and grey-scale depicts spectra at 20-minute intervals in between (black-to-grey). For reference, the black dotted-line depicts the UV-Vis spectra in DDI.

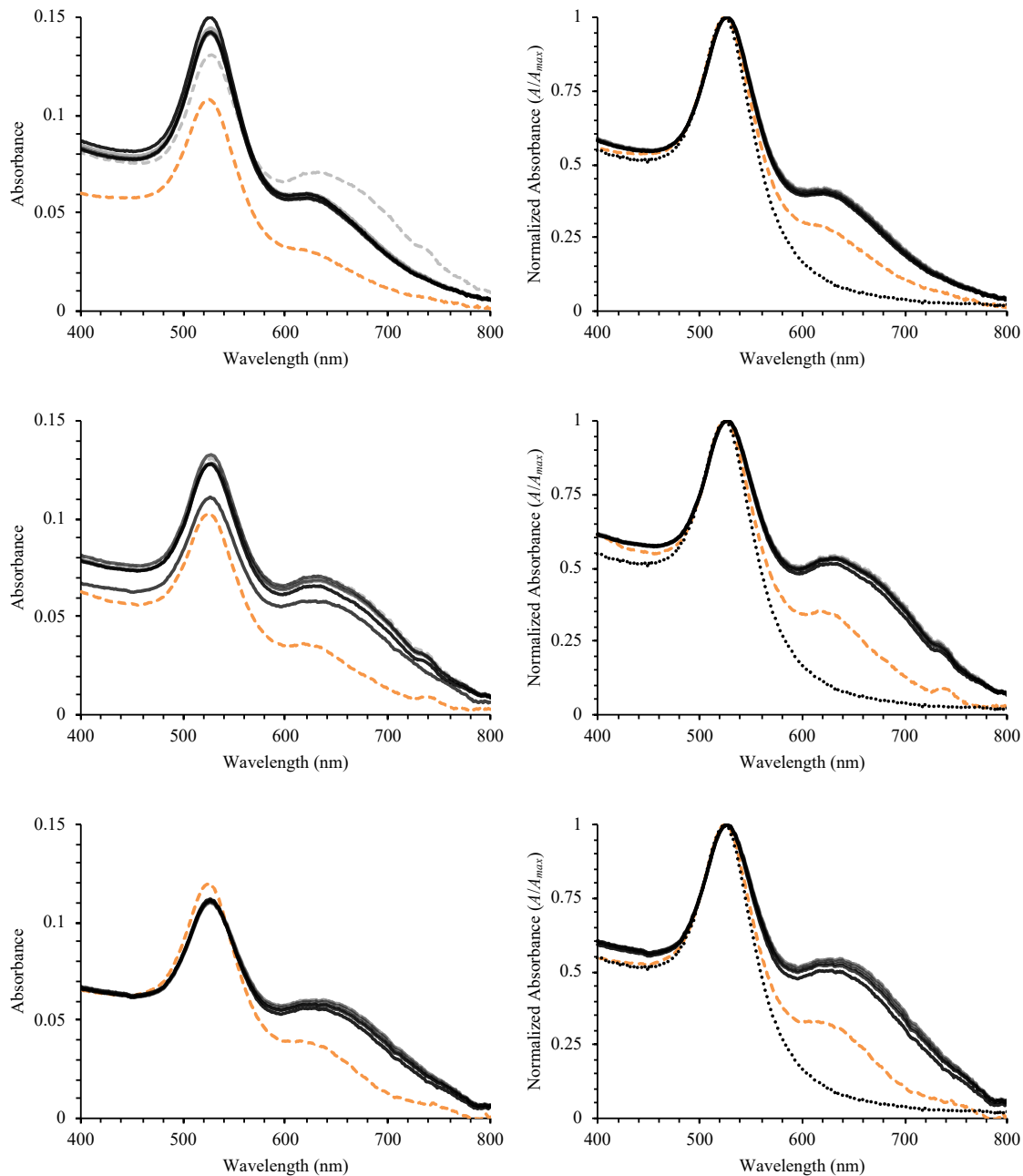


Figure C16. (Left) Background-corrected and (right) background-corrected and normalized (A/A_{max}) UV-Vis spectra for COOH-AuNPs in nitrification wastewater matrix. Orange dashed-line depicts UV-Vis spectra at $t \approx 0$ minutes, grey dashed-line depicts spectra at $t = 120$ minutes, and grey-scale depicts spectra at 20-minute intervals in between (black-to-grey). For reference, the black dotted-line depicts the UV-Vis spectra in DDI.

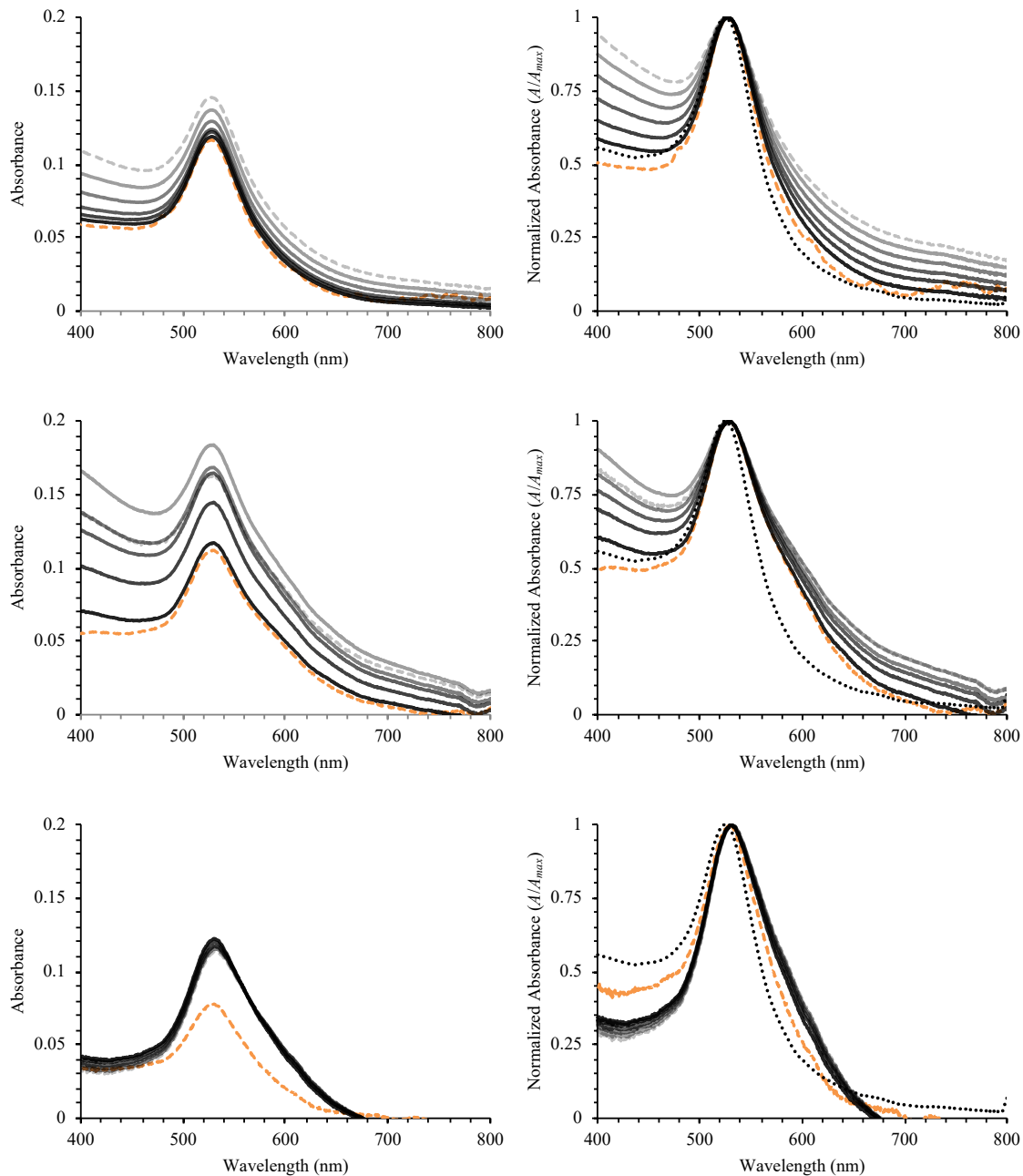


Figure C17. (Left) Background-corrected and (right) background-corrected and normalized (A/A_{max}) UV-Vis spectra for bPEI-AuNPs in influent wastewater matrix. Orange dashed-line depicts UV-Vis spectra at $t \approx 0$ minutes, grey dashed-line depicts spectra at $t = 120$ minutes, and grey-scale depicts spectra at 20-minutes intervals in between (black-to-grey). For reference, the black dotted-line depicts the UV-Vis spectra in DDI.

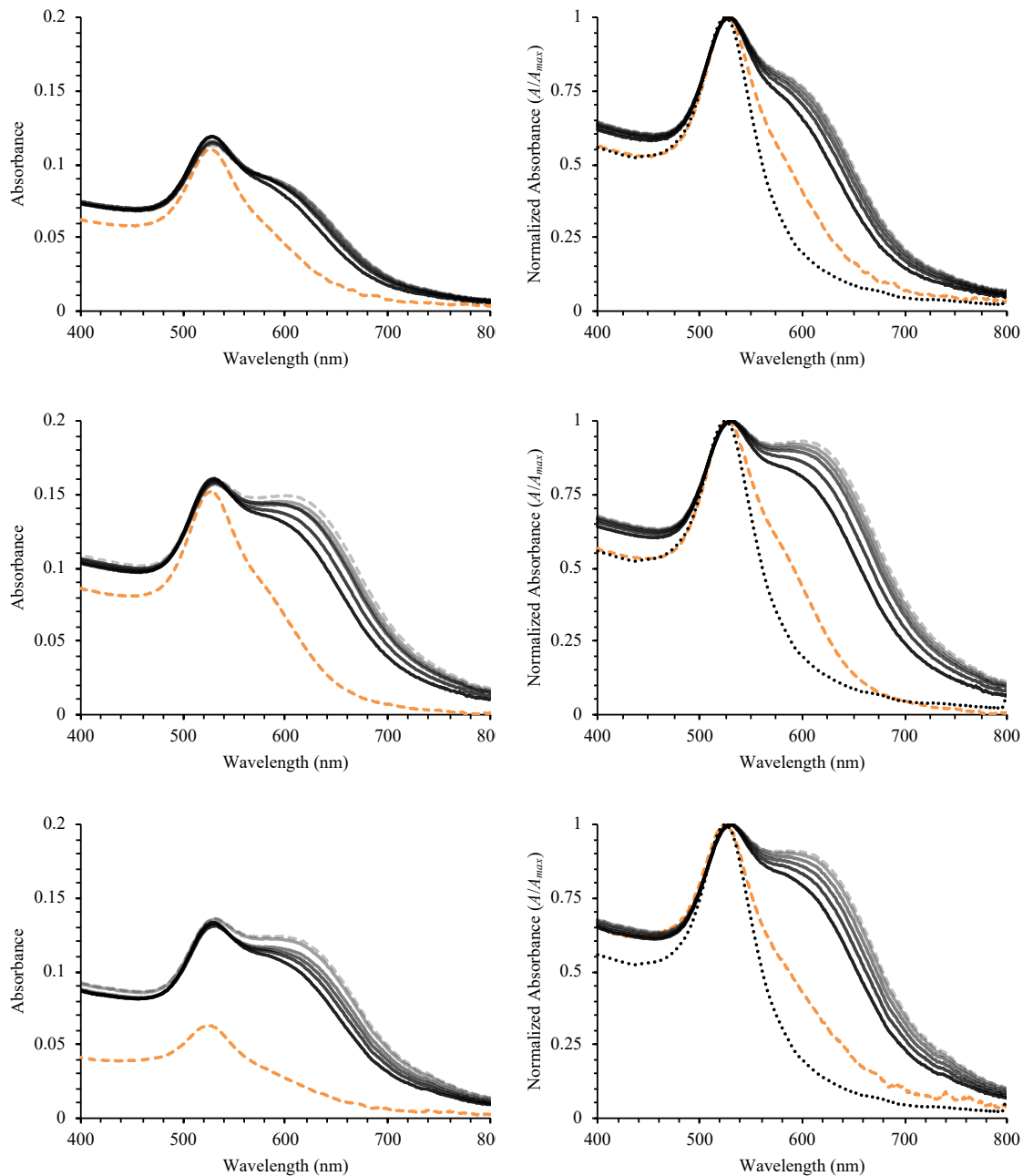


Figure C18. (Left) Background-corrected and (right) background-corrected and normalized (A/A_{max}) UV-Vis spectra for bPEI-AuNPs in denitrification wastewater matrix. Orange dashed-line depicts UV-Vis spectra at $t \approx 0$ minutes, grey dashed-line depicts spectra at $t = 120$ minutes, and grey-scale depicts spectra at 20-minutes intervals in between (black-to-grey). For reference, the black dotted-line depicts the UV-Vis spectra in DDI.

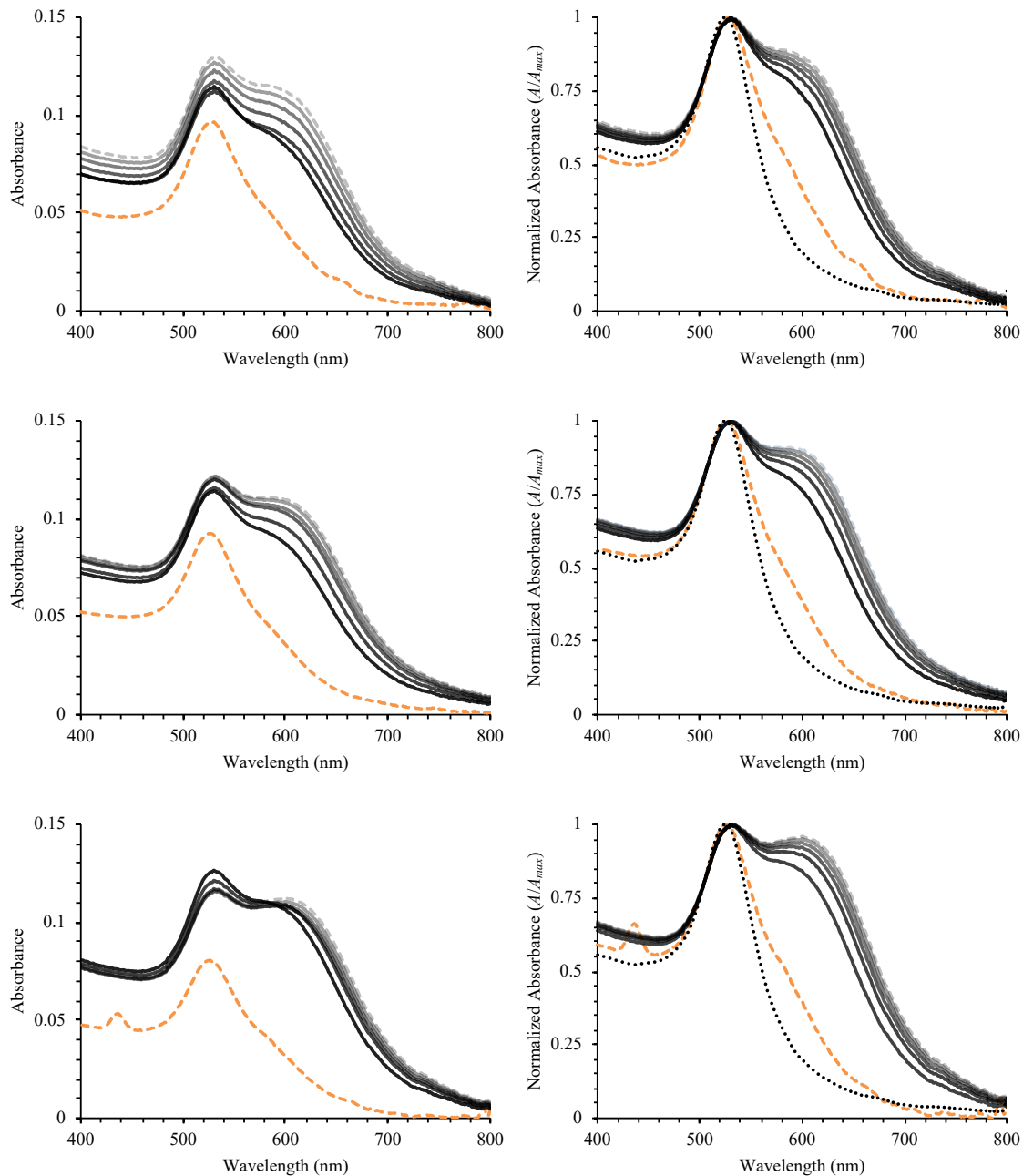


Figure C19. (Left) Background-corrected and (right) background-corrected and normalized (A/A_{max}) UV-Vis spectra for bPEI-AuNPs in nitrification wastewater matrix. Orange dashed-line depicts UV-Vis spectra at $t \approx 0$ minutes, grey dashed-line depicts spectra at $t = 120$ minutes, and grey-scale depicts spectra at 20-minutes intervals in between (black-to-grey). For reference, the black dotted-line depicts the UV-Vis spectra in DDI.

C11. Transmission Electron Microscopy Micrographs – Interparticle Distance Analysis

The transmission electron microscope (TEM) images were used to determine the average center-to-center separation distance (d_s) between neighboring particles. The average ratio between d_s and the nanoparticle diameter was then calculated for each AuNP type after incubating in a given wastewater matrix. To accomplish this, a typical TEM micrograph was analyzed using the software package Fiji (ImageJ)^{6,7} and the ParticleSizer v1.07 plugin⁸ according to the following procedure.

- 1) The centroid of each AuNP primary particle was identified by delineating each primary particle using the default settings of the ParticleSizer plugin⁸, except that the minimal ferret length and the minimum long and short ellipsis axes were each set to 3 pixels. These values were found to correctly delineate the AuNPs while minimizing the inclusion of non-AuNP particles (i.e., false-positives) and ‘lumping’ of adjacent primary particles.
- 2) Using the x- and y-coordinate of the centroid, the Euclidean center-to-center separation distance (d_s) between each pair of primary particles was calculated. To eliminate particle pairs that were either not adjacent or were overlapping (i.e., the primary particles were vertically stacked on top of each other, an artifact from analyzing a 3-D sample in 2-D), these distances were constrained by the lower- and upper-bounds shown in Table C4. These limits correspond to the average AuNP core diameter measured via TEM minus its lower 95% confidence interval and the hydrodynamic diameter measured via DLS plus its upper 95% confidence interval, respectively (Table 4.1). Based on an analysis without these constraints, the range in d_s were found to span ≈ 30 nm to $>1,000$ nm, with high values in d_s clearly indicating primary particle pairs that were not adjacent to each other.
- 3) The values of d_s retained after applying the bounds in Table C4 were then compiled and the distribution of the values and accompanying statistics were generated.

An illustrative example of these steps is shown in Figure C20, with the full results from this analysis shown in Figures C21 – C23.

Table C4. Lower- and upper-bounds applied to each AuNP type during TEM analysis.

Surface Coating	Lower Bound (d_c - Lower 95% C.I) (nm)	Upper Bound (D_h + Upper 95% C.I) (nm)
PEG	37	49.3
COOH	35	52.2
bPEI	37	52.9

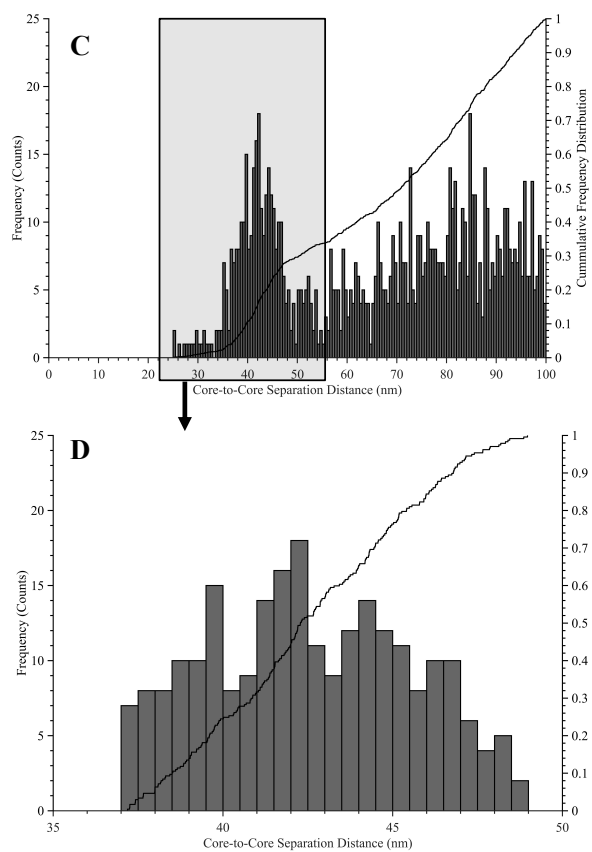
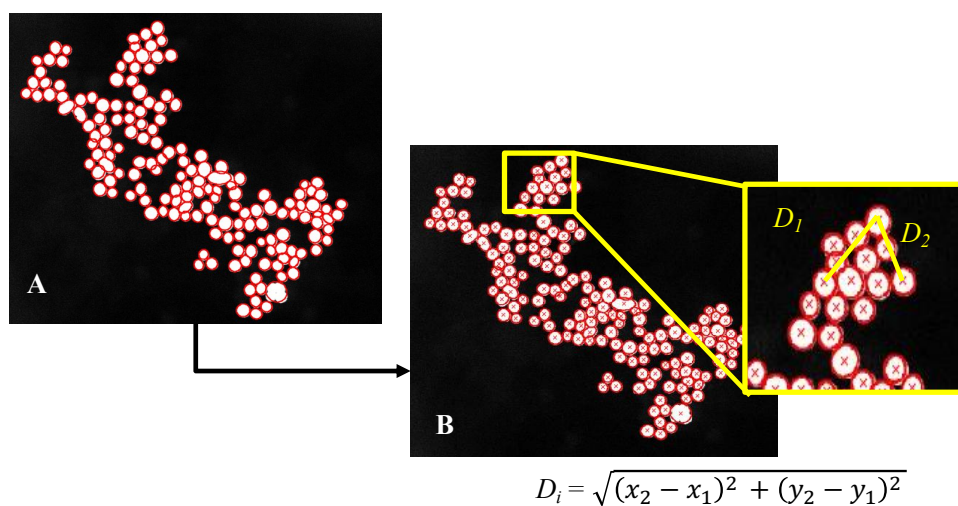


Figure C20. Illustrative example of center-to-center separation distances (d_s) calculated for PEG-AuNPs incubated in influent wastewater matrix: (a) delineation of primary particles and (b) identification of particle centroids (Steps 1 and 2); (c) distribution of d_s without constraints; and (d) distribution of d_s with constraints.

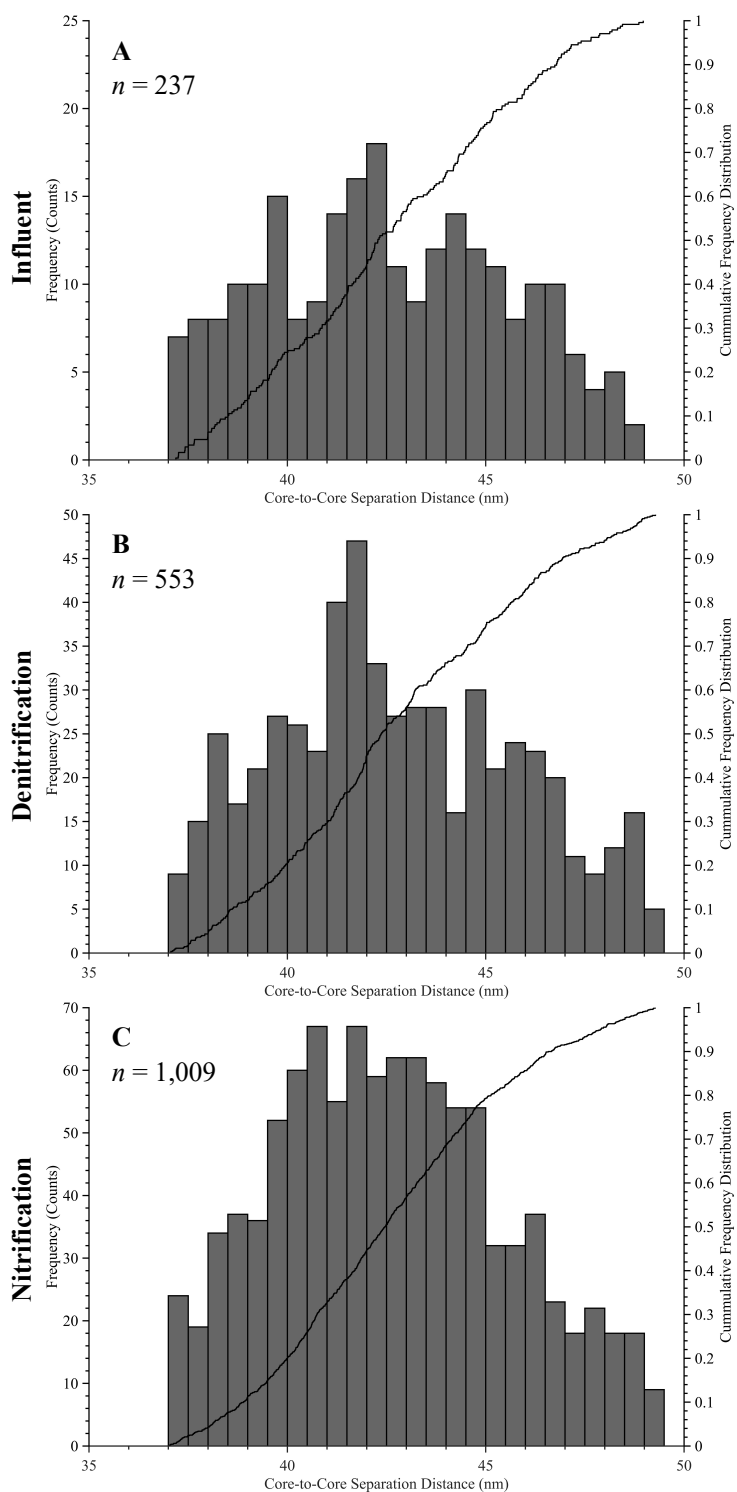


Figure C21. Distribution of center-to-center separation distances (d_s) calculated for PEG-AuNPs incubated in (a) influent, (b) denitrification, and (c) nitrification wastewater matrices after $t = 120$ minutes.

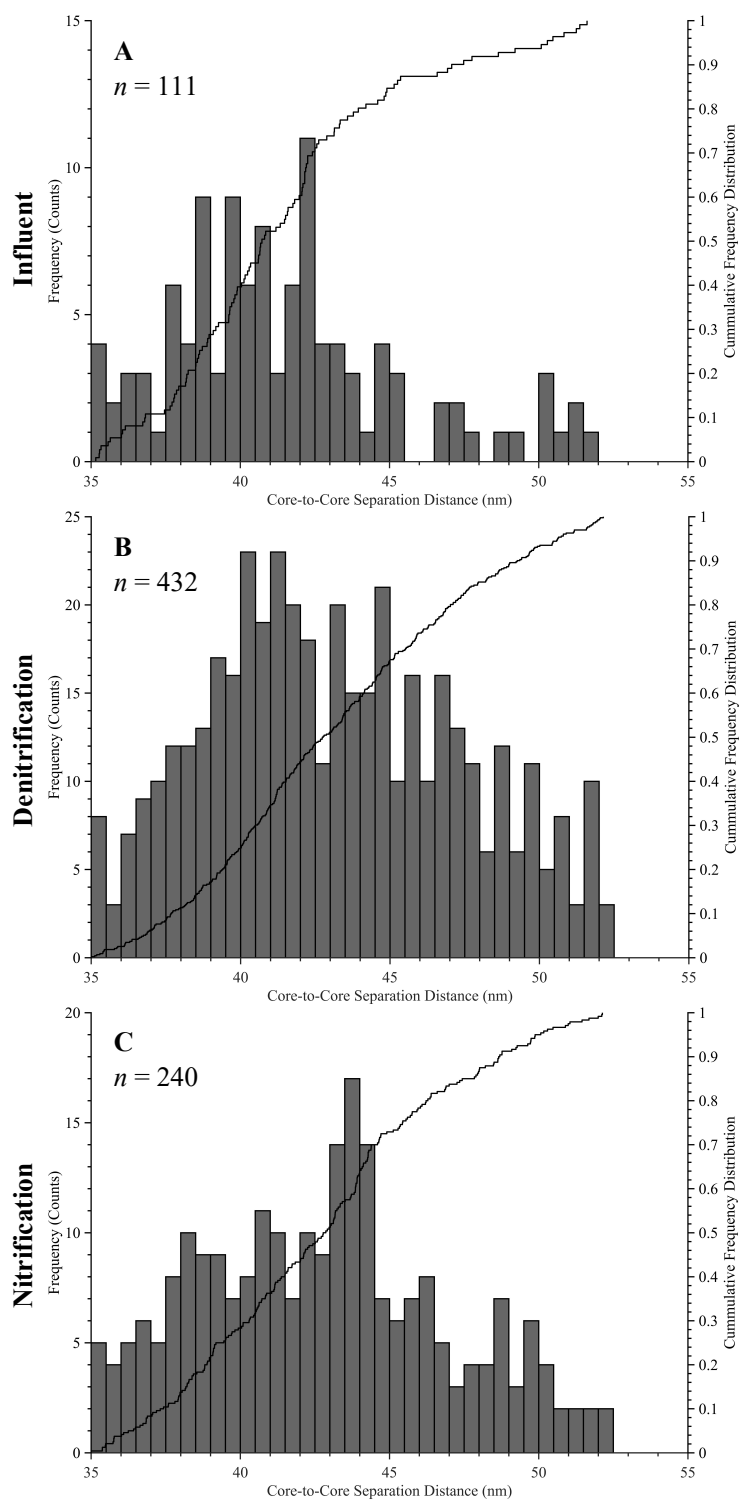


Figure C22. Distribution of center-to-center separation distances (d_s) calculated for COOH-AuNPs incubated in (a) influent, (b) denitrification, and (c) nitrification wastewater matrices after $t = 120$ minutes.

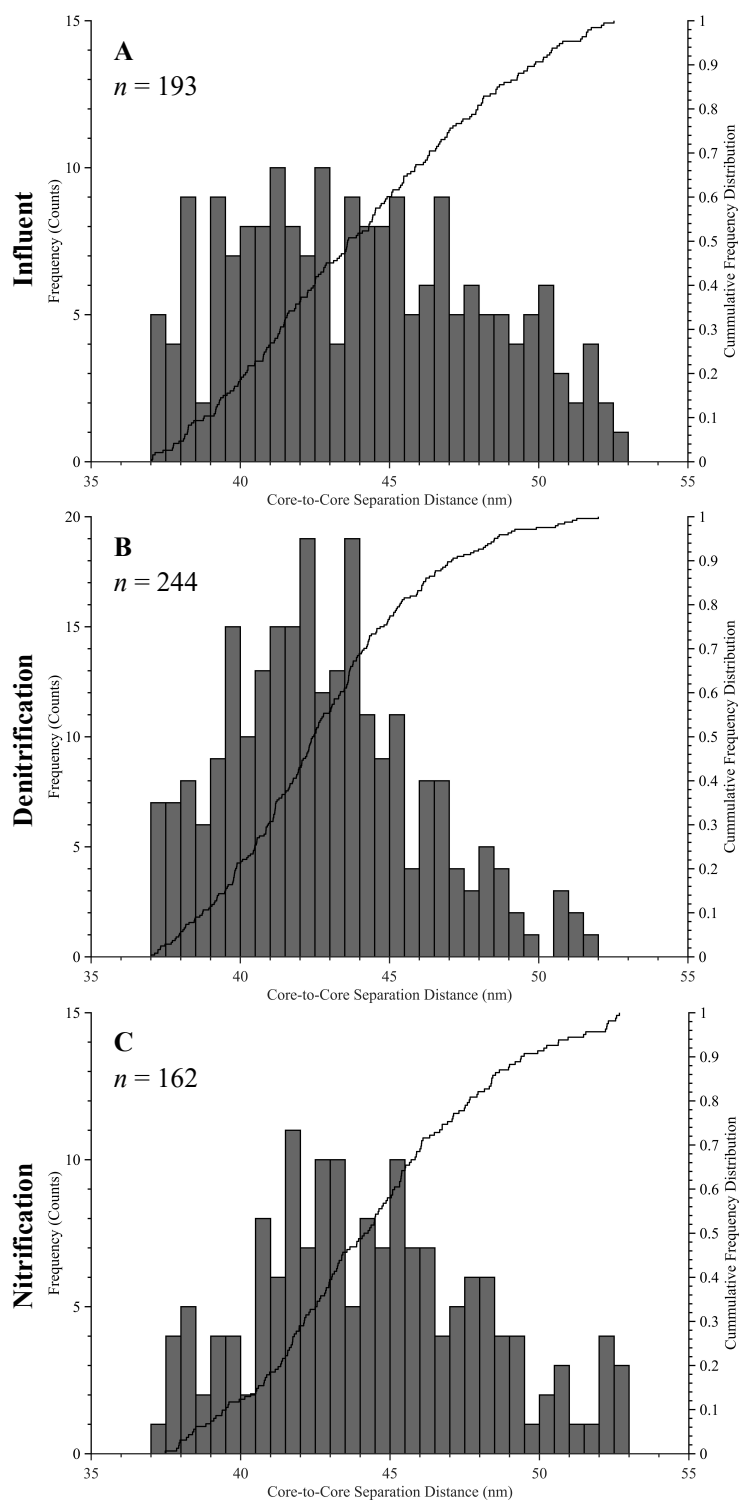


Figure C23. Distribution of center-to-center separation distances (d_s) calculated for bPEI-AuNPs incubated in (a) influent, (b) denitrification, and (c) nitrification wastewater matrices after $t = 120$ minutes.

C12. Transmission Electron Microscopy Micrographs – Matrix Exchange

Examples of the micrographs collected via transmission electron microscopy (TEM) after the AuNPs had gone through the double matrix exchange procedure via TFF are shown in Figure C24. The samples were prepared according to the procedures described in the main text.

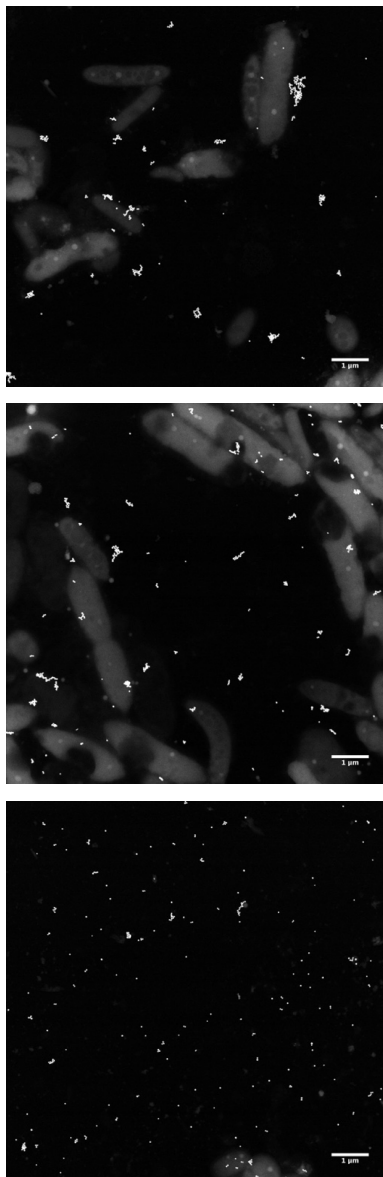


Figure C24. TEM-HAADF micrograph of (top) PEG-, (middle) COOH-, and (bottom) bPEI-AuNPs after incubating for ≈ 240 minutes during the double matrix exchange procedure.

C13. References

- 1 Henry, D. C. The cataphoresis of suspended particles. Part I. – The equation of cataphoresis. *Proc. Roy. Soc. A* 1931, **133** (821), 106.
- 2 Ohshima, H. A simple expression for Henry's function for the retardation effect in electrophoresis of spherical colloidal particles. *J. Colloid Interface Sci.* 1994, **11** (1), 269 – 271.
- 3 Hunter, R.J. *Foundations of Colloid Science, 2nd Edition* 2002. Oxford University Press, London, United Kingdom.
- 4 Benjamin, M. M.; Lawler, D.F. *Water Quality Engineering – Physical/Chemical Treatment Processes* 2013. John Wiley & Sons, Inc., Hoboken, New Jersey.
- 5 American Water Works Association (AWWA) *Standard Methods for the Examination of Water and Wastewater, 22nd Edition* 2012. American Public Health Association.
- 6 C. A. Schneider, W. S. Rasband and K. W. Eliceiri, NIH Image to ImageJ: 25 years of image analysis, *Nat. Methods*, 2012, **9**, 671–675.
- 7 J. Schindelin, I. Arganda-Carreras, E. Frise, V. Kaynig, M. Longair, T. Pietzsch, S. Preibisch, C. Rueden, S. Saalfeld, B. Schmid, J.-Y. Tinevez, D. J. White, V. Hartenstein, K. Eliceiri, P. Tomancak and A. Cardona, Fiji: an open-source platform for biological-image analysis, *Nat. Methods*, 2012, **9**, 676–682.
- 8 Wagner, T., ij-particlesizer: ParticleSizer 1.0.7 Zendo 10.5281/zenodo.56457, 2017.

D. SUPPLEMENTARY INFORMATION – FOURTH MANUSCRIPT

D1. Characterization of Pristine AuNPs

The manufacturer reported specifications and measured characteristics of the pristine AuNPs is provided in Table 5.1 (main text). The values were determined as follows:

Core Diameter (D_c): Manufacturer reported specification. Measured via transmission electron microscopy (TEM) using a JEM-1010 TEM (JEOL).

Intensity-weighted Hydrodynamic Diameter ($D_{h,initial}$): Measured in triplicate via dynamic light scattering (DLS) at 1 mg Au/L in pH-adjusted (pH \approx 7.4) 1 mM KCl (prepared in 0.2 μ m filtered 18.2 M Ω -cm Nanopure water [DDI; Barnstead]) using a 90-Plus Particle Size Analyzer (Brookhaven Instrument Corporation). Each replicate measurement ($n = 3$) was performed for 3-minutes.

Electrophoretic Mobility (μ_E): Measured in triplicate via phase analysis light scattering (PALS) at 5 mg Au/L in pH-adjusted (pH \approx 7.4) 1 mM KCl (prepared in 0.2 μ m filtered DDI) using a ZetaPALS (Brookhaven Instrument Corporation). Each replicate measurement ($n = 5$) was performed for 30 cycles. Details on the conversion of the measured μ_E to modelled zeta potential (ζ) are provided in the next section.

Surface Plasmon Resonance (λ_{SPR}): Measured via ultraviolet-visible light spectroscopy (UV-Vis) at 5 mg Au/L in 0.02 μ m filtered DDI using an Orion AquaMate 8000 (Thermo Scientific). Each replicate measurement ($n = 3$) was performed at $\lambda = 400 - 800$ nm at a scan rate of 1 nm/s using a 10 mm light-path quartz cuvette (VWR International).

D2. Zeta Potential Calculation in Simple Electrolyte Solution (1 mM KCl)

The measured μ_E , reported in Table 5.1 (main text), were converted to ζ according to Henry (1931) with the correction $f_1(\kappa a)$ applied according to Ohshima (1994), resulting in the following equation:

$$\zeta = \frac{3\mu_E\eta}{2\epsilon_w f_1(\kappa a)} = \frac{3\mu_E\eta}{2\epsilon_w \left(1 + \frac{1}{2 \left[1 + \frac{\delta}{\kappa a}\right]^3}\right)} \quad (\text{D1})$$

Where:

$$\delta = \frac{2.5}{1 + 2e^{-\kappa a}} \quad (\text{D2})$$

The definition of the variables in Equations D1 and D2, along with their corresponding values, are shown in Table D1.

Table D1. Inputs used to calculate ζ from μ_E .

Input	Value ^a	Source
Permittivity in Water (ϵ_w)	$6.95 \times 10^{-10} \text{ C}^2/\text{J}\cdot\text{m}$	Known – H ₂ O
Medium Dynamic Viscosity (η)	$1 \times 10^{-3} \text{ N}\cdot\text{s}/\text{m}^2$	Known – H ₂ O
Ohshima Fitting Parameter (δ)	1.31 – 1.32	Calculated per Hunter (2001)
Debye Length (κ)	0.104 nm^{-1}	Calculated per Benjamin & Lawler (2013)
Particle Radius (a)	7.7 nm	Measured (Table 5.1)

^a All values at 25 °C.

D3. Properties of Willamette River Water

Samples of the Willamette River water were obtained on February 25, March 5, and March 15, 2019 and were characterized according to the methods described in *Standard Methods for the Examination of Water and Wastewater, 22nd Edition* (American Public Health Association et al., 2012). All analyses were performed in triplicate and were completed according to their method-specific holding times. All samples that were collected for

analysis of the dissolved fraction were filtered within 3 hours after collection. Samples that were collected for total metals analysis were acid-preserved immediately upon collection. Samples that were collected for dissolved metals analysis were first filtered (using pre-washed filters) and then acid-preserved immediately following filtration. A summary of the results and the associated *Standard Methods* are provided in Table D2.

Table D2. Summary of Willamette River water quality parameters/characteristics.

Parameter	Feb. 25 th (PEG)	March 5 th (bPEI)	March 15 th (COOH)	Units	Method
Total Organic Carbon (TOC)	2.55 ± 0.06	1.65 ± 0.07	1.44 ± 0.09	mg C/L	Method 5310-B
Dissolved Organic Carbon (DOC)	2.47 ± 0.04	1.63 ± 0.04	1.49 ± 0.06	mg C/L	
<u>Dissolved Cations</u>					
Ca ²⁺	4.18 ± 0.22	5.11 ± 0.02	5.02 ± 0.46	mg/L	Method 3125
Mg ²⁺	1.85 ± 0.08	2.18 ± 0.26	2.31 ± 0.12	mg/L	
Na ⁺	4.10 ± 0.12	4.91 ± 0.56	4.60 ± 0.15	mg/L	
K ⁺	0.93 ± 0.08	0.79 ± 0.17	0.87 ± 0.19	mg/L	
Fe ³⁺	0.02 ± 0.05	0.04 ± 0.07	0.10 ± 0.41	mg/L	
<u>Dissolved Anions</u>					
F ⁻	N/D	N/D	0.66 ± 0.40	mg/L	Method 4110-C
Cl ⁻	3.16 ± 0.84	3.03 ± 0.39	3.44 ± 0.98	mg/L	
NO ₂ ⁻	N/D	N/D	N/D	mg/L	
NO ₃ ⁻	1.79 ± 0.48	2.15 ± 0.17	3.19 ± 0.59	mg/L	
PO ₄ ³⁻	N/D	N/D	N/D	mg/L	
SO ₄ ²⁻	4.07 ± 0.97	3.35 ± 0.20	3.54 ± 0.37	mg/L	
HCO ₃ ⁻	24.76	29.20	28.29	mg/L	Method 2320
pH	7.39	7.32	7.22		Probe
Total Suspended Solids (TSS)	104.6 ± 5.2	13.7 ± 11.2	11.3 ± 6.3	mg/L	Method 2540-D
Total Alkalinity	20.31	23.20	23.95	mg/L as CaCO ₃	Method 2320
Total Hardness	18.06 ± 0.87	22.26 ± 0.54	21.3 ± 2.22	mg/L as CaCO ₃	Method 2340-B

Error bars indicate ± 95% confidence interval ($n = 3$).

D4. Properties of Wastewater Matrix

The aquatic chemistry of the filtered wastewater matrix (prepared according to the procedure described in the main text) was determined according to the methods described in *Standard Methods for the Examination of Water and Wastewater, 22nd Edition* (American Public Health Association et al., 2012). The results are summarized in Table D3.

Table D3. Summary of primary clarifier effluent water quality parameters/characteristics.

Parameter	Feb. 26 th (PEG)	March 6 th (bPEI)	March 16 th (COOH)	Units	Method
Dissolved Organic Carbon (DOC)	10.2 ± 0.87	16.42 ± 0.61	17.66 ± 0.48	mg C/L	Method 5310-B
Conductivity	523.0	574.0	570.0	µS/cm	Probe
Ionic Strength	8.4	9.2	9.1	mM	Calculated ^a
pH	6.87	7.08	7.61		Probe
<u>Dissolved Cations</u>					
Ca ²⁺	15.69 ± 2.17	23.70 ± 1.6	23.02 ± 1.02	mg/L	
Mg ²⁺	6.63 ± 0.94	11.0 ± 0.91	11.10 ± 0.84	mg/L	
Na ⁺	21.96 ± 2.51	49.12 ± 4.32	50.36 ± 3.39	mg/L	Method 3125
K ⁺	3.90 ± 0.77	11.15 ± 1.33	9.51 ± 0.90	mg/L	
Fe ³⁺	0.05 ± 0.07	0.12 ± 0.05	0.14 ± 0.07	mg/L	
<u>Dissolved Anions</u>					
F ⁻	N/D	4.86 ± 0.19	6.98 ± 5.6	mg/L	
Cl ⁻	23.13 ± 6.38	50.14 ± 5.94	50.55 ± 6.89	mg/L	
NO ₂ ⁻	N/D	N/D	N/D	mg/L	Method 4110-C
NO ₃ ⁻	7.69 ± 11.55	6.13 ± 0.38	43.10 ± 5.22	mg/L	
PO ₄ ³⁻	N/D	9.64 ± 0.3	8.78 ± 1.04	mg/L	
SO ₄ ²⁻	18.05 ± 2.0	27.8 ± 2.53	25.69 ± 1.64	mg/L	
NH ₄ ⁺	13.53 ± 2.49	30.19 ± 1.22	36.43 ± 0.54	mg/L	Spectroquant ® Ammonium Cell Test Kit

Error bars indicate ± 95% confidence interval ($n = 3$)

^a Calculated using $I = 1.6 \times 10^{-5} \times \text{S.C.}^{133}$

D5. Testing and Storage of Tangential-Flow Filtration Cartridge

Testing. The ability of the 100 kDa molecular weight cut-off (MWCO) tangential-flow filtration (TFF) membrane to trap the AuNPs within the retentate was tested per the following:

- 1) A 250 mL sample containing the AuNPs was prepared by dispersing the COOH-AuNPs in the filtered wastewater matrix to $C_{NP} = 1.0$ mg/L ($V_{WW} = 245$ mL; $V_{NP} = 5$ mL).
- 2) Immediately upon dosing, 1 mL sample aliquots were collected in triplicate via calibrated pipette and transferred to separate 7 mL perfluoroalkoxy alkane (PFA) vials to measure the initial solution concentration. The remainder of the dispersion was incubated for ≈ 30 minutes.
- 3) After the incubation period, the AuNP/wastewater dispersion was circulated through the TFF cartridge according to the procedure described in the main text.
- 4) Upon completion of the concentration/separation process, 1 mL sample aliquots were collected from the TFF retentate in triplicate via calibrated pipette and transferred to separate 7 mL PFA vials to measure the final solution concentration.
- 5) The vessel containing the TFF permeate was briefly mixed via gentle shaking and 5 mL sample aliquots were collected in triplicate via calibrated pipette and transferred to separate 7 mL PFA vials to measure the permeate concentration.
- 6) All the samples were digested in fresh *aqua regia* (3:1 HCl:HNO₃) according to the procedure detailed below and analyzed via inductively-coupled plasma mass spectrometry (ICP-MS).

The results, shown in Table D4, indicate that $\approx 99\%$ of the AuNP mass was retained within the TFF system.

Table D4. Concentration of COOH-AuNPs in TFF permeate.

	Average Concentration ($\mu\text{g/L}$)
Initial Solution	1,135.4 \pm 344.8
Final Solution (Retentate)	5,886.1 \pm 312.5
Permeate	12.5 \pm 8.7

Error bars indicate \pm 95% confidence interval ($n = 3$).

Storage. Prior to each use, the TFF cartridge was flushed with ≥ 500 mL of DDI and then drained before the AuNP/wastewater dispersion was circulated. After each use, the TFF cartridge was cleaned by continuously circulating a solution of 0.5 M NaOH (prepared in DDI) through the TFF cartridge for >30 minutes followed by flushing the TFF cartridge with ≥ 500 mL of DDI. After draining, the TFF cartridge was filled with a 10% ethanol (EtOH) solution (prepared in DDI) and stored at 4 °C in the dark.

D6. Verification of Aged AuNP Sizes after Overnight Storage

After aging each AuNP type, the intensity-weighted hydrodynamic diameter (D_h) of the aged AuNPs was measured. Samples were analyzed in triplicate at $C_{NP} = 1$ mg Au/L in either filtered river water or TFF permeate by combining 2.4 mL of the selected matrix with 0.6 mL of the aged AuNP dispersion. After overnight storage (<12 hours), the D_h of the aged AuNPs was measured again in 0.2 μm -filtered DDI at $C_{NP} = 1$ mg Au/L. Each replicate measurement ($n = 3$) was performed for 3-minutes. The results, summarized in Table D5, indicate negligible changes in D_h after overnight storage.

Table D5. Intensity-weighted hydrodynamic diameter (D_h) of aged AuNPs measured before and after overnight storage.

Surface Coating	D_h Before Storage – Filtered River Water (nm)	D_h Before Storage – TFF Permeate (nm)	D_h After Storage – DDI (nm)
PEG	113.6 ± 7.7	116.4 ± 8.6	127.2 ± 4.1
COOH	250.5 ± 16.2	229.3 ± 3.7	255.4 ± 4.0
bPEI	216.1 ± 4.1	194.8 ± 3.2	215.3 ± 14.9

Error bars indicate ± 95% confidence interval ($n = 3$).

D7. Digestion Technique

Once all sample aliquots were generated for a given batch, each aliquot was acid-digested according to the following procedure:

1. Each aliquot, contained within either a 7 mL perfluoroalkoxy alkane (PFA) vial or a 100 mL polytetrafluoroethylene (PTFE) beaker, was placed on a hot plate, uncapped, and heated at 200 °C to evaporate off the water. The PFA vials were used for the small sample aliquots (5 mL) and the PTFE beakers were used for the large sample aliquots (30 mL).
2. Once a small amount of residue remained (≤ 1 mL), freshly-prepared *aqua regia* (3:1 ultrapure HCl:HNO₃) was added to each vessel and heated at 200 °C to evaporate off the *aqua regia*. The amount of *aqua regia* added to each vessel was as follows: 4 mL (3 mL:1 mL HCl: HNO₃) to the PFA vials and 8 mL (6 mL:2 mL HCl: HNO₃) to the PTFE beakers.
3. When a small drop of *aqua regia*/residue remained, the vessels were removed from the hot plate and allowed to cool to room temperature.
4. After cooling to room temperature, each sample was transferred to a pre-weighed 15-mL (PFA) or 50-mL (PTFE) polypropylene centrifuge tube (Falcon™, BD Biosciences). Each digestion vessel was triple-rinsed with $\approx 2\%$ *aqua regia* (diluted using DDI), with the rinsate transferred between each rinsing step.

5. After the final rinsing, each polypropylene centrifuge tube was re-weighed and the total, final volume was determined gravimetrically. The tubes were stored at 4 °C in the dark (in $\approx 2\%$ *aqua regia*) until analysis via ICP-MS.

D8. Digestion Technique – Spike/Recovery Testing

To verify that the digestion technique resulted in adequate recovery (i.e., $>90\%$) of the pristine and aged AuNPs, a spike/recovery test was performed. The intent of the spike/recovery test was to mimic the experimental procedure used in the batch experiments but generate a ‘worst-case’ scenario where no model ENMs are removed via centrifugation after mixing in the raw river water. To simulate this, samples of the pristine or aged AuNPs were spiked into samples of the centrifuged river water before digestion.

1. Six 15-mL polypropylene centrifugation vials (Falcon™, BD Biosciences) were each filled with 12 mL of raw river water and centrifuged at 3,500 rpm ($\approx 2,200\times$ RCF) for 5 minutes.
2. Immediately following centrifugation, an 8-mL sample of the supernatant was collected from each vial, transferred to a single, separate 50-mL polypropylene centrifugation vial, and gently mixed. This constituted the centrifuged river water and was used to prepare all subsequent samples.
3. Using 7-mL PFA vials, 5-mL samples containing the centrifuged river water were prepared in triplicate and dosed to a target initial AuNP concentration ($C_{NP,initial}$) of 250 $\mu\text{g/L}$ using either the pristine or the aged COOH-AuNPs (aged immediately prior to use).
 - a. For the pristine COOH-AuNPs, 4.975 mL of centrifuged river water was combined with 0.025 mL of the pristine COOH-AuNP dispersion. The concentration of the pristine COOH-AuNP stock dispersion was separately measured by preparing duplicate 5-mL samples containing DDI dosed to $C_{NP} = 250 \mu\text{g/L}$.
 - b. For the aged COOH-AuNPs, 4.875 mL of the centrifuged river water was combined with 0.125 mL of the aged COOH-AuNP/wastewater dispersion.

The concentration of the aged COOH-AuNP/wastewater dispersion was separately measured, as reported in Table D4 (Final Solution – Retentate).

- c. Three separate 7-mL PFA vials were prepared containing only the centrifuged river water and were used to quantify the background Au concentration in the river water.
4. All nine PFA vials were then acid digested according to the procedure outlined above and analyzed via ICP-MS.

The background Au concentration within the centrifuged river water was 11.4 ± 8.26 $\mu\text{g/L}$. The results of the samples spiked with the pristine and aged COOH-AuNPs is summarized in Table D6. To calculate the percent recovery, the actual dosing concentrations were re-calculated based on the measured concentrations of the COOH-AuNP stock dispersion ($C_{stock} = 45.0 \pm 1.6$ mg/L ; $n = 2$) and the aged COOH-AuNP/wastewater dispersion ($C_{retentate} = 5.90 \pm 0.31$ mg/L ; $n = 3$). The results indicate good recovery was obtained for both the pristine and aged COOH-AuNPs. Thus, the digestion technique was considered adequate to digest the samples collected during the batch experiments.

Table D6. Measured AuNP concentration and percent recovery of pristine and aged COOH-AuNPs in centrifuged river water.

Sample	Actual AuNP Dosing Concentration (Calculated) ($\mu\text{g/L}$)	Recovered AuNP Concentration (Measured) ($\mu\text{g/L}$)	Average Percent Recovery (%)
Pristine	224.8	259.1 ± 43.5	115.3 ± 19.4
Aged	147.2	145.0 ± 11.1	98.5 ± 7.5

Error bars indicate $\pm 95\%$ confidence interval ($n = 3$).

D9. Supporting Analytics – Pristine AuNPs in Filtered River Water

The characteristics of the pristine AuNPs were measured in 0.2 μm filtered river water, according to the following procedures:

DLS: The intensity-weighted hydrodynamic diameter (D_h) was measured over time via time-resolved dynamic light scattering (TR-DLS). Duplicate samples were prepared at 1 mg Au/L and measured immediately after dosing using a 90-Plus Particle Size Analyzer (Brookhaven Instrument Corporation) Each sample was analyzed via 120 measurements, each 15 seconds long (≈ 30 minutes).

PALS: The electrophoretic mobility (μ_E) was measured in via phase analysis light scattering (PALS). Triplicate samples were prepared at 5 mg Au/L, allowed to incubate for $\approx 20 - 30$ minutes, and then measured using a ZetaPALS (Brookhaven Instrument Corporation). Each replicate measurement ($n = 5$) was performed for 30 cycles.

UV-Vis: The surface plasmon resonance (λ_{SPR}) was measured via ultraviolet-visible light spectroscopy (UV-Vis). Triplicate samples were prepared at 5 mg Au/L, allowed to incubate for $\approx 20 - 30$ minutes, and then measured using an Orion AquaMate 8000 (Thermo Scientific). Each replicate measurement ($n = 3$) was performed at $\lambda = 400 - 800$ nm at a scan rate of 1 nm/s using a 10 mm light-path quartz cuvette (VWR International).

D10. Supporting Analytics – Aged AuNPs in Various Media

The characteristics of the aged AuNPs were measured in 0.2 μm filtered river water and TFF permeate, according to the procedures below. Due to the lower concentration of the aged AuNP/wastewater dispersion (≈ 5 mg Au/L; see Table D4), each sample was prepared at ≈ 1 mg Au/L.

DLS: The intensity-weighted hydrodynamic diameter (D_h) was measured via dynamic light scattering (DLS). Triplicate samples were prepared and measured using a 90-Plus Particle Size Analyzer (Brookhaven Instrument Corporation). Each sample was analyzed via 3 measurements, each 3 minutes long. The D_h of each AuNP type was also measured in DDI at the same conditions.

PALS: The electrophoretic mobility (μ_E) was measured via phase analysis light scattering (PALS). Triplicate samples were prepared, allowed to incubate for ≈ 20 – 30 minutes, and then measured using a ZetaPALS (Brookhaven Instrument Corporation). Each replicate measurement ($n = 5$) was performed for 30 cycles.

UV-Vis: The surface plasmon resonance (λ_{SPR}) was measured via ultraviolet-visible light spectroscopy (UV-Vis). Triplicate samples were prepared, allowed to incubate for ≈ 20 – 30 minutes, and then measured using an Orion AquaMate 8000 (Thermo Scientific). Each replicate measurement ($n = 3$) was performed at $\lambda = 400$ – 800 nm at a scan rate of 1 nm/s using a 10 mm light-path quartz cuvette (VWR International).

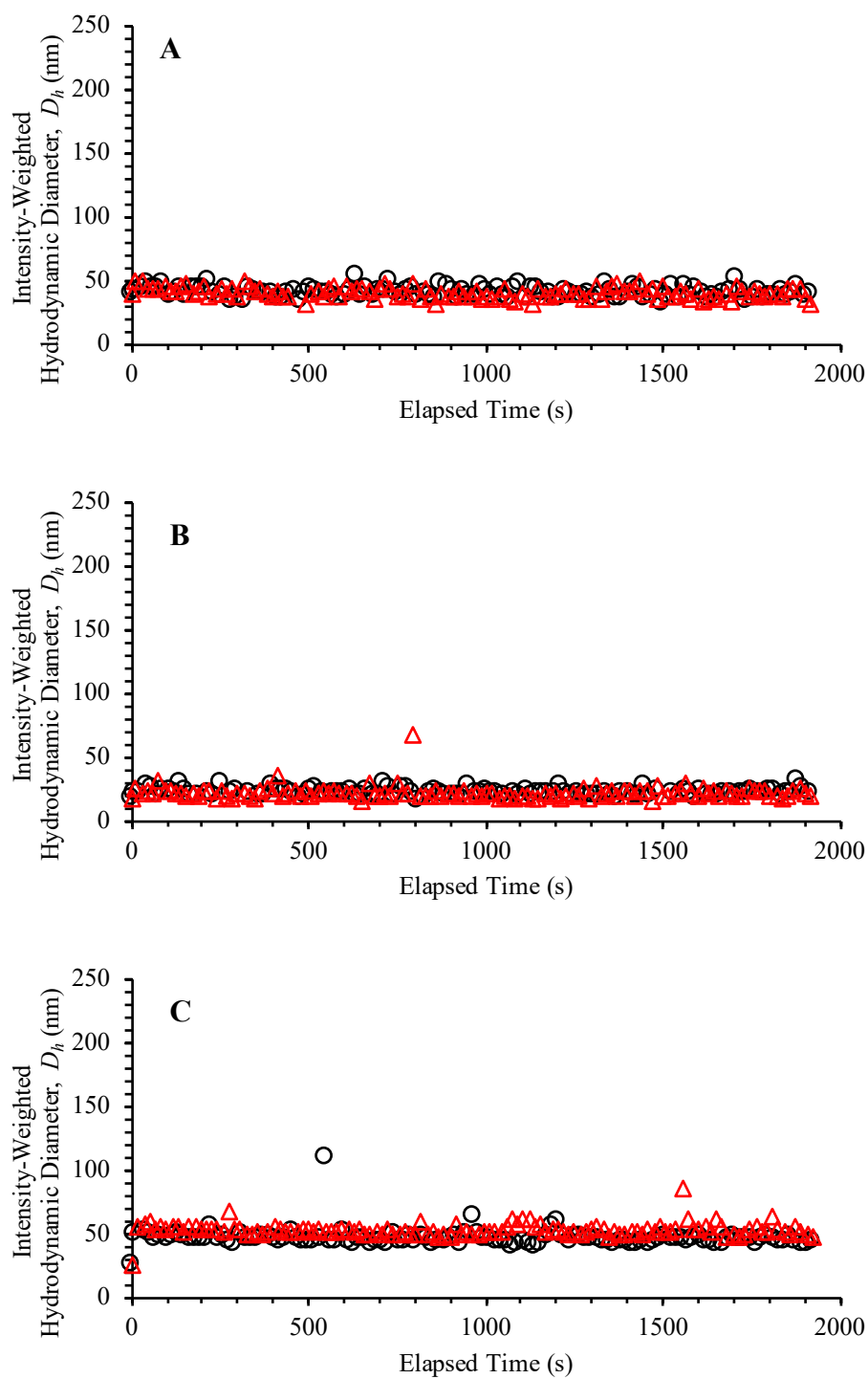
D11. TR-DLS of Pristine AuNPs in Filtered River Water

Figure D1. Intensity-weighted hydrodynamic diameter (D_h) as a function of time for pristine (a) PEG-AuNPs, (b) COOH-AuNPs, and (c) bPEI-AuNPs in filtered river water.

D12. Concentration of Pristine and Aged AuNPs in Centrifuged River Water and DDI Controls

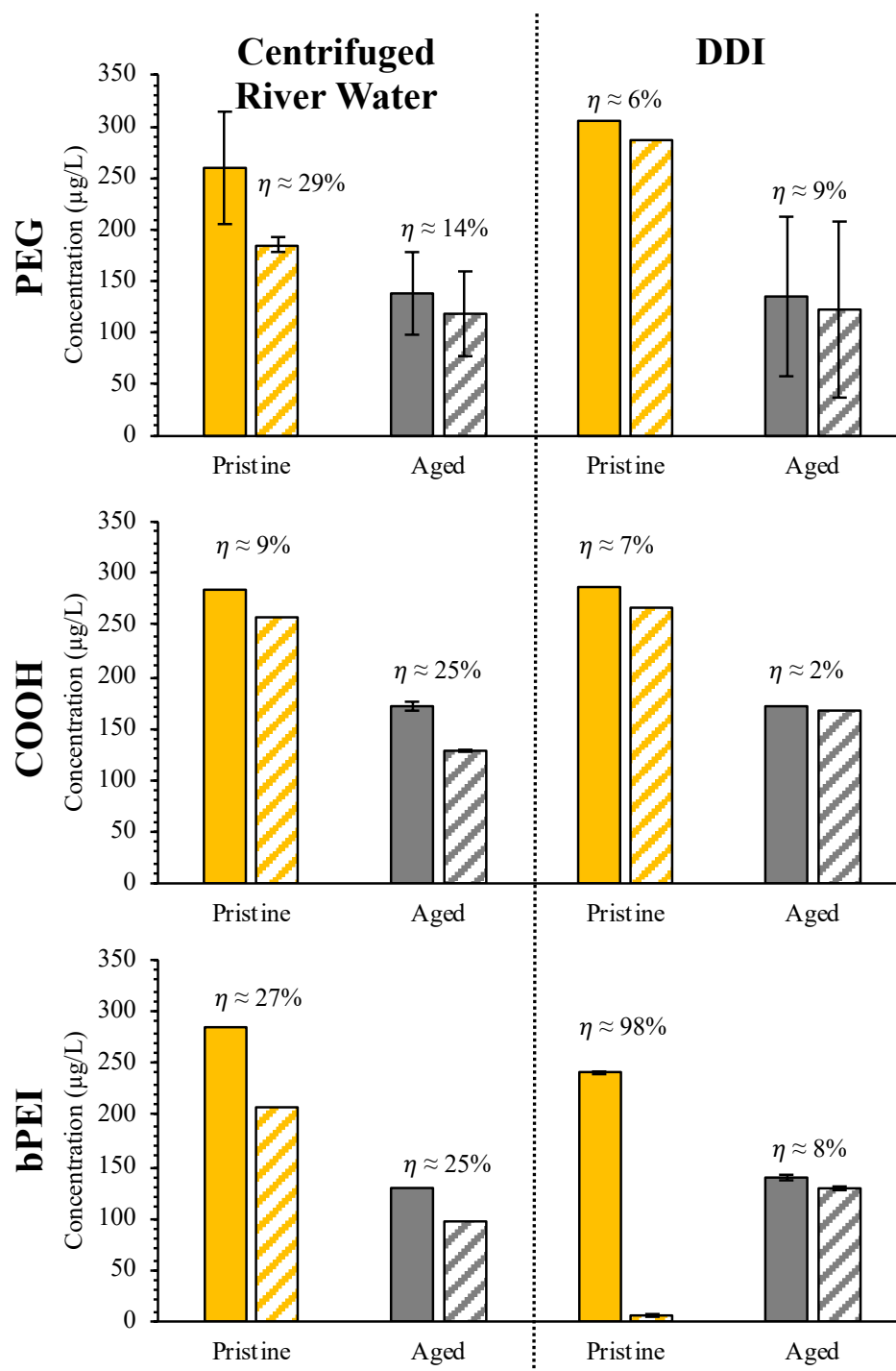


Figure D2. $C_{NP,initial}$ (solid) and $C_{NP,final}$ (hashed) for each AuNP type/form in centrifuged river water and DDI. When shown, error bars indicate \pm standard deviation ($n = 2$); otherwise, only a single measurement was available.

D13. UV-Vis Spectra of Pristine and Aged AuNPs in Various Media

The background-corrected and normalized UV-Vis spectra for the pristine and aged AuNPs were generated according to the procedures described previously. (Surette et al. 2019) Briefly, for each UV-Vis measurement, the background-corrected UV-Vis spectrum was generated by subtracting the blank-corrected background spectrum (measured prior to the addition of the AuNPs) from the UV-Vis spectrum measured after the addition of the AuNPs. The background-corrected and normalized (A/A_{max}) UV-Vis spectrum was generated by dividing the background-corrected absorbance at each wavelength (A) by the maximum absorbance (A_{max}) that was measured. A moving average ($n = 5$) was then applied to smooth the data. Due to the broadness of the UV-Vis spectra, in particular the aged COOH-AuNPs, the λ_{SPR} were identified at the approximate mid-point of the peak.

Table D7. Surface plasmon resonance (λ_{SPR}) of pristine and aged AuNPs in various media.

Surface Coating	Pristine AuNPs		Aged AuNPs	
	DDI (nm)	Filtered River Water (nm)	Filtered River Water (nm)	TFF Permeate (nm)
PEG	519.2 ± 1.9	518.8 ± 2.2	521.7 ± 0.7*	521.2 ± 3.6
COOH	518.5 ± 5.4	522.2 ± 1.4	574.5 ± 28.0*	580.3 ± 11.1*
bPEI	521.5 ± 2.2	529.6 ± 0.7*	538.0 ± 1.2*	532.8 ± 7.9*

Error bars indicate ± 95% confidence interval ($n = 3$).

* Indicates significant difference relative to λ_{SPR} measured in DDI ($\alpha = 0.05$; two-way t -test; $n = 3$).

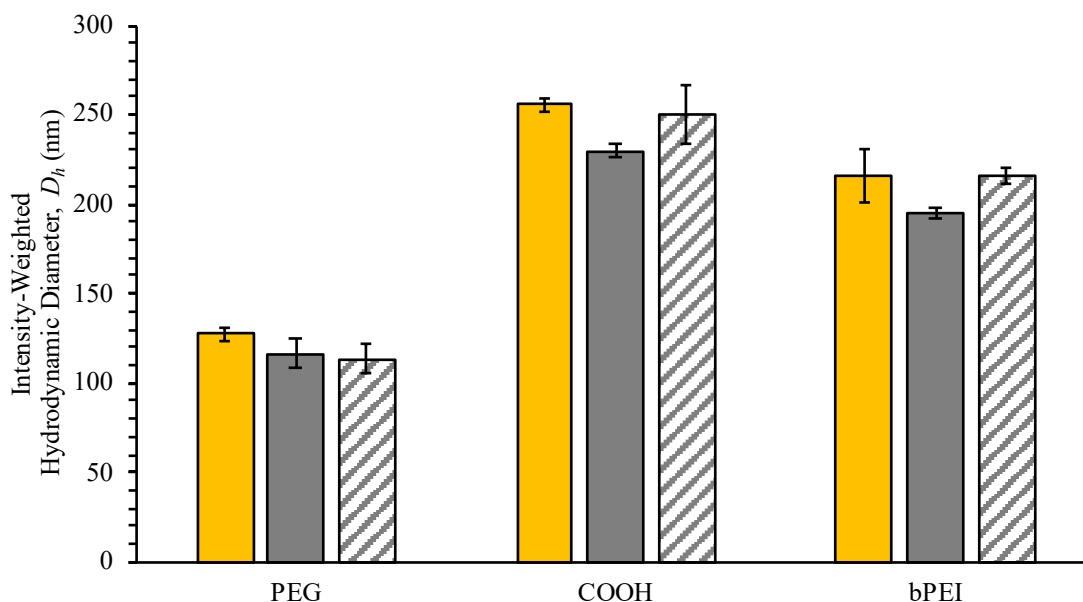
To calculate the full-width at half-max (FWHM), the wavelengths where $A/A_{max} = 0.5$ were identified. In all cases, this only occurred at a single wavelength $>\lambda_{SPR}$. As such, the FWHM was set to this wavelength and no further data treatment was performed. These results are summarized in Table D8.

Table D8. Full-width at half max (FWHM) of pristine and aged AuNPs in various media.

Surface Coating	Pristine AuNPs		Aged AuNPs	
	In DDI (nm)	In Filtered River Water (nm)	In Filtered River Water (nm)	In TFF Permeate (nm)
PEG	559	559.5	566.5	574.5
COOH	564	579.5	673.5	673
bPEI	571	599	578.5	575

D14. Intensity-weighted Hydrodynamic Diameter of Aged AuNPs in Various Media

The intensity-weighted hydrodynamic diameter (D_h) of the aged AuNPs was measured in DDI, TFF permeate and filtered river water, according to the procedures described previously. Due to the lower concentration of the aged AuNP/wastewater dispersion (≈ 5 mg Au/L; see Table D4), each sample was prepared at ≈ 1 mg Au/L.

**Figure D3.** Intensity-weighted hydrodynamic diameter of each aged AuNP type ($D_{h,aged}$) in DDI (solid gold); TFF permeate (solid grey); and filtered river water (hashed). Error bars indicate $\pm 95\%$ confidence interval ($n = 3$).

D15. References

- 1 Henry, D. C. The cataphoresis of suspended particles. Part I. – The equation of cataphoresis. *Proc. Roy. Soc. A* 1931, **133** (821), 106.
- 2 Ohshima, H. A simple expression for Henry's function for the retardation effect in electrophoresis of spherical colloidal particles. *J. Colloid Interface Sci.* 1994, **11** (1), 269 – 271.
- 3 Hunter, R.J. *Foundations of Colloid Science, 2nd Edition* 2002. Oxford University Press, London, United Kingdom.
- 4 Benjamin, M. M.; Lawler, D.F. *Water Quality Engineering – Physical/Chemical Treatment Processes* 2013. John Wiley & Sons, Inc., Hoboken, New Jersey.
- 5 *Standard Methods for the Examination of Water and Wastewater, 22nd Edition* 2012. American Public Health Association (APHA), American Water Works Association (AWWA), and Water Environment Foundation (WEF).